TAMPEREEN TEKNILLINEN YLIOPISTO
TAMPERE UNIVERSITY OF TECHNOLOGY

Markus Allén

Nonlinear Distortion in Wideband Radio Receivers and Analog-to-Digital Converters: Modeling and Digital Suppression

Julkaisu 1329 • Publication 1329

Tampere 2015

Tampereen teknillinen yliopisto. Julkaisu 1329
Tampere University of Technology. Publication 1329

Markus Allén

Nonlinear Distortion in Wideband Radio Receivers and Analog-to-Digital Converters: Modeling and Digital Suppression

Thesis for the degree of Doctor of Science in Technology to be presented with due permission for public examination and criticism in Tietotalo Building, Auditorium TB103, at Tampere University of Technology, on the 23rd of October 2015, at 12 noon.

Tampereen teknillinen yliopisto - Tampere University of Technology
Tampere 2015

Supervisor
Mikko Valkama, Professor
Department of Electronics and Communications Engineering
Tampere University of Technology
Tampere, Finland

Pre-examiners
Gerhard Fettweis, Professor
Vodafone Chair Mobile Communications Systems
Dresden University of Technology
Dresden, Germany

Peter Händel, Professor
Department of Signal Processing
Royal Institute of Technology (KTH)
Stockholm, Sweden

Opponent
Thomas Eriksson, Professor
Department of Signals and Systems
Chalmers University of Technology
Gothenburg, Sweden

Painopaikka:
Suomen Yliopistopaino Oy
Juvenes Print TTY
Tampere 2015

ISBN 978-952-15-3595-6 (printed)
ISBN 978-952-15-3611-3 (PDF)
ISSN 1459-2045

Abstract

Emerging wireless communications systems aim to flexible and efficient usage of radio spectrum in order to increase data rates. The ultimate goal in this field is a cognitive radio. It employs spectrum sensing in order to locate spatially and temporally vacant spectrum chunks that can be used for communications. In order to achieve that, flexible and reconfigurable transceivers are needed. A software-defined radio can provide these features by having a highly-integrated wideband transceiver with minimum analog components and mostly relying on digital signal processing. This is also desired from size, cost, and power consumption point of view. However, several challenges arise, from which dynamic range is one of the most important. This is especially true on receiver side where several signals can be received simultaneously through a single receiver chain. In extreme cases the weakest signal can be almost 100 dB weaker than the strongest one. Due to the limited dynamic range of the receiver, the strongest signals may cause nonlinear distortion which deteriorates spectrum sensing capabilities and also reception of the weakest signals. The nonlinearities are stemming from the analog receiver components and also from analog-to-digital converters (ADCs). This is a performance bottleneck in many wideband communications and also radar receivers. The dynamic range challenges are already encountered in current devices, such as in wideband multi-operator receiver scenarios in mobile networks, and the challenges will have even more essential role in the future.

This thesis focuses on aforementioned receiver scenarios and contributes to modeling and digital suppression of nonlinear distortion. A behavioral model for direct-conversion receiver nonlinearities is derived and it jointly takes into account RF, mixer, and baseband nonlinearities together with I/Q imbalance. The model is then exploited in suppression of receiver nonlinearities. The considered method is based on adaptive digital post-processing and does not require any analog hardware modification. It is able

to extract all the necessary information directly from the received waveform in order to suppress the nonlinear distortion caused by the strongest blocker signals inside the reception band.

In addition, the nonlinearities of ADCs are considered. Even if the dynamic range of the analog receiver components is not limiting the performance, ADCs may cause considerable amount of nonlinear distortion. It can originate, e.g., from undeliberate variations of quantization levels. Furthermore, the received waveform may exceed the nominal voltage range of the ADC due to signal power variations. This causes unintentional signal clipping which creates severe nonlinear distortion. In this thesis, a Fourier series based model is derived for the signal clipping caused by ADCs. Furthermore, four different methods are considered for suppressing ADC nonlinearities, especially unintentional signal clipping. The methods exploit polynomial modeling, interpolation, or symbol decisions for suppressing the distortion. The common factor is that all the methods are based on digital post-processing and are able to continuously adapt to variations in the received waveform and in the receiver itself. This is a very important aspect in wideband receivers, especially in cognitive radios, when the flexibility and state-of-the-art performance is required.

Preface

This thesis is based on research work carried out during the years 2010–2015 at the Department of Electronics and Communications Engineering (former Department of Communications Engineering), Tampere University of Technology, Tampere, Finland. I gratefully acknowledge the financial support of Tampere University of Technology Graduate School (during 2011–2014), Tampere Doctoral Programme in Information Science and Engineering (TISE), Jenny and Antti Wihuri Foundation, and Finnish Foundation for Technology Promotion (TES). Furthermore, the following project funding is acknowledged: Academy of Finland (project 116423 "Understanding and Mitigation of Analog RF Impairments in Multiantenna Transmission Systems" and project 251138 "Digitally-Enhanced RF for Cognitive Radio Devices"), Finnish Funding Agency for Technology and Innovation (Tekes, "Advanced Techniques for RF Impairment Mitigation in Future Wireless Radio Systems" and "Enabling Methods for Dynamic Spectrum Access and Cognitive Radio"), Austrian Competence Center in Mechatronics (ACCM), Technology Industries of Finland Centennial Foundation, Cassidian / EADS Deutschland GmbH, and Nokia Networks.

First and foremost I would like to thank my supervisor Prof. Mikko Valkama. His support, energetic mindset, and invaluable contact networks have enabled my career and basically everything I am today as a researcher. I hope that some day I will adopt even a tiny bit of his multitasking ability. I am also deeply grateful to Prof. Markku Renfors for sharing his knowledge in general and giving me an opportunity to find the lecturer in me. I also want to acknowledge all his efforts for our department and creating the exceptionally good atmosphere.

I am grateful to the thesis pre-examiners, Prof. Gerhard Fettweis and Prof. Peter Händel, for their valuable efforts. Furthermore, I am indebted to Prof. Thomas Eriksson for agreeing to act as an opponent in the public examination of my thesis.

I would like to express my gratitude to Georg Vallant, Simran Singh, Michael Epp, and Wolfgang Schlecker for making my research visit to Cassidian (currently Airbus Defence and Space GmbH), Germany, and all our collaboration ever since such a great pleasure. In addition, I would like to thank Michael Grimm and Prof. Reiner Thomä from Ilmenau University of Technology, Germany, for fruitful collaboration and the time spent together in Germany and in Finland. Furthermore, I would like to thank Semu Mäkinen, Marko Kosunen, and Prof. Jussi Ryynänen from the Department of Micro- and Nanosciences, Aalto University, for all the collaboration we have done. Also, I have found our latest collaboration with Nokia very useful and hence I would like to thank the people from Nokia, especially Jorma Pallonen and Hans Somerma.

Among all my colleagues, I am most indebted to Jaakko Marttila who has been working in close co-operation with me since 2008. It has been a great pleasure to realize together how things work in science and sometimes also in other fields. In addition to Jaakko, I would like to thank Toni Levanen and Jukka Talvitie for providing countless hours of musing and amusing activities inside and outside the university. You give me what I need when my head is full of (research) problems. I have been very fortunate to work with and be in contact with many great colleagues including Vesa Lehtinen, Ville Syrjälä, Lauri Anttila, Tero Isotalo, Pedro Figueiredo e Silva, Joonas Säe, Aki Hakkarainen, Timo Huusari, Janis Werner, Dani Korpi, Yaning Zou, Adnan Kiayani, and Ari Asp. I would like to thank you and all the other colleagues for scientific discussions and bringing your own personal touch to our academic working environment. In addition, I am grateful to Sari Kinnari, Soile Lönnqvist, Heli Ahlfors, Tarja Erälaukko, Kirsi Viitanen, and Marianna Jokila for all their help with practicalities and making things possible.

I am also extremely thankful to all my friends I have not yet mentioned here. Yes, it also includes you. I really appreciate those unforgettable midsummer celebrations and all other things we have experienced together. I also have to give some credit to Svenska Aeroplan AB and Valmet Automotive for creating products that one can really enjoy and rely on during work trips. During this thesis project I have found the greatness of Eino Leino and Edith Södergran. Their poems have given me inspiration, strength, and acceptance. It is peaceful to know that the sun is always up there, although sometimes the weather is cloudy.

Last but definitely not least, the people who deserve their own paragraph: my parents Anja and Matti as well as my brother Timo. I would like to sincerely express my warmest gratitude to you for always supporting me and believing in me. Especially I want to thank you for giving me my down-to-earth attitude.

Tampere, August 2015

Markus Allén

Table of Contents

List of Publications

This thesis is a compound thesis based on the following nine publications.

[P1] M. Allén, J. Marttila, and M. Valkama, "Digital post-processing for reducing A/D converter nonlinear distortion in wideband radio receivers," in *Conference Record of the 43th Asilomar Conference on Signals, Systems and Computers (Asilomar2009)*, Pacific Grove, CA, USA, Nov. 2009, pp. 1111–1114. DOI: 10.1109/ACSSC.2009.5470052

[P2] M. Allén, J. Marttila, and M. Valkama, "Modeling and mitigation of nonlinear distortion in wideband A/D converters for cognitive radio receivers," *International Journal of Microwave and Wireless Technologies*, vol. 2, no. 2, pp. 183–192, Apr. 2010. DOI: 10.1017/S1759078710000292

[P3] M. Allén, J. Marttila, and M. Valkama, "Digitally-enhanced wideband analog-digital interfaces for future cognitive radio devices," in *Proceedings of the 8th IEEE International NEWCAS Conference (NEWCAS2010)*, Montréal, QC, Canada, June 2010, pp. 361–364. DOI: 10.1109/NEWCAS.2010.5604009

[P4] M. Allén, J. Marttila, and M. Valkama, "Iterative signal processing for mitigation of wideband ADC nonidealities in cognitive radio receiver," in *Proceedings of the 19th European Signal Processing Conference (EUSIPCO2011)*, Barcelona, Spain, Aug. 2011, pp. 2279–2283.

[P5] M. Allén, T. Levanen, J. Marttila, and M. Valkama, "Iterative signal processing for mitigation of analog-to-digital converter clipping distortion in multiband OFDMA receivers," *Journal of Electrical and Computer Engineering*, vol. 2012, 16 pages. DOI: 10.1155/2012/532560

[P6] M. Allén, J. Marttila, and M. Valkama, "General clipping modeling and DSP-based mitigation for wideband A/D interface and RF front-end of emerging radio receivers," in *Proceedings of the IEEE 55th International Midwest Symposium on Circuits and Systems (MWSCAS2012)*, Boise, ID, USA, Aug. 2012, pp. 1148–1151. DOI: 10.1109/MWSCAS.2012.6292228

[P7] M. Allén, J. Marttila, M. Valkama, S. Mäkinen, M. Kosunen, and J. Ryynänen, "Digital linearization of direct-conversion spectrum sensing receiver," in *Proceedings of the 1st IEEE Global Conference on Signal and Information Processing (GlobalSIP2013)*, Austin, TX, USA, Dec. 2013, pp. 1158–1161. DOI: 10.1109/GlobalSIP.2013.6737112

[P8] M. Grimm, M. Allén, J. Marttila, M. Valkama, and R. Thomä, "Joint mitigation of nonlinear RF and baseband distortions in wideband direct-conversion receivers," *IEEE Transactions on Microwave Theory and Techniques*, vol. 62, no. 1, pp. 166–182, Jan. 2014. DOI: 10.1109/TMTT.2013.2292603

[P9] M. Allén, J. Marttila, M. Valkama, M. Grimm, and R. Thomä, "Digital post-processing based wideband receiver linearization for enhanced spectrum sensing and access," in *Proceedings of the 9th International Conference on Cognitive Radio Oriented Wireless Networks and Communications (CROWNCOM2014)*, Oulu, Finland, June 2014, 6 pages. DOI: 10.4108/icst.crowncom.2014.255428

Abbreviations

A/D	Analog-to-digital
ADC	Analog-to-digital converter
AF	Adaptive filter
AGC	Automatic gain control
AIC	Adaptive interference cancellation
BB	Baseband
BER	Bit error ratio
CP	Cyclic prefix
CR	Cognitive radio
DCR	Direct-conversion receiver
DNL	Differential nonlinearity
DSA	Dynamic spectrum access
DSP	Digital signal processing
E-AIC	Enhanced adaptive interference cancellation
EW	Electronic warfare
FIR	Finite impulse response
FS	Full scale
GSM	Global System for Mobile Communications
GSM-R	GSM-Railway
HCF	High code frequency
I/Q	In-phase/quadrature
IF	Intermediate frequency
IIP3	Input-referred third-order intercept point
IMD	Intermodulation distortion
INL	Integral nonlinearity

IRR	Image rejection ratio
ITU	International Telecommunication Union
ITU-R	ITU Radiocommunication Sector
LCF	Low code frequency
LMS	Least-mean-square
LNA	Low-noise amplifier
LS	Least squares
LSB	Least significant bit
LTE	Long-Term Evolution
LUT	Look-up table
MSI	Maximum selection interpolation
NLMS	Normalized least-mean-square
OFDM	Orthogonal frequency-division multiplexing
OFDMA	Orthogonal frequency-division multiple access
PA	Power amplifier
PAPR	Peak-to-average power ratio
PSD	Power spectral density
QPSK	Quadrature phase shift keying
RC-WL	Reduced-complexity widely-linear
RF	Radio frequency
RLS	Recursive least squares
SC	Subcarrier
SC-FDMA	Single-carrier frequency-division multiple access
SDR	Software-defined radio
SER	Symbol error ratio
SFDR	Spurious-free dynamic range
SL	Strictly-linear
SNDR	Signal-to-noise-and-distortion ratio
SNR	Signal-to-noise ratio
SQNR	Signal-to-quantization-noise ratio
UMTS	Universal Mobile Telecommunications System
WL	Widely-linear
WLAN	Wireless local area network

Symbols and Notations

$\mathbf{0}_{a\times b}$	Zero matrix of size $a \times b$
$A(t)$	Envelope of $x(t)$
$\hat{A}(n)$	Envelope of $\hat{x}(n)$
a_1, a_2	Complex coefficients in the simplified RF nonlinearity model
$a_{3\mathrm{I}}, a_{4\mathrm{I}}$	Real coefficients in I branch of simplified BB nonlinearity model
$a_{3\mathrm{Q}}, a_{4\mathrm{Q}}$	Real coefficients in Q branch of simplified BB nonlinearity model
B	Nominal number of bits in ADC
$\mathbf{b}$	Vector of data bits to be transmitted
$\hat{\mathbf{b}}$	Vector of received data bits
$b_1(t), b_2(t), b_3(t), \ldots$	Impulse responses for different RF nonlinearity terms
C	Clipping level for an ADC
$\tilde{C}(t)$	Modified clipping level for an ADC for modeling purposes
$c_{1,\ldots,M}^{(U_k)}$	Coded bits for the data symbol U_k in the OFDM subcarrier k
$\hat{c}_{1,\ldots,M}^{(U_k)}$	Estimate of coded bits related to the data symbol U_k
$c_{1\mathrm{I}}(t), c_{2\mathrm{I}}(t), \ldots$	Impulse responses for different BB nonlinearity terms in I branch
$c_{1\mathrm{Q}}(t), c_{2\mathrm{Q}}(t), \ldots$	Impulse responses for different BB nonlinearity terms in Q branch
$C_{\mathrm{H}}, C_{\mathrm{L}}$	Higher (H) and lower (L) clipping level for an ADC
$\tilde{C}_{\mathrm{H}}(t), \tilde{C}_{\mathrm{L}}(t)$	Modified higher and lower clipping level for an ADC
$C_{\mathrm{H,I}}, C_{\mathrm{L,I}}$	Higher and lower clipping level for the I branch ADC
$\tilde{C}_{\mathrm{H,I}}(t), \tilde{C}_{\mathrm{L,I}}(t)$	Modified clipping levels for the I branch ADC clipping model
$C_{\mathrm{I}}, C_{\mathrm{Q}}$	Clipping levels for I and Q branch ADCs
$\tilde{C}_{\mathrm{I}}(t), \tilde{C}_{\mathrm{Q}}(t)$	Modified clipping levels for I and Q branch ADCs
$C_{\mathrm{H,Q}}, C_{\mathrm{L,Q}}$	Higher and lower clipping level for the Q branch ADC
$\tilde{C}_{\mathrm{H,Q}}(t), \tilde{C}_{\mathrm{L,Q}}(t)$	Modified clipping levels for the Q branch ADC clipping model

$d(n)$	AIC main branch signal
$d_c(nT_s)$	Additive complex clipping distortion
$d_{c,\mathrm{I}}(nT_s), d_{c,\mathrm{Q}}(nT_s)$	Additive clipping distortion in I and Q branch
$D_{c,k}$	Clipping distortion in OFDM subcarrier k
$d_m(t)$	Complex Fourier coefficients in the clipping model
$d_{m,\mathrm{I}}(t)$	Real part of $d_m(t)$
$d_{m,\mathrm{Q}}(t)$	Imaginary part of $d_m(t)$
$DNL[l]$	Differential nonlinearity for the code bin l
$e(n)$	Combined nonlinearity estimate in AIC
f_1, f_2	Frequencies of a two-tone signal
f_c	Center frequency
f_{IF}	Intermediate frequency for a carrier included in $x(t)$
f_s	ADC sampling rate
g_m	I/Q mixer gain mismatch
$\mathbf{h}_{\mathrm{BP}}^{\mathrm{C}}$	Impulse response of the complex bandpass filter used in AIC
$\mathbf{h}_{\mathrm{BS}}^{\mathrm{C}}$	Impulse response of the complex bandstop filter used in AIC
$\mathbf{h}_{\mathrm{BS}}^{\mathrm{R}}$	Impulse response of the real bandstop filter used in AIC
H_k	Channel gain value in OFDM subcarrier k
$\hat{H}_k$	Estimate of channel gain value in OFDM subcarrier k
$\hat{H}_{D,k}$	Estimate of channel gain value in OFDM data subcarrier k
$\hat{H}_{P,k}$	Estimate of channel gain value in OFDM pilot subcarrier k
$\mathbf{h}_p$	Impulse response of the FIR filter employed in MSI method
$\mathbf{h}_{p,0}, \mathbf{h}_{p,1}, \ldots, \mathbf{h}_{p,L-1}$	Impulse responses of polyphase branch filters obtained from $\mathbf{h}_p$
$h(t)$	Radio channel impulse response
i	Iteration index
$IIP3_{\mathrm{RF,dBm}}$	IIP3 for RF nonlinearity expressed in dBm
$INL[l]$	Integral nonlinearity for the code bin l
$INL_{\mathrm{HCF}}[l]$	High code frequency part of $INL[l]$
$INL_{\mathrm{LCF}}[l, \omega]$	Low code frequency part of $INL[l]$ for input frequency ω
$INL_{\mathrm{noise}}[l, \omega]$	Noise part of $INL[l]$ for input frequency ω
$IRR_{\mathrm{m,dB}}$	Image rejection ratio of an I/Q mixer expressed in dB
J	Oversampling factor for an OFDM signal
j	Imaginary unit, $j^2 = -1$
k	OFDM subcarrier index
k_1, k_2	Complex coefficients in the mixer I/Q imbalance model
L	Oversampling factor
l	ADC output code index
M	Number of bits in a data symbol U_k
m	Fourier coefficient index

M_f	Adaptive filter length in AIC
N	Total number of subcarriers in an OFDM signal
n	Sample index
N_A	Number of active subcarriers in an OFDM signal
$P_{v,\mathrm{I}}, P_{v,\mathrm{Q}}$	Average of power levels of $v_{\mathrm{I}}(t)$ and $v_{\mathrm{Q}}(t)$
$Q[l]$	Width of code bin l
q	Nonlinearity order
Q_{ideal}	Ideal code bin width
R	Reference resistance
r	Symbol alphabet index
$r_{\mathrm{H,I}}(t), r_{\mathrm{L,I}}(t)$	Auxiliary variables for the I branch of the clipping model
$r_{\mathrm{H,Q}}(t), r_{\mathrm{L,Q}}(t)$	Auxiliary variables for the Q branch of the clipping model
$s(t), s_{\mathrm{I}}(t), s_{\mathrm{Q}}(t)$	Auxiliary variables for the zero-symmetric clipping models
$s_{\mathrm{H}}(t), s_{\mathrm{L}}(t)$	Auxiliary variables for the equal I and Q clipping model
$s_{\mathrm{H,I}}(t), s_{\mathrm{L,I}}(t)$	Auxiliary variables for the I branch of the clipping model
$s_{\mathrm{H,Q}}(t), s_{\mathrm{L,Q}}(t)$	Auxiliary variables for the Q branch of the clipping model
$\mathbf{s}(n)$	Combined vector of all nonlinearity modeling branches in AIC
$\mathbf{s}_{x^*}(n)$	Filtered nonlinearity branch vector for term $\hat{x}(n)^*$ in AIC
$\mathbf{s}_{A^2x}(n)$	Filtered nonlinearity branch vector for term $\hat{A}^2(n)\hat{x}(n)$ in AIC
$\mathbf{s}_{A^2x^*}(n)$	Filtered nonlinearity branch vector for term $\hat{A}^2(n)\hat{x}^*(n)$ in AIC
$\mathbf{s}_{x_{\mathrm{I}}^3}(n)$	Filtered nonlinearity branch vector for term $\mathrm{Re}[\hat{x}^3(n)]$ in AIC
$\mathbf{s}_{x_{\mathrm{Q}}^3}(n)$	Filtered nonlinearity branch vector for term $\mathrm{Im}[\hat{x}^3(n)]$ in AIC
$SQNR_{\mathrm{dB}}$	Signal-to-quantization-noise ratio expressed in dB
t	Time variable
T_s	OFDM symbol duration
U_k	Complex data symbol in OFDM subcarrier k
$\hat{U}_k$	Estimate of complex data symbol in OFDM subcarrier k
$u(t)$	OFDM signal to be transmitted
V_k	Non-clipped received signal value in OFDM subcarrier k
$\hat{V}_k$	Enhanced received signal value in OFDM subcarrier k
$\tilde{V}_k$	Clipped received signal value in OFDM subcarrier k
$\hat{\tilde{V}}_k$	Regenerated clipped received signal value in OFDM subcarrier k
$V_{\mathrm{max,eq}}$	Maximum amplitude value for zero-forcing channel equalizer
$V(t)$	Envelope of $v(t)$
$v(t)$	I/Q ADC input signal, $v(t) = v_{\mathrm{I}}(t) + jv_{\mathrm{Q}}(t)$
$\tilde{v}(n)$	Discrete-time I/Q ADC output signal, $\tilde{v}(n) = \tilde{v}_{\mathrm{I}}(n) + j\tilde{v}_{\mathrm{Q}}(n)$
$\tilde{v}(t)$	Continuous-time I/Q ADC output signal, $\tilde{v}(t) = \tilde{v}_{\mathrm{I}}(t) + j\tilde{v}_{\mathrm{Q}}(t)$
W_k	Additive white Gaussian noise in OFDM subcarrier k
$\mathbf{w}(n)$	Combined vector of all nonlinearity modeling branches in AIC

$\mathbf{w}_{x^*}(n)$	Adaptive filter for term $\hat{x}(n)^*$ in AIC
$\mathbf{w}_{A^2x}(n)$	Adaptive filter for term $\hat{A}^2(n)\hat{x}(n)$ in AIC
$\mathbf{w}_{A^2x^*}(n)$	Adaptive filter for term $\hat{A}^2(n)\hat{x}^*(n)$ in AIC
$\mathbf{w}_{x_{\mathrm{I}}^3}(n)$	Adaptive filter for term $\mathrm{Re}[\hat{x}^3(n)]$ in AIC
$\mathbf{w}_{x_{\mathrm{Q}}^3}(n)$	Adaptive filter for term $\mathrm{Im}[\hat{x}^3(n)]$ in AIC
$w(t)$	Additive white Gaussian noise
$x(t)$	Complex baseband equivalent of $x_{\mathrm{RF}}(t)$
$\hat{x}(n)$	AIC reference branch signal, coarse estimate of $x(t)$
$\hat{x}_{\mathrm{I}}(t)$	Real part of $\hat{x}(n)$
$\hat{x}_{\mathrm{Q}}(t)$	Imaginary part of $\hat{x}(n)$
$\tilde{x}(n)$	Received signal after AIC, estimate of $x(t)$
x_{FS}	Analog-to-digital converter full-scale voltage
$x_{\mathrm{I}}(t)$	Real part of $x(t)$
x_{IN}	Analog-to-digital converter input voltage
$x_{\mathrm{Q}}(t)$	Imaginary part of $x(t)$
$x_{\mathrm{RF}}(t)$	Received bandpass signal in the LNA input
$y(t)$	Complex baseband equivalent of $y'_{\mathrm{RF}}(t)$ after filtering
$\tilde{y}(t)$	Output of an I/Q mixer
$y'_{\mathrm{BB}}(t)$	Complex signal after the simplified BB nonlinearity model
$y'_{\text{BB-only}}(t)$	Output of simplified BB nonlinearity model when input is $x(t)$
$y_{\mathrm{I}}(t)$	Real part of $y(t)$
$\tilde{y}_{\mathrm{I}}(t)$	Real part of $\tilde{y}(t)$
$y_{\mathrm{I,BB}}(t)$	I branch signal after baseband nonlinearities
$y'_{\mathrm{I,BB}}(t)$	I branch signal after the simplified BB nonlinearity model
$y_{\mathrm{Q}}(t)$	Imaginary part of $y(t)$
$\tilde{y}_{\mathrm{Q}}(t)$	Imaginary part of $\tilde{y}(t)$
$y_{\mathrm{Q,BB}}(t)$	Q branch signal after baseband nonlinearities
$y'_{\mathrm{Q,BB}}(t)$	Q branch signal after the simplified BB nonlinearity model
$y_{\mathrm{RF}}(t)$	Bandpass signal in the LNA output
$y'_{\mathrm{RF}}(t)$	LNA output according to the simplified RF nonlinearity model
Z_k	Total clipping distortion in OFDM subcarrier k
$\hat{Z}_k$	Estimate of total clipping distortion in OFDM subcarrier k
$z(nT_s)$	Total complex clipping distortion in Bussgang-based model
α_1	Bussgang scaling factor for complex signal clipping
$\hat{\alpha}_1$	Estimate of Bussgang scaling factor for complex signal clipping
α_2	Bussgang scaling factor for complex conjugate signal interference
$\alpha_{\mathrm{I}}, \alpha_{\mathrm{Q}}$	Bussgang scaling factors for I and Q branch signal clipping
$\hat{\alpha}_{\mathrm{I}}, \hat{\alpha}_{\mathrm{Q}}$	Estimates of Bussgang scaling factors for I and Q signal clipping

β_{x^*}	NLMS constant for term $\hat{x}(n)^*$ in AIC
β_{A^2x}	NLMS constant for term $\hat{A}^2(n)\hat{x}(n)$ in AIC
$\beta_{A^2x^*}$	NLMS constant for term $\hat{A}^2(n)\hat{x}^*(n)$ in AIC
$\beta_{x_{\mathrm{I}}^3}$	NLMS constant for term $\mathrm{Re}[\hat{x}^3(n)]$ in AIC
$\beta_{x_{\mathrm{Q}}^3}$	NLMS constant for term $\mathrm{Im}[\hat{x}^3(n)]$ in AIC
γ	ADC clipping ratio; clipping level with respect to signal power
$\gamma_{\mathrm{I}}, \gamma_{\mathrm{Q}}$	ADC clipping ratios for I and Q branches
$\hat{\gamma}_{\mathrm{I}}, \hat{\gamma}_{\mathrm{Q}}$	Estimates of ADC clipping ratios for I and Q branches
$\delta_1, \delta_2, \ldots, \delta_6$	Auxiliary variables in the cascaded nonlinearity model
$\theta_c(t)$	Angular term of $v(t)$
ι	Multiplication index
$\lambda_1, \lambda_2, \ldots, \lambda_{10}$	Auxiliary variables in the cascaded nonlinearity model
$\boldsymbol{\mu}$	Combined LMS step-size vector in AIC
$\boldsymbol{\mu}_{x^*}$	LMS step-size vector for term $\hat{x}(n)^*$ in AIC
$\boldsymbol{\mu}_{A^2x}$	LMS step-size vector for term $\hat{A}^2(n)\hat{x}(n)$ in AIC
$\boldsymbol{\mu}_{A^2x^*}$	LMS step-size vector for term $\hat{A}^2(n)\hat{x}^*(n)$ in AIC
$\boldsymbol{\mu}_{x_{\mathrm{I}}^3}$	LMS step-size vector for term $\mathrm{Re}[\hat{x}^3(n)]$ in AIC
$\boldsymbol{\mu}_{x_{\mathrm{Q}}^3}$	LMS step-size vector for term $\mathrm{Im}[\hat{x}^3(n)]$ in AIC
σ_n	Standard deviation of $w(t)$
$\phi(t)$	Phase of $x(t)$
ϕ_m	I/Q Mixer phase mismatch
$\phi_v(t)$	Phase of $v(t)$
Ψ_r	Symbol alphabet, $r = 1, 2, 3, \ldots, 2^M$
Ω	Set of all OFDM subcarrier indices
ω	Angular frequency
Ω_A	Set of active OFDM subcarrier indices
ω_c	Angular center frequency of a signal
Ω_D	Set of data OFDM subcarrier indices
Ω_P	Set of pilot OFDM subcarrier indices
$\lvert\cdot\rvert$	Absolute value
$(\cdot)^*$	Complex conjugate
$*$	Convolution operator
$\mathrm{diag}(\cdot)$	Vector to diagonal matrix
$\mathrm{erf}(\cdot)$	Error function
$\lVert\cdot\rVert$	Euclidean norm
$\mathrm{E}[\cdot]$	Expected value
$\exp[\cdot]$	Natural exponential function
$\mathcal{F}\{\cdot\}$	Fourier transform

$\mathrm{Im}[\,\cdot\,]$	Imaginary part
$\mathcal{L}(\,\cdot\,)$	Log-likelihood ratio
$\max(\,\cdot\,)$	Maximum value
$p(\,\cdot\,)$	Symbol reliability
$\mathrm{Re}[\,\cdot\,]$	Real part
$(\,\cdot\,)^{\mathrm{T}}$	Transpose

CHAPTER 1

Introduction

Wireless communications systems are continuously present in our daily lives. No matter if it is business or pleasure, the amount of wirelessly transferred data is exponentially increasing. The current smart phones are able to take photos with the resolution of tens of megapixels and shoot high-bitrate 4K videos which people want to share immediately on social media. Also cloud services are more popular than ever for file backups and for everyday teamwork. These are examples of many current and forthcoming applications that require wireless communications systems with higher and higher data rates in both, downlink and uplink, directions. How to develop more and more efficient, yet reliable, systems and devices for these needs?

1.1 Background and Research Motivation

A traditional way of increasing data rates in wireless communications systems is to use more bandwidth. However, this is typically limited by the fact that the radio spectrum is a scarce resource. On the other hand, it has been shown that there are considerable temporal and spatial variations in the spectrum usage [49, 120]. This means that the spectral efficiency of communications waveforms should be as high as possible, but it is also very important that the spectrum usage on the whole is efficient and flexible.

Software-defined radio (SDR) is a modern concept for enabling flexible and reconfigurable transceivers [26, 62, 75]. These desired features are achieved by implementing most of the transceiver functionalities using digital signal processing (DSP). The SDR hardware platform is exactly what is needed for cognitive radios (CRs) which, in turn, make the efficient and flexible spectrum usage possible [64, 71]. A CR device sense the characteristics of its spectral environment and intelligently adapt its radio waveforms so that it can use temporarily and/or spatially vacant frequency channels. In a typical

scenario, the CR device is communicating as a secondary user without affecting the licensed or primary operation on the considered frequency band. The CR concept has been a remarkable research topic for over a decade. However, it is still far from being a mature technology. Industry is still looking for business opportunities in CRs and regulators are requiring strict reliability [83]. In addition to network level challenges, a CR will require the best available wideband SDR hardware.

Not only in SDRs but also in other communications systems, the current trend is towards flexible wideband radio receivers where selectivity is mainly implemented in digital domain. In addition to flexibility, this is motivated by cost efficiency and integrability which are offered by, e.g., direct-conversion receiver (DCR) architecture [75, 89]. This drives the development towards multicarrier/multiradio receivers where several carriers are received simultaneously through a single wideband receiver chain. In this context, the multicarrier does not refer to a modulation method but in general comprises multiple carriers that can be individual. Similarly, the multiradio refers to the reception of carriers with different radio access technologies. However, this kind of scenario sets stringent requirements for the linearity of receiver components such as amplifiers and mixers [90]. The requirements are basically stemming from the fact that modern communications waveforms tend to have high peak-to-average power ratio (PAPR) [25]. In addition, the even more important reason is that the simultaneously received carriers may have considerably different power levels which requires large dynamic range from the receiver. Otherwise, nonlinear distortion is caused to the received composite waveform which is likely to deteriorate the detection of the weakest carriers [25, 110]. In addition to receiver components, it is also very important that analog-to-digital converters (ADCs) have enough spurious-free dynamic range (SFDR) due to the same aforementioned reasons. ADCs have remarkably improved during the recent years when taking into account SFDR, sampling rate, resolution, and power consumption as a whole, but still the ADC might be the bottleneck of the wideband receiver [55, 70]. It is also worth noting that many modern radar systems employ similar receiver architectures and analog-to-digital (A/D) interfaces as communications systems. Therefore, radar receivers suffer from similar dynamic range challenges [96, 115].

Analog hardware development is always needed in order to make better and better components from the cost, size, power consumption, and performance point of view. For instance, there are lots of recent development in the analog design of blocker-tolerant wideband receivers [28, 101]. However, on top of that, DSP algorithms can give a major performance boost. This is typically referred as digitally-assisted analog or DSP-enhanced radio frequency (RF). Furthermore, DSP allows the usage of technology, such as the DCR architecture, which has been previously disregarded due to the poor performance [89]. Therefore, advances in DSP algorithms for suppressing receiver and ADC impairments, especially nonlinearities, are extremely important in putting the CR into practice and also in improving other wideband communications and radar

receivers. In fact, the potential of the DSP algorithms is twofold. On one hand, it is possible to push the receiver performance beyond the current state-of-the-art analog hardware. On the other hand, DSP can relax the hardware requirements on systems where the state-of-the-art performance is not required and therefore makes it possible to use smaller, less power consuming, and lower cost devices.

1.2 Thesis Scope and Objectives

The main objectives of the thesis are novel contributions to the modeling and digital suppression of nonlinearities in wideband radio receivers and A/D interfaces. The modeling requires understanding of the essential physical mechanisms of analog receiver components and considering them from the system-level perspective. In this manner, the nonlinearity models are potentially helpful for the suppression of nonlinear distortion and are still simple enough for practical implementations. Various nonlinear distortion suppression methods are proposed, since it is partially system and hardware specific issue what is the most feasible approach. Essentially, all the developed methods are evaluated with computer simulations and also with real analog hardware measurements. Most of the methods are fully digital meaning that analog hardware modifications are not needed and, what is more, the methods require only minimal amount of *a priori* signal information or no information at all for distortion suppression purposes. In general, the thesis mainly focuses on adaptive DSP approaches for wideband multicarrier/multiradio DCRs, CR sensing receivers, and wideband A/D interfaces. Although, the main scope is on wireless communications systems, many aspects are also applicable to radar systems which employ similar receiver architectures and ADCs.

1.3 Outline and Main Contributions of the Thesis

In general, this thesis discusses about nonlinear distortion in wideband radio receivers and A/D interfaces, contributing to nonlinearity modeling and especially to digital nonlinear distortion suppression. Essentially this is all about the dynamic range of the received waveforms and related receiver requirements. Therefore, dynamic range challenges are discussed in Chapter 2 which is followed by the description of essential nonlinearities in DCRs and A/D interfaces in Chapter 3. The technical contributions of the thesis are presented in Chapters 3–6 after which the thesis is concluded in Chapter 7. In short, the main contributions of the thesis are the following.

- A cascaded receiver nonlinearity model is derived which jointly takes into account the interactions between RF, mixer, and baseband (BB) nonlinearities together with in-phase/quadrature (I/Q) imbalance. The model is presented in Chapter 3 and is originating from [P8].

- The cascaded model is exploited in adaptive interference cancellation (AIC) method which is able to digitally suppress nonlinear receiver distortion caused by strong blocker signals. The AIC method is described in Chapter 4 together with performance results obtained with DCR hardware measurements. The topic is also considered in [P7–P9].

- A general Fourier series based signal clipping model for I/Q ADCs is derived in Chapter 5. It can be used to analyze separately each distortion order caused by unintentional I/Q ADC clipping in radio receivers. The modeling is related to [P2,P6].

- Several digital post-processing methods are proposed for the suppression of ADC nonlinearities including integral nonlinearity (INL) and especially clipping. The methods include AIC, enhanced adaptive interference cancellation (E-AIC), maximum selection interpolation (MSI), and decision-aided iterative clipping distortion suppression. These are discussed in Chapter 6 and also in [P1–P5].

Publications [P1–P9] provide additional details and more performance examples compared to what is discussed in this thesis summary. The mathematical notation of the thesis summary has been slightly changed from the associated publications. The reasons for that are twofold. Some variables have been changed to avoid overlap between chapters. On the other hand, some equations have been modified to have potentially more intuitive form. These modifications should provide a coherent and fluent reading experience.

1.4 Author's Contributions to the Publications

In general, D.Sc. Jaakko Marttila and Prof. Mikko Valkama have contributed to all publications [P1–P9] by sharing their ideas, solving problems, and providing other support during the research phase as well as when preparing the publication manuscripts.

In [P1–P6,P9], the author of this thesis has been the main contributor for mathematical derivations, simulations, measurements, and composing the publications. Related to the MSI method presented in [P3], M.Sc. Vesa Lehtinen shared his knowledge about polyphase structures and helped in filter design. D.Sc. Toni Levanen provided his experience on turbo coding and channel estimation during the algorithm development of [P5] and also when the author was performing the related simulations.

D.Sc. Michael Grimm is the first author of [P8] and the publication is also related to the topic of his monograph doctoral dissertation [38]. He performed all the measurements and most of the simulations of [P8]. However, this thesis also includes previously unpublished measurement results, solely made by the author of this thesis, using different RF hardware. The author of this thesis considerably contributed to the mathematical

derivation of the cascaded receiver nonlinearity model and also to the development of the nonlinearity suppression structure of [P8]. The final proposed suppression structure was an iterative process of pen-and-paper work as well as initial computer simulations. The author substantially contributed to this process. The author also participated to the writing of the manuscript although D.Sc. Michael Grimm was in charge. The author used the work presented in [P8] as a basis for [P9] and extended it by also considering calibration-based inverse modeling. The author performed all the simulations while D.Sc. Michael Grimm and Prof. Reiner Thomä provided constructive comments for the manuscript.

In [P7], all the simulations were performed by the author. M.Sc. Semu Mäkinen, D.Sc. Marko Kosunen, and Prof. Jussi Ryynänen shared their expertise on spectrum sensing and provided measurement-based spectrum sensing results from Otaniemi area, Espoo, Finland. They also partially contributed to the initial composition of the manuscript.

CHAPTER 2

Dynamic Range Challenges in Modern Radio Receivers

Modern wireless communications and radar systems employ wideband DCRs due to their flexibility, cost efficiency and integrability [75, 89, 92]. A block diagram of DCR architecture is presented in Figure 2.1. The RF front-end filters and amplifies the RF waveform captured by the antenna. The filtering is not used for strict channel selection but rather to prevent out-of-band signals entering the receiver. In the wideband receiver, the reception band may contain several signals for which the actual channel selection is performed later in digital domain. In order to improve the integrability of the receiver, some current structures completely omit the RF filter [27, 58]. After the low-noise amplifier (LNA), the RF waveform is down-converted to BB using an I/Q mixer. The lowpass filtering is employed to avoid aliasing in the A/D conversion and BB amplification is used for properly matching the received waveform to the full scale (FS) range of the ADC. As indicated in Figure 2.1, the term *radio receiver* is used in this thesis to refer to the whole analog receiver chain before the *A/D interface*. Both signal branches, I and Q, require their own ADC which are together called an I/Q ADC. After digitizing the waveform, the digital post-processing takes place. This includes DSP algorithms for suppressing nonlinear distortion and I/Q imbalance which are stemming from the components highlighted with different colors in Figure 2.1. The nonlinearities are discussed more in Chapter 3. The digital post-processing also includes all the traditional receiver processing such as channel selection filtering, channel equalization, signal demodulation, etc.

The following sections discuss the dynamic range challenges in this kind of wideband receivers. Various practical scenarios are considered from the spectrum access, spectrum sensing, and radars point of view. The purpose is to highlight the challenges that exist in

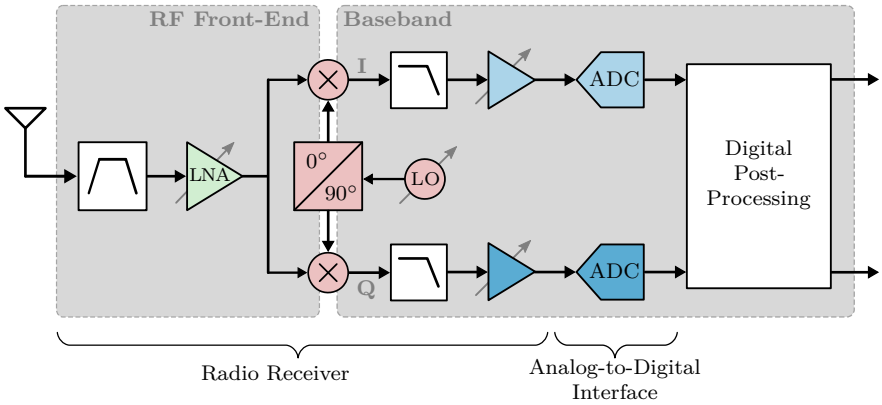

Figure 2.1: Conceptual wideband direct-conversion receiver block diagram highlighting the main sources of nonlinearity and I/Q imbalance.

the current and emerging real-world systems. Several DSP solutions for these challenges are then proposed later in the thesis.

2.1 Spectrum Access

In mobile cellular systems, the limited linearity of mobile devices is easy to understand due to their restricted size and cost. Nevertheless, the receiver nonlinearity can also be a great challenge in uplink. A wideband multicarrier/multiradio base station receiver can simultaneously receive several weak and strong signals through a single receiver chain. This kind of scenario is visualized in the spectrum illustrations of Figure 2.2. Due to the insufficient receiver and ADC linearity, the strong signals on Channels 2 and 4 are causing nonlinear distortion on top the weak signal on Channel 3 which practically deteriorates the demodulation of the weak signal. In practice, the dynamic range in the received waveform can be tens of dBs. For example, the specifications of Global System for Mobile Communications (GSM), Universal Mobile Telecommunications System (UMTS), and Long-Term Evolution (LTE) define blocker test scenarios requiring at least 70 dB SFDR and in reality the worst case scenarios can be even more challenging [2–4]. More nonlinearity requirements are considered, e.g., in [47]. In the uplink case, the blockers may originate from nearby or even co-located transmitters belonging to another cellular network operator or to completely another kinds of wireless systems. Therefore, the power levels of the blocker signals are uncontrollable from the base station receiver point of view. It is also worth noting that the blocker problem may be frequent since the base station receiver is stationary whereas, in downlink, the blocker situations for a mobile device are typically temporary, possibly a few percents of the operating time, due to the movements of the mobile.

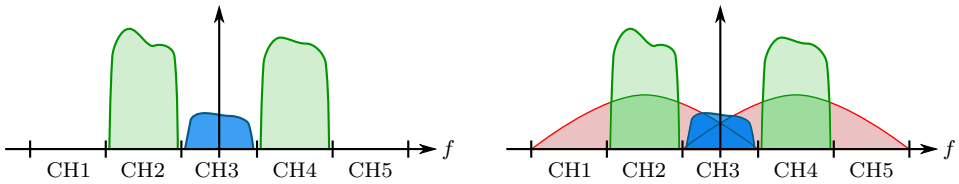

(a) Ideal Reception **(b)** Nonlinear Reception

Figure 2.2: Spectrum illustration of nonlinear distortion caused by receiver and ADC components due to limited dynamic range. Two strong signals are causing nonlinear distortion on top of the weak signal on Channel 3 and also to empty Channels 1 and 5.

Even if all the analog components in the receiver provides otherwise satisfactory performance, the bottleneck may be the A/D interface and possibly the automatic gain control (AGC) in front of it [120]. The FS range of the ADC should be used in order to maximize signal-to-noise ratio (SNR), but exceeding the FS range immediately causes clipping which is a very strong nonlinearity and quickly deteriorates the receiver performance [29, 111].

The dynamic range challenges in receivers stand out even more when dynamic spectrum access (DSA) is considered [77]. In short, DSA means increasing the efficiency of spectrum usage by exploiting spatiotemporally vacant frequency channels. This is the target especially in CRs which are expected to provide ultimate frequency-agility by accessing the vacant spectrum chunks, white spaces, which can be widely scattered in frequency domain. The hardware challenges are considered in more detail in [20, 74, 77, 90, 120]. Typical applications are broadband access and wireless local area networks (WLANs) exploiting, e.g., white spaces in television frequency spectrum [36,51]. The non-contiguous spectrum access is also a timely topic in mobile communications since carrier aggregation is used in LTE Advanced [1]. Basically this means that challenging dynamic range situations will occur in uplink as well as in downlink communications.

Yet another aspect related to dynamic range challenges is that even own transmitter may seriously interfere with the receiver of the same device. This is possible, e.g., in multimode transceivers supporting several wireless communications standards. When the uplink frequency band of one standard is close the downlink band of another standard, the strong transmitted signal is likely to cause nonlinear distortion in the co-located receiver due to, e.g., limited duplexer attenuation. However, the transmitted signal is known in the device and it is possible to suppress it in the receiver [42]. In fact, this can be considered as a step towards full-duplex radios where transmitting happens simultaneously with the reception at the same center frequency. This naturally requires suppression of own transmitted signal in the receiver. Full-duplex radios are an interesting topic of its own and are not explicitly discussed further in this thesis. The interested reader is referred to [66, 67].

2.2 Spectrum Sensing

An essential function in CRs is spectrum sensing. This is the key enabler for flexible spectrum-aware communications. The spectrum sensing practically means acquiring information from the environment in order to determine if there exist temporarily vacant spectrum chunks to be exploited for secondary user communications. Being one of the most challenging CR issues, an extremely large amount of different kinds of spectrum sensing algorithms have been proposed in recent years [12, 121, 122]. In the simplest form, spectrum sensing means measuring received energy on a certain frequency band and compare it to a predetermined noise threshold in order to tell if there is a signal or not. More advanced spectrum sensing algorithm can, e.g., exploit certain features of communications signals such as cyclostationarity.

The limited SFDR of the receiver and ADCs also makes the spectrum sensing very challenging [74, 93–95],[P7]. The nonlinear distortion affects different types of sensing algorithms in different manners which are easiest to describe using an example. Considering the scenario of Figure 2.2, the task of a spectrum sensing algorithm is to determine which channels are vacant and which are occupied by the primary users. Due to the strong signals on Channels 2 and 4, it is easy to sense that those are occupied. However, due to the nonlinear distortion on Channels 1 and 5, an energy detector would sense that those are occupied. This is called a false alarm. On the other hand, the energy detector would correctly sense that Channel 3 is occupied since adding more energy, nonlinear distortion in this case, means that the energy is even more above the noise threshold.

If a cyclostationary feature detector is used, the spectrum sensing results may be different than when using the energy detector in the scenario of Figure 2.2. Most probably also the feature detector would detect that Channels 1, 2, 4, and 5 are occupied. The false alarms on Channels 1 and 5 are caused due to the fact that the nonlinear distortion can have the same cyclic features as the signal from which the distortion is originating. However, the sensing result of Channel 3 depends on the situation. For instance, if the strong signals on Channels 2 and 4 have same cyclic features and the signals are synchronized, then Channel 3 would be detected as occupied. Alternatively, if the strong signals have different cyclic features, the weak signal on Channel 3 may be masked by the nonlinear distortion and the channel is sensed to be vacant. This situation is called missed detection and is typically considered very harmful since using the channel would interfere with the primary user signal.

In addition to communications systems, spectrum sensing is also needed in electronic warfare (EW) [108]. An EW system may need to scan several gigahertz of electromagnetic spectrum when trying to sense or even detect communications waveforms. Extremely large signal dynamics are likely occur and DSP could be used to suppress nonlinear distortion occurring in the receiver in order to sense even the weakest signals.

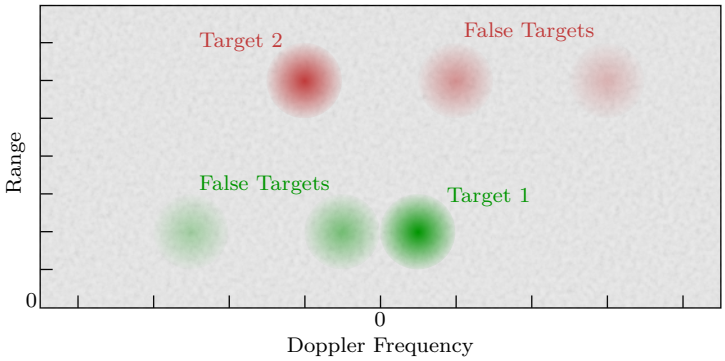

Figure 2.3: Conceptual range-Doppler map illustrating two real targets and several false targets due to nonlinear distortion and I/Q imbalance in pulse-Doppler radar receiver and A/D interface.

2.3 Radars

Although not being in the main focus of the thesis, it is worth discussing here shortly that also many radar systems suffer from similar dynamic range challenges as communications receivers [96]. Due to the effective radar signal processing, even very weak nonlinearity components may become visible from the noise. Typically the bottleneck in radar receivers is the linearity of the A/D interface because commonly used superheterodyne receivers are providing very good selectivity and also otherwise excellent performance. However, nowadays also in radar development, there is an increasing interest to employ direct-conversion receivers due to their integrability and generally excellent size and cost efficiency [115]. This means the same nonlinearity and I/Q imbalance challenges as in communications receivers. Therefore, also in radar systems there are a need for effective digital post-processing algorithms for suppressing nonlinear distortion. Due to the same receiver architecture and similar A/D interfaces, many distortion suppression algorithms designed for communications systems, such as ones discussed in this thesis, may turn out to be useful also in modern radar systems.

A pulse-Doppler radar can be considered as a practical example [96]. Large SFDR is required in the receiver in order to reliably detect small high-speed targets. A conceptual illustration of two targets in a range-Doppler map is given in Figure 2.3 which is a typical way of illustrating the velocities and distances of the targets. Due to the receiver and ADC nonlinearities as well as I/Q imbalance, also several false targets appear. In practice, I/Q imbalance causes a false target with the same velocity (Doppler frequency) but with opposite sign. Nonlinearities, in turn, cause false targets with higher velocities, and possibly with opposite sign, such as the false targets with triple velocity in Figure 2.3 due to the third-order nonlinearity.

CHAPTER 3

Nonlinear Distortion in Direct-Conversion Receivers and Analog-to-Digital Interfaces

Wideband receivers tend to be sensitive to nonlinear distortion caused by various receiver components. This applies especially to DCRs which have minimal analog selectivity. This chapter discusses in detail the most essential nonlinearity sources of DCRs. Section 3.1 deals with analog components and models their nonlinearities in one using a cascaded polynomial model derived originally in [P8]. ADC nonlinearities are separately covered in Section 3.2. Many aspects covered in this chapter are also applicable to other receiver architectures such as superheterodyne. The receiver nonlinearity model would require some changes but all the theory related to ADCs would be directly applicable to superheterodyne receivers.

3.1 Receiver Nonlinearities

Behavior of a receiver can be modeled in various ways depending on the purpose of the model. For example, when designing a circuit, it is essential to model accurately the behavior of each component on circuit level [54, 91]. However, this may be an unsuitable approach for some other purposes due to the complexity and the amount of information needed about the components. In digital suppression of receiver nonlinearities, for instance, the target is to use a model that is computationally simple, but still accurate

enough, and of which parameters are undemanding to obtain. This is discussed more in Chapter 4.

The following Subsections 3.1.1–3.1.3 form together the cascaded nonlinearity model illustrated in Figure 3.1. It is a behavioral system-level model which is able to capture the essential nonlinear behavior of a DCRs as is shown in Chapter 4 and [P8] with hardware measurements. The derived model also serves as the basis for the receiver linearization algorithm discussed in Chapter 4.

3.1.1 RF Nonlinearities

In DCRs, RF nonlinearities are mostly originating from an LNA as depicted in Figure 2.1. Although ideal amplifiers always have linear relationship between the input and output voltage, real-world amplifiers can achieve that only within very limited voltage range. A strong input signal saturates amplifier electronics and desired amplifier gain cannot be achieved [48, 61, 92]. This means nonlinear input-output relationship which causes nonlinear distortion, i.e. additional frequency components, to the output signal of the amplifier. In practice, due to the highly varying signal levels, it is not possible to avoid nonlinear behavior without sacrificing the amplifier efficiency [25, 61, 92].

In general, a nonlinear device featuring memory effects can be modeled on system level using Volterra series which can be thought as a Taylor series with memory [61, 92]. However, in practice, due to the extensive number of parameters in Volterra series, it is better to find a model of which complexity lies between Volterra and Taylor series. Various such models exist in the literature [61, 82, 92]. Using a generalized Hammerstein model [82], the LNA output can be expressed as

$$y_{\mathrm{RF}}(t) = b_1(t) * x_{\mathrm{RF}}(t) + b_2(t) * x_{\mathrm{RF}}^2(t) + b_3(t) * x_{\mathrm{RF}}^3(t) + \ldots, \tag{3.1}$$

where $*$ denotes convolution operator, $x_{\mathrm{RF}}(t)$ is the bandpass signal in the LNA input and $b_1(t), b_2(t), b_3(t), \ldots$ are impulse responses modeling memory effects separately for each nonlinearity term. Widely adopted convention of BB equivalent signal models are used in this thesis where possible [19, 92]. Hence, $x_{\mathrm{RF}}(t)$ can be presented as

$$x_{\mathrm{RF}}(t) = 2\,\mathrm{Re}[x(t)e^{j\omega_c t}] = x(t)e^{j\omega_c t} + x^*(t)e^{-j\omega_c t}, \tag{3.2}$$

where $x(t)$ is the complex BB equivalent signal of $x_{\mathrm{RF}}(t)$ and $\omega_c = 2\pi f_c$ is the angular center frequency. In addition, $(\cdot)^*$ denotes complex conjugate and j is the imaginary unit. It is worth noticing that $x(t)$ can contain anything from a single tone to several individual carrier waveforms at different complex intermediate frequencies (IFs). In the latter multicarrier down-conversion case, ω_c corresponds to the center frequency of the total RF signal to be down-converted. Moreover, $x(t)$ can be written in two equivalent

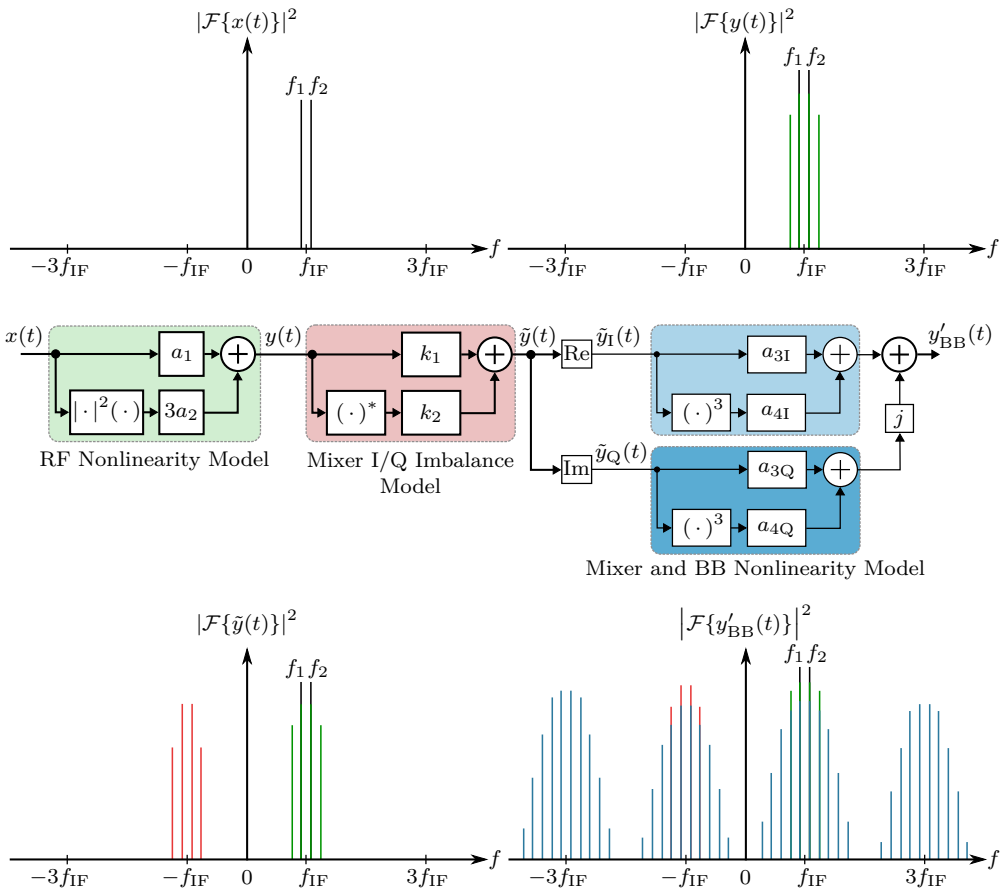

Figure 3.1: Cascaded nonlinearity model for direct-conversion receivers considering third-order RF and baseband nonlinearities in the presence of mixer and baseband I/Q imbalance. All stages are illustrated with power spectra of a two-tone signal.

forms so that

$$x(t) = A(t)e^{j\phi(t)} = x_{\mathrm{I}}(t) + jx_{\mathrm{Q}}(t), \tag{3.3}$$

where $A(t)$ and $\phi(t)$ are the total envelope and phase of the overall down-converted RF signal $x(t)$. In the second form, $x_{\mathrm{I}}(t) = A(t)\cos[\phi(t)]$ and $x_{\mathrm{Q}}(t) = A(t)\sin[\phi(t)]$ refer to the corresponding composite I and Q signals (real and imaginary part), respectively. By definition, the envelope is therefore $A(t) = |x(t)| = \sqrt{x_{\mathrm{I}}^2(t) + x_{\mathrm{Q}}^2(t)}$ and the phase $\phi(t) = \arctan[x_{\mathrm{Q}}(t)/x_{\mathrm{I}}(t)]$.

The model in (3.1) can be simplified, if it is desired to model only the terms that are within the reception band after down-conversion in the input of the ADC. In most systems, the new frequency components produced by even-order RF nonlinearities are far away from ω_c and therefore straightforward to filter out. This can be illustrated by

expressing the second-order term of (3.1) with the help of (3.2), which leads to

$$x_{\mathrm{RF}}^2(t) = 2A(t) + x^2(t)e^{j2\omega_c t} + [x^*(t)]^2 e^{-j2\omega_c t}. \tag{3.4}$$

It is apparent that the new frequency content appears around zero frequency and $\pm 2\omega_c$, but there is no term referring to the interesting band at ω_c. Although this typically guarantees that even-order distortion does not appear inside the reception band, there is one exception: if $x_{\mathrm{RF}}(t)$ contains several strong carriers having large frequency separation and the RF front-end is wide enough to receive all of them. It is then possible that even-order intermodulation distortion (IMD) components may fall inside the reception band, but even in that case, modern LNA topologies can alleviate the problem [90, 105, 114].

The most crucial RF nonlinearities are of odd order, because new frequency components are generated around ω_c. In typical RF front-ends, third-order nonlinearity is usually the strongest one. Higher orders tend to be below the receiver noise floor when operating clearly below the saturation level of the LNA (see Section 4.2). Therefore, a simplified RF nonlinearity model can be written as

$$y'_{\mathrm{RF}}(t) = a_1 x_{\mathrm{RF}}(t) + a_2 x_{\mathrm{RF}}^3(t), \tag{3.5}$$

where a_1 is a coefficient referring to the linear gain of the LNA and a_2 expresses the relative level of the third-order distortion. The coefficients a_1 and a_2 must be complex in order to model also AM/PM distortion of the LNA and not only AM/AM distortion [61]. The model in (3.5) is memoryless in order to simplify the following analysis and its notation. Memory effects can be taken into account later by replacing the nonlinearity term coefficients with filters making the model more accurate for wideband systems. This approach is used, e.g., in AIC which is discussed in Section 4.2. The coefficients in (3.5) have also direct relation to input-referred third-order intercept point (IIP3) which is a common way to measure nonlinearity through a two-tone test [24, 48, 61, 92]. For the RF nonlinearity, IIP3 can be expressed in dBm as

$$IIP3_{\mathrm{RF,dBm}} = 10\log_{10}\left(\frac{4}{3}\left|\frac{a_1}{a_2}\right|\frac{1000}{2R}\right), \tag{3.6}$$

where R is the reference resistance relating voltage values to power values. The simplified RF nonlinearity model is also shown in Figure 3.1 and illustrated with a two-tone example.

Furthermore, the latter term in (3.5), i.e. the nonlinearity contribution, can also be expressed as

$$\begin{aligned} &a_2 x_{\mathrm{RF}}^3(t) \\ &\quad = a_2\{x(t)e^{j\omega_c t} + x^*(t)e^{-j\omega_c t}\}^3 \\ &\quad = a_2\{x^3(t)e^{j3\omega_c t} + [x^*(t)]^3 e^{-j3\omega_c t} + 3A^2(t)x(t)e^{j\omega_c t} + 3A^2(t)x^*(t)e^{-j\omega_c t}\}. \end{aligned} \tag{3.7}$$

The new frequency content around ω_c generated by the RF nonlinearity is due to the term $3A^2(t)x(t)e^{j\omega_c t}$. The other terms in (3.7) do not hit the BB when the I/Q down-conversion is performed and those are filtered out by the lowpass filters in the BB stage of the DCR (see Figure 2.1). Consequently, the essential BB equivalent form of the RF nonlinearity model (3.5) is

$$y(t) = y_{\mathrm{I}}(t) + jy_{\mathrm{Q}}(t) = a_1 x(t) + 3a_2 A^2(t)x(t), \tag{3.8}$$

when the BB filtering is taken into account. The nonlinear term $3a_2A^2(t)x(t)$ causes IMD within the frequency band of $x(t)$ and also around it. This is because it is a third-order term and hence it has triple the bandwidth compared with $x(t)$. The third-order nature is evident since $A^2(t)x(t) = x^2(t)x^*(t)$. Equations for $y_{\mathrm{I}}(t)$ and $y_{\mathrm{Q}}(t)$ can be written separately as

$$y_{\mathrm{I}}(t) = a_1 x_{\mathrm{I}}(t) + 3a_2 A^2(t)x_{\mathrm{I}}(t) \tag{3.9a}$$

$$y_{\mathrm{Q}}(t) = a_1 x_{\mathrm{Q}}(t) + 3a_2 A^2(t)x_{\mathrm{Q}}(t). \tag{3.9b}$$

It is worth noticing that (3.9a) and (3.9b) are not completely independent. This is because both contain $A^2(t)$ which depends on $x_{\mathrm{I}}(t)$ and $x_{\mathrm{Q}}(t)$.

After the LNA, the RF signal goes into a wideband I/Q mixer which down-converts the signal to BB. In practice, the down-conversion is not ideal and some I/Q imbalance occurs which causes mirror frequencies into $y(t)$. The I/Q imbalance is caused by the relative amplitude mismatch g_m between I and Q branches as well as the phase mismatch ϕ_m. In general, I/Q imbalance can be time-dependent and frequency-selective, but these details are omitted at this point to simplify the analysis and notation here. However, those can be taken into account by extending the overall cascaded nonlinearity model derived in Subsection 3.1.3. A comprehesive presentation of I/Q imbalance is provided in [11] and references therein. Based on the aforementioned description, the model for the I/Q imbalance of the down-conversion stage is

$$\tilde{y}(t) = k_1 y(t) + k_2 y^*(t), \tag{3.10}$$

with the complex coefficients

$$k_1 = \frac{1}{2}\big(1 + g_{\mathrm{m}} e^{-j\phi_{\mathrm{m}}}\big), \tag{3.11a}$$

$$k_2 = \frac{1}{2}\big(1 - g_{\mathrm{m}} e^{j\phi_{\mathrm{m}}}\big). \tag{3.11b}$$

It is easy to see that the model does not affect the signal in the case of perfect I/Q balance ($g_{\mathrm{m}} = 1$, $\phi_{\mathrm{m}} = 0$), because $k_1 = 1$ and $k_2 = 0$. The RF-distorted signal with

mixer I/Q imbalance $\tilde{y}(t) = \tilde{y}_{\mathrm{I}}(t) + j\tilde{y}_{\mathrm{Q}}(t)$ can also be expressed as

$$\tilde{y}_{\mathrm{I}}(t) = y_{\mathrm{I}}(t), \tag{3.12a}$$

$$\tilde{y}_{\mathrm{Q}}(t) = g_{\mathrm{m}}\cos(\phi_{\mathrm{m}})y_{\mathrm{Q}}(t) - g_{\mathrm{m}}\sin(\phi_{\mathrm{m}})y_{\mathrm{I}}(t). \tag{3.12b}$$

The mixer I/Q imbalance model is also shown in Figure 3.1 and its input and output power spectra are illustrated with a two-tone signal. It is important to notice that in addition to the mirror image of the original signal $x(t)$, also the RF nonlinearity components are mirrored. In general, the strength of the mirror components depend on g_m and ϕ_m. This is typically expressed with the image rejection ratio (IRR) of the I/Q mixer which is defined in dB as

$$IRR_{\mathrm{m,dB}} = 20\log_{10}\left|\frac{k_1}{k_2}\right|. \tag{3.13}$$

This is a useful figure since it describes how many dBs below the mirror frequency components are in relation to the original frequency components. Typical IRR values in DCRs are from 25 dB to 40 dB without any DSP [10, 92]. Although I/Q imbalance itself is not a receiver nonlinearity, it fundamentally affects the nonlinear distortion created by the succeeding BB components as is seen in the following subsection.

3.1.2 Mixer and Baseband Nonlinearities

After the I/Q down-conversion, the signal encounters BB nonlinearities which occur in physically distinct I and Q branches as indicated in Figure 2.1. Therefore, I and Q nonlinearities are independent of each other. This is one of the main differences between RF and BB nonlinearities. Other difference is that also harmonics may fall inside the reception band, because the signal is on BB and hence individual carriers have only a relatively small IF.

The generalized Hammerstein model for BB nonlinearities can be written as

$$y_{\mathrm{I,BB}}(t) = c_{1\mathrm{I}}(t) * \tilde{y}_{\mathrm{I}}(t) + c_{2\mathrm{I}}(t) * \tilde{y}_{\mathrm{I}}^2(t) + c_{3\mathrm{I}}(t) * \tilde{y}_{\mathrm{I}}^3(t) + \ldots, \tag{3.14a}$$

$$y_{\mathrm{Q,BB}}(t) = c_{1\mathrm{Q}}(t) * \tilde{y}_{\mathrm{Q}}(t) + c_{2\mathrm{Q}}(t) * \tilde{y}_{\mathrm{Q}}^2(t) + c_{3\mathrm{Q}}(t) * \tilde{y}_{\mathrm{Q}}^3(t) + \ldots, \tag{3.14b}$$

where $c_{1\mathrm{I}}(t), c_{2\mathrm{I}}(t), \ldots$ and $c_{1\mathrm{Q}}(t), c_{2\mathrm{Q}}(t), \ldots$ are impulse responses modeling memory effects separately for each nonlinearity term in I and Q branch, respectively. Modeling I and Q branches separately is justified due to the aforementioned physical structure. Typically all BB components have slightly different characteristics due to process variations and therefore $c_{1\mathrm{I}}(t), c_{2\mathrm{I}}(t), \ldots$ and $c_{1\mathrm{Q}}(t), c_{2\mathrm{Q}}(t), \ldots$ are not equal which is sometimes called impulse response mismatch [11]. This causes BB I/Q imbalance to the signal. Furthermore, it is important to notice that (3.14a) and (3.14b) essentially model together

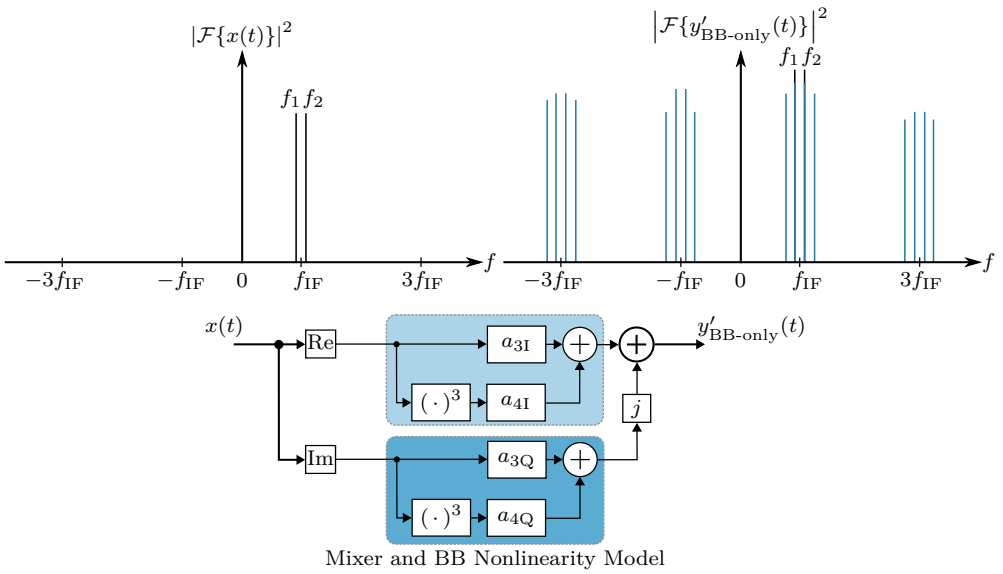

Figure 3.2: Simplified BB nonlinearity model for direct-conversion receivers considering essential third-order mixer and baseband nonlinearities individually for I and Q branches. Nonlinear effects and I/Q imbalance due to unequal I and Q branch coefficients are illustrated with the power spectrum of a two-tone signal.

the nonlinearities of all baseband components, such as amplifiers and ADCs, as well as mixer nonlinearities since the I/Q mixer outputs are at down-converted frequencies. This is an approximation that should hold reasonable well for any properly designed DCR. In the strict sense, the nonlinearities of each component should be modeled separately and then cascaded together which would result in an impractically large model.

The BB nonlinearity model in (3.14) can be simplified further as was the case with the RF nonlinearities. Modeling only third-order distortion is typically enough to capture the most significant distortions. Even-order BB distortion is typically located inside the reception frequency band, but it is highly attenuated due to practical analog circuit design solutions, such as differential signaling [54, 56, 91, 92]. Hence, the simplified BB model can be expressed as

$$y'_{\text{I,BB}}(t) = a_{3\text{I}}\tilde{y}_{\text{I}}(t) + a_{4\text{I}}\tilde{y}_{\text{I}}^3(t), \tag{3.15a}$$

$$y'_{\text{Q,BB}}(t) = a_{3\text{Q}}\tilde{y}_{\text{Q}}(t) + a_{4\text{Q}}\tilde{y}_{\text{Q}}^3(t), \tag{3.15b}$$

for the BB distorted signal $y'_{\text{BB}}(t) = y'_{\text{I,BB}}(t) + jy'_{\text{Q,BB}}(t)$ when $a_{3\text{I}}$, $a_{3\text{Q}}$, $a_{4\text{I}}$, and $a_{4\text{Q}}$ are real-valued scalar coefficients. Figure 3.2 illustrates how a two-tone signal is affected by the simplified BB nonlinearity model. In order to emphasize the BB effects, RF nonlinearities and mixer I/Q imbalance are omitted in this figure. This corresponds to replacing $\tilde{y}_{\text{I}}(t)$ and $\tilde{y}_{\text{Q}}(t)$ with $x_{\text{I}}(t)$ and $x_{\text{Q}}(t)$, respectively, in (3.15). Figure 3.2 shows

Table 3.1: All frequency components generated by the cascaded nonlinearity model listed from the lowest to the highest frequency (column-wise from top to bottom and from left to right) when excited with a two-tone signal having frequencies f_1 and f_2. The scenario is visualized in Figure 3.1.

Components around $-3f_{\mathrm{IF}}$	**Components around $-f_{\mathrm{IF}}$**	**Components around f_{IF}**	**Components around $3f_{\mathrm{IF}}$**
$3f_1 - 6f_2$	$4f_1 - 5f_2$	$5f_1 - 4f_2$	$6f_1 - 3f_2$
$2f_1 - 5f_2$	$3f_1 - 4f_2$	$4f_1 - 3f_2$	$5f_1 - 2f_2$
$f_1 - 4f_2$	$2f_1 - 3f_2$	$3f_1 - 2f_2$	$4f_1 - f_2$
$-3f_2$	$f_1 - 2f_2$	$2f_1 - f_2$	$3f_1$
$-f_1 - 2f_2$	$-f_2$	f_1	$2f_1 + f_2$
$-2f_1 - f_2$	$-f_1$	f_2	$f_1 + 2f_2$
$-3f_1$	$-2f_1 + f_2$	$-f_1 + 2f_2$	$3f_2$
$-4f_1 + f_2$	$-3f_1 + 2f_2$	$-2f_1 + 3f_2$	$-f_1 + 4f_2$
$-5f_1 + 2f_2$	$-4f_1 + 3f_2$	$-3f_1 + 4f_2$	$-2f_1 + 5f_2$
$-6f_1 + 3f_2$	$-5f_1 + 4f_2$	$-4f_1 + 5f_2$	$-3f_1 + 6f_2$

that the BB nonlinearities generate distortion around f_{IF} and $-3f_{\mathrm{IF}}$. Due to the unequal nonlinearity model coefficients, $a_{3\mathrm{I}} \neq a_{3\mathrm{Q}}$ and $a_{4\mathrm{I}} \neq a_{4\mathrm{Q}}$, also mirror components are created around $-f_{\mathrm{IF}}$ and $3f_{\mathrm{IF}}$. Taking into account the whole cascaded model (including RF nonlinearities, mixer I/Q imbalance and BB nonlinearities) as indicated in (3.15), even more components are produced. This is illustrated in the bottom right spectrum of Figure 3.1. In total, there are 40 frequency components when a two-tone signal is used as an input. The exact frequencies of these components are listed in Table 3.1. This is a theoretical result and it is good to remember that in practice many of these components are below the noise floor.

3.1.3 Cascaded Nonlinearity Model

This subsection analyzes more carefully the cascaded nonlinearity model derived in previous subsections. Although (3.15) and the associated equations contain all the necessary information, it is not straightforward to see the exact nonlinearity structure it causes. The cascaded nonlinearity model becomes much easier to interpret when it is written out using $x(t)$. In this context, complex equations are more intuitive and, in the end, also more concise. Further details on separate I and Q presentations can be found from [P8]. In complex form, (3.15) is first expressed as

$$y'_{\mathrm{BB}}(t) = \delta_1 y(t) + \delta_2 [y^*(t)]^3 + \delta_3 |y(t)|^2 y(t) + \delta_4 y^*(t) + \delta_5 y^3(t) + \delta_6 |y(t)|^2 y^*(t), \quad (3.16)$$

where $\delta_1, \delta_2, \ldots, \delta_6$ are auxiliary variables containing different combinations of $a_{3\mathrm{I}}, a_{4\mathrm{I}}$, $a_{3\mathrm{Q}}, a_{4\mathrm{Q}}$, k_1, and k_2. These are defined in Table 3.2 with and without I/Q imbalance. Now the cascaded nonlinearity model can be written in terms of $x(t)$ resulting

$$\begin{aligned} y'_{\mathrm{BB}}(t) = {} & \delta_1\lambda_1 x(t) + \delta_4\lambda_1^* x^*(t) \\ & + (\delta_1\lambda_2 + \delta_3\lambda_3)A^2(t)x(t) + (\delta_4\lambda_2^* + \delta_6\lambda_3^*)A^2(t)x^*(t) \\ & + \delta_2\lambda_4[x^*(t)]^3 + \delta_5\lambda_4^* x^3(t) \\ & + \delta_3\lambda_5 A^4(t)x(t) + \delta_6\lambda_5^* A^4(t)x^*(t) \\ & + \delta_2\lambda_6 A^2(t)[x^*(t)]^3 + \delta_5\lambda_6^* A^2(t)x^3(t) \\ & + \delta_3\lambda_7 A^6(t)x(t) + \delta_6\lambda_7^* A^6(t)x^*(t) \\ & + \delta_2\lambda_8 A^4(t)[x^*(t)]^3 + \delta_5\lambda_8^* A^4(t)x^3(t) \\ & + \delta_3\lambda_9 A^8(t)x(t) + \delta_6\lambda_9^* A^8(t)x^*(t) \\ & + \delta_2\lambda_{10} A^6(t)[x^*(t)]^3 + \delta_5\lambda_{10}^* A^6(t)x^3(t), \end{aligned} \tag{3.17}$$

where $\lambda_1, \lambda_2, \ldots, \lambda_{10}$ are auxiliary variables with different combinations of a_1 and a_2 which are defined in Table 3.3.

The most important aspect in (3.17) is that the essential nonlinearity structure is more visible. First of all, two cascaded third-order nonlinearities create terms up to ninth order. If $x(t)$ contains only a single carrier around f_{IF}, then (3.17) can be interpreted so that the terms containing $x(t)$ create new signal content around f_{IF} whereas the terms containing $[x^*(t)]^3$ create signal content around $-3f_{\mathrm{IF}}$. If any mixer and/or BB I/Q imbalance occur, there are also terms including $x^*(t)$ and $x^3(t)$ which create signal content around $-f_{\mathrm{IF}}$ and $3f_{\mathrm{IF}}$, respectively. This means that without any I/Q imbalance every other term in (3.17) reduces to zero (the latter one on each row). Additionally, the cascaded nonlinearity model also contains different powers of $A(t)$. These can be interpreted as spectral re-growth of the nonlinearity term content. For example, the term $A^2(t)x(t)$ has triple the bandwidth compared to $x(t)$. It is worth noticing that if $x(t)$ consists of several carriers with different complex IFs, the interpretations of the model becomes more complicated because the intermodulation between the carriers is not directly visible from (3.17) although the equation is modeling the IMD correctly. As a summary, all the nonlinearity terms of the cascaded nonlinearity model are listed in Table 3.4 and the contribution of each term is illustrated with a spectrum using a two-tone example.

Table 3.2: Auxiliary variables $\delta_1, \delta_2, \ldots, \delta_6$ for the cascaded nonlinearity model.

Without any I/Q imbalance	**Including only BB I/Q imbalance**
$\delta_1 = \frac{a_{3\mathrm{I}}+a_{3\mathrm{Q}}}{2}$	$\delta_1 = \frac{a_{3\mathrm{I}}+a_{3\mathrm{Q}}}{2}$
$\delta_2 = \frac{a_{4\mathrm{I}}+a_{4\mathrm{Q}}}{8}$	$\delta_2 = \frac{a_{4\mathrm{I}}+a_{4\mathrm{Q}}}{8}$
$\delta_3 = 3\frac{a_{4\mathrm{I}}+a_{4\mathrm{Q}}}{8}$	$\delta_3 = 3\frac{a_{4\mathrm{I}}+a_{4\mathrm{Q}}}{8}$
$\delta_4 = 0$	$\delta_4 = \frac{a_{3\mathrm{I}}-a_{3\mathrm{Q}}}{2}$
$\delta_5 = 0$	$\delta_5 = \frac{a_{4\mathrm{I}}-a_{4\mathrm{Q}}}{8}$
$\delta_6 = 0$	$\delta_6 = 3\frac{a_{4\mathrm{I}}-a_{4\mathrm{Q}}}{8}$
Including both mixer and BB I/Q imbalance	
$\delta_1 = \frac{a_{3\mathrm{I}}+a_{3\mathrm{Q}}}{2}k_1 + \frac{a_{3\mathrm{I}}-a_{3\mathrm{Q}}}{2}k_2^*$	
$\delta_2 = \frac{a_{4\mathrm{I}}-a_{4\mathrm{Q}}}{8}\left[k_2^3 + 3(k_1^*)^2 k_2\right] + \frac{a_{4\mathrm{I}}+a_{4\mathrm{Q}}}{8}\left[(k_1^*)^3 + 3k_1^* k_2^2\right]$	
$\delta_3 = 3\frac{a_{4\mathrm{I}}-a_{4\mathrm{Q}}}{8}\left[k_1^2 k_2 + \lvert k_2\rvert^2 k_2^* + 2\lvert k_1\rvert^2 k_2^*\right] + 3\frac{a_{4\mathrm{I}}+a_{4\mathrm{Q}}}{8}\left[k_1^*(k_2^*)^2 + \lvert k_1\rvert^2 k_1 + 2\lvert k_2\rvert^2 k_1\right]$	
$\delta_4 = \frac{a_{3\mathrm{I}}+a_{3\mathrm{Q}}}{2}k_2 + \frac{a_{3\mathrm{I}}-a_{3\mathrm{Q}}}{2}k_1^*$	
$\delta_5 = \frac{a_{4\mathrm{I}}-a_{4\mathrm{Q}}}{8}\left[k_1^3 + 3k_1(k_2^*)^2\right] + \frac{a_{4\mathrm{I}}+a_{4\mathrm{Q}}}{8}\left[(k_2^*)^3 + 3k_1^2 k_2^*\right]$	
$\delta_6 = 3\frac{a_{4\mathrm{I}}-a_{4\mathrm{Q}}}{8}\left[k_1 k_2^2 + \lvert k_1\rvert^2 k_1^* + 2\lvert k_2\rvert^2 k_1^*\right] + 3\frac{a_{4\mathrm{I}}+a_{4\mathrm{Q}}}{8}\left[(k_1^*)^2 k_2^* + \lvert k_2\rvert^2 k_2 + 2\lvert k_1\rvert^2 k_2\right]$	

Table 3.3: Auxiliary variables $\lambda_1, \lambda_2, \ldots, \lambda_{10}$ for the cascaded nonlinearity model.

$\lambda_1 = a_1$	$\lambda_6 = 9(a_1^*)^2 a_2^*$
$\lambda_2 = 3a_2$	$\lambda_7 = 9a_1^* a_2^2 + 18a_1\lvert a_2\rvert^2$
$\lambda_3 = a_1\lvert a_1\rvert^2$	$\lambda_8 = 27a_1^*(a_2^*)^2$
$\lambda_4 = (a_1^*)^3$	$\lambda_9 = 27a_2\lvert a_2\rvert^2$
$\lambda_5 = 3a_1^2 a_2^* + 6\lvert a_1\rvert^2 a_2$	$\lambda_{10} = 27(a_2^*)^3$

Table 3.4: All the terms generated by the cascaded nonlinearity model.

#	Term	Interpretation	Example spectrum	I/Q representation
1	$x(t)$	Original undistorted signal	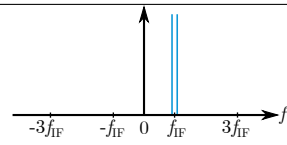	$x_I(t) + jx_Q(t) = x(t)$
2	$A^2(t)x(t)$	3rd-order IMD	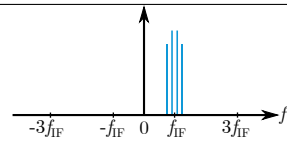	$x_I^3(t) + jx_Q^3(t)$ $= \frac{3}{4}A^2(t)x(t)$ $+ \frac{1}{4}[x^*(t)]^3$
3	$[x^*(t)]^3$	3rd-order harmonics	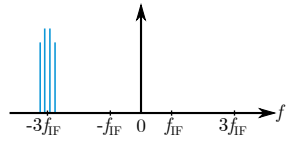	
4	$A^4(t)x(t)$	5th-order IMD	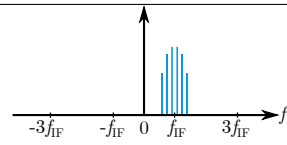	$[x_I^3(t) + jx_Q^3(t)]A^2(t)$ $= \frac{3}{4}A^4(t)x(t)$ $+ \frac{1}{4}A^2(t)[x^*(t)]^3$
5	$A^2(t)[x^*(t)]^3$	IMD of 3rd-order harmonics (5th order)	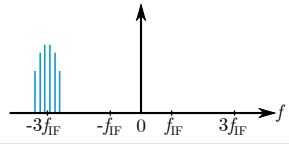	
6	$A^6(t)x(t)$	7th-order IMD	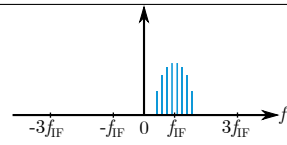	$[x_I^3 + jx_Q^3]A^4(t)$ $= \frac{3}{4}A^6(t)x(t)$ $+ \frac{1}{4}A^4(t)[x^*(t)]^3$
7	$A^4(t)[x^*(t)]^3$	IMD of 3rd-order harmonics (7th order)	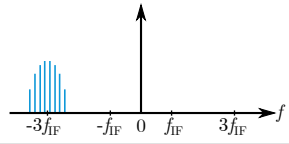	
8	$A^8(t)x(t)$	9th-order IMD	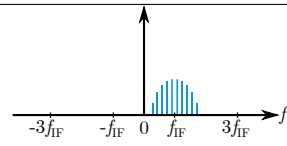	$[x_I^3 + jx_Q^3]A^6(t)$ $= \frac{3}{4}A^8(t)x(t)$ $+ \frac{1}{4}A^6(t)[x^*(t)]^3$
9	$A^6(t)[x^*(t)]^3$	IMD of 3rd-order harmonics (9th order)	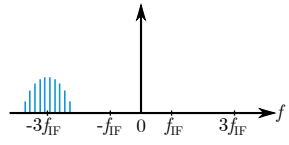	

+ complex conjugates of all the above terms if any I/Q imbalance occurs in the mixer and/or BB.

3.2 Analog-to-Digital Converter Nonlinearities

ADCs are inherently nonlinear devices. This is true even in ideal case since quantization is a nonlinear operation [37, 54, 91]. Therefore the number of quantization bits sets fundamental limits for the amplitude accuracy. In Figure 3.3, ideal quantization is illustrated with a blue dash line. However, signal-to-quantization-noise ratio (SQNR) also depends on sampling rate because oversampling reduces the amount of quantization noise inside the desired signal band. This is typically formulated as

$$SQNR_{\mathrm{dB}} = 6.02B + 1.76 + 10\log_{10}(L) \tag{3.18}$$

for a FS sinusoidal signal when ADC resolution is B bits and L is the oversampling factor [54]. The required oversampling factor can be further optimized by exploiting quantization noise shaping which is used in sigma-delta ADCs [54, 103]. However, sigma-delta ADCs and their imperfections are omitted from this thesis due to the size of the topic. It is thoroughly discussed in [78, 103] and references therein.

In the most general level, a typical ADC consists of a sample-and-hold circuit followed by a quantizer [7, 54, 76, 91]. Since even ideal ADCs are nonlinear, typically ADC nonlinearities refer to the nonlinear behavior that is only occurring in non-ideal ADCs. This includes, e.g., unintentional deviations of the quantization levels from the ideal ones and improper input signal conditioning. These topics are covered within this subsection. It is also important to understand that, in addition to the nonlinearities, real-world ADCs tend to have also other non-idealities, such as sample-and-hold circuit impairments and sampling clock jitter [54, 63, 76]. However, these non-idealities are outside the scope of the thesis.

Various ADC architectures exist which all have their advantages and disadvantages in different applications [7, 54, 76, 91]. However, most of them can be characterized with standardized performance metrics [50]. From the nonlinearities point of view, especially important are differential nonlinearity (DNL) and INL, because those describe unintentional deviations of the quantization levels. More specifically, INL expresses the difference between the actual and ideal code transition thresholds. An example is shown in Figure 3.3. After correcting static gain and offset, INL can be defined as

$$INL[l] = \frac{T[l] - T_{\mathrm{ideal}}[l]}{Q_{\mathrm{ideal}}} \tag{3.19}$$

for the output code index l [50]. For a B-bit ADC, $l = 0, 1, \ldots, 2^B - 1$. INL is commonly measured in least significant bits (LSBs), but sometimes also in percentage of ADC FS or in absolute value (volts or amperes) [50, 76]. It is also worth being aware that in addition to (3.19) also slightly different definitions for INL exist [50, 76, 91].

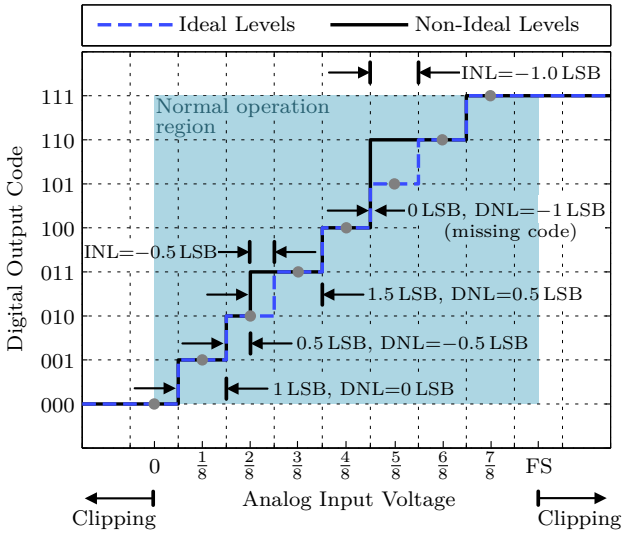

Figure 3.3: Example of ideal and non-ideal quantization levels for an unipolar quantizer having $B = 3$ bits. The illustration highlights both differential and integral nonlinearities as well as clipping.

After correcting static gain, DNL defines the relative difference between the actual code bin width $Q[l]$ and the ideal code bin width Q_{ideal}. Therefore

$$DNL[l] = \frac{Q[l] - Q_{\text{ideal}}}{Q_{\text{ideal}}} \tag{3.20}$$

for the output code index l, where $Q[l] = T[l+1] - T[l]$. Note that the widths of the first and the last code bin, $Q[0]$ and $Q[2^B - 1]$, are not generally defined [50]. A situation where $DNL[l] = -1\,\text{LSB}$ is called a missing code which means that the specific output code l never appears at the ADC output. This situation is also illustrated in Figure 3.3, where the code 101 is a missing code. Figure 3.4 shows an example of measured DNL in LSBs for a 12-bit ADC over the whole FS range. DNL is relatively small here due to the calibration of the ADC. The important point is that DNL typically looks random and does not seem to have any specific structure. However, DNL actually contains correlated and uncorrelated part. This becomes evident when looking at the INL of the same ADC in Figure 3.4. The INL clearly has a structure and this is specifically due to the correlated part of the DNL, because INL can be thought as a running sum of DNL corrected by the gain error [76].

For modeling purposes, INL can be further divided into three parts

$$INL[l, \omega] = INL_{\text{HCF}}[l] + INL_{\text{LCF}}[l, \omega] + INL_{\text{noise}}[l, \omega], \tag{3.21}$$

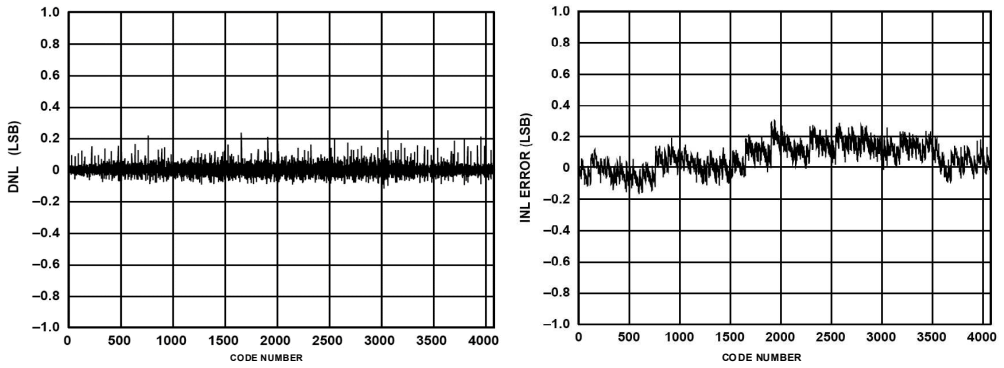

Figure 3.4: Example of measured DNL and INL from a 12-bit ADC [50], © 2011 IEEE.

namely high code frequency (HCF), low code frequency (LCF), and noise part [15, 16, 43, 81]. The model also includes angular frequency ω in order to take into account frequency selectivity which is a realistic assumption for wideband ADCs. The LCF part gives polynomial shape for the INL and in frequency-selective case it can be modeled with a Hammerstein model. The HCF part mainly models the quantizer imperfections, which depend on the ADC (quantizer) architecture, and therefore $INL_{\mathrm{HCF}}[l]$ is approximately frequency independent [15, 16, 43]. The HCF can be modeled as piecewise linear on top of which there is additive noise $INL_{\mathrm{noise}}[l, \omega]$. More details on how ADC architecture affects on INL can be found from [88]. As can be concluded from (3.19) and (3.21), INL can be measured and also compensated in various ways without exact knowledge of the underlying circuit structure, see, e.g., [72] and references therein. This makes INL a convenient concept since it can originate from various sources, e.g., from the generation of reference voltages and comparator non-idealities [76, 91]. The cascaded receiver nonlinearity model derived in Section 3.1 also covers the $INL_{\mathrm{LCF}}[l, \omega]$ part of the INL due to the polynomial structure.

Compared with DNL/INL, much more severe nonlinear distortion can occur in ADCs due to the signal clipping [7, 29, 68, 76, 111]. As indicated by Figure 3.3, an ADC has a certain analog input voltage range within which the analog input signal is digitized as desired. Anytime the input signal is outside this voltage range, it gets clipped. Formally,

$$l = \begin{cases} 0 & \forall x_{\mathrm{IN}} \leq Q_{\mathrm{ideal}}/2, \\ 2^B - 1 & \forall x_{\mathrm{IN}} > x_{\mathrm{FS}} - 3Q_{\mathrm{ideal}}/2, \end{cases} \tag{3.22}$$

for the ADC input voltage x_{IN} when the ADC FS voltage range is from 0 to x_{FS}. Although typically receivers are designed so that clipping would not occur, it is not always possible to avoid improper input signal conditioning. Received signal power may change very rapidly due to changes in signal propagation environment (fading etc.) and also because of suddenly appearing strong blocker signals [28, 110, 120]. In these

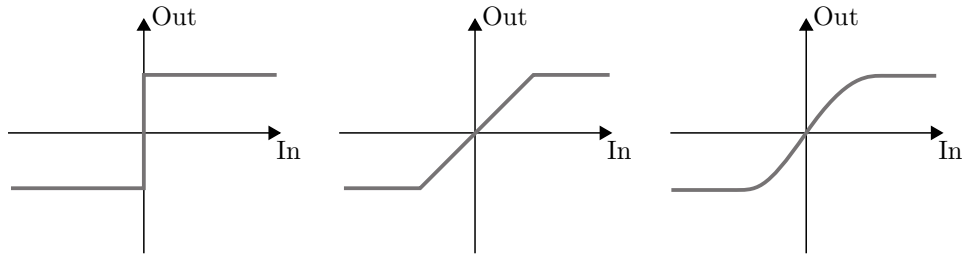

(a) Limiter **(b)** Hard Clipping **(c)** Soft Clipping

Figure 3.5: Input-output characteristics of different clipping concepts.

situations, the AGC of the receiver may not follow fast enough the changes in signal dynamics and clipping occurs. In general, high PAPR of received waveform makes it challenging to optimally utilize the FS range of the ADC [25]. SNR is maximized when the FS range is fully utilized, but exceeding it immediately causes clipping which means strong nonlinear distortion for the signal.

As a clarification for the terminology, Figure 3.5 is provided. A 1-bit quantizer is basically a limiter (Figure 3.5a) which only preserves the sign information of the input signal. On the other hand, multi-bit quantizers have hard clipping input-output characteristics (Figure 3.5b) as defined in (3.22). This means that an ideal ADC produces linear output (apart from quantization) within FS input range but outside the range the output is heavily nonlinear. This differs from amplifiers and many other analog components that typically follow the soft clipping curve illustrated in Figure 3.5c. There the output is weakly nonlinear already with input levels that still do not completely saturate the component. Therefore, the concepts of second- and third-order intercept points as well as 1-dB compression point are much more useful for amplifiers than for ADCs [7]. However, it is possible to derive, among others, IIP3 for ADC if needed, e.g., in receiver link budget analysis [57]. It is also worth noting that the clipping terminology is not strictly defined in the literature. Sometimes, e.g., the limiter is called hard clipping and the hard clipping is called soft clipping or hard limiter. More about ADC clipping modeling is discussed in Chapter 5.

CHAPTER 4

Digital Suppression of Receiver Nonlinearities

The main focus of the chapter is on AIC which is a purely DSP-based feed-forward algorithm for suppressing receiver nonlinearities. It is able to extract, directly from the received signal itself, all the information it needs for the suppression of nonlinear distortion. Therefore, AIC adapts itself during the signal reception according to any changes in nonlinearities or signal scenario. Using AIC for the suppression of receiver nonlinearities is also discussed in [P8] and more applications are considered in [P7, P9].

4.1 Background and State of the Art

In order to minimize the amount of nonlinear distortion in a receiver, it is good to avoid the generation of the distortion in the first place. One this kind of distortion avoidance approach is proposed in [77]. According to the proposal, excessive distortion is avoided in CR by tuning RF front-end filter parameters in optimal manner based on spectrum sensing results. Also [74] discusses about avoiding nonlinear distortion in CR receivers by considering the spectral locations of strong blocker signals. Since avoiding nonlinear distortion is difficult in practice, other kind of ideology is to let the distortion occur and then cancel it out. Adaptive cancellation methods, mainly focusing on even-order distortion, have been proposed, e.g., in [23, 32, 35]. The method in [35] replicates the occurring second-order distortion and subtracts it from the signal after the mixer. On the contrary, [23] digitizes low-frequency distortion with a secondary receiver branch and uses it for second-order distortion cancellation by means of DSP. The proposal in [32] employs adaptive DSP algorithm to introduce intentional mismatch in a mixer so that second-order distortion is cancelled. In addition, a technique for cancelling strong

blockers in RF front-end is proposed [27]. In SDR context, [101] considered both analog and digital methods to suppress strong out-of-band blockers which could fall on top of the desired signal due to harmonic mixing. A common feature for all aforementioned approaches is that additional hardware is needed in the receiver or at least some specific requirements are set to analog receiver components.

AIC is able suppress nonlinear distortion with DSP without any additional analog hardware. Originally the AIC concept was proposed in [106, 114] for suppressing receiver nonlinearities. The aforementioned references together with [105] essentially cover both the RF and BB receiver nonlinearities, but do not explicitly consider their joint effects as in Section 3.1. The complete receiver chain linearization using AIC is also discussed in [38–40] along with applicability to scenarios such as spectrum sensing with energy detection and coexisting GSM networks, especially concerning GSM-Railway (GSM-R). Effects of RF front-end nonlinearities to spectrum sensing with energy detectors and cyclostationary feature detectors for vestigial single sideband signals are considered in [94]. AIC is proposed for suppressing nonlinear distortion and consequently improving the detection performance. Further mathematical analysis and additional detection improvement methods are given by the same authors in [95]. Compared to AIC, a very similar post-processing method is also proposed in [73] for suppressing nonlinear distortion stemming from the RF receiver front-end. Another kind of adaptive post-processing method is considered in [31] for linearizing a single bandlimited signal by exploiting the nonlinear distortion outside the signal band.

Introducing one or more additional receiver branches in order to provide reference information for AIC is proposed in [58–60, 124]. Separate reception of a desired signal and a blocker signal with distinct receiver chains followed by AIC after A/D conversion is proposed in [124]. In [58, 59], the regeneration of nonlinear distortion is performed in analog side on a secondary receiver branch and then AIC is employed in digital domain. This idea has been developed further in [60] which exploits several receiver branches for nonlinearity regeneration in order to also suppress high-order distortion. Although these approaches require additional analog receiver components, they have potential for better distortion suppression in extreme situations. In addition, it is possible to suppress nonlinear distortion stemming from blockers outside the digitized frequency band which cannot be done with the original purely digital AIC. In general, it can be concluded that the vast variety of AIC-related publications clearly indicates the versatility of the AIC concept.

4.2 Adaptive Interference Cancellation

This section provides detailed description of AIC concept in its pure digital form. In other words, all the processing is performed for the digitized received signal without a need

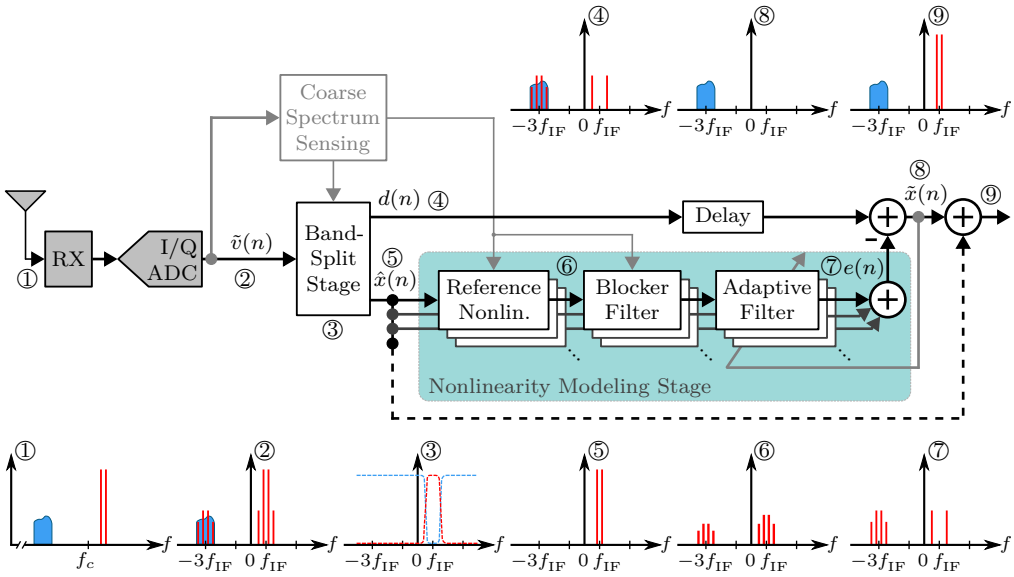

Figure 4.1: Block diagram for AIC suppressing nonlinear receiver distortion. Conceptual spectra exemplify the processing in scenario where a strong two-tone blocker signal causes nonlinear distortion especially on top of the weak modulated signal.

for any additional analog hardware. The nonlinear distortion suppression performance is verified by the conducted RF laboratory measurements.

4.2.1 Algorithm Description

This description of AIC algorithm focuses on scenario where it is desired to suppress nonlinear receiver distortion from the whole reception band, which is useful, e.g., in spectrum sensing receivers. It is also possible to clean only a specific sub-band, but this scenario is not considered until Subsection 4.2.2 in which the most important practical aspects regarding AIC are highlighted. Figure 4.1 describes AIC by means of a block diagram and simple conceptual spectrum illustrations. The spectra show an example case where a strong two-tone signal is received together with a weak modulated signal (Spectrum 1). Due to the receiver nonlinearities, the two-tone blocker causes distortion especially on top of the weak signal. The received and digitized waveform is denoted with $\tilde{v}(n)$ and is illustrated in Spectrum 2 of Figure 4.1.

The AIC processing begins with a *band-split stage* as depicted in Figure 4.1. The signal $\tilde{v}(n)$ is split into a main branch $d(n)$ and a reference branch $\hat{x}(n)$. The main branch (Spectrum 4) contains all the received signal content except the blocker(s) where as the reference branch (Spectrum 5) contains only the blocker(s). The splitting is performed with appropriate bandpass (reference branch) and bandstop (main branch) filters which are illustrated in Spectrum 3.

Next step in the AIC processing is a *nonlinearity modeling stage*. The basic idea here is to regenerate the nonlinear distortion occurred in the receiver using $\hat{x}(n)$ in the reference branch and then subtract it from the main branch in order to suppress the nonlinear distortion in $d(n)$. The nonlinearity modeling is performed with the help of reference nonlinearities matching the distortion structure in the received signal. The reference nonlinearities can be, e.g., some of the terms from Table 3.4 which are applied to $\hat{x}(n)$. This is illustrated in Spectrum 6. Then the nonlinearity estimates are filtered with a blocker filter which attenuates the frequency content on blocker band(s), see Spectrum 7. This is done to match the estimates better to $d(n)$ which do not have any content on blocker band(s) due to the band-split filtering. The fundamental reason for this blocker filtering on both branches is to avoid strong signal correlation on the blocker(s) which could heavily bias adaptive filter (AF) learning. The AFs are used here to match the regenerated nonlinear distortion to the received signal. This must be done because the reference nonlinearities itself does not have correct amplitude nor phase. In the simplest case, the AF means a single complex coefficient for each nonlinearity term. However, if the receiver have considerable frequency selectivity, the single complex coefficients should be replaced with multitap filters. The filter adaptation can be done with various algorithms minimizing the power of the remainder of the main branch signal $d(n)$ and the regenerated distortion $e(n)$. One option is to use the traditional least-mean-square (LMS) algorithm [45, 52] which, among other options, are discussed later in this subsection.

After successfully subtracting the regenerated distortion $e(n)$ with appropriate weights (adaptive filters) from $d(n)$, a cleaner received signal is achieved. Due to the blocker filtering, this cleaned signal $\tilde{x}(n)$ does not contain the original blocker(s) as illustrated in Spectrum 8. If it is desired that also the blocker(s) is/are passed to next processing stages, the blocker(s) can be added back after the AIC processing as illustrated with a dash line on the right side of Figure 4.1, resulting Spectrum 9.

The whole AIC processing can be aided by *coarse spectrum sensing* as shown in Figure 4.1. The basic idea is to locate the strongest blockers, if this information is not available *a priori*. The specific parameters of interest are bandwidths and center frequencies of the blockers which are required for designing the band-split filters. These parameters are straightforward to extract, e.g., in frequency domain using energy detection. This is rather undemanding task since the interest is only on strongest signals in contrast to more traditional spectrum sensing where typically even the weakest signals, near the noise floor, are of interest [12, 121, 122]. The filter designing here is a traditional digital filter optimization task which is exhaustively discussed in various DSP books, e.g., in [45, 52]. One practical approach is to have a bank of pre-designed prototype filters for different blocker bandwidths and then use them according to the blocker scenario at hand. Tuning the center frequency of the filters is straightforward since it can be done by multiplying the impulse response of the filter with an exponential tone signal having the

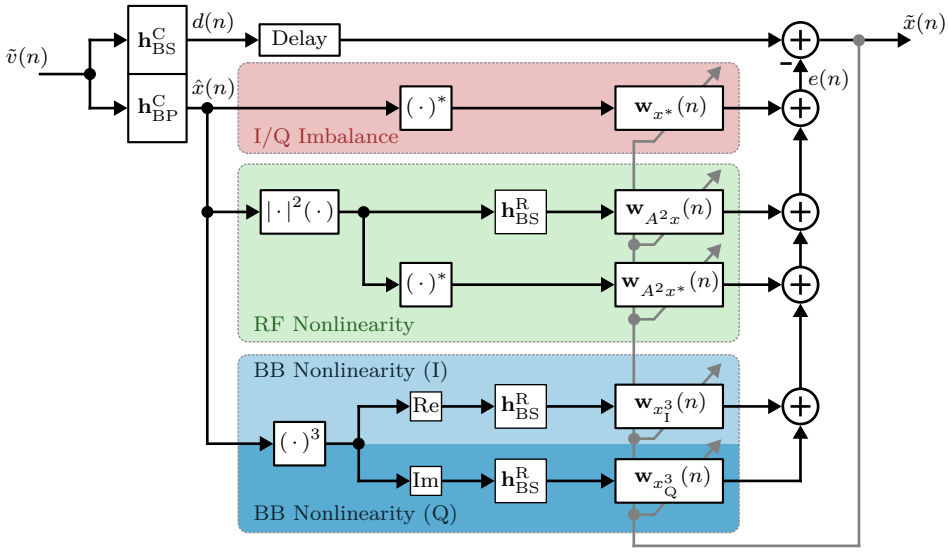

Figure 4.2: Band-split and nonlinearity modeling stages of AIC for suppressing RF and BB nonlinearities as well as mixer and BB I/Q imbalance in a direct-conversion receiver.

targeted center frequency. Other purpose of use for the coarse spectrum sensing could be estimation of what kind of nonlinear functions are needed in the nonlinearity modeling stages. This kind of estimation can be done by comparing strongest distortion locations to the strongest blocker locations. However, this should be backed up by following the learned AFs to verify that each nonlinearity term in the model is useful. This kind of adaptive nonlinearity term selection helps in optimizing the computational complexity with respect to the hardware and signal scenario at hand.

In general, the optimal nonlinearity modeling structure for AIC depends on the analog receiver hardware and signal scenarios. It is possible to achieve very good suppression performance also with a pre-selected fixed nonlinearity modeling structure. One potential structure for suppressing RF and BB receiver nonlinearities as well as I/Q imbalance is shown in Figure 4.2 and was originally proposed in [P8]. The impulse responses of the complex band-split filters are denoted with vectors $\mathbf{h}^{\mathrm{C}}_{\mathrm{BS}}$ and $\mathbf{h}^{\mathrm{C}}_{\mathrm{BP}}$, referring to bandstop and bandpass filters, respectively. The real version of the same bandstop filter is denoted with $\mathbf{h}^{\mathrm{R}}_{\mathrm{BS}}$. The proposed nonlinearity modeling stage includes five parallel branches implementing the most dominant distortion terms in optimized manner. In fact, these terms are the first three terms from Table 3.4 and their complex conjugates, excluding the direct term $\hat{x}(n)$ itself. Using the cascaded nonlinearity model derived in Section 3.1, it can be observed that with realistic gain and IIP3 values, the first three terms are the most dominant ones. This is verified by an example of relative term powers shown in Figure 4.3 by using (3.17) without any I/Q imbalance. The essential information and mathematical notation of the selected terms are gathered in Table 4.1, where $\hat{A}(n)$

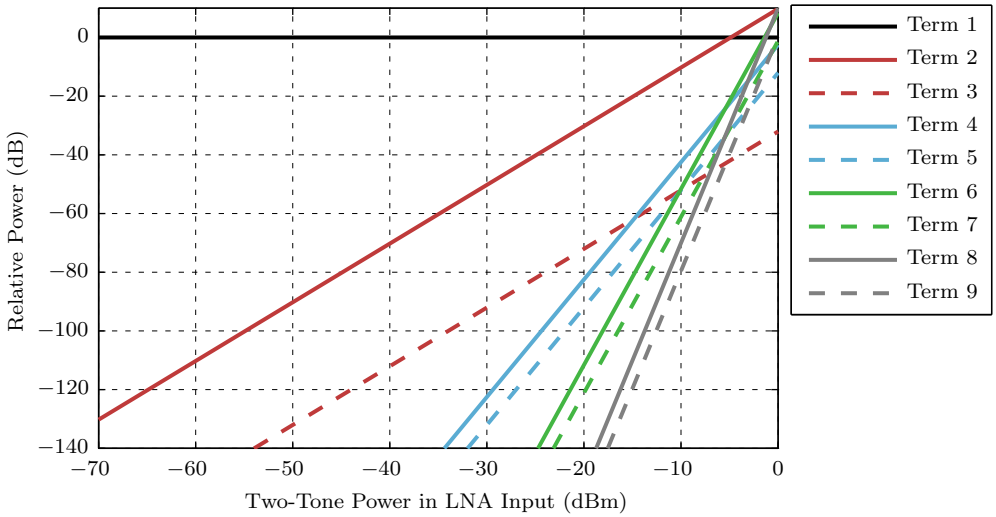

Figure 4.3: Relative powers of the cascaded nonlinearity model terms with a two-tone input when RF gain is 20 dB, RF IIP3 is 0 dBm, and BB IIP3 is 30 dBm. The relative power compares the power of the strongest frequency component of the nonlinearity term to the power of one of two tones in Term 1 (linear term). The term numbering is in accordance with Table 3.4.

denotes the envelope of $\hat{x}(n)$. The structure of Figure 4.2 is optimized in a sense that the real filter $\mathbf{h}_{\mathrm{BS}}^{\mathrm{R}}$ is employed, where possible, instead of the complex one and it is completely omitted from the branches where no blocker filtering is necessary. Furthermore, Term 1 is associated with strictly-linear (SL) adaptive filtering which means that a complex AF is to be found for $\hat{x}^*(n)$. Term 2, in turn, employs widely-linear (WL) adaptive filtering since typically also its complex conjugate causes essential nonlinearity contribution in DCRs. WL means that $\hat{A}^2(n)\hat{x}(n)$ and $\hat{A}^2(n)\hat{x}^*(n)$ both have their own separate complex AFs [5, 10, 11]. This is the case also for Term 3. However, the computational complexity is smaller if reduced-complexity widely-linear (RC-WL) adaptive filtering is exploited. To be more specific, WL filtering would mean finding complex AFs $\mathbf{w}_{x^3}(n)$ and $\mathbf{w}_{x_c^3}(n)$ for the complex term $\hat{x}^3(n)$ and for its complex conjugate, but RC-WL is exploiting the fact that it is equivalent to find complex AFs $\mathbf{w}_{x_{\mathrm{I}}^3}(n)$ and $\mathbf{w}_{x_{\mathrm{Q}}^3}(n)$ for the real and imaginary parts of $\hat{x}^3(n)$ and hence reduce computational complexity [11, 85]. Formally,

$$\mathbf{w}_{x^3}(n) * \hat{x}^3(n) + \mathbf{w}_{x_c^3}(n) * [\hat{x}^*(n)]^3 = \mathbf{w}_{x_{\mathrm{I}}^3}(n) * \mathrm{Re}[\hat{x}^3(n)] + \mathbf{w}_{x_{\mathrm{Q}}^3}(n) * \mathrm{Im}[\hat{x}^3(n)], \quad (4.1)$$

which is based on the fact that

$$\mathbf{w}_{x_{\mathrm{I}}^3}(n) = \mathrm{Re}[\mathbf{w}_{x^3}(n)] + \mathrm{Re}[\mathbf{w}_{x_c^3}(n)] + j\big\{\mathrm{Im}[\mathbf{w}_{x^3}(n)] + \mathrm{Im}[\mathbf{w}_{x_c^3}(n)]\big\}, \quad (4.2a)$$

$$\mathbf{w}_{x_{\mathrm{Q}}^3}(n) = \mathrm{Im}[\mathbf{w}_{x_c^3}(n)] - \mathrm{Im}[\mathbf{w}_{x^3}(n)] + j\big\{\mathrm{Re}[\mathbf{w}_{x^3}(n)] - \mathrm{Re}[\mathbf{w}_{x_c^3}(n)]\big\}. \quad (4.2b)$$

Table 4.1: Selected terms for the nonlinearity modeling stage of AIC.

Term #	Equation	Filtering	Vector notation	Adaptive filters
Term 1	$\hat{x}^*(n)$	SL	$\mathbf{s}_{x^*}(n)$	$\mathbf{w}_{x^*}(n)$
Term 2	$\hat{A}^2(n)\hat{x}(n)$	WL	$\mathbf{s}_{A^2x}(n), \mathbf{s}_{A^2x^*}(n)$	$\mathbf{w}_{A^2x}(n), \mathbf{w}_{A^2x^*}(n)$
Term 3	$\hat{x}^3(n)$	RC-WL	$\mathbf{s}_{x^3_{\mathrm{I}}}(n), \mathbf{s}_{x^3_{\mathrm{Q}}}(n)$	$\mathbf{w}_{x^3_{\mathrm{I}}}(n), \mathbf{w}_{x^3_{\mathrm{Q}}}(n)$

Hence, RC-WL is a very convenient concept. However, it cannot be applied for Term 2 because $\hat{A}^2(n)\hat{x}(n)$ should be filtered with $\mathbf{h}^{\mathrm{R}}_{\mathrm{BS}}$ (to avoid correlation with the original blocker) but its complex conjugate $\hat{A}^2(n)\hat{x}^*(n)$ should not be filtered (to avoid filtering out essential components from the blocker mirror band). This forces to use WL instead of RC-WL for Term 2.

As mentioned earlier, AF learning can be done in numerous ways. A typical sample-wise adaptive algorithm is LMS and its many variations. Also, e.g., recursive least squares (RLS) could be used. Although RLS is more complex than LMS, it converges faster. In general, the adaptive algorithms have trade-offs between solution accuracy, convergence rate, and computational complexity [45,52]. Optimal block-wise least squares (LS) solution is also possible to use in some communications systems. For example, orthogonal frequency-division multiplexing (OFDM) signals are typically processed block-wise in frequency domain anyway, so block-wise AF learning is a logical choice. As an example, RC-WL LMS is shown here using the notation from Figure 4.2. It is proven in [85] that RC-WL LMS has the same complexity as SL LMS while also achieving the same mean square error and convergence rate. First, signals from all five distortion branches are combined into the vector $\mathbf{s}(n)$ so that

$$\mathbf{s}(n) = \left[\mathbf{s}_{x^*}(n), \mathbf{s}_{A^2x}(n), \mathbf{s}_{A^2x^*}(n), \mathbf{s}_{x^3_{\mathrm{I}}}(n), \mathbf{s}_{x^3_{\mathrm{Q}}}(n)\right]^{\mathrm{T}}, \tag{4.3}$$

where individual $\mathbf{s}$-vectors include filtering with $\mathbf{h}^{\mathrm{R}}_{\mathrm{BS}}$, if indicated in Figure 4.2. The AF length is M_f meaning that also the length of each individual $\mathbf{s}$-vector is M_f and therefore the length of $\mathbf{s}(n)$ is $5M_f$. Each individual $\mathbf{s}$-vector contain the nth sample followed by $M_f - 1$ previous samples, e.g., $\mathbf{s}_{x^*}(n) = [\hat{x}^*(n), \hat{x}^*(n-1), \ldots, \hat{x}^*(n-M_f+1)]^{\mathrm{T}}$. Similarly, also AFs are gathered in a single vector $\mathbf{w}(n)$, namely,

$$\mathbf{w}(n) = \left[\mathbf{w}_{x^*}(n), \mathbf{w}_{A^2x}(n), \mathbf{w}_{A^2x^*}(n), \mathbf{w}_{x^3_{\mathrm{I}}}(n), \mathbf{w}_{x^3_{\mathrm{Q}}}(n)\right]^{\mathrm{T}}. \tag{4.4}$$

Now, the LMS adaptation of all AFs is straightforward. If no *a priori* information is available, the combined AF vector is initialized with zeros, i.e.,

$$\mathbf{w}(0) = \mathbf{0}_{5M_f \times 1}. \tag{4.5}$$

Then, the combined AF-filtered output is

$$e(n) = \mathbf{w}^{\mathrm{H}}(n)\mathbf{s}(n) \tag{4.6}$$

for all $n = 0, 1, 2, \ldots$, which is then used in the error calculation step as

$$\tilde{x}(n) = d(n) - e(n). \tag{4.7}$$

As a final step, the AFs are updated so that

$$\mathbf{w}(n+1) = \mathbf{w}(n) + \mathrm{diag}(\boldsymbol{\mu})\tilde{x}^*(n)\mathbf{s}(n), \tag{4.8}$$

where $\mathrm{diag}(\cdot)$ converts the vector to a diagonal matrix. The LMS step sizes are in vector $\boldsymbol{\mu}$ consisting of an M_f-length step-size vector for each distortion branch, i.e., $\boldsymbol{\mu} = [\boldsymbol{\mu}_{x^*}, \boldsymbol{\mu}_{A^2x}, \boldsymbol{\mu}_{A^2x^*}, \boldsymbol{\mu}_{x_{\mathrm{I}}^3}, \boldsymbol{\mu}_{x_{\mathrm{Q}}^3}]^{\mathrm{T}}$. In this general notation, each AF-tap of each nonlinearity branch may have its own step size. For example, the first branch have step sizes $\boldsymbol{\mu}_{x^*} = [\mu_{x^*}(0), \mu_{x^*}(1), \ldots, \mu_{x^*}(M_f - 1)]^{\mathrm{T}}$. For more convenient tuning of the step sizes, normalized least-mean-square (NLMS) can be used [45]. LMS and NLMS algorithms are identical except that NLMS step sizes are scaled with respect to powers of the distortion branch signals. Formally, the whole combined NLMS step-size vector is

$$\boldsymbol{\mu}_{\mathrm{N}} = \left[\frac{\mu_{x^*}(0)}{\beta_{x^*} + \left\|\mathbf{s}_{x^*}(n)\right\|^2}, \frac{\mu_{x^*}(1)}{\beta_{x^*} + \left\|\mathbf{s}_{x^*}(n)\right\|^2}, \ldots, \frac{\mu_{x_{\mathrm{Q}}^3}(M_f - 1)}{\beta_{x_{\mathrm{Q}}^3} + \left\|\mathbf{s}_{x_{\mathrm{Q}}^3}(n)\right\|^2} \right], \tag{4.9}$$

where additional selectable constants β_{x^*}, β_{A^2x}, $\beta_{A^2x^*}$, $\beta_{x_{\mathrm{I}}^3}$, and $\beta_{x_{\mathrm{Q}}^3}$ are used to prevent the denominator of (4.9) to be close to zero.

4.2.2 Practical Aspects

Previous subsection described AIC for suppressing nonlinear receiver distortion from the whole reception band. It is also possible to focus on suppressing nonlinear distortion from a specific sub-band in order to enhance demodulation of a weak individual IF carrier under influence of strong neighboring blocker signals. This is a realistic scenario, e.g., in systems with flexible digital channel selection. This kind of processing requires only a simple change to the AIC structure of Figure 4.2 in which the bandpass filter should be replaced with a bandstop filter and the bandstop filters are changed to bandpass filters. Effectively this means that the sub-band of interest is picked with the bandpass filter in the main branch and rest of the reception band is used for modeling the nonlinear distortion in the reference branch. This approach does not necessarily require the knowledge of blocker locations and bandwidths (coarse spectrum sensing) since all the signal content outside the target band is used in the reference branch. However, the

performance of the approach may be further enhanced by passing only the strongest blockers into the nonlinearity modeling stage. Practically this means bandpass filtering for the blockers as in the whole reception band cleaning scenario. In this manner, the amount of unwanted received nonlinear distortion passing into the nonlinearity modeling stage is reduced.

It is important to highlight here that AIC is capable of performing efficiently in multi-blocker scenarios. The reference branch signal $\hat{x}(n)$ can contain more than one blocker. This is put into practice, e.g., by designing $\mathbf{h}_{\mathrm{BP}}^{\mathrm{C}}$ to have multiple passbands. Other option is to design own bandpass filter for each blocker and then sum them together to form $\hat{x}(n)$. Since nonlinearity modeling terms, such as $(\cdot)^3$, are basically sample-wise operations, it does not matter if $\hat{x}(n)$ contains one or multiple blockers. The nonlinear distortion is anyway produced correctly. Therefore, unlike claimed in [38], AIC is inherently able to model the IMD between the blockers using the structure shown in Figure 4.2. There is no need for any additional nonlinearity modeling branches due to multiple blockers and hence the computational complexity of AIC is almost independent of the number of blockers. Only the band-split stage may be slightly more complicated when filtering multiple blockers.

Regarding the nonlinearity modeling stage of AIC, it is important to make sure that sample rate is high enough during the processing. Originally the nonlinear distortion occurs in the analog part of the receiver where aliasing cannot happen and hence it is also essential to avoid aliasing when modeling the distortion in digital domain. For example, if the sampling rate of the ADC is f_s and the same rate is used throughout the digital processing, maximum received blocker frequency can be then $f_s/6$ in order to avoid aliasing of third-order nonlinearities. Naturally, it would be desired to support blocker frequencies until $f_s/2$ and this is possible by temporarily increasing the sample rate during the nonlinearity modeling of Figure 4.2. It should be emphasized that this is required only in the digital processing and does not affect the actual sampling rate of the ADC. A straightforward rule would be that the digital modeling of third-order nonlinearities needs interpolation to the sample rate of $3f_s$ in order to avoid aliasing since those can have triple bandwidth. However, the requirement can be loosened by accepting aliasing to the frequencies higher than $f_s/2$. This means that third-order nonlinearities can be modeled using the sample rate of $2f_s$ and still all the *harmful* aliasing to frequencies between $-f_s/2$ and $f_s/2$ is avoided. This principle is illustrated in Figure 4.4. Generally, qth-order nonlinearities require at least the sample rate of $\frac{q+1}{2}f_s$. For high distortion orders, this yields to significantly smaller sample rate compared to the nominal qf_s sample rate required to completely avoid aliasing.

It is also good to understand that Figure 4.2 provides only one possible nonlinearity modeling structure. It may be too complex or too simple for some applications. However, it is straightforward to reduce or increase the number of parallel branches in nonlinearity modeling. As discussed on previous subsection, in some systems it may be even feasible

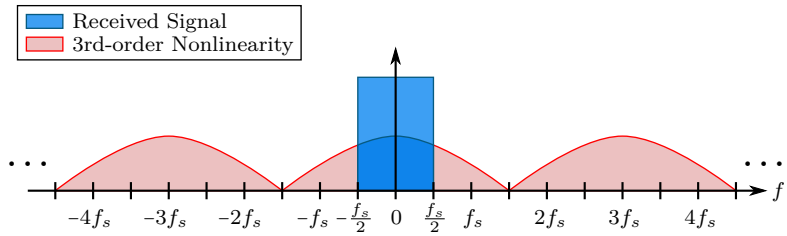

(a) No aliasing when sample rate is $3f_s$

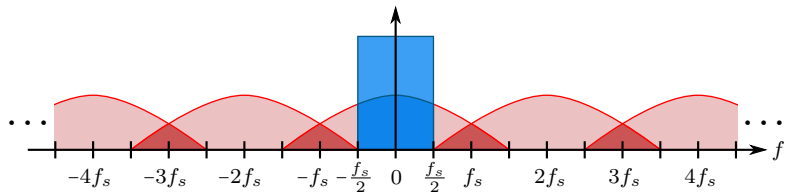

(b) Only harmless aliasing when sample rate is $2f_s$

Figure 4.4: Digital modeling of nonlinear receiver distortion requires increased sample rate in order to avoid harmful aliasing. For third-order nonlinearities, aliasing is totally avoided by having sample rate of $3f_s$, but even $2f_s$ is enough to avoid harmful aliasing on the original received signal band.

to adaptively select the appropriate nonlinearity terms during signal reception. In general, the nonlinearity modeling branches may contain any nonlinearities matching to the used hardware. For DCRs, the good starting point is the terms mentioned in Table 3.4 and similarly also even-order terms. If even higher degree of freedom is desired, literature provides plenty of options, see, e.g., [69] and references therein. Although the aforementioned reference is concentrating on power amplifiers (PAs), some of the nonlinearity models may also be applicable to amplifiers in receivers. For PAs, [69] is showing that very accurate modeling results are obtain using envelope memory polynomials which, in short, means polynomials considering both the current signal envelope value and also its previous values.

Yet another practical aspect about AIC is that the processing may not have to be running all the time during the signal reception. If there is practically no nonlinear distortion and therefore high signal-to-noise-and-distortion ratio (SNDR), AIC should be turned off. The reasons are twofold. First of all, computing power is saved when unnecessary processing is avoided. Secondly, AIC may in some cases even deteriorate already good SNDR. This may stem, e.g., from nonlinearity modeling mismatches or errors in learned AFs due to the fact that the considered blocker signals are not strong compared to other signals.

In order to efficiently use AIC, it is good to understand its limitations. Those are considered in the following list.

- **Out-of-band blockers:** AIC cannot suppress distortion stemming from blockers that are outside the digitized reception band although their distortion would fall inside the reception band. Only the distortion stemming from blockers present in the nonlinearity modeling stage of AIC can be suppressed. Since AIC is fully digital, it does not have access to the blockers that are outside the digitized reception band.

- **Blocker in-band distortion:** The nonlinear distortion inside the blocker bands affects the nonlinearity modeling since the modeling uses the received blockers as a reference. AIC performs well if the amount of nonlinear distortion inside the blocker bands is on decent level.

- **Blocker in-band distortion suppression:** Although AIC is able to suppress nonlinear distortion from the whole reception band, this does not include the blocker bands. In the nonlinearity modeling stage, $\mathbf{h}_{\mathrm{BS}}^{\mathrm{C}}$ is used as a blocker filter to attenuate frequency content at the blocker bands and hence the received nonlinear distortion is not suppressed from the blocker bands. As depicted in Figure 4.1, blockers can be added back in the end of AIC processing, but the blockers contain all the original in-band distortion. This is typically not a problem even if it is desired to demodulate the blocker signals. Since blockers are the strongest signals, they also have the best SNDR among all the received signals.

- **Filter transition bands:** The suppression performance is generally rather limited on the transition bands of the band-split filters $\mathbf{h}_{\mathrm{BP}}^{\mathrm{C}}$ and $\mathbf{h}_{\mathrm{BS}}^{\mathrm{C}}$. This may be a problem if there is a very weak signal right next to a strong blocker signal. To a certain extent this can be compensated by increasing the filter order and thus making the transition bands narrower still achieving enough stopband attenuation.

- **Nonlinearity term correlation:** The selected nonlinearity modeling terms may affect the convergence of AF learning. If several nonlinearity terms have contribution on same frequencies, they have time-domain correlation which may make the adaptation of AFs more challenging since the adaptation is based on the common $\tilde{x}(n)$.

However, in general, it can be said that AIC is very favorable algorithm since it is fully digital and does not require any additional analog hardware. This makes it possible to implement AIC also in already existing receivers. Furthermore, Exact *a priori* information about analog receiver components is not needed and AIC is able to continuously track changes, e.g., due to component aging, temperature variations or deliberate gain tuning.

Table 4.2: Parameters of the measured signal scenario.

	Parameter	Value
General	Center frequency	1800 MHz
	Reception bandwidth	100 MHz
Desired signal	Type	LTE uplink / SC-FDMA
	Bandwidth	10 MHz
	Intermediate frequency	−15 MHz
	Subcarrier modulation	16-QAM
Blockers	Type	LTE downlink / OFDMA
	Bandwidth	10 MHz
	Intermediate frequencies	10 MHz and 35 MHz
	Subcarrier modulation	16-QAM
AIC	Adaptation	NLMS
	Nonlinearity terms	$\hat{x}^*(n)$, $\hat{A}^2(n)\hat{x}(n)$, $\hat{A}^2(n)\hat{x}^*(n)$, $\mathrm{Re}[\hat{x}^3(n)]$, $\mathrm{Im}[\hat{x}^3(n)]$
	Length of adaptive filters	2 taps
	NLMS step sizes	$\boldsymbol{\mu}_{x^*} = \begin{bmatrix}0.03\\0.03\end{bmatrix}$, $\boldsymbol{\mu}_{A^2x} = \begin{bmatrix}2\\2\end{bmatrix}$, $\boldsymbol{\mu}_{A^2x^*} = \begin{bmatrix}0.4\\0.4\end{bmatrix}$, $\boldsymbol{\mu}_{x^3_\mathrm{I}} = \begin{bmatrix}0.001\\0.001\end{bmatrix}$, $\boldsymbol{\mu}_{x^3_\mathrm{Q}} = \begin{bmatrix}0.2\\0.2\end{bmatrix}$
	NLMS constants	$\beta_{x^*} = 10^{-4}, \beta_{A^2x} = 10^{-13}, \beta_{A^2x^*} = 10^{-13}$, $\beta_{x^3_\mathrm{I}} = 10^{-15}, \beta_{x^3_\mathrm{Q}} = 10^{-14}$

4.2.3 Measurement Examples

This subsection provides new, previously unpublished, RF measurement results for suppressing receiver nonlinearities using AIC exactly as described in Subsection 4.2.1. A cellular network uplink scenario is considered where a wideband base station is trying to receive a weak signal under influence of two strong blocker signals originating from other networks. The essential parameters are gathered in Table 4.2. In the measurements, the composite analog RF waveform consisting of the aforementioned signal scenario is generated with a vector signal transceiver [84]. The waveform PAPR is 11 dB which can be considered as a high number but, at the same time, it is also a realistic number for wideband multicarrier reception scenarios. The RF waveform is then fed into a realistic DCR which is comprised of an external LNA [46] followed by a pre-commercial base station receiver hardware.

The received digitized waveform is illustrated in Figure 4.5 when the average power in the LNA input is −26 dBm. Due to the receiver nonlinearities and I/Q imbalance, the strong blockers cause IMD and mirror-image distortion which partially fall on top of the weak desired signal. When AIC employed, a substantial amount of distortion

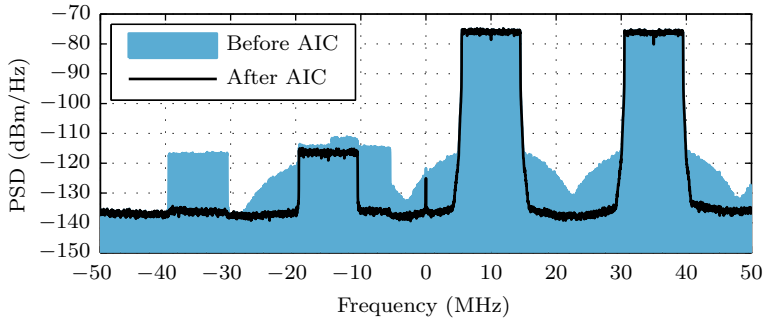

Figure 4.5: Illustration of the considered signal scenario when the average power in the LNA input is −26 dBm. AIC is able to considerably suppress the distortion stemming from receiver nonlinearities and I/Q imbalance.

is suppressed. From the weak desired signal point of view, SNDR is enhanced from −0.75 dB to 16.2 dB meaning that symbol error ratio (SER) is improved from 70 % to 0.7 %. Another kind of view to AIC is given in Figure 4.6 by illustrating the input-output characteristics of the whole receiver chain with and without AIC. The characteristics have been calculated using the original generated waveform and the received digitized waveform. It is clear that AIC is able to make the receiver more linear. However, even after AIC, fully linear characteristics are not obtained. This is due to the fact that AIC does not suppress nonlinear distortion from the blocker signal bands as is discussed in Subsection 4.2.2. Nevertheless, the nonlinear distortion is effectively suppressed from other signal bands which is essential. Although the nonlinearity may seem small in this linear presentation for the overall waveform, it has a significant effect for the weak signal since the overall dynamic range is tens of dBs.

In this currently considered scenario, the two-tap AFs of AIC are adapted using NLMS and their adaptation behavior is shown in Figure 4.7. Here, the magnitude of the first tap of each AF is plotted as a function of sample index n. For example, the magnitude of the first tap of $\mathbf{w}_{x^*}(n)$ is denoted with $\left|w_{x^*,1}(n)\right|$. In the measured receiver hardware set-up, the LNA is the main source of IMD whereas the rest of the receiver mainly produces mirror-image distortion but practically no IMD. This is the reason for the smooth adaptation of $\mathbf{w}_{x^*}(n)$ and $\mathbf{w}_{A^2x}(n)$. The other three nonlinearity terms are below the noise floor and therefore those are not relevant in this case, which is seen as less stable AF adaptation behavior. However, the adaptation still produces values that are in the ball park of the optimal LS solutions. In practice, these last three nonlinearity terms could be omitted when using AIC for this particular receiver, but those are considered here in order to illustrate many of the aspects discussed in Subsection 4.2.2.

Figure 4.8 provides a broader view to the AIC performance. In the considered signal scenario, the powers of the two blockers are varied while keeping the power of the weak

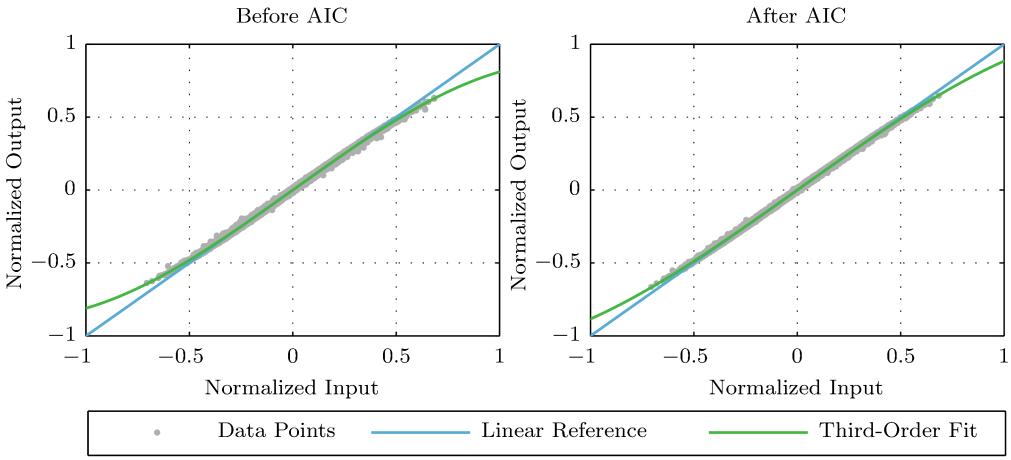

Figure 4.6: Input-output characteristics for the whole receiver chain (I branch) obtained using the original generated waveform and the received digitized waveform when the average power in the LNA input is −26 dBm.

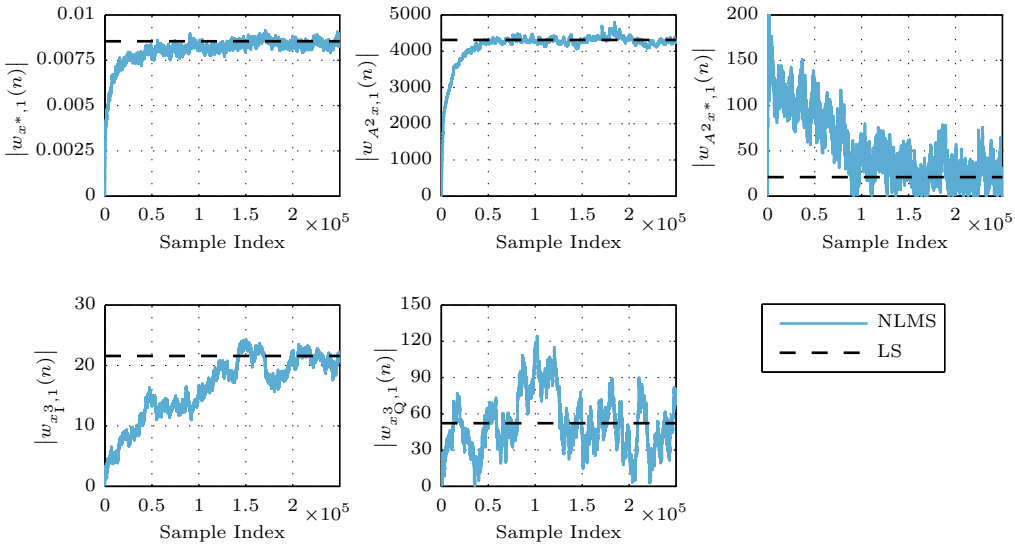

Figure 4.7: Adaptation of the first tap of the adaptive filters using NLMS. Also the optimal LS solution is shown for reference.

desired signal fixed. The results illustrate the SNDR and SER of the weak desired signal before and after AIC. Significant gain is achieved in wide power range. For example, if the target is maximum of 1 % SER, it is possible to tolerate approximately 15 dB stronger blockers when using AIC in this signal scenario. However, for the very low received signal powers, AIC does not provide any gain since practically there is not any

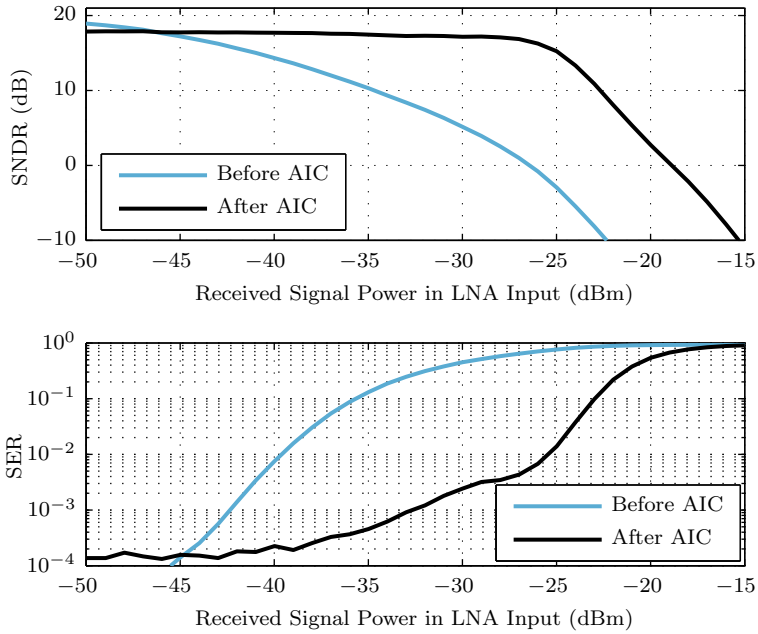

Figure 4.8: Performance of AIC illustrated with SNDR and SER of the weak desired signal when the power of the blockers is varied.

nonlinear distortion. In fact, from the SNDR and SER point of view, AIC may even slightly decrease the performance as can be seen on the left side of Figure 4.8. However, this is not critical since the SER is still so low that zero bit error ratio (BER) would be achieved. In practice, it is beneficial to bypass AIC when SNDR is high because this also decreases power consumption due to the decreased computational load.

More measured performance examples, with different hardware and signal scenarios, are given in [P8] using a SDR USRP N210 with a wideband WBX front-end [33, 34]. In addition, [P7] shows how AIC is able to enhance spectrum sensing reliability of energy detectors and cyclostationary feature detectors under the influence of receiver nonlinearities. Conceptual differences and performance comparison between AIC and a calibration-based post-inverse method for suppressing DCR nonlinearities are discussed in [P9].

CHAPTER 5

Fourier Series Based Clipping Model for Analog-to-Digital Converters

When input signal level is outside the full-scale range of an ADC, the signal is clipped. This causes severe nonlinear distortion which may block the whole signal reception. In order to better understand the structure of clipping distortion, a mathematical model is derived here through Fourier analysis. The derivations are based on [P2] and [P6]. The clipping model also has potential in providing information for clipping distortion suppression purposes.

5.1 General Clipping Model

An I/Q ADC, consisting of separate converters for I and Q branches, is assumed in the following ADC clipping model. This is illustrated in Figure 5.1. Quantization and sampling are omitted from the model in order focus on the clipping phenomenon itself. In practice, sampling is likely to cause aliasing due to the high-order distortion the ADC clipping is causing. The derived clipping model is directly applicable for discrete-time signals although it is not explicitly denoted in the equations.

The I/Q ADC input signal is generally defined as

$$v(t) = V(t)e^{j\theta_c(t)} = V(t)\cos\theta_c(t) + jV(t)\sin\theta_c(t) = v_{\mathrm{I}}(t) + jv_{\mathrm{Q}}(t), \tag{5.1}$$

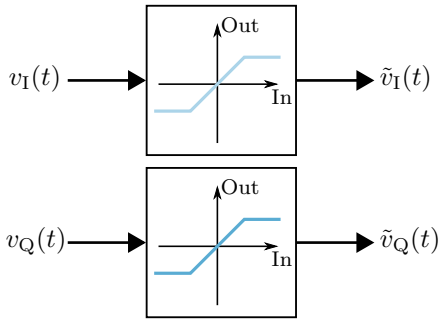

Figure 5.1: Illustration of an I/Q ADC from clipping modeling point of view. I and Q branch have separate converters and therefore signal clipping is also occurring independently.

where $V(t)$ is the signal envelope of $v(t)$ and $\theta_c(t) = \omega_c t + \phi_v(t)$ consists of the angular center frequency ω_c and the signal phase $\phi_v(t)$. As illustrated in Figure 5.1, the input-output characteristics are of hard clipping type. Within the limits of the linear region, i.e. within the ADC FS range, the I/Q ADC clipping model output is the same as the input. Outside the linear region, the output always equals to the higher or lower clipping level. Formally, the I/Q ADC clipping model output is expressed as

$$\tilde{v}_{\mathrm{I}}(t) = \begin{cases} v_{\mathrm{I}}(t), & C_{\mathrm{L,I}} \leq v_{\mathrm{I}}(t) \leq C_{\mathrm{H,I}} \\ C_{\mathrm{H,I}}, & v_{\mathrm{I}}(t) > C_{\mathrm{H,I}} \\ C_{\mathrm{L,I}}, & v_{\mathrm{I}}(t) < C_{\mathrm{L,I}}, \end{cases} \tag{5.2a}$$

$$\tilde{v}_{\mathrm{Q}}(t) = \begin{cases} v_{\mathrm{Q}}(t), & C_{\mathrm{L,Q}} \leq v_{\mathrm{Q}}(t) \leq C_{\mathrm{H,Q}} \\ C_{\mathrm{H,Q}}, & v_{\mathrm{Q}}(t) > C_{\mathrm{H,Q}} \\ C_{\mathrm{L,Q}}, & v_{\mathrm{Q}}(t) < C_{\mathrm{L,Q}}, \end{cases} \tag{5.2b}$$

where $C_{\mathrm{H,I}}, C_{\mathrm{L,I}}$ are the higher and lower clipping level for the I branch, respectively, where as $C_{\mathrm{H,Q}}, C_{\mathrm{L,Q}}$ are the clipping levels similarly for the Q branch. In continuation, it is further assumed that $C_{\mathrm{H,I}} \geq 0$, $C_{\mathrm{L,I}} \leq 0$, $C_{\mathrm{H,Q}} \geq 0$, and $C_{\mathrm{L,Q}} \leq 0$. This is the most general definition for I/Q ADC clipping as it allows the clipping to be non-symmetric with respect to zero and unequal in I and Q branches. Another point worth highlighting is that the I/Q ADC clipping is a memoryless phenomenon. In other words, signal clipping depends only on the instantaneous signal level independently of previous signal levels.

The target here is to derive a clipping model that expresses the I/Q ADC output signal $\tilde{v}(t) = \tilde{v}_{\mathrm{I}}(t) + j\tilde{v}_{\mathrm{Q}}(t)$ using Fourier series. This way it is possible to examine separately the different orders of clipping distortion. The basics of Fourier series are explained, e.g., in [19, 52]. In addition, [19] presents Fourier analysis for a limiter in case of real bandpass signals. In a certain sense, the modeling in this chapter can be seen as a significant extension of the analysis in [19]. By the definition of complex Fourier

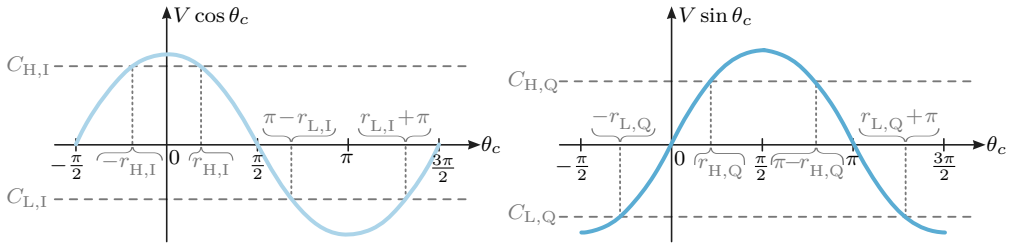

(a) I Branch Clipping **(b)** Q Branch Clipping

Figure 5.2: Illustration of I and Q branch clipping for ADC input signals $v_{\mathrm{I}}(t)$ and $v_{\mathrm{Q}}(t)$ as a function of angle θ_c when time t is held fixed. In addition, the integration intervals for deriving clipping model Fourier coefficients have been marked.

series, the I/Q ADC output signal can be written as

$$\tilde{v}(t) = \sum_{m=-\infty}^{\infty} d_m(t) e^{jm\theta_c(t)}, \tag{5.3}$$

where $d_m(t) = d_{m,\mathrm{I}}(t) + j d_{m,\mathrm{Q}}(t)$ are Fourier coefficients. Due to the instantaneous nature of clipping, the Fourier coefficients are defined to be time-dependent. By using the general definitions of Fourier series separately for I and Q branches, the coefficients can be found with

$$d_{m,\mathrm{I}}(t) = \frac{1}{2\pi} \int_{2\pi} \tilde{v}_{\mathrm{I}}(t) e^{-jm\theta_c(t)} \, \mathrm{d}\theta_c(t), \tag{5.4a}$$

$$d_{m,\mathrm{Q}}(t) = \frac{1}{2\pi} \int_{2\pi} \tilde{v}_{\mathrm{Q}}(t) e^{-jm\theta_c(t)} \, \mathrm{d}\theta_c(t). \tag{5.4b}$$

It is important to note here that the Fourier coefficient definitions above are calculated by integrating with respect to $\theta_c(t)$. This way it is possible to exploit the fact that $v(t)$ can be seen as a periodic function of θ_c (with a period of 2π) when the time is held fixed. Therefore, $\theta_c(t)$ itself nor $v(t)$ does not have to be periodic in time. Another way to look at this concept is to consider that in a single moment of time the signal $v(t)$ can basically have any value depending on $V(t)$ and $\theta_c(t)$. In general level it is difficult say anything about $V(t)$ other than $V(t) \geq 0$. However, $e^{j\theta_c}$ has period of 2π and hence all the possible values of θ_c can be covered by considering only a single period of 2π. The I and Q branch clipping as a function of θ_c is visualized in Figure 5.2.

In order to solve the integrals in (5.4a) and (5.4b), the integration interval of 2π should be divided into five shorter intervals as illustrated in Figure 5.2. The division is done according to the points where the function crosses clipping levels. These points are straightforwardly defined using the well-known trigonometric identities. In order

Table 5.1: Auxiliary variables, r's and s's, for the I/Q ADC clipping model.

$r_{\mathrm{H,I}}(t) = \arccos \dfrac{\tilde{C}_{\mathrm{H,I}}(t)}{V(t)}$	$s_{\mathrm{H,I}}(t) = \sin\big(r_{\mathrm{H,I}}(t)\big) = \sqrt{1 - \left(\dfrac{\tilde{C}_{\mathrm{H,I}}(t)}{V(t)}\right)^2}$
$r_{\mathrm{L,I}}(t) = \arccos \dfrac{-\tilde{C}_{\mathrm{L,I}}(t)}{V(t)}$	$s_{\mathrm{L,I}}(t) = \sin\big(r_{\mathrm{L,I}}(t)\big) = \sqrt{1 - \left(\dfrac{\tilde{C}_{\mathrm{L,I}}(t)}{V(t)}\right)^2}$
$r_{\mathrm{H,Q}}(t) = \arcsin \dfrac{\tilde{C}_{\mathrm{H,Q}}(t)}{V(t)}$	$s_{\mathrm{H,Q}}(t) = \cos\big(r_{\mathrm{H,Q}}(t)\big) = \sqrt{1 - \left(\dfrac{\tilde{C}_{\mathrm{H,Q}}(t)}{V(t)}\right)^2}$
$r_{\mathrm{L,Q}}(t) = \arcsin \dfrac{-\tilde{C}_{\mathrm{L,Q}}(t)}{V(t)}$	$s_{\mathrm{L,Q}}(t) = \cos\big(r_{\mathrm{L,Q}}(t)\big) = \sqrt{1 - \left(\dfrac{\tilde{C}_{\mathrm{L,Q}}(t)}{V(t)}\right)^2}$

to keep the notation concise, auxiliary variables $r_{\mathrm{H,I}}(t)$, $r_{\mathrm{L,I}}(t)$, $r_{\mathrm{H,Q}}(t)$, and $r_{\mathrm{L,Q}}(t)$ are defined according to the left column of Table 5.1. Now, the Fourier coefficient equations (5.4a) and (5.4b) can be rewritten as

$$\begin{aligned} d_{m,\mathrm{I}}(t) = \frac{1}{2\pi}\Bigg[& \int_{-\pi/2}^{-r_{\mathrm{H,I}}(t)} v_{\mathrm{I}}(t) e^{-jm\theta_c(t)}\,\mathrm{d}\theta_c(t) + \int_{-r_{\mathrm{H,I}}(t)}^{r_{\mathrm{H,I}}(t)} C_{\mathrm{H,I}} e^{-jm\theta_c(t)}\,\mathrm{d}\theta_c(t) \\ & + \int_{r_{\mathrm{H,I}}(t)}^{\pi - r_{\mathrm{L,I}}(t)} v_{\mathrm{I}}(t) e^{-jm\theta_c(t)}\,\mathrm{d}\theta_c(t) + \int_{\pi - r_{\mathrm{L,I}}(t)}^{r_{\mathrm{L,I}}(t)+\pi} C_{\mathrm{L,I}} e^{-jm\theta_c(t)}\,\mathrm{d}\theta_c(t) \\ & + \int_{r_{\mathrm{L,I}}(t)+\pi}^{3\pi/2} v_{\mathrm{I}}(t) e^{-jm\theta_c(t)}\,\mathrm{d}\theta_c(t)\Bigg], \end{aligned} \tag{5.5a}$$

$$\begin{aligned} d_{m,\mathrm{Q}}(t) = \frac{1}{2\pi}\Bigg[& \int_{-\pi/2}^{-r_{\mathrm{L,Q}}(t)} C_{\mathrm{L,Q}} e^{-jm\theta_c(t)}\,\mathrm{d}\theta_c(t) + \int_{-r_{\mathrm{L,Q}}(t)}^{r_{\mathrm{H,Q}}(t)} v_{\mathrm{Q}}(t) e^{-jm\theta_c(t)}\,\mathrm{d}\theta_c(t) \\ & + \int_{r_{\mathrm{H,Q}}(t)}^{\pi - r_{\mathrm{H,Q}}(t)} C_{\mathrm{H,Q}} e^{-jm\theta_c(t)}\,\mathrm{d}\theta_c(t) + \int_{\pi - r_{\mathrm{H,Q}}(t)}^{r_{\mathrm{L,Q}}(t)+\pi} v_{\mathrm{Q}}(t) e^{-jm\theta_c(t)}\,\mathrm{d}\theta_c(t) \\ & + \int_{r_{\mathrm{L,Q}}(t)+\pi}^{3\pi/2} C_{\mathrm{L,Q}} e^{-jm\theta_c(t)}\,\mathrm{d}\theta_c(t)\Bigg]. \end{aligned} \tag{5.5b}$$

Due to the fact that the domain of $\arcsin(x)$ and $\arccos(x)$ is $-1 \leq x \leq 1$, the clipping model above is assuming that the signal envelope $V(t)$ is always clipped (or at the clipping level) from above and below simultaneously in I and Q branches. Naturally, nothing compels clipping to occur in I and Q branches or especially from above and below at the same time. This restriction in the clipping model is avoided by modifying the clipping levels. All clipping levels that are not exceeded for a certain t, should be set equal to $\pm V(t)$ which means that the value is within the defined domain but not limited by the clipping level. Formally,

$$\tilde{C}_{\mathrm{H,I}}(t) = \begin{cases} C_{\mathrm{H,I}}, & \forall t : V(t) \geq C_{\mathrm{H,I}} \\ V(t), & \forall t : V(t) < C_{\mathrm{H,I}}, \end{cases} \tag{5.6a}$$

$$\tilde{C}_{\mathrm{L,I}}(t) = \begin{cases} C_{\mathrm{L,I}}, & \forall t : V(t) \geq -C_{\mathrm{L,I}} \\ -V(t), & \forall t : V(t) < -C_{\mathrm{L,I}}, \end{cases} \tag{5.6b}$$

$$\tilde{C}_{\mathrm{H,Q}}(t) = \begin{cases} C_{\mathrm{H,Q}}, & \forall t : V(t) \geq C_{\mathrm{H,Q}} \\ V(t), & \forall t : V(t) < C_{\mathrm{H,Q}}, \end{cases} \tag{5.6c}$$

$$\tilde{C}_{\mathrm{L,Q}}(t) = \begin{cases} C_{\mathrm{L,Q}}, & \forall t : V(t) \geq -C_{\mathrm{L,Q}} \\ -V(t), & \forall t : V(t) < -C_{\mathrm{L,Q}}. \end{cases} \tag{5.6d}$$

After derivations, the Fourier coefficients $d_m(t)$ are denoted in piecewise manner for different m's as given in (5.7a)–(5.7d). For $m = 0$:

$$\begin{aligned} d_0(t) = \\ &\tfrac{1}{\pi}\big\{V(t)\big(s_{\mathrm{L,I}}(t) - s_{\mathrm{H,I}}(t)\big) + \tilde{C}_{\mathrm{H,I}}(t) r_{\mathrm{H,I}}(t) + \tilde{C}_{\mathrm{L,I}}(t) r_{\mathrm{L,I}}(t) \\ &\quad + j\big[V(t)\big(s_{\mathrm{L,Q}}(t) - s_{\mathrm{H,Q}}(t)\big) + \tilde{C}_{\mathrm{H,Q}}(t)\big(\tfrac{\pi}{2} - r_{\mathrm{H,Q}}(t)\big) + \tilde{C}_{\mathrm{L,Q}}(t)\big(\tfrac{\pi}{2} - r_{\mathrm{L,Q}}(t)\big)\big]\big\}, \end{aligned} \tag{5.7a}$$

for $m = \pm 1$:

$$\begin{aligned} d_m(t) = \\ &\tfrac{V(t)}{2} \pm \tfrac{1}{2\pi}\big\{V(t)\big[r_{\mathrm{L,Q}}(t) \mp r_{\mathrm{L,I}}(t) + r_{\mathrm{H,Q}}(t) \mp r_{\mathrm{H,I}}(t)\big] \\ &\qquad + \tilde{C}_{\mathrm{H,Q}}(t) s_{\mathrm{H,Q}}(t) \pm \tilde{C}_{\mathrm{H,I}}(t) s_{\mathrm{H,I}}(t) - \tilde{C}_{\mathrm{L,Q}}(t) s_{\mathrm{L,Q}}(t) \mp \tilde{C}_{\mathrm{L,I}}(t) s_{\mathrm{L,I}}(t)\big\}, \end{aligned} \tag{5.7b}$$

for $m = \pm 2, \pm 4, \ldots$:

$$\begin{aligned} d_m(t) = \\ &\tfrac{1}{\pi m(m^2-1)}\big\{mV(t)\big[s_{\mathrm{H,I}}(t)\cos\big(mr_{\mathrm{H,I}}(t)\big) - s_{\mathrm{L,I}}(t)\cos\big(mr_{\mathrm{L,I}}(t)\big)\big] \\ &\qquad - \tilde{C}_{\mathrm{H,I}}(t)\sin\big(mr_{\mathrm{H,I}}(t)\big) - \tilde{C}_{\mathrm{L,I}}(t)\sin\big(mr_{\mathrm{L,I}}(t)\big) \\ &\qquad + j\big[mV(t)\big[s_{\mathrm{H,Q}}(t)\cos\big(mr_{\mathrm{H,Q}}(t)\big) - s_{\mathrm{L,Q}}(t)\cos\big(mr_{\mathrm{L,Q}}(t)\big)\big] \\ &\qquad\quad + \tilde{C}_{\mathrm{H,Q}}(t)\sin\big(mr_{\mathrm{H,Q}}(t)\big) + \tilde{C}_{\mathrm{L,Q}}(t)\sin\big(mr_{\mathrm{L,Q}}(t)\big)\big]\big\}, \end{aligned} \tag{5.7c}$$

and for $m = \pm 3, \pm 5, \ldots$:

$$
\begin{aligned}
d_m(t) = \\
&\tfrac{1}{\pi m(m^2-1)} \big\{ mV(t) \big[s_{\mathrm{H,I}}(t) \cos\big(mr_{\mathrm{H,I}}(t)\big) + s_{\mathrm{L,I}}(t) \cos\big(mr_{\mathrm{L,I}}(t)\big) \\
&\qquad + s_{\mathrm{H,Q}}(t) \sin\big(mr_{\mathrm{H,Q}}(t)\big) + s_{\mathrm{L,Q}}(t) \sin\big(mr_{\mathrm{L,Q}}(t)\big) \big] \\
&\quad - \tilde{C}_{\mathrm{H,I}}(t) \sin\big(mr_{\mathrm{H,I}}(t)\big) + \tilde{C}_{\mathrm{L,I}}(t) \sin\big(mr_{\mathrm{L,I}}(t)\big) \\
&\quad - \tilde{C}_{\mathrm{H,Q}}(t) \cos\big(mr_{\mathrm{H,Q}}(t)\big) + \tilde{C}_{\mathrm{L,Q}}(t) \cos\big(mr_{\mathrm{L,Q}}(t)\big) \big\}.
\end{aligned}
\tag{5.7d}
$$

The Fourier coefficients above also take advantage of the additional auxiliary variables $s_{\mathrm{H,I}}(t)$, $s_{\mathrm{L,I}}(t)$, $s_{\mathrm{H,Q}}(t)$, and $s_{\mathrm{L,Q}}(t)$ which are defined in the right column of Table 5.1. The notation of $\pm$ and $\mp$ in (5.7) is used so that the upper signs in an equation are valid at the same time and correspondingly the lower signs.

In summary, the clipped output signal of an I/Q ADC can be expressed with a Fourier series according to (5.3) using the Fourier coefficients from (5.7). The derived model provides a convenient frequency-domain interpretation for the clipping phenomenon. This is stemming from the fact that each m refers to the mth harmonic of ω_c. The Fourier coefficient definitions in (5.7) may look complicated, but in the end those just provide a single weighting factor for each harmonic of ω_c.

The whole clipping concept is better illustrated using a simulated example. This is provided in Figure 5.3. The waveform is a band-limited OFDM signal with bandwidth of 8 MHz and center frequency of 10 MHz. The signal has 8192 subcarriers of which 6817 are active while the subcarrier modulation is 64-QAM. The high sample rate of 200 MHz is used in order to illustrate the most essential clipping distortion without aliasing. Channel effects, transceiver impairments and noise are omitted to focus on the clipping phenomenon itself. The upper part of Figure 5.3 shows the first 200 samples of the time-domain waveform. On top of the original signal there is plotted the clipped signal when the clipping levels are $C_{\mathrm{H,I}} = 1.4$, $C_{\mathrm{L,I}} = -0.6$, $C_{\mathrm{H,Q}} = 0.8$, and $C_{\mathrm{L,Q}} = -0.7$. In addition, there is also time-domain illustration of one of the most dominant clipping distortion component $m = -3$. This is possible to plot separately due to the derived clipping model. It shows excellently the instantaneous nature of clipping: there is distortion only when either I or Q signal or both are clipped, i.e., when the signal envelope is clipped. Below the time-domain illustrations of Figure 5.3, there is the power spectral density (PSD) of the original signal together with the clipped signal PSD. With the help of the derived clipping model, different distortion orders are highlighted separately in the bottom part of the figure. Equal clipping in I and Q branches would cause odd-order clipping distortion so that every other order has an opposite sign, i.e, $m = +1, -3, +5, -7, \ldots$, but unequal clipping between I and Q causes also additional mirror terms, $m = -1, +3, -5, +7, \ldots$, to appear. The even-order distortion, $m = 0, \pm 2, \pm 4, \ldots$, is due to the non-symmetry of the clipping with respect to zero. The exact Fourier coefficients in the simpler cases are considered in the following section.

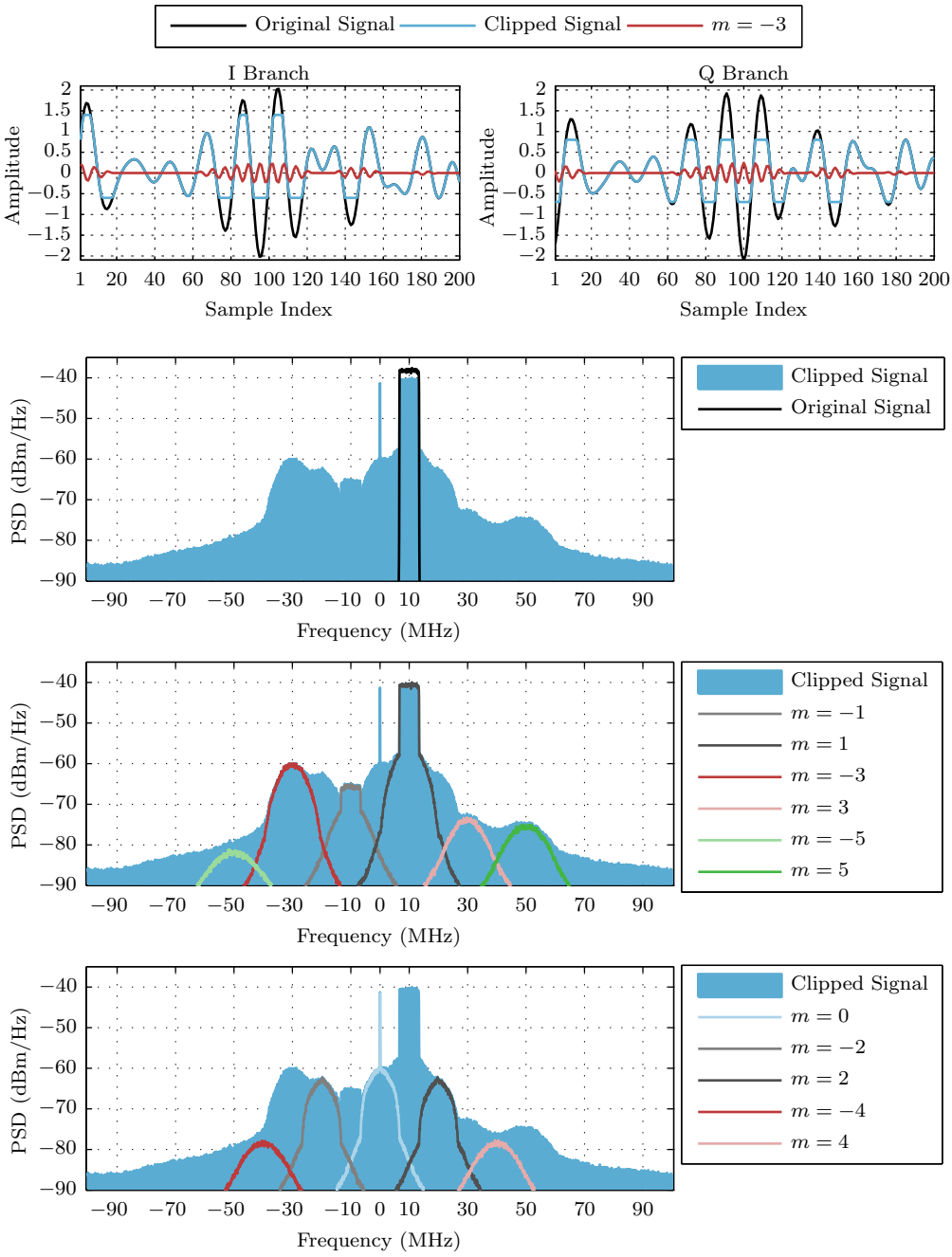

Figure 5.3: Example of an OFDM signal having center frequency of 10 MHz clipping levels being $C_{\mathrm{H,I}} = 1.4$, $C_{\mathrm{L,I}} = -0.6$, $C_{\mathrm{H,Q}} = 0.8$, and $C_{\mathrm{L,Q}} = -0.7$. Part of the time-domain waveform is shown on the top and below are spectrum illustrations. In addition to original and clipped signal, a few distortion orders are plotted separately using the derived clipping model.

5.2 Simplified Clipping Models

In practice, I/Q ADCs are typically implemented as a single integrated circuit. Therefore, the I and Q branch converters can be matched relatively well. The matching reduces the amount of clipping distortion seen in the output of the I/Q ADC. This also brings possibilities to simplify the general clipping model derived in the previous section.

First simplification to consider is to have equal clipping in I and Q branches, but still allow the clipping to be non-symmetric with respect to zero. This means that it is enough to determine two clipping levels, the higher and lower one, which are equal for I and Q, namely C_{H} and C_{L}. The definition of Fourier series is exactly the same as in Section 5.1, but now the Fourier coefficient equations reduce to

$$d_m(t) = \begin{cases} \frac{1+j}{\pi}\big[V(t)\big(s_{\mathrm{L}}(t) - s_{\mathrm{H}}(t)\big) + \tilde{C}_{\mathrm{H}}(t)r_{\mathrm{H,I}}(t) + \tilde{C}_{\mathrm{L}}(t)r_{\mathrm{L,I}}(t)\big], & m = 0 \\ V(t) + \frac{1}{\pi}\big[V(t)\big(-r_{\mathrm{L,I}}(t) - r_{\mathrm{H,I}}(t)\big) \\ \qquad +\tilde{C}_{\mathrm{H}}(t)s_{\mathrm{H}}(t) - \tilde{C}_{\mathrm{L}}(t)s_{\mathrm{L}}(t)\big], & m = +1 \\ \frac{1-j}{\pi m(m^2-1)}\big\{mV(t)\big[s_{\mathrm{H}}(t)\cos\big(mr_{\mathrm{H,I}}(t)\big) - s_{\mathrm{L}}(t)\cos\big(mr_{\mathrm{L,I}}(t)\big)\big] \\ \qquad -\tilde{C}_{\mathrm{H}}(t)\sin\big(mr_{\mathrm{H,I}}(t)\big) - \tilde{C}_{\mathrm{L}}(t)\sin\big(mr_{\mathrm{L,I}}(t)\big)\big\}, & m = \pm 2, \pm 6, \dots \\ \frac{1+j}{\pi m(m^2-1)}\big\{mV(t)\big[s_{\mathrm{H}}(t)\cos\big(mr_{\mathrm{H,I}}(t)\big) - s_{\mathrm{L}}(t)\cos\big(mr_{\mathrm{L,I}}(t)\big)\big] \\ \qquad -\tilde{C}_{\mathrm{H}}(t)\sin\big(mr_{\mathrm{H,I}}(t)\big) - \tilde{C}_{\mathrm{L}}(t)\sin\big(mr_{\mathrm{L,I}}(t)\big)\big\}, & m = \pm 4, \pm 8, \dots \\ \frac{2}{\pi m(m^2-1)}\big\{mV(t)\big[s_{\mathrm{H}}(t)\cos\big(mr_{\mathrm{H,I}}(t)\big) + s_{\mathrm{L}}(t)\cos\big(mr_{\mathrm{L,I}}(t)\big)\big] \\ \qquad -\tilde{C}_{\mathrm{H}}(t)\sin\big(mr_{\mathrm{H,I}}(t)\big) + \tilde{C}_{\mathrm{L}}(t)\sin\big(mr_{\mathrm{L,I}}(t)\big)\big\}, & m = -3, +5, \dots \\ 0, & m = -1, +3, \dots \end{cases} \tag{5.8}$$

where $s_{\mathrm{H}}(t) = s_{\mathrm{H,I}}(t) = s_{\mathrm{H,Q}}(t)$ and $s_{\mathrm{L}}(t) = s_{\mathrm{L,I}}(t) = s_{\mathrm{L,Q}}(t)$. Logically, also the clipping levels are modified similarly as in the general case which means that $\tilde{C}_{\mathrm{H}}(t) = \tilde{C}_{\mathrm{H,I}}(t) = \tilde{C}_{\mathrm{H,Q}}(t)$ and $\tilde{C}_{\mathrm{L}}(t) = \tilde{C}_{\mathrm{L,I}}(t) = \tilde{C}_{\mathrm{L,Q}}(t)$. Comparing the Fourier coefficients in (5.8) with the general ones in (5.7), it is easy to notice that every other odd distortion order ($m = -1, +3, -5, \dots$) are not created due to the Fourier coefficient being zero. This is because, for these particular orders, equal clipping distortion contributions in I and Q branches cancel each other out. This can also be interpreted so that due to equal I and Q branch clipping there are no mirror images. The even orders are different in nature since they always occur symmetrically on both sides of zero frequency. A graphical illustration is given in Figure 5.4. It is showing exactly the same OFDM signal scenario as in Figure 5.3, but now the clipping is identical in I and Q branch so that $C_{\mathrm{H}} = 1.4$

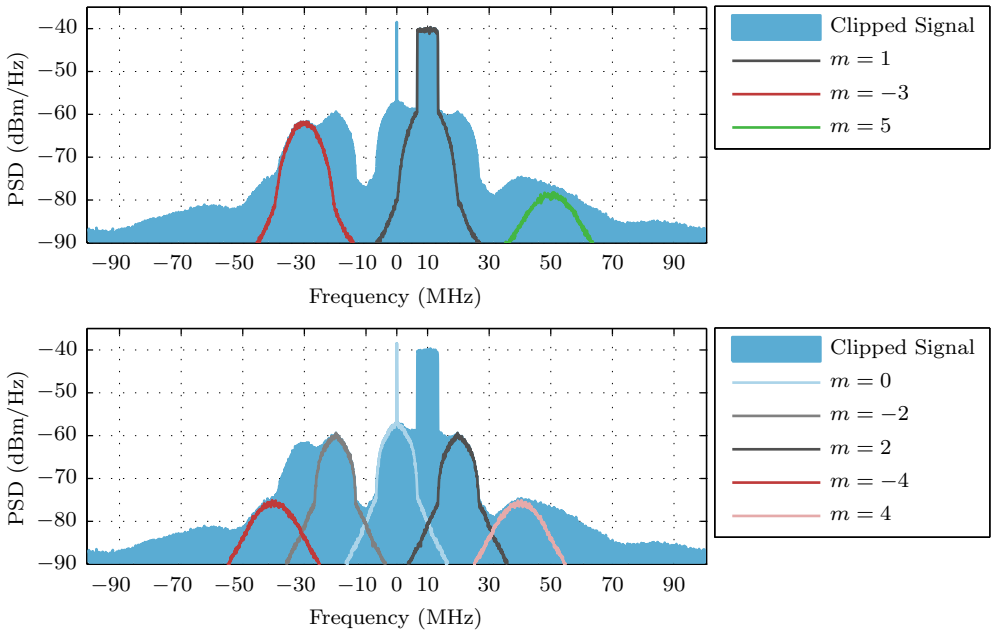

Figure 5.4: Example of an OFDM signal having center frequency of 10 MHz clipping levels being $C_{\mathrm{H}} = 1.4$ and $C_{\mathrm{L}} = -0.6$. On top of the clipped signal, the most essential distortion orders are plotted separately according to Fourier coefficients in (5.8).

and $C_{\mathrm{L}} = -0.6$. The spectrum illustration verifies the lack of every other odd distortion order ($m = -1, +3, -5, \dots$).

The next simplification to the clipping model is to assume clipping to be symmetrical with respect to zero. However, this zero-symmetric clipping is let to be unequal in I and Q branches which have clipping levels C_{I} and C_{Q}, respectively. This makes the Fourier coefficients to reduce to

$$d_m(t) = \begin{cases} 0, & m = 0, \pm 2, \pm 4, \dots \\ \frac{V(t)}{2} \pm \frac{1}{\pi}\left[V(t)\big(r_{\mathrm{Q}}(t) \mp r_{\mathrm{I}}(t)\big) + \tilde{C}_{\mathrm{Q}}(t) s_{\mathrm{Q}}(t) \pm \tilde{C}_{\mathrm{I}}(t) s_{\mathrm{I}}(t)\right], & m = \pm 1 \\ \frac{2}{\pi m(m^2-1)}\big\{mV(t)\big[s_{\mathrm{I}}(t)\cos\big(mr_{\mathrm{I}}(t)\big) + s_{\mathrm{Q}}(t)\sin\big(mr_{\mathrm{Q}}(t)\big)\big] \\ \qquad -\tilde{C}_{\mathrm{I}}(t)\sin\big(mr_{\mathrm{I}}(t)\big) - \tilde{C}_{\mathrm{Q}}(t)\cos\big(mr_{\mathrm{Q}}(t)\big)\big\}, & m = \pm 3, \pm 5, \dots \end{cases} \tag{5.9}$$

where $r_{\mathrm{I}}(t) = r_{\mathrm{H,I}}(t) = r_{\mathrm{L,I}}(t)$ and $r_{\mathrm{Q}}(t) = r_{\mathrm{H,Q}}(t) = r_{\mathrm{L,Q}}(t)$ as well as $s_{\mathrm{I}}(t) = s_{\mathrm{H,I}}(t) = s_{\mathrm{L,I}}(t)$ and $s_{\mathrm{Q}}(t) = s_{\mathrm{H,Q}}(t) = s_{\mathrm{L,Q}}(t)$. Since clipping is now zero-symmetric, the modified clipping levels for calculation purposes are $\tilde{C}_{\mathrm{I}}(t) = \tilde{C}_{\mathrm{H,I}}(t) = -\tilde{C}_{\mathrm{L,I}}(t)$ and $\tilde{C}_{\mathrm{Q}}(t) = \tilde{C}_{\mathrm{H,Q}}(t) = -\tilde{C}_{\mathrm{L,Q}}(t)$. As can be seen from (5.9), even distortion orders does

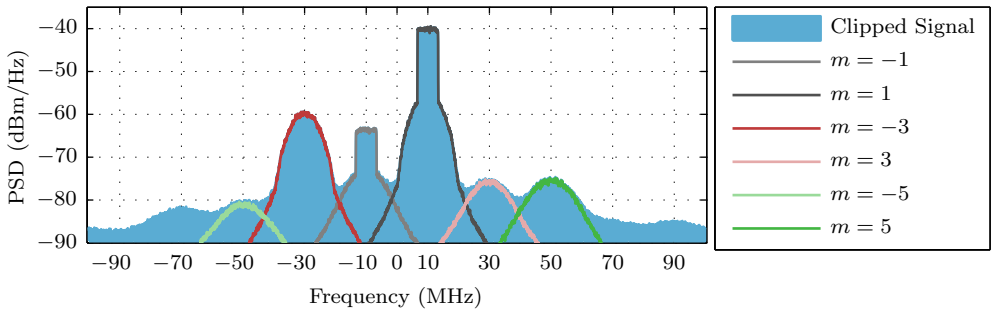

Figure 5.5: Example of an OFDM signal having center frequency of 10 MHz clipping levels being $C_{\mathrm{I}} = 1.0$ and $C_{\mathrm{Q}} = 0.8$. On top of the clipped signal, the most essential distortion orders are plotted separately according to Fourier coefficients in (5.9).

not appear due to the zero-symmetry of clipping. However, all odd orders have non-zero Fourier coefficients. Figure 5.5 illustrates this scenario using the same OFDM signal example as in previous illustrations, but now $C_{\mathrm{I}} = 1.0$ and $C_{\mathrm{Q}} = 0.8$. As expected, only odd-order distortion appears. The power levels of $m = -1, +3, -5, \ldots$ relative to $m = +1, -3, +5, \ldots$ power levels depend on the inequality of C_{I} and C_{Q}. Very small inequality on clipping levels indicates low power levels of $m = -1, +3, -5, \ldots$ components.

If $C_{\mathrm{I}} = C_{\mathrm{Q}} = C$, the clipping is identical in I and Q branches. In addition, the clipping is symmetric with respect to zero. This is the most simple I/Q ADC clipping case and leads to Fourier coefficients

$$d_m(t) = \begin{cases} 0, & m = 0, \pm 2, \pm 4, \ldots \\ 0, & m = -1, +3, -5, \ldots \\ V(t) + \frac{2}{\pi}\left[\tilde{C}(t)s(t) - V(t)r_{\mathrm{I}}(t)\right], & m = +1 \\ \frac{4}{\pi m(m^2-1)}\left[mV(t)s(t)\cos\left(mr_{\mathrm{I}}(t)\right) - \tilde{C}(t)\sin\left(mr_{\mathrm{I}}(t)\right)\right], & m = -3, +5, -7, \ldots \end{cases} \tag{5.10}$$

where $s(t) = s_{\mathrm{I}}(t) = s_{\mathrm{Q}}(t)$. It is evident that only clipping distortion of orders $m = +1, -3, +5, -7, \ldots$ appear. Figure 5.6 shows once again the same OFDM signal example, but this time the clipping level is $C = 1.0$. Since significant aliasing does not occur, the different clipping distortion orders are easily distinguishable in the spectrum. However, the amount of clipping distortion is huge even in the simplest case and it can significantly harm the reception of signals. Different digital approaches to suppress clipping distortion in the A/D interface of a radio receiver is discussed in Chapter 6.

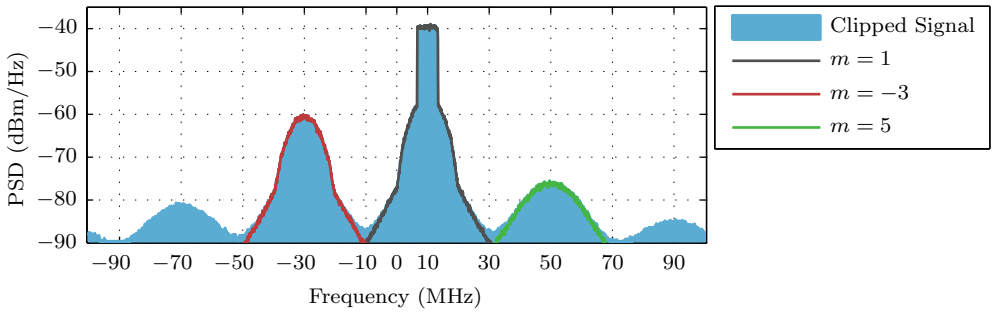

Figure 5.6: Example of an OFDM signal having center frequency of 10 MHz clipping level being $C = 1.0$. On top of the clipped signal, the most essential distortion orders are plotted separately according to Fourier coefficients in (5.10).

Table 5.2: Summary of different clipping scenarios for an I/Q ADC.

Scenario	**Clipping levels**	**Fourier coefficients**
Non-symmetric clipping unequally in I and Q	$C_{\mathrm{H,I}} \neq -C_{\mathrm{L,I}}, C_{\mathrm{H,Q}} \neq -C_{\mathrm{L,Q}}$ $C_{\mathrm{H,I}} \neq C_{\mathrm{H,Q}}, C_{\mathrm{L,I}} \neq C_{\mathrm{L,Q}}$	(5.7)
Non-symmetric clipping equally in I and Q	$C_{\mathrm{H,I}} \neq -C_{\mathrm{L,I}}, C_{\mathrm{H,Q}} \neq -C_{\mathrm{L,Q}}$ $C_{\mathrm{H}} = C_{\mathrm{H,I}} = C_{\mathrm{H,Q}}, C_{\mathrm{L}} = C_{\mathrm{L,I}} = C_{\mathrm{L,Q}}$	(5.8)
Zero-symmetric clipping unequally in I and Q	$C_{\mathrm{I}} = C_{\mathrm{H,I}} = -C_{\mathrm{L,I}}, C_{\mathrm{Q}} = C_{\mathrm{H,Q}} = -C_{\mathrm{L,Q}}$ $C_{\mathrm{H,I}} \neq C_{\mathrm{H,Q}}, C_{\mathrm{L,I}} \neq C_{\mathrm{L,Q}}$	(5.9)
Zero-symmetric clipping equally in I and Q	$C = C_{\mathrm{H,I}} = -C_{\mathrm{L,I}} = C_{\mathrm{H,Q}} = -C_{\mathrm{L,Q}}$	(5.10)

Different clipping scenarios for an I/Q ADC are summarized in Table 5.2. It is always possible to use the most general model of (5.7), but in appropriate cases the simplified models (5.8)–(5.10) may be more straightforward to use and computationally less complex. The simplified models also have more potential for extracting information for clipping distortion suppression purposes due to the lower number of variables.

CHAPTER 6

Digital Suppression of Analog-to-Digital Converter Nonlinearities

This chapter considers several methods for suppressing ADC nonlinearities by digital means in radio receivers. The focus is on scenarios where multiple signals are concurrently received with a single receiver. In addition to INL suppression, suppressing unintentional receiver-side signal clipping occurring in I/Q ADC is considered here in detail. The methods and results are based on [P1–P5].

6.1 Background and State of the Art

ADC post-correction, in general, is a very extensively researched topic. Typical approaches include look-up tables (LUTs), dithering, and black-box modeling [13, 72]. Recent developments also combine a static LUT with model-based dynamic correction in order to suppress INL in wideband applications [16, 80, 116]. The challenge in many INL suppression methods is that extensive off-line calibration is required. It is acceptable in stable operation conditions such as in measurement and instrumentation applications. However, many wireless radio systems are in continuously changing environments. This is due to, e.g., mobile terminal movement, time-varying channel, dynamic user allocations, and temperature variations. Therefore, real-time adaptive methods are desired for suppressing INL of ADCs in communications receivers. Section 6.2 considers AIC for reducing INL in a wideband reception scenario consisting of multiple signals with large dynamic range.

It is important to highlight here the difference between deliberate *transmitter-side* clipping and unintentional *receiver-side* clipping. Clipping is one of the most often considered methods for reducing signal PAPR in radio *transmitters* [53, 65]. The idea is to clip the signal to avoid transmitter components to cause nonlinear distortion and concurrently maximize the PA efficiency. This is typically done by limiting the amplitude of the digital complex waveform to be transmitted. Then, on the receiver side, the clipping distortion is suppressed by using an appropriate method such as the ones proposed in [6, 22, 104, 123]. In this scenario, the clipping is a deliberate operation which can be controlled very accurately and an optimal clipping level can be chosen considering the trade-off between the amount of PAPR reduction and introduced clipping distortion. The clipping level information is delivered to the receiver and therefore clipping distortion suppression can be done in effective manner. It has been shown that clipping or other transmitter-side memoryless nonlinearities can improve the performance of OFDM systems when signal detection is performed in optimal manner in the receiver [41].

This thesis is related to nonlinearities of receivers and A/D interfaces which means that the unintentional *receiver-side* clipping is in the focus here. Suppressing ADC clipping distortion is challenging since the clipping is time-varying and uncontrollable. Depending on the suppression methods, it may be difficult to estimate the radio channel, clipping levels or other essential parameters. The channel estimation problem with nonlinearly distorted pilots is addressed, e.g., in [109]. In [118], Kalman filter based approach is considered for clipped OFDM signals when the clipping level is unknown. In addition to aforementioned estimation challenges, the clipping distortion suppression may be limited by the channel/receiver noise. These aspects are discussed more in the following sections. Compared to PAPR reduction methods, the digital suppression of unintentional ADC clipping is a less discussed topic in the current literature. Nevertheless, ADC clipping due to high PAPR of OFDM signals is acknowledged in [97]. Two digital post-processing methods are proposed to suppress ADC clipping distortion in OFDM systems. The first method exploits clipping distortion in empty subcarriers whereas the second one is based on statistical properties of Gaussian signals and noise. Another kind of, more general, ADC clipping suppression method is proposed in [113]. It exploits oversampling A/D conversion and interpolation to recover clipped samples. This is discussed more in Section 6.4 together with another interpolation-based method proposed in [P3]. Yet another kind of ADC clipping suppression method is proposed in [112]. It exploits data from two physically separated sensors in cooperative manner to suppress the clipping distortion.

Although this thesis considers digital post-processing methods for suppressing ADC clipping, it is worth knowing that also more hardware-oriented approaches exist. For instance, ADCs with deliberately non-uniform quantization characteristics can be exploited [102]. One practical companding example is presented in [117] where a com-

pressing switched-capacitor filter is used in front of an ADC with a digital expanding decoder. Together this combination is shown to provide 12 dB more dynamic range in a WLAN receiver.

6.2 Adaptive Interference Cancellation

The concept of AIC is thoroughly discussed in Chapter 4 for suppressing receiver nonlinearities. Here in this chapter, AIC is applied to ADC nonlinearities. The only difference in AIC implementation between receiver and ADC nonlinearities is in the nonlinearity modeling stage. As discussed in Section 3.2, the LCF part of INL typically has a polynomial shape and therefore it can be conveniently modeled in the nonlinearity modeling stage of AIC. A receiver has separate ADCs for I and Q branches which means that both ADCs have their own INL behavior. Therefore also the nonlinearity model should consider them separately. In addition, the INL shape depends on the physical structure of the ADC and this determines what kind of a polynomial model should be employed [76, 88]. In general, terms $\hat{x}_{\mathrm{I}}^2(n), \hat{x}_{\mathrm{I}}^3(n), ...$ and $\hat{x}_{\mathrm{Q}}^2(n), \hat{x}_{\mathrm{Q}}^3(n), ...$ can be used in the nonlinearity modeling stage of AIC for INL suppression. Here, $\hat{x}(n) = \hat{x}_{\mathrm{I}}(t) + j\hat{x}_{\mathrm{Q}}(t)$ refers to the band-split stage output signal in the reference branch. In very wideband cases, also frequency selectivity should be considered by using multi-tap AFs in AIC.

Figure 6.1 shows a simulation example of INL suppression by using I/Q AIC. The considered signal scenario consists of five signals with different IFs, bandwidths and power levels. The signal of interest is the weak quadrature phase shift keying (QPSK) signal at 3 MHz. Other four signals, especially the strongest one at -1 MHz, are interfering with the weak QPSK signal due to the INL of the I/Q ADC. In the simulation, a commercial 10-bit I/Q ADC [8] is considered and it is simulated with the behavioral model provided by the manufacturer [17]. AIC is employed here to suppress nonlinear ADC distortion from the signal band of interest at 3 MHz by using the third-order terms $\hat{x}_{\mathrm{I}}^3(n)$ and $\hat{x}_{\mathrm{Q}}^3(n)$ in the nonlinearity modeling stage. After AIC, the SNDR of the weak signal at 3 MHz is enhanced from 6.4 dB to 10 dB. This snapshot example works as a proof of concept that the LCF part of the INL can be reduced using a low-order polynomial model. Therefore, it is essentially included in the BB part of the cascaded receiver nonlinearity model discussed in Section 3.1 and is straightforward to extend if also even-order nonlinearities are of concern. In addition, this means that using AIC to jointly suppress INL and receiver nonlinearities is feasible and also simple.

Much more challenging nonlinearity to suppress is ADC clipping. It cannot be considered as a weak nonlinearity. However, AIC still have potential in suppressing clipping distortion. Based on Chapter 5, clipping in I/Q ADC mostly causes odd-order nonlinear distortion. Therefore, proper terms to consider in the nonlinear distortion modeling stage of AIC are $\hat{x}_{\mathrm{I}}^3(n), \hat{x}_{\mathrm{I}}^5(n), \hat{x}_{\mathrm{I}}^7(n), ...$ and $\hat{x}_{\mathrm{Q}}^3(n), \hat{x}_{\mathrm{Q}}^5(n), \hat{x}_{\mathrm{Q}}^7(n), ...$ Due to

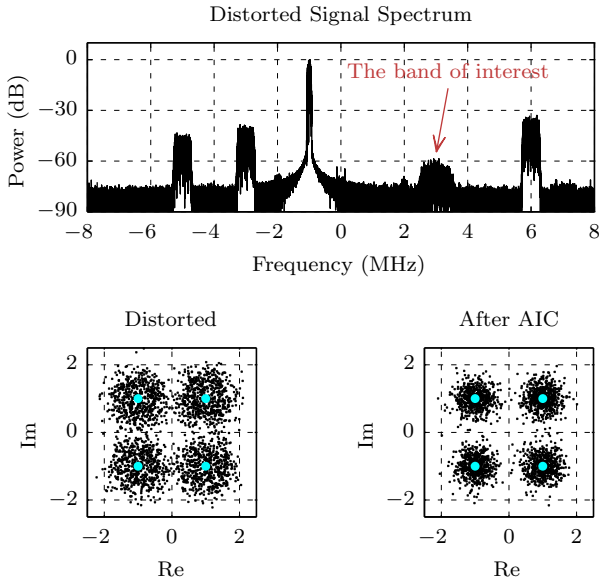

Figure 6.1: Simulation example about reducing the INL of an I/Q ADC using AIC. The upper part of the figure shows the distorted signal spectrum after A/D conversion and the lower part shows demodulated signal constellations for the weak QPSK signal at 3 MHz before and after AIC.

the fact that clipping is a strong nonlinearity, it is typically not enough to model only third-order distortion but also higher orders are needed. In addition to the polynomial modeling, there is also an alternative approach. It is possible to model the clipping distortion by clipping the time-domain waveform $\hat{x}(n)$ appropriately in the nonlinearity modeling stage of AIC. This is extremely simple from the computational complexity point of view since a single clipping operation (in I and Q branches) models all the required distortion terms. However, the real challenge is to accurately estimate the clipping levels in the receiver during its operation. Due to the strong nonlinear nature of clipping, a small error in the clipping level estimate may significantly affect the clipping distortion suppression performance. Other challenge in AIC is the nonlinear distortion inside the blockers bands, which affects the nonlinearity modeling accuracy since it is based on received blocker signals. Stronger clipping means more distortion inside the blocker bands and hence this fundamentally limits how strong clipping distortion can be suppressed with AIC. It is worth noting that this limitation exist independent of which nonlinearity modeling approach is chosen.

Performance example of AIC in suppressing clipping distortion is given later in Subsection 6.4.2 with laboratory measurements using commercial I/Q ADC hardware. In order to compare AIC with its alternatives, two other methods are introduced first in Sections 6.3 and 6.4.

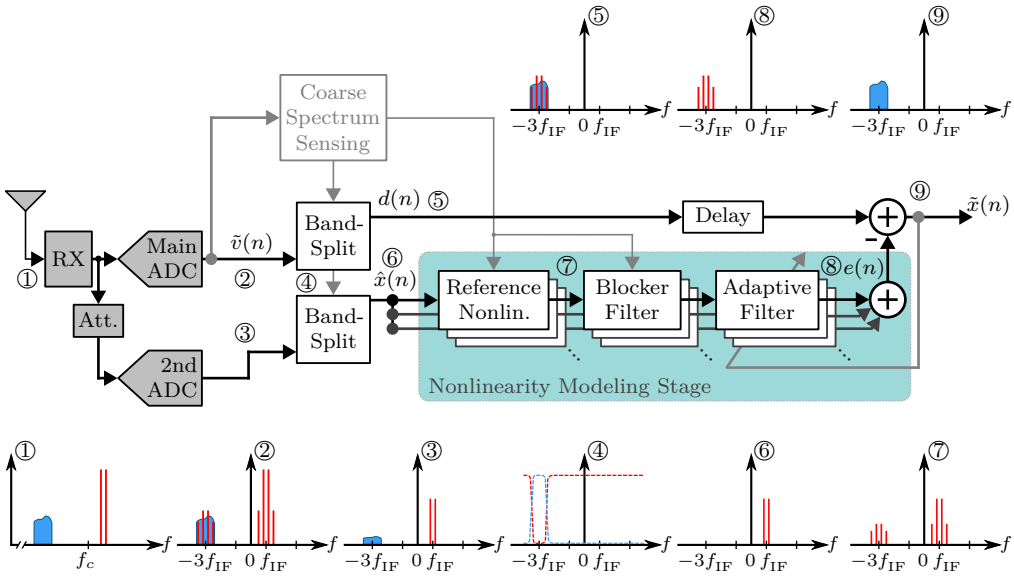

Figure 6.2: Block diagram for E-AIC suppressing nonlinear distortion stemming from the main ADC. Conceptual spectra exemplify the processing in scenario where a strong two-tone blocker signal causes nonlinear distortion especially on top of the weak modulated signal and E-AIC is focused on cleaning the weak signal band.

6.3 Enhanced Adaptive Interference Cancellation

The ideology of E-AIC is motivated by the fundamental limitation of AIC that the distortion suppression performance may reduce due to the excessive amount of nonlinear distortion inside the blocker bands which affects the nonlinearity modeling accuracy. This is a potential risk especially during ADC clipping which can generate lots of nonlinear distortion. E-AIC alleviates this challenge by introducing a secondary ADC. It is fed with the attenuated version of the received signal which is going through the main ADC. The attenuation should guarantee that clipping does not occur or at least the clipping is milder in the secondary ADC. Therefore, there is also less nonlinear distortion inside the blocker bands and by using this signal in the nonlinearity modeling stage, more accurate modeling results can be obtained.

The whole E-AIC concept is depicted in Figure 6.2. Compared with the original AIC concept (Figure 4.1), the only concrete difference is that the reference branch signal is obtained by using the secondary ADC. In addition, the simplified spectrum illustrations of Figure 6.2 depict suppressing nonlinear distortion from the weak modulated signal band where as the similar spectrum illustrations of Figure 4.1 show nonlinearity suppression for the whole reception band.

Since E-AIC requires a secondary ADC, it cannot be considered as fully digital approach. However, the requirements for the additional analog hardware are very low.

The secondary AIC can have poorer specifications, especially lower resolution, than the main ADC which makes the secondary ADC less expensive and less power hungry. This is possible since the target is to digitize only the strongest blockers with the secondary ADC and hence it does not need to have dynamic range to capture any weak signals. The E-AIC ideology could also be extended to suppression of receiver nonlinearities. In that case, a whole secondary receiver chain would be needed in which attenuated version of the received signal suffers less from nonlinearities and therefore is able to provide more linear perception of the blockers for the E-AIC nonlinearity modeling stage.

Performance example of E-AIC in suppressing clipping distortion is given later in Subsection 6.4.2 with laboratory measurements using commercial I/Q ADC hardware. The example compares E-AIC with the other methods discussed in Sections 6.2 and 6.4.

6.4 Maximum Selection Interpolation

This section involves multirate signal processing and polyphase structures. Introduction to these topics are given, e.g., in [44, 52]. When a digitized waveform contains clipped samples, it is known that those are erroneous and can be considered as lost samples. One traditional approach is to use interpolation to replace the lost samples with estimates obtained from adjacent non-clipped samples that are more reliable. This is especially potential approach if the signal happens to be band-limited and oversampled. Figure 6.3a gives an example of a received waveform obtained with oversampling A/D conversion during which the waveform is clipped. The oversampled waveform can be represented as a polyphase decomposition [52]. Therefore each polyphase branch is depicted with a different color and symbol in Figure 6.3a. In the oversampled waveform, consecutive samples contain redundant information which means that a clipped sample can be recovered based on the corresponding samples in other polyphase branches. This is possible by employing fractional delay filters [79]. In Figure 6.3a, e.g., the clipped samples in Branch 1 can be recovered by exploiting Branches 2, 3, and 4.

6.4.1 Algorithm Description

Based on the aforementioned concept, MSI method is proposed in [P3] for suppressing ADC clipping distortion. The block diagram of the MSI method is given in Figure 6.3b. A received band-limited signal is digitized with an oversampling ADC and after that the polyphase decomposition is formed. There are L polyphase branches when the oversampling factor is L. It is essential to know which samples are clipped and which are not. Clipping detection is typically straightforward since many ADCs provide out-of-range indicator (see, e.g., [9]). All non-clipped samples can be passed through without any special processing which in practice means filtering with a filter corresponding to a pure delay. For a clipped sample, other polyphase branches provide estimates.

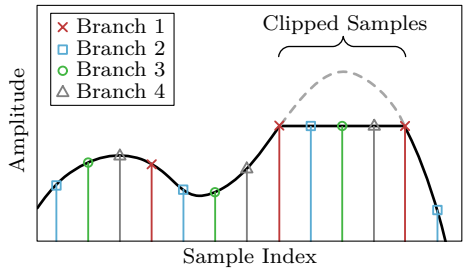

(a) Time-domain illustration of a clipped waveform having $L = 4$

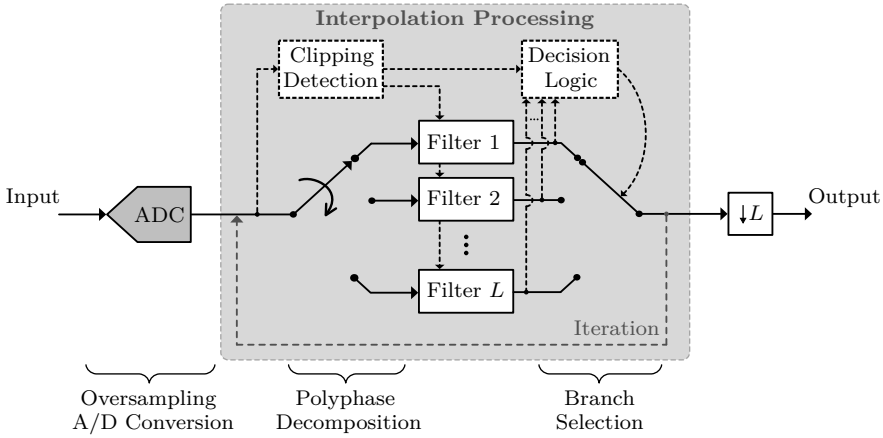

(b) Block diagram of MSI method to recover clipped samples

Figure 6.3: (a) Example of a received clipped waveform obtained with an ADC having oversampling factor of 4. The polyphase branches are depicted with different colors and symbols. (b) Block diagram of maximum selection interpolation method which recovers clipped samples by using fractional delay filters.

The decision logic then selects the best estimate among the branches by selecting the one having the largest absolute value. The selected estimate then replaces the clipped sample in the oversampled waveform. If there would be only a single clipped sample, the selected estimate would provide very reliable results. However, the estimates are poorer if there are more than $L - 1$ consecutive clipped samples in the oversampled waveform. The same applies also if there are clipped samples in all polyphase branches within the length of the polyphase branch filter. This problem can be alleviated by iterating the interpolation processing several times as indicated in Figure 6.3b. In this manner, more accurate estimates are obtained since more and more information is extracted from the adjacent samples. The logic behind this is the following. In the first iteration round the totally unreliable clipped samples are replaced with more accurate estimates. Then in the second iteration round there are no clipped samples anymore and this allows even more accurate estimates to be found. However, it is worth noting that the maximum

absolute value selection criterion does not guarantee convergence. Therefore, excessive iteration should be avoided. The whole MSI processing, including iteration, is performed for the oversampled signal. After the processing the sample rate can be reduced as indicated by the down-sampling block on the right side of Figure 6.3b.

The polyphase branch filters of MSI can be designed using various approaches. For example, all-pass filters implementing desired fractional delays for all polyphase branches could be used. Another approach is to first design a lowpass finite impulse response (FIR) filter of which passband corresponds to the bandwidth of the received band-limited signal. This essentially corresponds to a typical decimation filter having the normalized bandwidth of $\frac{1}{L}$. The impulse response of this FIR filter is denoted with $\mathbf{h}_p = [h_p(0), h_p(1), h_p(2), \dots]^{\mathrm{T}}$. Then the actual polyphase branch filters are obtained as a polyphase decomposition of $\mathbf{h}_p$. Formally, the impulse responses of the polyphase branch filters are

$$\mathbf{h}_{p,0} = [h_p(0), h_p(L), h_p(2L), \dots]^{\mathrm{T}}, \tag{6.1a}$$

$$\mathbf{h}_{p,1} = [h_p(1), h_p(L+1), h_p(2L+1), \dots]^{\mathrm{T}}, \tag{6.1b}$$

$$\vdots$$

$$\mathbf{h}_{p,L-1} = [h_p(L-1), h_p(2L-1), h_p(3L-1), \dots]^{\mathrm{T}}. \tag{6.1c}$$

The clipping detection entity in Figure 6.3b assigns the impulse response $\mathbf{h}_{p,0}$ always for the polyphase branch containing the clipped sample of interest and the other impulse responses accordingly to other polyphase branches. For example, if the clipped sample of interest is in the second polyphase branch, the Filters 1, 2, ..., L of Figure 6.3b are $\mathbf{h}_{p,L-1}, \mathbf{h}_{p,0}, \mathbf{h}_{p,1}, \dots, \mathbf{h}_{p,L-2}$, respectively.

6.4.2 Performance Evaluation and Comparison With Other Methods

The performance of the MSI method is evaluated with laboratory measurements using a commercial 14-bit I/Q ADC [9]. The results are presented in Figure 6.4. The signal scenario contains five modulated signals with different IFs, bandwidths, and power levels resulting in PAPR of 7 dB for the overall waveform. The sampling rate is 64 MHz in order to provide enough oversampling for MSI method. The time- and frequency-domain illustrations of Figure 6.4 shows the effect of I/Q ADC clipping when the clipping level is 6 dB above the average power of the overall waveform.

The bottom part of Figure 6.4 compares the clipping distortion suppression performance of several methods by showing SNDR gain results as a function of clipping ratio (clipping level with respect to average signal power level). The SNDR gain indicates that how much the suppression method is able to enhance the SNDR of the weak signal at

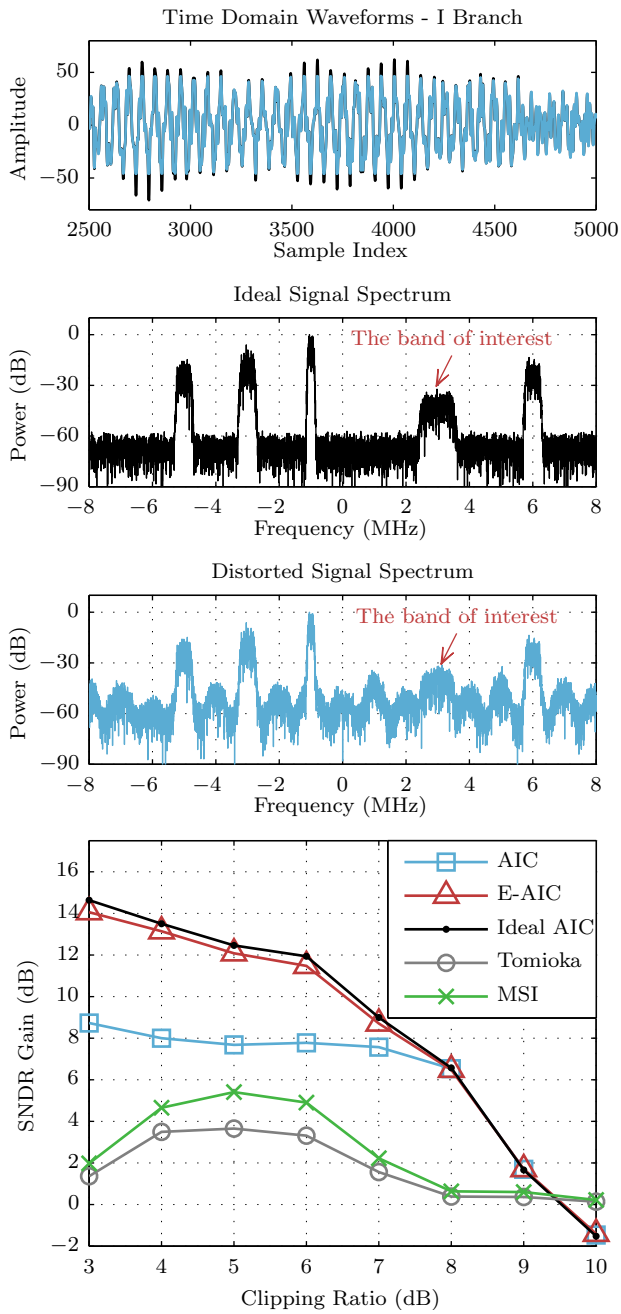

Figure 6.4: Measured clipping distortion suppression results using a 14-bit I/Q ADC hardware. Time- and frequency-domain plots illustrates the effect of clipping when the clipping level is 6 dB above the average power level of the overall waveform. The bottom figure shows SNDR gain for the weak signal at 3 MHz using different clipping distortion suppression methods. Tomioka method refers to [113].

3 MHz. The performance of MSI method is compared with another interpolation-based method proposed by T. Tomioka *et al.* in [113]. For both methods 32-tap polyphase branch filters are used and four iteration rounds are performed. Based on the results, the MSI method gives more SNDR gain than Tomioka's although the computational complexity of the MSI method lower. This is stemming from the fact that MSI does not require preliminary polynomial spline interpolation stage which is used in Tomioka's method to decrease estimation error due to multiple clipped samples involved in the estimation process. Additionally, MSI uses carefully designed polyphase branch filters whereas Tomioka's method employs truncated sinc functions. It is generally known that using a truncated sinc impulse response provides poor stopband attenuation [44, 119]. Furthermore, MSI and Tomioka's method have different decision logic for the estimate selection which also affects the performance. However, the practical performance of both methods is limited by other ADC nonlinearities.

Figure 6.4 also provides SNDR gain results for AIC and E-AIC when third-, fifth-, and seventh-order nonlinearities are used in the nonlinearity modeling stage. The E-AIC methods employs 7-bit secondary I/Q ADC with 7-dB input attenuation. In practice, the secondary I/Q ADC was implemented by using the same 14-bit I/Q ADC hardware during the measurements and then digitally reducing the resolution to seven bits afterwards. According to the SNDR gain results, both AIC and E-AIC are outperforming the interpolation-based methods. This is mainly because AIC and E-AIC are able to suppress, in addition to clipping, also other nonlinearities of third-, fifth-, and seventh-order. E-AIC is even able to almost reach the ideal AIC performance. Here the ideal AIC refers to AIC when a perfect undistorted signal is used in the reference branch. It is natural for all the methods that SNDR gain is lower for mild clipping levels (8–10 dB) since there is not much clipping distortion to be suppressed.

6.5 Decision-Aided Iterative Clipping Distortion Suppression

An I/Q ADC clipping distortion suppression method considered in this section is specifically targeted for multiuser/multichannel OFDM systems. The clipping distortion is gradually suppressed using an iterative process in which data symbol/bit decisions are exploited. Since demodulation of multiuser data is required, the suppression method is more suitable to be implemented in base stations for uplink scenarios, but also downlink scenarios may be possible on cooperative communications systems. The decision-aided iterative clipping distortion suppression method has been originally proposed in [P4, P5]. It is based on the PAPR reduction scheme considered in [22, 123], but essential modifications have been needed to make it suitable for suppressing I/Q ADC clipping distortion.

6.5.1 Algorithm Description

An OFDM symbol to be transmitted can be expressed in time domain at BB as

$$u(t) = \frac{1}{\sqrt{N}} \sum_{k=-\frac{N}{2}}^{\frac{N}{2}-1} U_k e^{j2\pi kt/T_s}, \quad 0 \leq t \leq T_s, \tag{6.2}$$

where U_k is the complex data symbol in subcarrier (SC) k and T_s is the OFDM symbol duration. The OFDM symbol includes N_A active SCs while the oversampling factor is J and hence the total number of SCs is $N = JN_A$. The SC indices are denoted with a set $\Omega = \{-\frac{N}{2}, -\frac{N}{2}+1, \ldots, \frac{N}{2}-1\}$. The active SCs carry the data symbols U_k, $k \in \Omega_A = \{-\frac{N_A}{2}, \ldots, -1, 1, \ldots, \frac{N_A}{2}\}$ whereas inactive SCs contain zeros so that $U_k = 0, k \in \Omega \setminus \Omega_A$. Cyclic prefix (CP) is omitted from the equations for notational convenience. It does not have any influence on I/Q ADC clipping due to the memoryless nature of clipping. However, CP is included in the simulations and measurements discussed later in this section since it is essential to avoid intersymbol interference due to a frequency-selective channel.

The top part of Figure 6.5 illustrates a typical OFDM transmitter. The data bits in vector $\mathbf{b}$ are first turbo encoded and interleaved resulting in the coded bits $c_{1,\ldots,M}^{(U_k)}$, $k \in \Omega_A$, where M denotes the number of bits in a data symbol. Those bits are then mapped to data symbols U_k, $k \in \Omega_A$ after which the time-domain signal with CP is formed and transmitted on the radio channel.

The decision-aided iterative clipping distortion suppression method for an OFDM receiver is illustrated among typical OFDM processing on the bottom part of Figure 6.5. Generally, the received waveform in the I/Q ADC input is $v(t) = v_{\mathrm{I}}(t) + jv_{\mathrm{Q}}(t) = h(t) * u(t) + w(t)$, where $h(t)$ is the radio channel impulse response and $w(t)$ is additive white Gaussian noise. The I/Q ADC clips the signal according to (5.2). Assuming clipping to be zero-symmetric, the clipping levels are C_{I} and C_{Q}. The clipping levels can also be expressed with respect to the signal power, called clipping ratios, so that

$$\gamma_{\mathrm{I}} = \frac{C_{\mathrm{I}}}{\sqrt{P_{v,\mathrm{I}}}} \quad \text{and} \quad \gamma_{\mathrm{Q}} = \frac{C_{\mathrm{Q}}}{\sqrt{P_{v,\mathrm{Q}}}}, \tag{6.3}$$

where $P_{v,\mathrm{I}}$ and $P_{v,\mathrm{Q}}$ are the average power levels of the non-clipped signals in I and Q branches. These clipping ratios describe how strong the clipping actually is for the received signal. The clipping distortion suppression method described here relies on Bussgang's theorem [18] which has been proven to be an adequate model for clipping distortion [86, 87, 100]. According to the theorem, clipping attenuates the signal $v(t)$ and causes additive clipping distortion which is uncorrelated with the non-clipped $v(t)$.

Formally, the I/Q ADC output is

$$\tilde{v}_{\mathrm{I}}(nT_s) = \alpha_{\mathrm{I}} v_{\mathrm{I}}(nT_s) + d_{c,\mathrm{I}}(nT_s), \tag{6.4a}$$

$$\tilde{v}_{\mathrm{Q}}(nT_s) = \alpha_{\mathrm{Q}} v_{\mathrm{Q}}(nT_s) + d_{c,\mathrm{Q}}(nT_s), \tag{6.4b}$$

where α_{I} and α_{Q} are the scaling factors and the additive clipping distortion is denoted with $d_{c,\mathrm{I}}(nT_s)$ and $d_{c,\mathrm{Q}}(nT_s)$. The model assumes $v_{\mathrm{I}}(nT_s)$ and $v_{\mathrm{Q}}(nT_s)$ to be Gaussian and hence the scaling factors are related to clipping ratios in the following manner

$$\alpha_{\mathrm{I}} = \frac{\mathrm{E}[v_{\mathrm{I}}(nT_s)\tilde{v}_{\mathrm{I}}(nT_s)]}{\mathrm{E}[v_{\mathrm{I}}(nT_s)v_{\mathrm{I}}(nT_s)]} = \mathrm{erf}\left(\frac{\gamma_{\mathrm{I}}}{\sqrt{2}}\right), \tag{6.5a}$$

$$\alpha_{\mathrm{Q}} = \frac{\mathrm{E}[v_{\mathrm{Q}}(nT_s)\tilde{v}_{\mathrm{Q}}(nT_s)]}{\mathrm{E}[v_{\mathrm{Q}}(nT_s)v_{\mathrm{Q}}(nT_s)]} = \mathrm{erf}\left(\frac{\gamma_{\mathrm{Q}}}{\sqrt{2}}\right), \tag{6.5b}$$

where the error function is

$$\mathrm{erf}(x) = \frac{2}{\sqrt{\pi}} \int_0^x e^{-t^2}\, \mathrm{d}t. \tag{6.6}$$

Details for deriving (6.5) are given in [21, 86, 100]. Furthermore, the I/Q ADC output (6.4) can be expressed as a complex signal

$$\begin{aligned} \tilde{v}(nT_s) &= \alpha_{\mathrm{I}} v_{\mathrm{I}}(nT_s) + d_{c,\mathrm{I}}(nT_s) + j[\alpha_{\mathrm{Q}} v_{\mathrm{Q}}(nT_s) + d_{c,\mathrm{Q}}(nT_s)] \\ &= \alpha_1 v(nT_s) + \alpha_2 v^*(nT_s) + d_c(nT_s) \\ &= \alpha_1 v(nT_s) + z(nT_s), \end{aligned} \tag{6.7}$$

where $\alpha_1 = (\alpha_{\mathrm{I}} + \alpha_{\mathrm{Q}})/2$, $\alpha_2 = (\alpha_{\mathrm{I}} - \alpha_{\mathrm{Q}})/2$, the complex clipping distortion $d_c(nT_s) = d_{c,\mathrm{I}}(nT_s) + j d_{c,\mathrm{Q}}(nT_s)$, and the total complex clipping distortion $z(nT_s) = \alpha_2 v^*(nT_s) + d_c(nT_s)$. It is straightforward to see from (6.7) that the original non-clipped $v(nT_s)$ can be recovered using $\tilde{v}(nT_s)$, if good enough estimates of α_1 and $z(nT_s)$ are obtained. This is the fundamental idea behind the clipping distortion suppression method considered in this section.

As illustrated in Figure 6.5, the received clipped OFDM signal is first processed in a conventional manner including CP removal, transformation to frequency domain, channel equalization, mapping symbols to bits, deinterleaving, and finally decoding. Due to the clipping distortion, obtained data bit estimates $\hat{\mathbf{b}}$ may not be perfect. However, if reasonable amount of bit estimates are good, it is possible to enhance the the poor bit estimates through to following clipping distortion suppression processing. First, the bit estimates are used for regenerating an estimate of the received signal with and without clipping. The clipping distortion estimate is then the difference of those two received signal estimates. After that, the clipping distortion estimate is subtracted from the

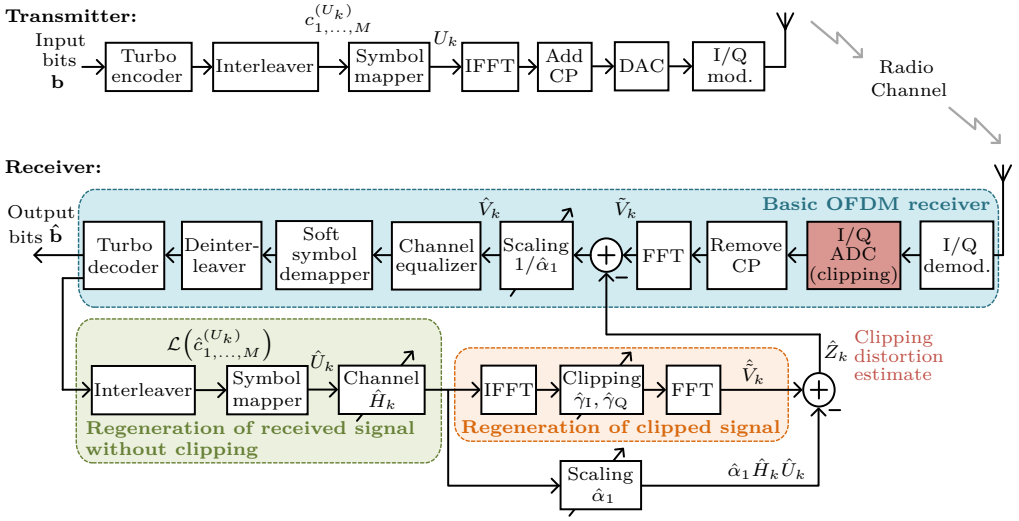

Figure 6.5: Block diagrams of OFDM transmitter and decision-aided iterative clipping distortion suppressing receiver. The unintentional clipping distortion is produced by the I/Q ADC due to improper input signal conditioning.

original received signal. Now there should be less clipping distortion in the received signal and it provides more reliable bit estimates. This, in turn, provides more accurate clipping distortion estimate and hence the whole processing can be iterated in order to obtain more and more reliable bit estimates. The following paragraphs provide more detailed mathematical description of the clipping distortion suppression method. Its key steps are also summarized in Table 6.1.

The following mathematical notation considers only a single OFDM symbol for simplification. The clipping distortion suppression is anyway performed subcarrier-wise and thus it can be implemented with almost any processing block length. In practical receiver, the processing block length may be one or more OFDM symbols depending on the implementation of the conventional receiver functions such as channel equalization, deinterleaving, and channel decoding. For reference, the received signal without clipping is expressed in frequency domain after I/Q ADC and after removing CP as

$$V_k = H_k U_k + W_k, \quad k \in \Omega, \tag{6.8}$$

where H_k is the channel gain and W_k is the additive white Gaussian noise for the kth SC. On the other hand, if I/Q ADC clipping occurs, the frequency-domain signal is then

$$\begin{aligned} \tilde{V}_k &= \alpha_1 V_k + \alpha_2 V_{-k}^* + D_{c,k} \\ &= \alpha_1 (H_k U_k + W_k) + \alpha_2 (H_{-k}^* U_{-k}^* + W_{-k}^*) + D_{c,k} \\ &= \alpha_1 H_k U_k + Z_k + \alpha_1 W_k + \alpha_2 W_{-k}^*, \quad k \in \Omega, \end{aligned} \tag{6.9}$$

Table 6.1: Algorithm for the decision-aided iterative clipping distortion suppression.

Initialization: for all $k \in \Omega_A$

1. Set $i = 0$, $\hat{\alpha}_1^{(0)} = 1$, and $\hat{Z}_k^{(0)} = 0$
2. Obtain channel estimates $\hat{H}_k^{(i)}$ using signal $\hat{V}_k^{(i)} = (1/\hat{\alpha}_1^{(i)})(\tilde{V}_k - \hat{Z}_k^{(i)})$
3. Perform channel equalization as $\hat{V}_k^{(i)}/\hat{H}_k^{(i)}$
4. Demap symbols $\hat{V}_k^{(i)}/\hat{H}_k^{(i)}$ to bits, deinterleave, and decode to obtain output data bits $\hat{\mathbf{b}}^{(i)}$

Iteration: Increase i by one and do the following steps for all $k \in \Omega_A$

5. Create $\hat{U}_k^{(i)}$ based on the coded bits $\hat{c}_{1,\ldots,M}^{(U_k^{(i-1)})}$ (hard) or $\mathcal{L}\left(\hat{c}_{1,\ldots,M}^{(U_k^{(i-1)})}\right)$ (soft)
6. Estimate clipping ratios $\hat{\gamma}_{\mathrm{I}}^{(i)}$ and $\hat{\gamma}_{\mathrm{Q}}^{(i)}$ as well as attenuation factor $\hat{\alpha}_1^{(i)}$
7. Clip $\hat{H}_k^{(i-1)}\hat{U}_k^{(i)}$ according to $\hat{\gamma}_{\mathrm{I}}^{(i)}$ and $\hat{\gamma}_{\mathrm{Q}}^{(i)}$ in *time domain* to produce $\hat{\tilde{V}}_k^{(i)}$
8. Calculate clipping distortion estimate $\hat{Z}_k^{(i)} = \hat{\tilde{V}}_k^{(i)} - \hat{\alpha}_1^{(i)}\hat{H}_k^{(i-1)}\hat{U}_k^{(i)}$
9. Remove the distortion from the received signal, i.e., $\hat{V}_k^{(i)} = (1/\hat{\alpha}_1^{(i)})(\tilde{V}_k - \hat{Z}_k^{(i)})$
10. Obtain new channel estimates $\hat{H}_k^{(i)}$ using signal $\hat{V}_k^{(i)}$
11. Perform channel equalization as $\hat{V}_k^{(i)}/\hat{H}_k^{(i)}$
12. Demap symbols $\hat{V}_k^{(i)}/\hat{H}_k^{(i)}$ to bits, deinterleave, and decode to obtain output data bits $\hat{\mathbf{b}}^{(i)}$

where the total clipping distortion is $Z_k = \alpha_2 H_{-k}^* U_{-k}^* + D_{c,k}$, $k \in \Omega$. This follows the notation of (6.7). As shown in Figure 6.5, before the clipping distortion suppression, conventional OFDM processing is performed, i.e., the received data symbols $\tilde{V}_k$, $k \in \Omega_A$ are equalized, mapped to soft bits, deinterleved, and finally decoded. The channel equalization is based on the channel estimates $\hat{H}_k$, $k \in \Omega_A$ which is considered in more detail in Subsection 6.5.2.

The first step in the clipping distortion suppression is to acquire an estimate of the originally transmitted signal, namely, $\hat{U}_k$, $k \in \Omega$ using the bit estimates after turbo decoder as indicated in Figure 6.5. In order to implement this, it is not necessary to re-encode the data bit estimates $\hat{\mathbf{b}}$, but the soft-coded bit estimates $\mathcal{L}\big(\hat{c}_{1,\ldots,M}^{(U_k)}\big)$, $k \in \Omega_A$, can be used directly from the turbo decoder output after interleaving to obtain soft symbol estimates. Here, $\hat{c}_{1,\ldots,M}^{(U_k)}$ refers to the hard bit estimates related to the data symbol U_k and $\mathcal{L}\big(\hat{c}_{1,\ldots,M}^{(U_k)}\big)$ denotes log-likelihood ratio values for $\hat{c}_{1,\ldots,M}^{(U_k)}$ [14, 30, 98]. Another, less complex, option is to obtain hard symbol estimates by using the hard bit estimates $\hat{c}_{1,\ldots,M}^{(U_k)}$. Both options, soft and hard symbol estimates, are considered in the performance evaluation in Subsection 6.5.3. Since an estimate of the received signal without clipping is needed, the estimate of the transmitted signal is exposed to the channel estimates, i.e., $\hat{H}_k\hat{U}_k$, $k \in \Omega_A$.

The next step is to obtain a regenerated version of the clipped received signal, namely $\hat{\tilde{V}}_k$, $k \in \Omega_A$. The clipping is performed in time domain using the clipping ratio estimates $\hat{\gamma}_\mathrm{I}$ and $\hat{\gamma}_\mathrm{Q}$ since the true clipping ratios, γ_I and γ_Q, are not known. The clipping ratio estimates $\hat{\gamma}_\mathrm{I}$ and $\hat{\gamma}_\mathrm{Q}$ can be calculated similarly as in (6.3) by first approximating the required parameters. The clipping levels C_I and C_Q should be fairly accurately known from the FS range of the ADC or then the clipping levels can be deduced from the maximum values in the clipped received signal. The average power levels of the non-clipped signals, $P_{v,\mathrm{I}}$ and $P_{v,\mathrm{Q}}$, can be estimated from the hard symbol estimates $\hat{U}_k$, $k \in \Omega$. After obtaining $\hat{\tilde{V}}_k$, $k \in \Omega_A$, it is used for extracting the clipping distortion estimate

$$\hat{Z}_k = \hat{\tilde{V}}_k - \hat{\alpha}_1 \hat{H}_k \hat{U}_k, \quad k \in \Omega_A. \tag{6.10}$$

This is exploiting Bussgang's theorem as was discussed earlier related to (6.7). The estimated scaling factor $\hat{\alpha}_1 = (\hat{\alpha}_\mathrm{I} + \hat{\alpha}_\mathrm{Q})/2$ is calculated according to (6.5) using $\hat{\gamma}_\mathrm{I}$ and $\hat{\gamma}_\mathrm{Q}$. The final processing step involves enhancing the received signal using the clipping distortion estimate. Formally, the signal after clipping distortion suppression is

$$\hat{V}_k = \frac{1}{\hat{\alpha}_1}\Big(\tilde{V}_k - \hat{Z}_k\Big), \quad k \in \Omega_A. \tag{6.11}$$

This signal is then used in the next iteration round starting with the channel estimation and equalization. Clipping distortion suppression performance improves in every iteration since all the estimates are improved. In practice, the maximum performance is determined by the noise involved in the I/Q ADC clipping W_k, $k \in \Omega$, and also by the accuracy of the estimates $\hat{\gamma}_\mathrm{I}$, $\hat{\gamma}_\mathrm{Q}$, and $\hat{H}_k$, $k \in \Omega$.

6.5.2 Channel Estimation and Equalization

There are vast amount of ways to obtain the channel estimates and it is also partially system- and standard-specific issue. Therefore, this subsection does not try to cover all the possible aspects of channel estimation and equalization, but rather provides an example of a possible approach. It is also employed in the simulations and measurements discussed in the next subsection regarding the performance evaluation of the clipping distortion suppression method.

It is considered here that the active SC set Ω_A contains evenly distributed pilot SCs denoted with a set Ω_P. This means that the data SCs form a set $\Omega_D = \Omega_A \setminus \Omega_P$. Following the traditional zero-forcing channel equalization principle, the channel estimates can be calculated for the pilot SCs as

$$\hat{H}_{P,k} = \frac{\hat{V}_k}{U_k}, \quad k \in \Omega_P. \tag{6.12}$$

These estimates are then used to acquire channel estimates for the data SCs Ω_D using interpolation. This can be done by inserting zeros between $\hat{H}_{P,k}$, $k \in \Omega_P$ so that there is a zero for each Ω_D and the filtering with a properly designed FIR lowpass interpolation filter. In practice, the bandwidth of the lowpass filter corresponds to the original data bandwidth. It is worth noting that since $\hat{H}_{P,k}$, $k \in \Omega_P$ are in frequency domain, also the interpolation is performed there. It means that the zero-padded channel estimates are convolved with the impulse response of the lowpass filter in frequency domain.

After the first clipping distortion suppression iteration round, there are data symbol estimates which can be exploited in the channel estimation together with the pilot symbols. Since some symbol errors are probable, all the data-symbol-based channel estimates may not be as reliable as the pilot-based channel estimates. One approach proposed in [P5] is to take into account the symbol reliabilities $p(U_k)$, $k \in \Omega_A$, when obtaining the channel estimates. Exploiting both the data symbol estimates and pilots, the channel estimates can be calculated as

$$\hat{H}_k = \frac{p(U_k)}{2}\hat{H}_{D,k} + \left[1 - \frac{p(U_k)}{2}\right]\hat{H}_{P,k}, \quad k \in \Omega_A, \tag{6.13}$$

where the data-symbol-based estimates are $\hat{H}_{D,k} = \hat{V}_k/\hat{U}_k$, $k \in \Omega_D$. The data-symbol-based estimates are not needed for the pilot SCs and therefore $p(U_k) = 0$, $k \in \Omega_P$. For the data SCs, the reliabilities are calculated as

$$p(U_k) = \prod_{\iota=1}^{M} \frac{\exp\left[\hat{c}_\iota^{(U_k)}\mathcal{L}\left(\hat{c}_\iota^{(U_k)}\right)\right]}{1 + \exp\left[\mathcal{L}\left(\hat{c}_\iota^{(U_k)}\right)\right]}, \quad k \in \Omega_D. \tag{6.14}$$

In optimal situation, (6.13) and (6.14) are recalculated on every iteration round. However, some optimization in computational complexity can be achieved, if the recalculation is not performed for the most realiable SCs.

Due to the clipping distortion and zero-forcing channel equalizer, there can be extremely large amplitude values in the output of the equalizer. These large values cause problems for the soft symbol demapper assuming Gaussian noise. Therefore, the large amplitude values, which are known to be erroneous anyway, should be limited before fed into the soft symbol demapper. A reasonable amplitude limit for the channel equalizer output is

$$V_{\max,\mathrm{eq}} = \max_r \left\|\Psi_r\right\| + \frac{3.29}{\sqrt{2}}\sigma_n, \tag{6.15}$$

where Ψ_r, $r = 1, 2, \ldots, 2^M$, denotes all the possible values in the symbol alphabet and σ_n is the standard deviation of the Gaussian noise $w(t)$. The scaling factor $\frac{3.29}{\sqrt{2}}$ corresponds to the 99.9 % confidence level of complex Gaussian distribution [125].

In general, it can be said that I/Q ADC clipping limits the channel estimation accuracy. On the other hand, the accuracy of the channel estimates affects the clipping distortion suppression since it is based on data bit decisions. More research is needed to find an optimal channel estimation approach when I/Q ADC clipping occurs.

6.5.3 Performance Evaluation

The performance of the decision-aided iterative clipping distortion suppression method is evaluated in an uplink scenario of two users in adjacent channels. Each user is individually experiencing a block-fading extended Vehicular A channel of ITU Radiocommunication Sector (ITU-R) [107]. The signal of User 1 is 15 dB weaker than the signal of User 2 when those are simultaneously received by a base station receiver. The composite signal of two users gets unintentionally clipped in the I/Q ADC of the receiver and especially the weaker User 1 suffers from the clipping distortion originating from its own signal and also from the signal of User 2. This scenario is first simulated and then also evaluated with laboratory measurements. The essential parameters are collected in Table 6.2. Furthermore, the simulated scenario is illustrated in Figure 6.6. The time-domain plot illustrates the composite waveform of Users 1 and 2 before and after clipping when the clipping ratio is $\gamma = \gamma_{\mathrm{I}} = \gamma_{\mathrm{Q}} = 6\,\mathrm{dB}$. The spectrum plot before clipping illustrates the effect of the simulated frequency-selective channel whereas the lower spectrum plot indicates the deteriorating effect of clipping, especially for User 1.

Figure 6.7a illustrates how the average BER of User 1 improves from iteration to iteration when the clipping distortion suppression method is employed. The two curves represent the average BER before and after the turbo decoder when the clipping ratio is $\gamma = 6\,\mathrm{dB}$. The SNR for User 1 is 21.9 dB. The arrows indicate the information flow in the receiver, namely D refers to decoding process whereas F means the feedback stage containing the clipping distortion suppression. It can be concluded that the clipping distortion effectively deteriorates the turbo decoder performance, but by suppressing the clipping distortion, it is possible to achieve BER that is close to the BER of the non-clipped signal. As discussed in Subsection 6.5.1, the performance of the non-clipped case cannot be exactly achieved due to the noise of the received signal and inaccuracies in estimating the clipping ratio γ and the channel estimates $\hat{H}_k$, $k \in \Omega_A$. The significance of the noise as a limiting factor in clipping distortion suppression increases when SNR is poor. The situation becomes more challenging also when clipping is stronger as in Figure 6.7b where $\gamma = 2\,\mathrm{dB}$. The clipping distortion suppression still radically enhances the performance, but more iteration rounds are needed in order to achieve the best possible BER.

More insight into, how the clipping ratio affects the BER of User 1, is given in Figure 6.8a. It is clear that the average BER is poorer when strong clipping occurs (γ is small). This is especially true since only five iterations of clipping distortion suppression

Table 6.2: Parameters of the multiuser uplink scenario.

Parameter	Value
Number of users	2
FFT size	2048
Active subcarriers per user	512
Scattered pilots per user	64
CP length	$\frac{1}{16}$ (128 samples)
Sampling rate	30.72 MHz
Subcarrier spacing	15 kHz
Subcarrier modulation	16-QAM ($M = 4$)
Channel profile	Extended ITU-R Vehicular A [107]
Channel codec	Turbo codec (Max-Log-MAP) [14, 30, 98]
Coding rate	$\frac{1}{2}$
Coded block length	3584 bits (2 OFDM symbols)
Decoding iterations	Max. 5
Clipping suppression iterations	5 or 10

is performed here, although more iterations could be beneficial when clipping is strong. Furthermore, Figure 6.8a also illustrates the effect of channel estimation accuracy by comparing the performance when using perfect channel knowledge (True CH) and when channel estimation is performed as described in Subsection 6.5.2 (Est. CH). There is practically no difference when clipping is mild, but the channel estimation is limiting the performance when clipping is strong. This conclusion can be made because the SNR of User 1 before clipping is 21.9 dB for all the clipping ratios.

Finally, measurement-based results with real hardware are given in Figure 6.8b. The same two-user scenario is considered and also here the SNR of User 1 is 21.9 dB. The fading channel model is digitally applied to the digital transmit waveform which is then converted to analog domain using a baseband signal generator [99]. After that, the waveform is digitized and clipped with a 14-bit I/Q ADC [9]. Figure 6.8b shows that the clipping distortion suppression method perform successfully also in real measurements. It can be also concluded that the performance is almost the same regardless of whether hard or soft data symbol estimates are used for received signal regeneration in the feedback branch.

More simulation results and discussion on computational complexity of the clipping distortion suppression method is given in [P5]. In addition, a modified version of the method is proposed in which the clipping distortion suppression is iterated on symbol level and only in the end, after all iterations, the enhanced data symbols are decoded. This significantly decreases the computational complexity but, according to the results, without considerably affecting the performance.

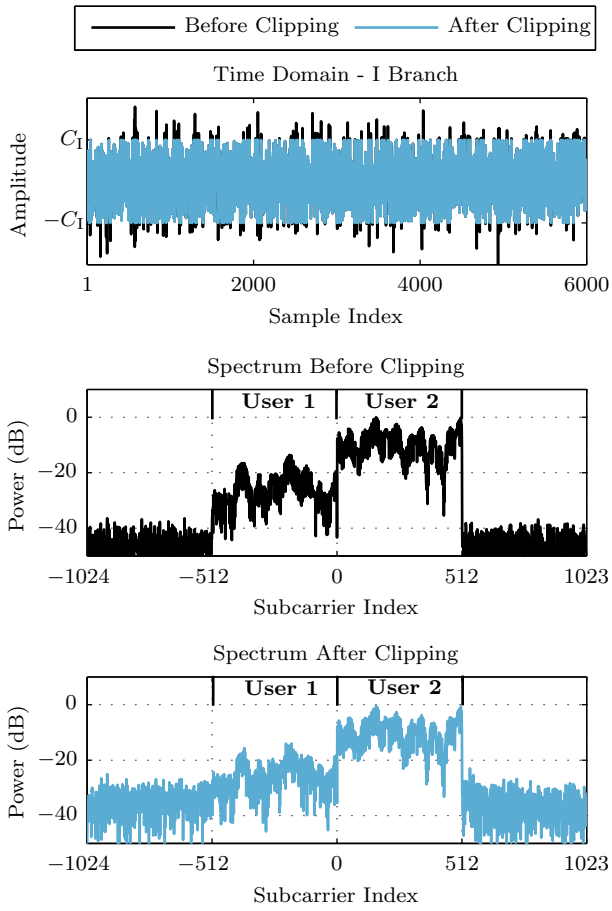

Figure 6.6: Time- and frequency-domain illustrations of the simulated multiuser uplink scenario. Each user individually experience block-fading extended ITU-R Vehicular A channel. In the base station receiver, the composite signal of two users gets unintentionally clipped by an I/Q ADC, the clipping ratio being $\gamma = 6\,\mathrm{dB}$.

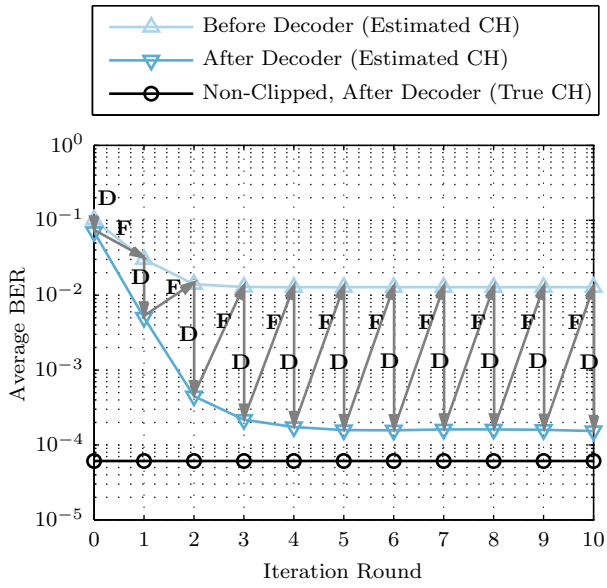

(a) Clipping ratio $\gamma = 6\,\mathrm{dB}$

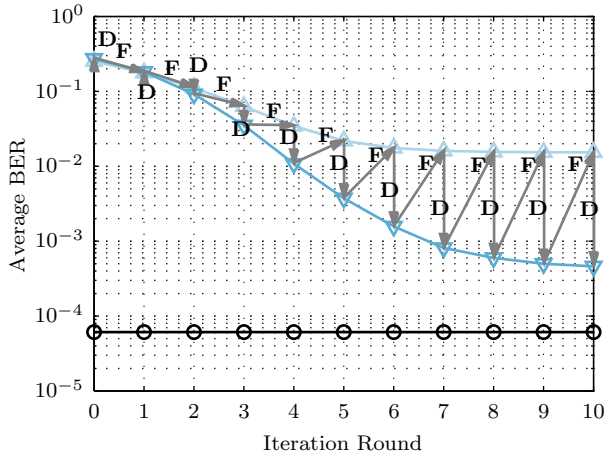

(b) Clipping ratio $\gamma = 2\,\mathrm{dB}$

Figure 6.7: Simulated average BER of User 1 as a function of clipping distortion suppression iterations for two different clipping ratios. Iteration round 0 refers to original received signal without clipping distortion suppression. Arrows indicate the decoding (D) and clipping suppression feedback (F) stages.

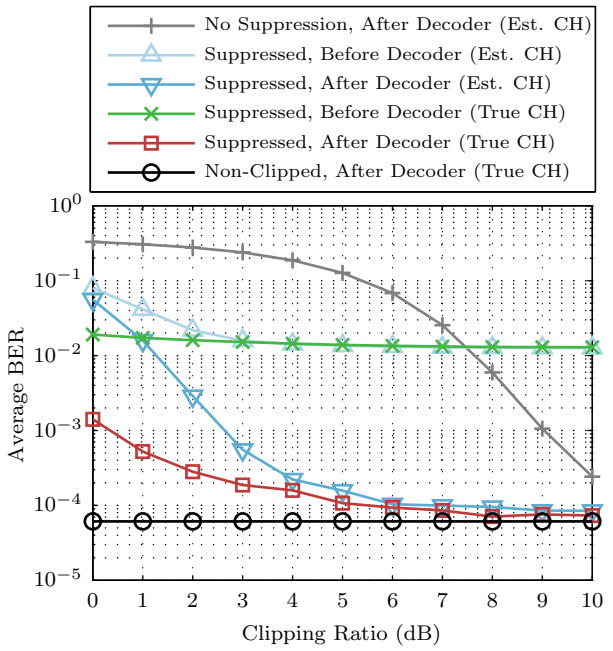

(a) Simulated

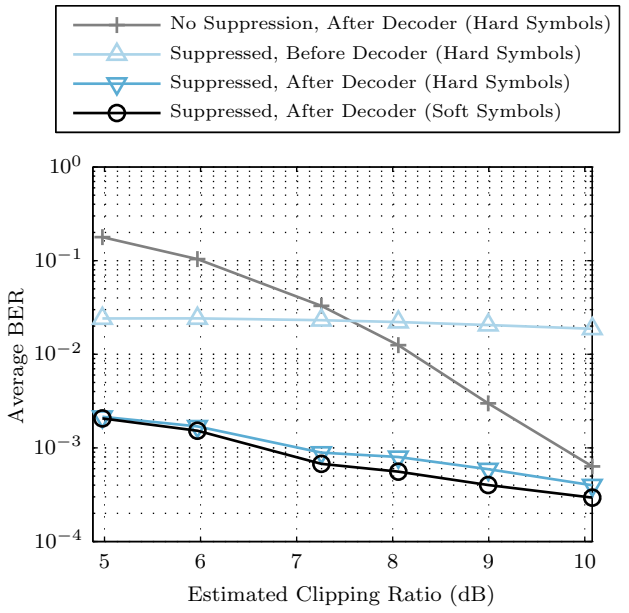

(b) Measured

Figure 6.8: Average BER of User 1 as a function of clipping ratio γ in (a) simulations and (b) laboratory measurements. The number of clipping distortion suppression iterations is five.

CHAPTER 7

Conclusions

This concluding chapter highlights the key aspects and the main results of the thesis. Due to the vast variety of quickly evolving systems employing wideband radio receivers, optimal yet practical state-of-the-art modeling and digital suppression of nonlinear distortion in the receivers and A/D interfaces require continuous research efforts. Therefore, the potential directions for further research is discussed in the second section of this chapter.

7.1 Main Results

This thesis contributes to system-level modeling of nonlinearities in DCRs and A/D interfaces. The purpose of the models is to provide understanding to the nonlinearity phenomena themselves and especially to help suppressing nonlinear distortion in multi-carrier/multiradio receivers and A/D interfaces. A cascaded receiver nonlinearity model was derived based on polynomials for considering the joint effects of RF, mixer and BB stages. This cascaded modeling is important since the RF distortion becomes further distorted by BB nonlinearities and I/Q imbalance. Although the full cascaded model is rather long, it has a very logical structure since every nonlinearity term can be related to a certain spectral location and bandwidth. Furthermore, the model coefficients are related to gains, IIP3s, and IRRs of different stages and therefore it is straightforward to analyze which of the model terms are relevant. It was shown with realistic parameters that significant portion of the terms were below the receiver noise floor and the model can be considerably shortened. The cascaded model was specifically derived for DCRs, but the same approach with small changes could be applied also for other receiver architectures, such as superheterodyne.

Another model introduced in this thesis was a general signal clipping model for I/Q ADCs. It is based on Fourier series with time-dependent Fourier coefficients. The model works as a tool to analyze the clipping distortion in frequency domain. Since clipping causes many different nonlinearity orders, it is convenient that each order can be considered separately. The derived model provides exact weights and spectral shapes for all nonlinearity orders. The model clearly shows how zero-symmetric clipping equally in I and Q branch ADCs causes only odd-order distortion and every other order is on the negative side of the complex spectrum. Furthermore, the model shows that unequal I/Q clipping causes mirror-image interference to appear and, what is more, non-symmetric clipping with respect to zero creates also even-order distortion. The clipping model is valid for any receiver architecture employing I/Q ADCs. It is also valid for all traditional uniform ADC architectures.

The thesis also provided several methods for suppressing nonlinear distortion in wideband radio receivers and A/D interfaces. The performance of the methods has been verified with simulations and also with RF laboratory measurements using real hardware. AIC method was shown to be a very versatile approach for suppressing many kinds of nonlinearities. First of all, it is a fully digital adaptive post-processing method requiring minimal *a priori* information about the receiver itself or the signal scenario. This makes it easy to implement and it may also be applicable to already existing systems. By exploiting the aforementioned cascaded receiver nonlinearity model, AIC is able to jointly suppress nonlinear distortion of RF and BB stages as well as I/Q imbalance. It was also shown to be able to reduce nonlinear distortion caused by the INL of the ADC. Moreover, by using an appropriate nonlinearity model, AIC was shown to suppress also unintentional I/Q ADC clipping distortion. Generally, AIC is applicable to multicarrier reception scenarios where strong blockers are causing nonlinear distortion all over the reception band. However, AIC is not capable of suppressing distortion stemming from blockers that are outside the reception band and also it does not suppress the distortion in the blockers themselves.

In addition to AIC, also several other distortion suppression methods were proposed for unintentional receiver-side I/Q ADC clipping. A modified version of the AIC, called E-AIC, was shown to provide superior clipping distortion suppression performance due to its less distorted reference signal obtained by an additional low-resolution ADC. Without any additional analog hardware, an interpolation-based clipping distortion suppression method, called MSI, also provided rather good performance. However, it requires that the A/D conversion is of oversampling type. Furthermore, a decision-aided iterative clipping distortion suppression method was shown to provide very promising performance in an OFDMA signal scenario. In general, it can be concluded that even strong nonlinear distortion, such as I/Q ADC clipping, can be suppressed to a certain extent by digital means. It is, however, a system-specific issue what is the most effective and practical method.

7.2 Further Development

The derived cascaded receiver nonlinearity model provides a good frame to include also other receiver impairments. This joint model could be then used for impairment mitigation. In general, it is an interesting topic to study further how the proposed distortion suppression methods perform when there are other dominating receiver impairments, e.g., phase noise.

The Fourier series based I/Q ADC clipping model is convenient for analyzing separately each distortion order the clipping is causing. Future research could consider how the model can be efficiently exploited in clipping distortion suppression. This could include, e.g., extracting information about the non-clipped signal envelope or clipping levels.

Since AIC has proven its versatility, it would definitely be interesting to develop it further. For instance, there exist vast amount of different nonlinearity models in the current literature of which feasibility could be evaluated from the AIC point of view. The real question is that is it possible to find more robust and more accurate nonlinearity models matching to the analog receiver hardware which would provide better distortion suppression performance without excessively increasing the computational complexity. Another interesting question is that what is the optimal spectrum sensing approach for providing information about blocker bandwidths and center frequencies needed for AIC band-split stage filtering. In this context, the optimality should be considered from the accuracy and computational complexity point of view. This study item could also include developing an algorithm for optimal automatic selection of nonlinearity modeling terms based on the spectrum sensing results and the previously found adaptive filters coefficients.

The decision-aided iterative clipping distortion suppression method requires accurate channel estimation which is challenging due to clipping. Further research is needed to determine an optimal channel estimation approach under unintentional I/Q ADC clipping. The iterative method was concluded to be effective for OFDMA scenarios, but in the future, also other scenarios could be considered.

In general, digital nonlinearity suppression methods have been shown to be very effective and typically outperforming purely analog implementations. However, if even better performance is desired, DSP should work in close cooperation with the analog receiver parts. The tasks that are challenging for analog circuits, should be performed in digital domain, but similarly also digitally challenging tasks may be feasible in analog domain. In practice, this leads to advanced digitally-controlled analog circuits. Naturally, this raises challenges in many levels, e.g., the analog and digital structures should be designed together due to the inherent interactions. However, this combination may provide synergies in the future that cannot be achieved by any other means, but it requires ultimate understanding from both, analog and digital, worlds.

References

[1] *LTE; Evolved Universal Terrestrial Radio Access (E-UTRA); Carrier aggregation enhancements; User Equipment (UE) and Base Station (BS) radio transmission and reception*, 3GPP TR 36.823 version 11.0.1 Release 11, Sep. 2013.

[2] *Digital cellular telecommunications system (Phase 2+); Radio transmission and reception*, 3GPP TS 45.005 version 11.4.0 Release 11, Jan. 2014.

[3] *LTE; Evolved Universal Terrestrial Radio Access (E-UTRA); Base Station (BS) radio transmission and reception*, 3GPP TS 36.104 version 11.7.0 Release 11, Jan. 2014.

[4] *Universal Mobile Telecommunications System (UMTS); Base Station (BS) radio transmission and reception (FDD)*, 3GPP TS 25.104 version 11.8.0 Release 11, Jan. 2014.

[5] T. Adali, H. Li, and R. Aloysius, "On properties of the widely linear MSE filter and its LMS implementation," in *Proceedings of the 43rd Annual Conference on Information Sciences and Systems (CISS2009)*, Baltimore, MD, Mar. 2009, pp. 876–881.

[6] R. AliHemmati, P. Azmi, and F. Marvasti, "Clipping noise cancellation in uplink MC-CDMA system using signal reconstruction from non-uniform samples," in *Proceedings of International Conference on Telecommunications (ICT2008)*, St. Petersburg, Russia, June 2008.

[7] Analog Devices, *The Data Conversion Handbook*, W. Kester, Ed. Burlington, MA: Newnes, 2005.

[8] Analog Devices, *AD9218 Data Sheet*, Rev. C, Dec. 2006. [Online]. Available: http://www.analog.com/media/en/technical-documentation/data-sheets/AD9218.pdf

[9] Analog Devices, *AD9418 Data Sheet*, Rev. B, Nov. 2010. [Online]. Available: http://www.analog.com/media/en/technical-documentation/data-sheets/AD9248.pdf

[10] L. Anttila, M. Valkama, and M. Renfors, "Circularity-based I/Q imbalance compensation in wideband direct-conversion receivers," *IEEE Transactions on Vehicular Technology*, vol. 57, no. 4, pp. 2099–2113, July 2008.

[11] L. Anttila, "Digital front-end signal processing with widely-linear signal models in radio devices," Ph.D. dissertation, Department of Communications Engineering, Tampere University of Technology, Tampere, Finland, 2011.

[12] E. Axell, G. Leus, E. G. Larsson, and H. V. Poor, "Spectrum sensing for cognitive radio: State-of-the-art and recent advances," *IEEE Signal Processing Magazine*, vol. 29, no. 3, pp. 101–116, May 2012.

[13] E. Balestrieri, P. Daponte, and S. Rapuano, "A state of the art on ADC error compensation methods," *IEEE Transactions on Instrumentation and Measurement*, vol. 54, no. 4, pp. 1388–1394, Aug. 2005.

[14] C. Berrou, A. Glavieux, and P. Thitimajshima, "Near Shannon limit error-correcting coding and decoding: Turbo-codes," in *Conference Record of IEEE International Conference on Communications (ICC1993)*, vol. 2, Geneva, Switzerland, May 1993, pp. 1064–1070.

[15] N. Björsell, "Modeling analog to digital converters at radio frequency," Ph.D. dissertation, School of electrical Engineering, KTH, Stockholm, Sweden, 2007.

[16] N. Björsell and P. Händel, "Dynamic behavior models of analog to digital converters aimed for post-correction in wideband applications," in *Proceedings of XVIII IMEKO World Congress 11th Workshop on ADC Modelling and Testing*, Rio de Janeiro, Brazil, Sep. 2006.

[17] B. Brannon and T. MacLeod, "How ADIsimADC models an ADC," Analog Devices, Application Note AN-737, Rev. B, 2009. [Online]. Available: http://www.analog.com/media/en/technical-documentation/application-notes/AN_737.pdf

[18] J. J. Bussgang, "Crosscorrelation functions of amplitude-distorted gaussian signals," MIT Research Laboratory of Electronics, Technical Report 216, Mar. 1952.

[19] A. B. Carlson, P. B. Crilly, and J. C. Rutledge, *Communication Systems: An Introduction to Signals and Noise in Electrical Communication*, 4th ed. New York, NY: McGraw-Hill, 2002.

[20] W. J. Chappell, E. J. Naglich, C. Maxey, and A. C. Guyette, "Putting the radio in 'software-defined radio': Hardware developments for adaptable RF systems," *Proceedings of the IEEE*, vol. 102, no. 3, pp. 307–320, Mar. 2014.

[21] L. Cheded, "Invariance property of gaussian signals: A new interpretation, extension and applications," *Circuits, Systems and Signal Processing*, vol. 16, no. 5, pp. 523–536, Sep. 1997.

[22] H. Chen and A. M. Haimovich, "Iterative estimation and cancellation of clipping noise for OFDM signals," *IEEE Communications Letters*, vol. 7, no. 7, pp. 305–307, July 2003.

[23] H.-H. Chen, P.-C. Huang, C.-K. Wen, and J.-T. Chen, "Adaptive compensation of even-order distortion in direct conversion receivers," in *Proceedings of IEEE 58th Vehicular Technology Conference (VTC2003-Fall)*, vol. 1, Orlando, FL, Oct. 2003, pp. 271–274.

[24] J. E. Chen, *Modeling RF Systems*, The Designer's Guide Community, Nov. 2011. [Online]. Available: http://www.designers-guide.org/Modeling/modeling-rf-systems.pdf

[25] P. Cruz and N. B. Carvalho, "PAPR evaluation in multi-mode SDR transceivers," in *Proceedings of the 38th European Microwave Conference (EuMC2008)*, Amsterdam, The Netherlands, Oct. 2008, pp. 1354–1357.

[26] P. Cruz, N. B. Carvalho, and K. A. Remley, "Designing and testing software-defined radios," *IEEE Microwave Magazine*, vol. 11, no. 4, pp. 83–94, June 2010.

[27] H. Darabi, "A blocker filtering technique for SAW-less wireless receivers," *IEEE Journal of Solid-State Circuits*, vol. 42, no. 12, pp. 2766–2773, Dec. 2007.

[28] H. Darabi, D. Murphy, M. Mikhemar, and A. Mirzaei, "Blocker tolerant software defined receivers," in *Proceedings of the 40th European Solid State Circuit Conference (ESSCIRC2014)*, Venice Lido, Italy, Sep. 2014, pp. 35–42.

[29] D. Dardari, "Joint clip and quantization effects characterization in OFDM receivers," *IEEE Transactions on Circuits and Systems I: Regular Papers*, vol. 53, no. 8, pp. 1741–1748, Aug. 2006.

[30] D. Divsalar and F. Pollara, "Turbo codes for PCS applications," in *Proceedings of IEEE International Conference on Communications (ICC1995)*, vol. 1, Seattle, WA, June 1995, pp. 54–59.

[31] K. Doğançay, "Blind compensation of nonlinear distortion for bandlimited signals," *IEEE Transactions on Circuits and Systems I: Regular Papers*, vol. 52, no. 9, pp. 1872–1882, Sep. 2005.

[32] K. Dufrêne and R. Weigel, "Adaptive IP2 calibration scheme for direct-conversion receivers," in *Proceedings of IEEE Radio and Wireless Symposium (RWS2006)*, San Diego, CA, Jan. 2006, pp. 111–114.

[33] Ettus Research, *WBX 50–2200 MHz Rx/Tx (40 MHz) RF Daughterboard for USRP*. [Online]. Available: http://www.ettus.com/product/details/WBX/

[34] Ettus Research, *USRP N200/N210 Networked Series Data Sheet*, Sep. 2012. [Online]. Available: http://www.ettus.com/content/files/07495_Ettus_N200-210_DS_Flyer_HR_1.pdf

[35] M. Faulkner, "DC offset and IM2 removal in direct conversion receivers," *IEE Proceedings – Communications*, vol. 149, no. 3, pp. 179–184, June 2002.

[36] A. B. Flores, R. E. Guerra, E. W. Knightly, P. Ecclesine, and S. Pandey, "IEEE 802.11af: a standard for TV white space spectrum sharing," *IEEE Communications Magazine*, vol. 51, no. 10, pp. 92–100, Oct. 2013.

[37] R. M. Gray and D. L. Neuhoff, "Quantization," *IEEE Transactions on Information Theory*, vol. 44, no. 6, pp. 2325–2383, Oct. 1998.

[38] M. Grimm, "Dirty RF signal processing for mitigation of receiver front-end non-linearity," Ph.D. dissertation, Electronic Measurement Research Lab, Ilmenau University of Technology, Ilmenau, Germany, 2014.

[39] M. Grimm, R. K. Sharma, M. Hein, and R. Thomä, "DSP-based mitigation of RF front-end non-linearity in cognitive wideband receivers," *Frequenz*, vol. 66, no. 9–10, pp. 303–310, Sep. 2012.

[40] M. Grimm, R. K. Sharma, M. Hein, R. Thomä, and R. Zemmari, "Improved BER performance in GSM by mitigating non-linear distortions in the receiver," in *Proceedings of the 43rd European Microwave Conference (EuMC2013)*, Nuremberg, Germany, Oct. 2013, pp. 565–568.

[41] J. Guerreiro, R. Dinis, and P. Montezuma, "On the optimum multicarrier performance with memoryless nonlinearities," *IEEE Transactions on Communications*, vol. 63, no. 2, pp. 498–509, Feb. 2015.

[42] H. Habibi, E. J. G. Janssen, Y. Wu, P. G. M. Baltus, and J. W. M. Bergmans, "Analysis of an adaptive nonlinear interference suppressor for wireless multimode transceivers," *IEEE Transactions on Vehicular Technology*, vol. 64, no. 3, pp. 926–941, Mar. 2015.

[43] P. Händel, N. Björsell, and M. Jansson, "Model based dynamic characterization of analog-digital-converters at radio frequency," in *Proceedings of the 9th International*

Symposium on Signal Processing and Its Applications (ISSPA2007), Sharjah, United Arab Emirates, Feb. 2007.

[44] f. j. harris, *Multirate Signal Processing for Communication Systems*. Upper Saddle river, NJ: Prentice Hall PTR, 2004.

[45] S. Haykin, *Adaptive Filter Theory*, 4th ed. Upper Saddle river, NJ: Prentice Hall, 2002.

[46] HD Communications, *HD24089 500–6000MHz Low Noise Amplifier*. [Online]. Available: http://www.rfcomp.com/download/product_specs/low_noise/HD24089specs.pdf

[47] C. L. Heng and W. Y. Ali-Ahmad, "Non-linearity requirements for UMTS and DVB RF receivers with higher blocking margins," in *Proceedings of IEEE International Workshop on Radio-Frequency Integration Technology (RFIT2007)*, Singapore, Dec. 2007, pp. 131–134.

[48] F. Horlin and A. Bourdoux, *Digital Compensation for Analog Front-Ends: A New Approach to Wireless Transceiver Design*. Chichester, England: Wiley, 2008.

[49] M. Höyhtyä, M. Matinmikko, X. Chen, J. Hallio, J. Auranen, R. Ekman, J. Röning, J. Engelberg, J. Kalliovaara, T. Taher, A. Riaz, and D. Roberson, "Measurements and analysis of spectrum occupancy in the 2.3–2.4 GHz band in Finland and Chicago," in *Proceedings of the 9th International Conference on Cognitive Radio Oriented Wireless Networks and Communications (CROWNCOM2014)*, Oulu, Finland, June 2014.

[50] *IEEE Standard for Terminology and Test Methods for Analog-to-Digital Converters*, IEEE Std 1241-2010 (Revision of IEEE Std 1241-2000), Jan. 2011.

[51] *Standard for Local and metropolitan area networks – Specific requirements – Part 22: Cognitive Wireless RAN Medium Access Control (MAC) and Physical Layer (PHY) specifications: Policies and procedures for operation in the TV Bands*, IEEE Std 802.22-2011, June 2011.

[52] E. C. Ifeachor and B. W. Jervis, *Digital Signal Processing: A Practical Approach*, 2nd ed. Harlow, England: Prentice Hall, 2002.

[53] T. Jiang and Y. Wu, "An overview: Peak-to-average power ratio reduction techniques for OFDM signals," *IEEE Transactions on Broadcasting*, vol. 54, no. 2, pp. 257–268, June 2008.

[54] D. A. Johns and K. W. Martin, *Analog Integrated Circuit Design*. Wiley, 1997.

[55] B. E. Jonsson, "A survey of A/D-converter performance evolution," in *Proceedings of the 17th IEEE International Conference on Electronics, Circuits, and Systems (ICECS2010)*, Athens, Greece, Dec. 2010, pp. 766–769.

[56] J. L. Karki, "Designing for low distortion with high-speed op amps," *Texas Instruments Analog Applications Journal*, pp. 25–33, July 2001. [Online]. Available: http://www.ti.com/lit/an/slyt133/slyt133.pdf

[57] J. L. Karki, "Calculating noise figure and third-order intercept in ADCs," *Texas Instruments Analog Applications Journal*, pp. 11–15, July 2003. [Online]. Available: http://www.ti.com/lit/an/slyt090/slyt090.pdf

[58] E. A. Keehr and A. Hajimiri, "Equalization of third-order intermodulation products in wideband direct conversion receivers," *IEEE Journal of Solid-State Circuits*, vol. 43, no. 12, pp. 2853–2867, Dec. 2008.

[59] E. A. Keehr and A. Hajimiri, "Digitally assisted equalization of third-order intermodulation products in wideband direct conversion receivers," *International Journal of Microwave and Wireless Technologies*, vol. 1, no. 4, pp. 377–385, Aug. 2009.

[60] E. A. Keehr and A. Hajimiri, "Successive regeneration and adaptive cancellation of higher order intermodulation products in RF receivers," *IEEE Transactions on Microwave Theory and Techniques*, vol. 59, no. 5, pp. 1379–1396, May 2011.

[61] P. B. Kenington, *High-Linearity RF Amplifier Design*. Norwood, MA: Artech House, 2000.

[62] P. B. Kenington, *RF and Baseband Techniques for Sofware Defined Radio*. Norwood, MA: Artech House, 2005.

[63] W. Kester, "Aperture time, aperture jitter, aperture delay time—removing the confusion," Analog Devices, Tutorial MT-007, Rev. A, Oct. 2008. [Online]. Available: http://www.analog.com/media/en/training-seminars/tutorials/MT-007.pdf

[64] M. Kitsunezuka, K. Kunihiro, and M. Fukaishi, "Efficient use of the spectrum," *IEEE Microwave Magazine*, vol. 13, no. 1, pp. 55–63, Jan./Feb. 2012.

[65] Z. Kollár, L. Varga, B. Horváth, P. Bakki, and J. Bitó, "Evaluation of clipping based iterative PAPR reduction techniques for FBMC systems," *The Scientific World Journal*, vol. 2014, Jan. 2014.

[66] D. Korpi, L. Anttila, V. Syrjälä, and M. Valkama, "Widely linear digital self-interference cancellation in direct-conversion full-duplex transceiver," *IEEE Journal on Selected Areas in Communications*, vol. 32, no. 9, pp. 1674–1687, Sep. 2014.

[67] D. Korpi, T. Riihonen, V. Syrjälä, L. Anttila, M. Valkama, and R. Wichman, "Full-duplex transceiver system calculations: Analysis of ADC and linearity challenges," *IEEE Transactions on Wireless Communications*, vol. 13, no. 7, pp. 3821–3836, July 2014.

[68] R. Kumar, D. Taggart, and G. Goo, "Performance analysis of analog-to-digital converters for wideband digitally modulated signals," in *Proceedings of IEEE Aerospace Conference 2004*, vol. 2, Big Sky, MT, Mar. 2004, pp. 1375–1382.

[69] P. Landin, "Digital baseband modeling and correction of radio frequency power amplifiers," Ph.D. dissertation, School of Electrical Engineering, KTH, Stockholm, Sweden, 2012.

[70] B. Le, T. W. Rondeau, J. H. Reed, and C. W. Bostian, "Analog-to-digital converters," *IEEE Signal Processing Magazine*, vol. 22, no. 6, pp. 69–77, Nov. 2005.

[71] Y.-C. Liang, K.-C. Chen, G. Y. Li, and P. Mähönen, "Cognitive radio networking and communications: An overview," *IEEE Transactions on Vehicular Technology*, vol. 60, no. 7, pp. 3386–3407, Sep. 2011.

[72] H. F. Lundin, "Characterization and correction of analog-to-digital converters," Ph.D. dissertation, School of electrical Engineering, KTH, Stockholm, Sweden, 2005.

[73] Y. Ma and Y. Yamao, "Blind nonlinear compensation technique for RF receiver front-end," in *Proceedings of the 43rd European Microwave Conference (EuMC2013)*, Nuremberg, Germany, Oct. 2013, pp. 1527–1530.

[74] D. H. Mahrof, E. A. M. Klumperink, J. C. Haartsen, and B. Nauta, "On the effect of spectral location of interferers on linearity requirements for wideband cognitive radio receivers," in *Proceedings of IEEE Symposium on New Frontiers in Dynamic Spectrum (DySPAN2010)*, Singapore, Apr. 2010.

[75] P.-I. Mak, S.-P. U, and R. P. Martins, "Transceiver architecture selection: Review, state-of-the-art survey and case study," *IEEE Circuits and Systems Magazine*, vol. 7, no. 2, pp. 6–25, Second Quarter 2007.

[76] F. Maloberti, *Data Converters*. Dordrecht, The Netherlands: Springer, 2007.

[77] P. F. Marshall, "Cognitive radio as a mechanism to manage front-end linearity and dynamic range," *IEEE Communications Magazine*, vol. 47, no. 3, pp. 81–87, Mar. 2009.

[78] J. Marttila, "Quadrature sigma-delta modulators for reconfigurable A/D interface and dynamic spectrum access: Analysis, design principles and digital post-processing," Ph.D. dissertation, Department of Electronics and Communications Engineering, Tampere University of Technology, Tampere, Finland, 2014.

[79] F. Marvasti, Ed., *Nonuniform Sampling: Theory and Practice*. New York, NY: Kluwer Academic / Plenum Publishers, 2001.

[80] S. Medawar, P. Händel, B. Murmann, N. Björsell, and M. Jansson, "Dynamic calibration of undersampled pipelined ADCs by frequency domain filtering," *IEEE Transactions on Instrumentation and Measurement*, vol. 62, no. 7, pp. 1882–1891, July 2013.

[81] L. Michaeli, P. Michalko, and J. Šaliga, "Unified ADC nonlinearity error model for SAR ADC," *Measurement*, vol. 41, no. 2, pp. 198–204, Feb. 2008.

[82] D. R. Morgan, Z. Ma, J. Kim, M. G. Zierdt, and J. Pastalan, "A generalized memory polynomial model for digital predistortion of RF power amplifiers," *IEEE Transactions on Signal Processing*, vol. 54, no. 10, pp. 3852–3860, Oct. 2006.

[83] M. Mustonen, M. Matinmikko, D. Roberson, and S. Yrjölä, "Evaluation of recent spectrum sharing models from the regulatory point of view," in *Proceedings of the 1st International Conference on 5G for Ubiquitous Connectivity (5GU2014)*, Levi, Finland, Nov. 2014, pp. 11–16.

[84] National Instruments, *NI PXIe-5645R Device Specifications*, May 2015. [Online]. Available: http://www.ni.com/pdf/manuals/373914c.pdf

[85] F. G. A. Neto, V. H. Nascimento, and M. T. M. Silva, "Reduced-complexity widely linear adaptive estimation," in *Proceedings of the 7th International Symposium on Wireless Communication Systems (ISWCS2010)*, York, United Kingdom, Sep. 2010, pp. 399–403.

[86] H. Ochiai and H. Imai, "Performance of the deliberate clipping with adaptive symbol selection for strictly band-limited OFDM systems," *IEEE Journal on Selected Areas in Communications*, vol. 18, no. 11, pp. 2270–2277, Nov. 2000.

[87] H. Ochiai and H. Imai, "Performance analysis of deliberately clipped OFDM signals," *IEEE Transactions on Communications*, vol. 50, no. 1, pp. 89–101, Jan. 2002.

[88] H. Pan and A. A. Abidi, "Spectral spurs due to quantization in nyquist ADCs," *IEEE Transactions on Circuits and Systems I: Regular Papers*, vol. 51, no. 8, pp. 1422–1439, Aug. 2004.

[89] B. Razavi, "Design considerations for direct-conversion receivers," *IEEE Transactions on Circuits and Systems II: Analog and Digital Signal Processing*, vol. 44, no. 6, pp. 428–435, June 1997.

[90] B. Razavi, "Cognitive radio design challenges and techniques," *IEEE Journal of Solid-State Circuits*, vol. 45, no. 8, pp. 1542–1553, Aug. 2010.

[91] B. Razavi, *Principles of Data Conversion System Design*. New York, NY: Wiley-IEEE Press, 1995.

[92] B. Razavi, *RF Microelectronics*, 2nd ed. Upper Saddle River, NJ: Pearson, 2012.

[93] E. Rebeiz and D. Cabric, "How wideband receiver nonlinearities impact spectrum sensing," in *Proceedings of IEEE Global Conference on Signal and Information Processing (GlobalSIP2013)*, Austin, TX, Dec. 2013, pp. 1178–1181.

[94] E. Rebeiz, A. Shahed hagh ghadam, M. Valkama, and D. Cabric, "Suppressing RF front-end nonlinearities in wideband spectrum sensing," in *Proceedings of the 8th International Conference on Cognitive Radio Oriented Wireless Networks (CROWNCOM2013)*, Washington, DC, July 2013, pp. 87–92.

[95] E. Rebeiz, A. Shahed hagh ghadam, M. Valkama, and D. Cabric, "Spectrum sensing under RF non-linearities: Performance analysis and DSP-enhanced receivers," *IEEE Transactions on Signal Processing*, vol. 63, no. 8, pp. 1950–1964, Apr. 2015.

[96] M. A. Richards, J. A. Scheer, and W. A. Holm, Eds., *Principles of Modern Radar: Basic Principles*. Raleigh, NC: SciTech Publishing, 2010.

[97] R. Rietman and J.-P. Linnartz, "Peak restoration in OFDM receiver with clipping A/D converter," *IEEE Transactions on Wireless Communications*, vol. 7, no. 12, pp. 5177–5181, Dec. 2008.

[98] P. Robertson, E. Villebrun, and P. Hoeher, "A comparison of optimal and sub-optimal MAP decoding algorithms operating in the log domain," in *Proceedings of IEEE International Conference on Communications (ICC1995)*, vol. 2, Seattle, WA, June 1995, pp. 1009–1013.

[99] Rohde & Schwarz, *R&S AFQ100A I/Q Modulation Generator Specifications*, Ver. 03.01, Jan. 2014. [Online]. Available: http://cdn.rohde-schwarz.com/pws/dl_downloads/dl_common_library/dl_brochures_and_datasheets/pdf_1/AFQ100A_AFQ100B_dat_sw_en_5214-0799-22_v0301.pdf

[100] H. E. Rowe, "Memoryless nonlinearities with gaussian inputs: Elementary results," *The Bell System Technical Journal*, vol. 61, no. 7, pp. 1519–1525, Sep. 1982.

[101] Z. Ru, N. A. Moseley, E. A. M. Klumperink, and B. Nauta, "Digitally enhanced software-defined radio receiver robust to out-of-band interference," *IEEE Journal of Solid-State Circuits*, vol. 44, no. 12, pp. 3359–3375, Dec. 2009.

[102] M. Santos, N. Horta, and J. Guilherme, "A survey on nonlinear analog-to-digital converters," *Integration, the VLSI Journal*, vol. 47, no. 1, pp. 12–22, Jan. 2014.

[103] R. Schreier and G. C. Temes, *Understanding Delta-Sigma Data Converters*. Hoboken, NJ: Wiley-IEEE Press, 2005.

[104] L. Sendrei, S. Marchevský, N. Michailow, and G. Fettweis, "Iterative receiver for clipped GFDM signals," in *Proceedings of the 24th International Conference Radioelektronika (RADIOELEKTRONIKA2014)*, Bratislava, Slovak Republic, Apr. 2014.

[105] A. Shahed hagh ghadam, "Contributions to analysis and DSP-based mitigation of nonlinear distortion in radio transceivers," Ph.D. dissertation, Department of Communications Engineering, Tampere University of Technology, Tampere, Finland, 2011.

[106] A. Shahed hagh ghadam, M. Valkama, and M. Renfors, "Adaptive compensation of nonlinear distortion in multicarrier direct-conversion receivers," in *Proceedings of IEEE Radio and Wireless Conference (RAWCON2004)*, Atlanta, GA, Sep. 2004, pp. 35–38.

[107] T. B. Sørensen, P. E. Mogensen, and F. Frederiksen, "Extension of the ITU channel models for wideband (OFDM) systems," in *Proceedings of IEEE 62nd Vehicular Technology Conference (VTC2005-Fall)*, vol. 1, Dallas, TX, Sep. 2005, pp. 392–396.

[108] A. E. Spezio, "Electronic warfare systems," *IEEE Transactions on Microwave Theory and Techniques*, vol. 50, no. 3, pp. 633–644, Mar. 2002.

[109] J. Šterba, J. Gazda, M. Deumal, and D. Kocur, "Iterative algorithm for nonlinear noise cancellation and channel re-estimation in nonlinearly distorted OFDM system," in *Proceedings of IEEE 8th International Symposium on Applied Machine Intelligence and Informatics (SAMI2010)*, Herl'any, Slovakia, Jan. 2010, pp. 65–70.

[110] C. Svensson, "The blocker challenge when implementing software defined radio receiver RF frontends," *Analog Integrated Circuits and Signal Processing*, vol. 64, no. 2, pp. 81–89, Aug. 2010.

[111] D. Taggart, R. Kumar, Y. Krikorian, G. Goo, J. Chen, R. Martinez, T. Tam, and E. Serhal, "Analog-to-digital converter loading analysis considerations for satellite communications systems," in *IEEE Aerospace Conference (IEEEAC2007)*, Big Sky, MT, Mar. 2007.

[112] S.-K. Ting and A. H. Sayed, "Mitigation of clipping in sensors," in *Proceedings of IEEE International Conference on Acoustics, Speech, and Signal Processing (ICASSP2013)*, Vancouver, Canada, May 2013, pp. 5934–5938.

[113] T. Tomioka, R. Sakata, T. Horiguchi, T. Tomizawa, and K. Inoue, "A/D converter clipping noise suppression for high-sensitivity carrier-sensing of cognitive radio transceiver," in *Proceedings of IEEE Global Telecommunications Conference (GLOBECOM2007)*, Washington, DC, Nov. 2007, pp. 4170–4174.

[114] M. Valkama, A. Shahed hagh ghadam, L. Anttila, and M. Renfors, "Advanced digital signal processing techniques for compensation of nonlinear distortion in wideband multicarrier radio receivers," *IEEE Transactions on Microwave Theory and Techniques*, vol. 54, no. 6, pp. 2356–2366, June 2006.

[115] G. Vallant, M. Allén, S. Singh, M. Epp, S. Chartier, and M. Valkama, "Direct downconversion architecture performance in compact pulse-doppler phased array radar receivers," in *Proceedings of IEEE 13th Topical Meeting on Silicon Monolithic Integrated Circuits in RF Systems (SiRF2013)*, Austin, TX, Jan. 2013, pp. 102–104.

[116] G. Vallant, M. Epp, M. Allén, M. Valkama, and F. K. Jondral, "System-level mitigation of undersampling ADC nonlinearity for high-IF radio receivers," *Frequenz*, vol. 66, no. 9–10, pp. 311–319, Sep. 2012.

[117] S. Wang, V. Maheshwari, and W. A. Serdijn, "Instantaneously companding baseband SC low-pass filter and ADC for 802.11a/g WLAN receiver," in *Proceedings of IEEE International Symposium on Circuits and Systems (ISCAS2010)*, Paris, France, May 2010, pp. 2215–2218.

[118] W. D. Wellisch, I. A. Ulian, and A. N. Barreto, "Iterative correction of clipped OFDM signals with unknown clipping levels," in *Proceedings of IEEE 77th Vehicular Technology Conference (VTC2013-Spring)*, Dresden, Germany, June 2013.

[119] S. Winder, *Analog and Digital Filter Design*, 2nd ed. Burlington, MA: Newnes, 2002.

[120] J. Yang, R. W. Brodersen, and D. Tse, "Addressing the dynamic range problem in cognitive radios," in *Proceedings of IEEE International Conference on Communications (ICC2007)*, Glasgow, Scotland, June 2007, pp. 5183–5188.

[121] T. Yücek and H. Arslan, "A survey of spectrum sensing algorithms for cognitive radio applications," *IEEE Communications Surveys & Tutorials*, vol. 11, no. 1, pp. 116–130, First Quarter 2009.

[122] Y. Zeng, Y.-C. Liang, A. T. Hoang, and R. Zhang, "A review on spectrum sensing for cognitive radio: Challenges and solutions," *EURASIP Journal on Advances in Signal Processing*, vol. 2010, Jan. 2010.

[123] H. Zhang, X.-G. Xia, Q. Zhang, and W. Zhu, "Iterative decision-aided clipping compensation and its application to scalable video transmission with multiband OFDM," *IEEE Transactions on Vehicular Technology*, vol. 56, no. 2, pp. 756–765, Mar. 2007.

[124] Q. Zou, M. Mikhemar, and A. H. Sayed, "Digital compensation of cross-modulation distortion in software-defined radios," *IEEE Journal of Selected Topics in Signal Processing*, vol. 3, no. 3, pp. 348–361, June 2009.

[125] D. Zwillinger, Ed., *CRC Standard Mathematical Tables and Formulae*, 32nd ed. Boca Raton, FL: CRC Press, 2012.

Publications

Publication 1

M. Allén, J. Marttila, and M. Valkama, "Digital post-processing for reducing A/D converter nonlinear distortion in wideband radio receivers," in *Conference Record of the 43th Asilomar Conference on Signals, Systems and Computers (Asilomar2009)*, Pacific Grove, CA, USA, Nov. 2009, pp. 1111–1114. DOI: 10.1109/ACSSC.2009.5470052

© 2009 IEEE. Reprinted, with permission, from the Conference Record of the 43th Asilomar Conference on Signals, Systems and Computers (Asilomar2009).

In reference to IEEE copyrighted material which is used with permission in this thesis, the IEEE does not endorse any of Tampere University of Technology's products or services. Internal or personal use of this material is permitted. If interested in reprinting/republishing IEEE copyrighted material for advertising or promotional purposes or for creating new collective works for resale or redistribution, please go to http://www.ieee.org/publications_standards/publications/rights/rights_link.html to learn how to obtain a License from RightsLink.

Digital Post-Processing for Reducing A/D Converter Nonlinear Distortion in Wideband Radio Receivers

Markus Allén, Jaakko Marttila and Mikko Valkama
Department of Communications Engineering
Tampere University of Technology
P.O. Box 553, FI-33101, Tampere, FINLAND
markus.allen@tut.fi, jaakko.marttila@tut.fi, mikko.e.valkama@tut.fi

***Abstract*—This article addresses the reduction of analog-to-digital (A/D) converter nonlinearities in radio receivers using digital signal processing (DSP). The main focus is on wideband A/D conversion where a collection of different waveforms at different frequency channels is digitized as a whole. The overall dynamic range in such composite signal can easily be in the order of tens of dB's, especially in the emerging cognitive radio type developments, and the nonlinear distortion due to strong carriers can easily block the weaker signal bands. In this article, DSP-based post-processing is proposed and demonstrated for reducing the effects of A/D converter integral nonlinearities (INL), stemming from unintentional deviations in the quantization intervals, as well as clipping due to improper input conditioning in wideband radio receiver context.**

Keywords-A/D converter; radio receiver; nonlinear distortion; integral nonlinearity; clipping; interference cancellation

I. INTRODUCTION

One of the main trends in designing and implementing radio transmitters and receivers for different wireless systems is to implement more and more of the transceiver functionalities using DSP [1]. In such transceiver implementations, especially on the receiver side, the performance of the A/D interface can easily become of a limiting factor to the whole receiver performance, particularly in cases where the dynamic range of the digitized waveform is high [2]-[5]. One fundamental issue is the inherent trade-off between resolution (number of bits) and speed (sampling rate), which is fairly well understood in the existing literature [6]-[8]. Other important issues in radio receiver context are signal distortion due to sampling jitter and A/D converter nonlinearities [2]-[8].

In this article, we focus on the A/D converter nonlinearity aspects. This is becoming an increasingly important issue in the emerging wireless systems, like IMT-Advanced [9], in which the spectrum allocation of individual terminals can be strongly scattered over a wide range of frequencies. In such cases, and also in more traditional radio systems in which most of the selectivity filtering in the terminal is implemented using DSP, the dynamic range of the digitized signal can be tens of dB's (even 50-60 dB). Similar or even more challenging input conditions are also expected in the emerging cognitive radio type developments where the available spectrum chunks can be heavily scattered over several hundreds of MHz total bandwidth. In this kind of scenarios, any nonlinearities in the A/D converter can cause severe intermodulation distortion (IMD) due to strong incoming signals which can easily block the weak desired signal bands [3]-[5]. Practical sources of nonlinearities in A/D converters are, e.g., integral and differential nonlinearity (INL and DNL) stemming from the unintentional deviations in the consecutive quantization levels, and clipping type distortion due to improper input signal conditioning (crossing the converter full scale voltage range).

Correction of A/D converter nonidealities has generally been studied rather widely in the literature, see, e.g., [2], [6], [10] and the references therein. Typical post-processing solutions are based on either look-up table methods or black-box modeling and identification type approaches. Most of these methods require specific off-line calibration signals and are thus mainly designed for measurement and instrumentation purposes in which the operating environment is typically very stable. On the radio terminal side, on the other hand, the operating conditions of the used electronics components as well as also the received waveform characteristics can both be easily heavily time-varying, implying that off-line calibration based approaches are not directly applicable. In this article, building on proper nonlinearity modeling, on-line DSP-based post-processing for reducing the intermodulation distortion in wideband A/D converters is proposed. Adaptive filtering based approach utilizing adaptive interference cancellation (AIC) is deployed and demonstrated to be able to considerably reduce the effects of INL and clipping at the weak desired signal bands in wideband radios. Compared to the existing literature, the proposed approach has the benefit of being able to tune the correction capabilities on a received packet-by-packet basis to the most sensitive (weak) parts of the received spectrum. This is seen very critical in the emerging future cognitive radio type developments.

II. A/D CONVERTER NONLINEARITIES IN RADIOS

In an ideal quantizer, based on the number of bits B, the overall full scale (FS) voltage range of the converter is uniformly divided into quantization levels. This is illustrated in Fig. 1. One source of nonlinear distortion, other than ordinary

This work was supported by the Academy of Finland (under the project "Understanding and Mitigation of Analog RF Impairments in Multiantenna Transmission Systems"), the Finnish Funding Agency for Technology and Innovation (Tekes, under the project "Advanced Techniques for RF Impairment Mitigation in Future Wireless Radio Systems") and the Technology Industries of Finland Centennial Foundation.

uniform quantization noise, is then coming from *unintentional deviations of the quantization levels* from the nominal ones [6], [10], [13]. This can be further divided into differential nonlinearity (DNL) and integral nonlinearity (INL). DNL refers to the differences in the actual codewidths (relative to ideal codewidth) while INL refers to the corresponding differences in consecutive quantization thresholds. Mathematically these are given by [6], [13]

$$DNL(k) = \frac{Q_{true}(k) - Q}{Q} \tag{1}$$

and

$$INL(k) = \frac{T_{true}(k) - T(k)}{Q} \tag{2}$$

where Q denotes the nominal quantization step (code width), k is the output code index and $T(k)$ denotes the nominal quantization threshold for code k. While DNL characteristics from output code to another can be typically fairly random, the INL behavior can have more deterministic shape [6], [10]. An example of typical INL as a function of the converter output code is given in Fig. 2.

Another clear source of nonlinear distortion is related to the *input signal conditioning* of the incoming signal relative to the converter full scale voltage FS. Any input dynamics exceeding the FS voltage range will essentially be *clipped* by the quantizer, i.e.,

$$k = \begin{cases} 0 & \forall x_{\mathrm{IN}} \le Q/2 \\ 2^{B-1} & \forall x_{\mathrm{IN}} > x_{\mathrm{FS}} - 3Q/2 \end{cases} \tag{3}$$

where x_{IN} denotes the converter input voltage and a FS voltage range of $0 \ldots x_{FS}$ is assumed. This is also illustrated in Fig. 1.

In radio receivers, both DNL and INL as well as clipping will cause intermodulation distortion [3], [6], [7], [11]. The dominant part of such distortion or spurious components is stemming from the deterministic INL behavior and also from possible clipping. Here both of these are essentially modeled using polynomial modeling of the form

$$\begin{aligned} x'_{\mathrm{IN}} &= g(x_{\mathrm{IN}}) \\ &= a_0 + a_1 x_{\mathrm{IN}} + a_2 x_{\mathrm{IN}}^2 + a_3 x_{\mathrm{IN}}^3 + \ldots \end{aligned} \tag{4}$$

which is then followed by an ideal quantizer. This is illustrated in Fig. 3 and is a fairly established modeling approach in the literature, see, e.g., [6], [10]-[12]. Typically the 2nd, 3rd, 5th and 7th order components are the most dominant ones. In case of clipping, fixed-order polynomial approximations (with odd orders) apply only within a given finite input dynamics [11]. For more details on clipping modeling with bandpass signals, refer to [14].

III. Digital Post-Processing

In this Section, stemming partially from the earlier studies related to receiver mixer and low noise amplifier (LNA) nonlinearities in [15] and [16], an adaptive interference cancellation based post-processing method is proposed for removing the intermodulation distortion due to A/D converter nonlinearities from the weak signal bands. A conceptual block-diagram is given in Fig. 4. First band-split filtering is applied to a block of digitized samples such that the most sensitive (weak) signal bands are isolated from the rest of the sampled signal spectrum (including the strong blocking signals). Then, for a given weak signal band, the interfering IMD frequencies are regenerated using polynomial signal processing and filtered using an adaptive filter whose output(s) are subtracted from the weak signal band. The coefficients of the adaptive filter stage are

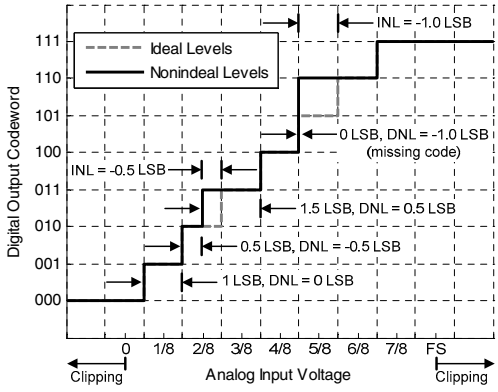

Fig. 1. Principal illustration of ideal and nonideal quantization with $B = 3$ bits. Both differential and integral nonlinearities (DNL, INL) as well as clipping are shown.

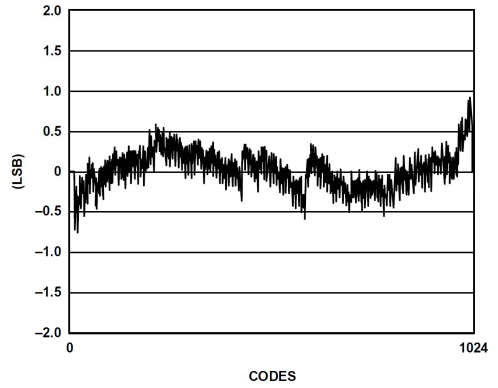

Fig. 2. Measured INL characteristics of 10-bit A/D converter AD9218 [17] as a function of output code k.

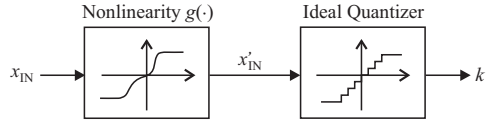

Fig. 3. Modeling A/D converter nonlinearities as a cascade of a memoryless polynomial followed by an ideal quantizer.

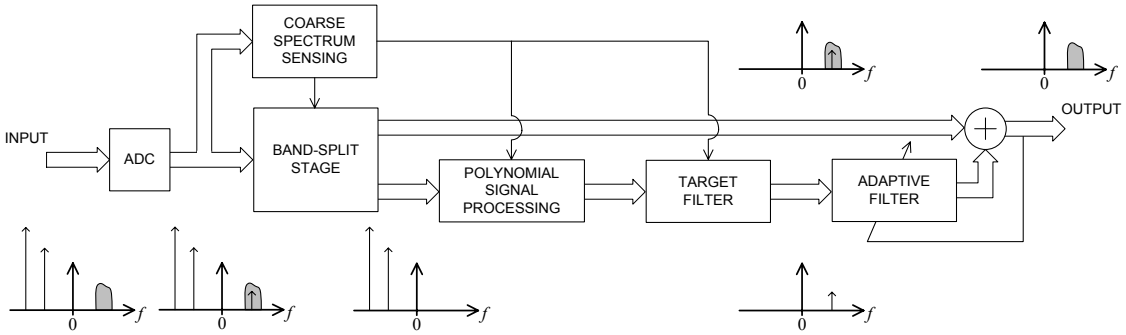

Fig. 4. Adaptive interference cancellation based digital post-processing scheme to reduce A/D converter nonlinear distortion at a weak signal band originating from strong blocking signals. In above, only a single IMD frequency is depicted on top of the weak signal for illustration purposes.

controlled such that the interference power at the weak signal band is minimized. The characteristics of the polynomial signal processing block, in turn, depend directly on the order of the IMD components being cancelled. In practice, different order IMD components can be processed either in parallel or serial manner, depending on the amount of computational resources, each having its own adaptive filter coefficients.

The overall coefficient adaptation, degrees of IMD being cancelled as well as the design of the band-split filtering stage can be controlled on a received packet-by-packet basis using an outer-loop control mechanism. This can be done based on coarse measurements of the spectrum density of the received packet using, e.g., FFT. Based on this spectrum sensing, the band-split filter characteristics are first tuned to isolate the most sensitive signal bands. Furthermore sensing the locations of the strongest signal energy levels (relative to the weak bands) gives the basis for choosing the IMD orders being cancelled. After this outer loop processing, the actual adaptive filter coefficients are controlled using e.g. the well-known least-mean-square (LMS) algorithm to minimize the IMD power at the overall output signal. These will be demonstrated in the following.

IV. Examples and Obtained Results

In this Section, practical examples are given to demonstrate the applicability of the proposed post-processing concept. Both INL as well as clipping effects are demonstrated and commercially available A/D converters are used in the experiments, covering both simulated as well as measured data.

A. Simulation Experiment for INL Reduction

Here a 10-bit off-the-shelf A/D converter [17] is experimented whose INL characteristics are shown in Fig. 2. An example received waveform consisting of 5 frequency channels with different channel bandwidths and power levels is deployed whose spectrum is illustrated in Fig. 5. The overall dynamic range in this experiment is in the order of 60 dB. The A/D converter sampling frequency is 32 MHz (both I and Q rails) and a converter model [18] provided by the component vendor is deployed in the simulations. In this example, 3rd order IMD of the strongest signal located at around -1 MHz is falling on top of the weak signal located at 3 MHz due to the INL. Example demodulated signal constellations without and with proposed digital post-processing are illustrated in the lower part of Fig. 5 for the weak QPSK signal located at 3 MHz. In the post-processing implementation, plain cubic operators are used as the polynomial signal processing blocks, independently for both I and Q branches, to regenerate the interfering IMD frequencies. Furthermore, independent single-tap adaptive filters are used then to weight and subtract the IMD estimates from the weak signal band. The well-known LMS algorithm is used in adaptive filter implementation with an adaptation block size of 5,000 samples. Clearly the proposed processing is able to reduce the intermodulation distortion effects considerably at the weak signal band.

B. Clipping Mitigation Using Measured Signals

Next the case of waveform clipping due to improper A/D converter input conditioning is demonstrated. Here realistic radio signal laboratory measurements combined with true-world 14-bit commercial A/D converter board [19] are used, instead of computer simulations, to emphasize practicality. For simplicity, 2 channel input waveform is used whose spectrum is illustrated in Fig. 6 together with the actual time-domain waveform characteristics. The used sampling frequency is 16 MHz for the I and Q rails. State-of-the-art laboratory signal generators are deployed to generate the measurement waveforms, and blocks of the digitized I and Q signals are stored into memory and loaded into PC for post-processing implementation.

Due to clipping, part of the energy of the strong signal at -1 MHz is falling on top of the weaker signal located at 3 MHz, which is again a QPSK signal. The digitized signal is next processed using the proposed post-processing targeting to reduce the IMD due to clipping from the weaker signal band. In this case, due to the nature of the clipping process, 3rd, 5th and 7th order operators are used in the reference generation, all being further weighted with separate two-tap adaptive filters and subtracted from the weak signal observation. Again LMS algorithm is used to control the adaptive filter parameters. The corresponding demodulated signal constellation of the weak signal is illustrated in Fig. 7, both without compensation (left part) and with compensation (right part). Clearly the post-processing is again able to reduce the distortion at the weak signal band in a considerable manner.

V. CONCLUSIONS

This article addressed the A/D converter nonlinear distortion with special emphasis on wideband radio receivers with high dynamic range for the digitized signal. Adaptive interference cancellation based digital post-processing was proposed to reduce the intermodulation distortion from the weak signal bands, stemming from either converter integral nonlinearity or input clipping (converter saturation), and originating from strong blocking signals. Both computer simulations and laboratory measurements based examples were used to demonstrate the applicability of the proposed post-processing, with commercially available A/D converters. The obtained results indicate that the observable signal-to-noise-and-distortion ratio (SNDR) at the weak signal bands can be considerably improved using the proposed technique. Future work will include more complete performance measurements and evaluations, and building a real-time prototype implementation using FPGA's.

REFERENCES

[1] P.-I. Mak, S.-P. U, and R. P. Martins, "Transceiver architecture selection: review, state-of-the-art survey and case study", *IEEE Circuits and Systems Mag.*, vol. 7, 2nd quarter 2007, pp. 6-25.

[2] A. Rusu, D. Rodriguez de Llera Gonzalez, and M. Ismail, "Reconfigurable ADCs enable smart radios for 4G wireless connectivity," *IEEE Circuits and Devices Mag.*, vol. 22, no. 3, pp. 6-11, May-June 2006.

[3] T. Araujo and R. Dinis, "Analytical evaluation and optimization of the ADC (analog-to-digital converter) in software radio architectures," in *Proc. IEEE Global Telecommun. Conf.* (GLOBECOM-04), Dallas, TX, USA, 2004, pp. 1066-1070, vol. 2.

[4] J. Yang, R. W. Brodersen and D. Tse, "Addressing the dynamic range problem in cognitive radios," in *Proc. IEEE Int. Conf. Communications* (ICC-07), pp. 5183-5188, June 24-28, 2007, Glasgow, Scotland.

[5] N. Vun, A.B. Premkumar, "ADC systems for SDR digital front-end," in *Proc. Int. Symp. Consumer Electronics* (ISCE-05), June 14-16, 2005, pp. 359–363.

[6] F. Maloberti, *Data Converters*. Dordrecht, The Netherlands: Springer, 2008.

[7] J. A. Wepman, "Analog-to-digital converters and their applications in radio receivers," *IEEE Commun. Mag.*, vol. 33, pp. 39-45, May 1995.

[8] R. H. Walden, "Analog-to-digital converter survey and analysis," *IEEE J. Selected Areas in Communications*, vol. 17, no. 4, pp. 539-550, April 1999.

[9] ITU-R, *Requirements Related to Technical Performance for IMT-Advanced Radio Interface(s)*, Report ITU-R M.2134, Dec. 2008. Available online at http://www.itu.int/.

[10] P. Arpaia, P. Daponte, and S. Rapuano, "A state of the art on ADC modeling," *Elsevier J. Comput. Standards & Interfaces*, vol. 26, pp. 31–42, Jan. 2004.

[11] D. Dardari, "Joint clip and quantization effects characterization in OFDM receivers," *IEEE Trans. Circuits Syst. I*, vol. 53, no. 8, Aug. 2006, pp. 1741–1748.

[12] L. Michaeli, P. Michalko, and J. Saliga, "Unified ADC nonlinearity error model for SAR ADC," *Elsevier J. Measurement*, vol. 41, pp. 198–204, Feb. 2008.

[13] IEEE-SA Standards Board, *IEEE Standard for Terminology and Test Methods for Analog-to-Digital Converters*, IEEE Std #1241-2000, June 2001.

[14] M. Allén, J. Marttila and M. Valkama, "Modeling and mitigation of nonlinear distortion in wideband A/D converters for cognitive radio receivers," in preparation.

[15] M. Valkama, A. Shahed, L. Anttila, and M. Renfors, "Advanced digital signal processing techniques for compensation of nonlinear distortion in wideband multicarrier radio receivers," *IEEE Trans. Microwave Theory and Techniques*, vol. 54, pp. 2356-2366, June 2006.

[16] E. Keehr and A. Hajimiri, "Equalization of IM3 products in wideband direct-conversion receivers," *IEEE J. Solid-State Circuits*, vol. 43, pp. 2853-2867, Dec. 2008.

[17] Analog Devices, *AD9218 Data Sheet*, rev. C, Dec. 2006. Available online at http://www.analog.com/

[18] Analog Devices, "How ADIsimADC models an ADC," application note AN-737, rev. B, 2009. Available online at http://www.analog.com/

[19] Analog Devices, *AD9248 Data Sheet*, rev. A, March 2005. Available online at http://www.analog.com/

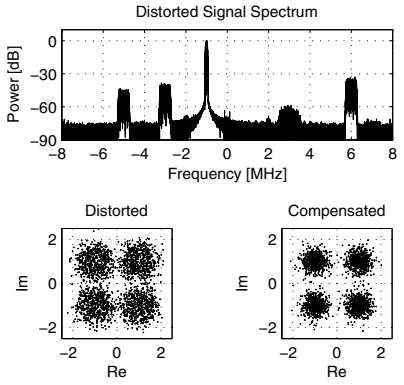

Fig. 5. Upper part: Spectrum of the received signal with 5 frequency channels and 60 dB dynamic range, 10-bit A/D converter. Lower part: Demodulated signal constellations of the weak QPSK signal at 3 MHz without and with post-processing.

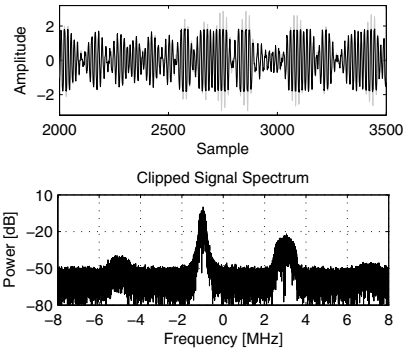

Fig. 6. Upper part: Measured time-domain digitized waveform under clipping (black) and the corresponding ideal unclipped waveform (gray). Lower part: Spectrum of the measured waveform under clipping. Third-order IMD of the stronger signal at -1 MHz is masking the weaker signal at 3 MHz. 14-bit A/D converter was used.

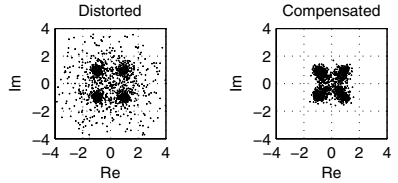

Fig. 7. Measured demodulated signal constellations of the weak QPSK signal at 3 MHz without and with post-processing under clipping.

Publication 2

M. Allén, J. Marttila, and M. Valkama, "Modeling and mitigation of nonlinear distortion in wideband A/D converters for cognitive radio receivers," *International Journal of Microwave and Wireless Technologies*, vol. 2, no. 2, pp. 183–192, Apr. 2010. DOI: 10.1017/S1759078710000292

© 2010 The European Microwave Association (Eu*M*A) and Cambridge University Press. Reprinted with permission.

International Journal of Microwave and Wireless Technologies, 2010, 2(2), 183–192. © Cambridge University Press and the European Microwave Association, 2010
doi:10.1017/S1759078710000292

Modeling and mitigation of nonlinear distortion in wideband A/D converters for cognitive radio receivers

MARKUS ALLÉN, JAAKKO MARTTILA AND MIKKO VALKAMA

This article discusses the reduction of nonlinearities in analog-to-digital (A/D) converters using digital signal processing (DSP). Also modeling of certain essential nonlinearities is considered in detail. The main focus is on wideband radio receivers, such as the emerging cognitive radio applications, where a collection of signals at different frequency channels is converted to digital domain as a whole. Therefore, the overall dynamic range can easily be in the order of tens of dBs and thus even mild nonlinear distortion can cause strong carriers to block weaker signal bands. In this article, a mathematical model for clipping distortion due to improper input signal conditioning is derived through Fourier analysis. Additionally, stemming from the analysis an adaptive DSP-based post-processing method for reducing the effects of clipping and integral nonlinearity (INL) in A/D converters is presented with illustrative examples using both computer simulations and laboratory radio signal measurements.

Keywords: A/D converter, Cognitive radio receiver, Nonlinear distortion, Integral nonlinearity, Clipping, Interference cancelation

Received 23 October 2009; Revised 15 February 2010; first published online 27 April 2010

I. INTRODUCTION

Nowadays a trend in radio transceiver development is toward multi-standard designs where more and more of the functionalities are implemented with digital signal processing (DSP). Therefore, the number of separate transmitter and receiver chains can be reduced and manufacturing costs are decreased [1]. From the receiver point of view, this means using a simple architecture, e.g., low-IF or direct conversion receiver where a single mixing stage is employed. Only coarse filtering is performed in analog domain, so the received signal has high bandwidth throughout the receiver analog signal processing chain and thus requires special considerations, e.g., about linearity issues, when designing components for the receiver [1–3]. This is particularly true if the incoming signal has high dynamic range, e.g., due to several independent radio signals on different frequency bands.

These aspects are ultimately culminated under the so-called cognitive radio concepts, in which the given radio hardware is to be utilized and reconfigured to access any available radio system and also to carry out the communication at any available sub-parts or chunks of the overall radio spectrum, the overall processed bandwidths being in the several hundreds of MHz range [3–5]. In such scenarios, the performance requirements for the sampling and A/D conversion stage become extremely stringent.

Aforementioned receiver considerations imply that the A/D converter is likely to become the limiting component for the performance of the receiver due to strict requirements regarding to dynamic range, resolution, and sampling speed [2–5]. The inherent trade-off between the last two has been discussed in detail in the existing literature [6–9]. In the mobile terminal side, also power dissipation constraints limit the possible analog-to-digital (A/D) converter choices. Other important issues in radio receiver context are signal distortion caused by sampling jitter and A/D converter nonlinearities [2–9].

This article focuses on the A/D converter nonlinearity aspects from the modeling and DSP-based mitigation points of view. This issue has increasing interest due to the emerging wireless systems, such as IMT-Advanced [10], in which the spectrum allocation of individual terminals can be strongly scattered over a wide range of frequencies. Hence, the dynamic range of the signal to be digitized can be in the order of tens of dBs (even 50–60 dB). In such scenarios, any nonlinearities in the A/D converter can cause severe intermodulation distortion (IMD). This is because the incoming signal contains strong signal bands which can, without doubt, block weaker desired signal bands if the IMD is falling on top of the weak bands [2–5]. In practice, considerable sources of nonlinearities in A/D converters are, e.g., differential and integral nonlinearity (DNL and INL) [6] as well as clipping. The DNL and INL are originating from unintentional deviations of the quantization levels, whereas clipping is stemming from improper input signal conditioning, i.e., exceeding the full scale (FS) voltage range of the A/D converter. The clipping phenomenon is deeply analyzed in this article by proposing a mathematical model based on Fourier-type analysis with time-variant coefficients.

Mitigation of A/D converter nonidealities has gained growing interest in recent years and, in general, it has been covered rather extensively in the literature, e.g., [4, 6, 11, 12] and the references therein. Typically, the proposed mitigation

Department of Communications Engineering, Tampere University of Technology, P.O. Box 553, FI-33101 Tampere, Finland.
Corresponding author:
M. Allén
Email: markus.allen@tut.fi

solutions are based on digital post-processing exploiting look-up tables or black-box modeling with identification stage(s). These kinds of approaches usually require accurate off-line calibration and are therefore mainly suitable for very stable operation environment, such as measurement and instrumentation applications. The situation is quite different in wireless radio systems, especially in mobile terminals, where operating conditions of the electronic components can vary considerably. In addition, the received waveform characteristics are likely to be heavily time varying, e.g., due to channel conditions, mobile terminal movement, and user allocations. Therefore, off-line calibration based or static compensation approaches are not directly applicable. This article discusses proper techniques for modeling A/D converter nonlinearities and then presents an on-line digital post-processing method based on adaptive filtering for reducing nonlinear distortion in wideband A/D converters. Adaptive interference cancelation (AIC) method is shown to noticeably reduce the effects of INL and clipping at weak signal bands in the presence of strong blocking signals. AIC is very dynamic approach being able to adapt its characteristics on a received packet-by-packet basis and thus it can concentrate its whole potential for removing the distortion from the most sensitive signal bands. In the emerging cognitive radio-type applications [3], this kind of ability to adapt is especially critical. Notice also that similar interference cancelation techniques have been proposed and demonstrated for reducing nonlinear distortion of mixers and low noise amplifiers in wideband receiver context in [13] and [14]. Furthermore, to the best of our knowledge, the only prior-art contribution in the field of clipping mitigation in radio receivers is the one by Tomioka *et al.* [15]. This will be used as a reference technique in the performance evaluations.

The rest of the article is organized as follows. Section II describes typical nonlinearities that are limiting the performance of wideband A/D converters. After that, a Fourier-analysis-based model for zero-symmetric clipping is proposed in Section III. The model gives a basic description of the clipping behavior and it is then used as grounds for the AIC method proposed in Section IV. Then in Section V, concrete performance examples are given for the proposed post-processing method. Finally, Section VI concludes the article.

II. TYPICAL NONLINEARITIES IN A/D CONVERTERS

In ideal quantization, the overall FS input voltage range of the converter is uniformly divided into quantization levels according to the number of bits B. This is illustrated in Fig. 1 for an unipolar quantizer. In addition to ordinary uniform quantization noise, one reason for nonlinear distortion is unintentional deviations of the quantization levels from the ideal ones [6, 11, 16]. This phenomenon can be described by means of DNL and INL. DNL refers to the relative difference between the actual code width $Q(k)$ and the ideal code width Q_{ideal}. INL, for one, defines the difference between the actual and ideal code transition threshold, i.e., $T(k)$ and $T_{ideal}(k)$, respectively. Mathematically, these are given by [6, 16]

$$DNL(k) = \frac{Q(k) - Q_{ideal}}{Q_{ideal}} \tag{1}$$

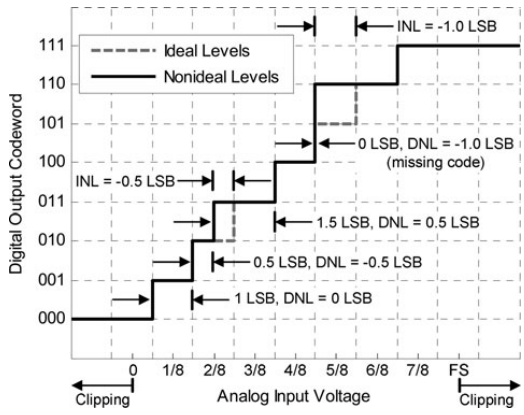

Fig. 1. Principal illustration of quantization levels for ideal and nonideal unipolar quantizer with $B = 3$ bits. Both differential and integral nonlinearities (DNL, INL) as well as clipping are shown.

and

$$INL(k) = \frac{T(k) - T_{ideal}(k)}{Q_{ideal}}, \tag{2}$$

where k denotes the output code index having values between 0 and 2^{B-1}. Another interpretation for INL is thinking it as integral of the DNL. Although DNL behavior from output code to another is typically fairly random, the INL behavior can have more deterministic shape [6, 11]. A real-life example of typical INL error as a function of converter output code is shown in Fig. 2. As proposed in [12], INL can be further divided to three separate parts for modeling purposes so that

$$\begin{aligned} INL(T(k)) = {} & INL_{HCF}(T(k)) + INL_{LCF}(T(k)) \\ & + INL_{Noise}(T(k)), \end{aligned} \tag{3}$$

where $INL_{HCF}(T(k))$, $INL_{LCF}(T(k))$, and $INL_{Noise}(T(k))$ refer to a high code frequency (HCF), a low code frequency, and a noise component, respectively. The LCF part describes slow fluctuation which is evident, e.g., in Fig. 2. Additionally, the HCF component depicts rapid architecture-dependent variations, usually modeled as piecewise linear, on top of the LCF. Finally, the noise is part of the INL which is not described by LCF or HCF.

Another potential source of severe nonlinear distortion is clipping due to the improper input conditioning of the incoming signal. It is probable that automatic gain control of the receiver cannot react fast enough all the time if the incoming signal has large peak-to-average power ratio (PAPR). In an A/D converter any input dynamics exceeding the FS voltage range will essentially be limited by the quantizer, i.e.,

$$k = \begin{cases} 0 & \forall x_{IN} \leq Q_{ideal}/2, \\ 2^{B-1} & \forall x_{IN} > x_{FS} - 3Q_{ideal}/2, \end{cases} \tag{4}$$

where x_{IN} denotes the converter input voltage and an FS voltage range of $0 \ldots x_{FS}$ is assumed. The clipping behavior of quantizer is also illustrated through a transfer function in Fig. 1.

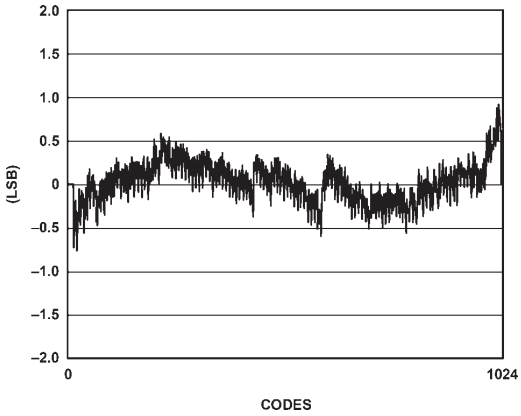

Fig. 2. Measured typical INL error curve of 10-bit A/D converter AD9218 [18] as a function of output code k.

Both DNL and INL as well as clipping will cause IMD in radio receivers, which can be especially harmful in wideband cases [2, 6, 7, 17]. Significant part of the spurious components due to IMD are originating from the LCF component of INL and especially from clipping (if taking place). For interference cancelation purposes, described in Section IV, both of these can be modeled with polynomial equation

$$x'_{IN} = g(x_{IN}) = a_0 + a_1 x_{IN} + a_2 x_{IN}^2 + a_3 x_{IN}^3 + \cdots \quad (5)$$

followed by an ideal quantizer (in cascade) as illustrated in Fig. 3. It is shown also in [12] that LCF component of INL can be represented with a polynomial as in (5). Additionally, it is shown in the literature that the polynomial model is applicable for many nonlinearity-related issues [6, 11, 17, 19]. For the clipping modeling it is proposed in [20]. When considering INL, the low order, such as second, third, and fourth, distortion components are usually the most dominant ones, but the exact impact of the orders varies between A/D converter structures [6, 12]. In case of symmetric clipping, only odd order distortion is generated. This is mathematically shown in the next section.

III. MATHEMATICAL MODEL FOR CLIPPING

In this section, a mathematical model for zero-symmetric[1] hard clipping is derived through Fourier analysis. It allows, e.g., analyzing the impact of different distortion orders separately from the amplitude and phase point of view. Altogether the target of the analysis is to understand and model the impact of A/D converter clipping in cases where the overall waveform dynamics of the incoming signal is dominated by a strong noninteresting blocking carrier or carriers. More specifically, a model that reveals the induced IMD at weak signal bands is derived, which to the best of our knowledge cannot be found from the existing literature of the field. Then the derived intermodulation model is also used in

[1]To be specific, we assume in the analysis that the converter voltage range is located symmetrically w.r.t. zero and that the input waveform has no bias.

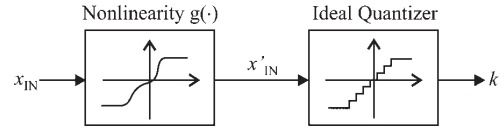

Fig. 3. A cascade structure consisting of a memoryless polynomial and an ideal quantizer for modeling A/D nonlinearities such as INL and clipping.

Section IV to develop digital post-processing-based interference cancelation techniques for reducing the signal distortion induced by clipping at weak signal bands.

For simplicity of presentation, it is assumed that only a single analytic bandpass signal, being located at intermediate-frequency (IF) f_c after initial downconversion, is entering the converter. This is illustrated in Fig. 4. The time-domain waveform is first written in the general I/Q bandpass signal notation as

$$\begin{aligned} v_{IN}(t) &= A(t)\cos\theta_c(t) + jA(t)\sin\theta_c(t) \\ &= v_{IN,I}(t) + jv_{IN,Q}(t), \end{aligned} \quad (6)$$

where $A(t)$ is the envelope of the signal and $\theta_c(t)$ consists of angular frequency ω_c and phase $\phi(t)$ so that $\theta_c(t) = \omega_c t + \phi(t)$. Due to the instantaneous nature of clipping, its effects have to be considered sample-by-sample basis. At time instances when the signal envelope $A(t)$ does not exceed clipping level V_o, the output signal $v_{OUT}(t)$ equals to $v_{IN}(t)$. Otherwise $v_{IN}(t)$ gets clipped. Hence, the output signal is defined first as

$$v_{OUT}(t) = \begin{cases} v_{IN}(t) & \forall t{:}|A(t)| < V_o, \\ v_{CL}(t) & \forall t{:}|A(t)| \geq V_o, \end{cases} \quad (7)$$

where $v_{CL}(t)$ describes the clipped parts of the signal. Now, let us first consider only the I branch of $v_{CL}(t)$, denoted with $v_{CL,I}(t)$, to simplify the notation. According to the definition of symmetric hard clipping, $v_{CL,I}(t)$ can be written as

$$v_{CL,I}(t) = \begin{cases} v_{IN,I}(t), & |V_{IN,I}(t)| < V_o, \\ +V_o, & V_{IN,I}(t) \geq V_o, \\ -V_o, & V_{IN,I}(t) \leq -V_o, \end{cases} \quad (8)$$

at time instances when $|A(t)| \geq V_o$.

Fourier series can be deployed to model the behavior of $v_{CL,I}(t)$. The whole model is heavily time dependent due to variations in the signal envelope $A(t)$. Therefore, Fourier

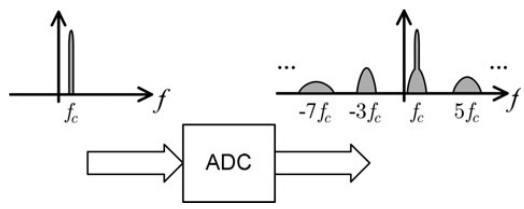

Fig. 4. Principal illustration of the clipping distortion due to improper input signal conditioning in the analog-to-digital converter (ADC). An analytic bandpass signal at center frequency of f_c causes odd order nonlinear distortion due to zero-symmetric clipping.

coefficients $a_{n,I}(t)$ have to be also time varying as a function of $A(t)$. From the definition of Fourier series it can be derived that

$$v_{CL,I}(t) = \sum_{n=1}^{\infty} |2a_{n,I}(t)| \cos\left(n\theta_c(t) + \arg a_{n,I}(t)\right), \tag{9}$$

where

$$a_{n,I}(t) = \frac{1}{2\pi}\int_{2\pi} v_{CL,I}(t)e^{-jn\theta_c(t)}\mathrm{d}\theta_c(t). \tag{10}$$

For a single time instant the function $\theta_c(t)$ has one specific value. All the possible values of $\theta_c(t)$ are within the period of 2π as formulated in (10). Note that it is not required that $\theta_c(t)$ nor $v_{IN}(t)$ is periodic in time. The periodicity exploited in (10) is stemming from the fact that $v_{CL,I}(t)$ can be seen as a periodic function of θ_c when time is held fixed. This is illustrated in Fig. 5 with an example choice of integration intervals that can be used in further derivation of the Fourier coefficients. By taking advantage of the condition $A\cos(\theta_c) = V_o$ and the definition in (8), the equation of Fourier coefficients can be written as

$$\begin{aligned} a_{n,I}(t) = \frac{1}{2\pi}\Bigg[& \int_{-\pi/2}^{-\arccos(V_o/A(t))} v_{IN,I}(t)e^{-jn\theta_c(t)}\mathrm{d}\theta_c(t) \\ & + \int_{-\arccos(V_o/A(t))}^{\arccos(V_o/A(t))} V_o e^{-jn\theta_c(t)}\mathrm{d}\theta_c(t) \\ & + \int_{\arccos(V_o/A(t))}^{\pi-\arccos(V_o/A(t))} v_{IN,I}(t)e^{-jn\theta_c(t)}\mathrm{d}\theta_c(t) \\ & + \int_{\pi-\arccos(V_o/A(t))}^{\arccos(V_o/A(t))+\pi} -V_o e^{-jn\theta_c(t)}\mathrm{d}\theta_c(t) \\ & + \int_{\arccos(V_o/A(t))+\pi}^{(3\pi/2)} v_{IN,I}(t)e^{-jn\theta_c(t)}\mathrm{d}\theta_c(t)\Bigg]. \end{aligned} \tag{11}$$

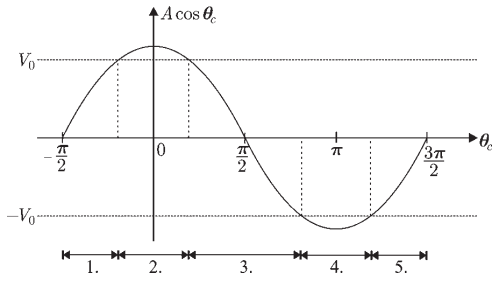

Fig. 5. A real bandpass signal $v_{CL,I}(t)$ drawn as a function of θ_c consisting of angular frequency and phase when time t is held fixed so that the signal envelope $A(t)$ can be considered to be constant. In addition, one possible choice of integration intervals 1–5 for deriving the Fourier coefficients is illustrated based on clipping level V_o.

After rather straightforward derivations, the final form of equation for the Fourier coefficients is defined in three parts where auxiliary variable $r_I(t) = \arccos(v_o/A(t))$ is used. The Fourier coefficients are given by

$$a_{n,I} = \frac{A(t)}{2} - \frac{A(t)}{\pi}r_I(t) + \frac{V_o}{\pi}\sqrt{1-\left(\frac{V_o}{A(t)}\right)^2} \tag{12}$$

for $n = \pm 1$,

$$\begin{aligned} a_{n,I}(t) = & \frac{-2V_o\sin\left(nr_I(t)\right)}{\pi n(n^2-1)} \\ & + \frac{2n\sqrt{A^2(t)-V_o^2}\cos\left(nr_I(t)\right)}{\pi n(n^2-1)} \end{aligned} \tag{13}$$

for $n = \pm 3, \pm 5, \pm 7, \ldots$ and

$$a_{n,I}(t) = 0 \tag{14}$$

for $n = 0, \pm 2, \pm 4, \ldots$.

It is justified to assume same clipping level V_o also for the Q branch, because voltage ranges of two A/D converters can be matched relatively well in practice. This is especially true when dual A/D converter architecture is used. Based on this assumption and exploiting the symmetry of Fourier series for I/Q signal, the model for complex $v_{CL}(t)$ can be written as

$$\begin{aligned} & v_{CL}(t) = \sum_{n=-\infty}^{\infty} 2a_{n,I}(t)e^{jn\theta_c(t)}, \\ & n = (-1)^{k-1}(2k-1) \text{ and } k \in \mathbb{N}\backslash\{0\}. \end{aligned} \tag{15}$$

This final form of the model shows that symmetric hard clipping creates only odd order distortion and for an I/Q signal every second odd distortion order is negative.

As an illustrative example, Fig. 6 shows spectra of an arbitrary complex bandpass signal at center frequency of 10 MHz before and after zero-symmetric clipping. The distortion of odd orders is clearly identifiable at frequencies around -30, 50, -70 MHz etc. A short block of time domain behavior of the signal (I branch) is illustrated in Fig. 7. Furthermore, the third order distortion ($n = -3$) of the clipped signal is plotted according to (15) which corresponds to the distortion around -30 MHz in Fig. 6. It is clearly visible that nonlinear distortion appears only at time instances when the envelope of the original waveform is clipped. It can be also seen that the third-order distortion waveform has (three times) higher center frequency than the original signal.

In general, the model in (15) gives an analytical closed-form description for the intermodulation components caused by clipping around different integer multiples of the center frequency of the incoming blocking carrier. In the next section, this modeling is used as the basis to develop DSP techniques to reduce this intermodulation energy from the weak signal bands. For computation simplicity, the mapping between the complex envelopes of the original blocking signal band (after clipping, $n = 1$) and the different IMD products ($n = -3, 5, -7, 9, \ldots$) is approximated using polynomials. This will be described in more details below.

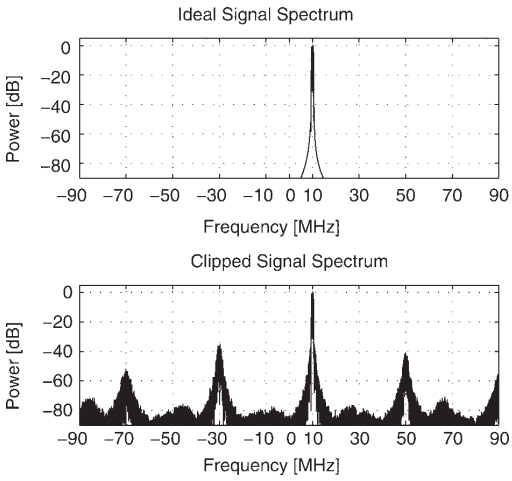

Fig. 6. Upper spectrum illustrates an arbitrary communications signal at the center frequency of 10 MHz. After zero-symmetric clipping of the signal (lower spectrum) the distortion of odd orders is clearly visible.

IV. ADAPTIVE INTERFERENCE CANCELATION

This section describes a digital post-processing method based on AIC for reducing IMD caused by A/D converter nonlinearities. The main principle of AIC is stemming from the earlier studies related to receiver mixer and low noise amplifier nonlinearities in [13, 14] and more A/D converter related considerations described initially in [21].

A conceptual block diagram is presented in Fig. 8 including simplified spectrum figures. Due to nonlinearities in A/D converter the digitized signal contains IMD which is illustrated in spectrum *B* of Fig. 8 with two blocker signals and a weak signal band (see spectrum *A*). First step is to apply band-split filtering to a block of samples in order to separate the weakest, i.e., the most sensitive signal band(s) from the rest of the sampled spectrum which includes strong blocking signals. The separation is illustrated with spectrums *C* and *D* in Fig. 8. Target is to regenerate the IMD components at the weak signal band by using the separated signal containing the strong blocking signals. This is done with polynomial signal processing which models the nonlinearity according to (5). Then target filter is used to pass only the distortion at the weak signal band. The outcome is illustrated in spectrum *E* of Fig. 8. The characteristics of the nonlinearity modeling block depend directly on the order of the IMD components being canceled and thus varies between different situations and applications.

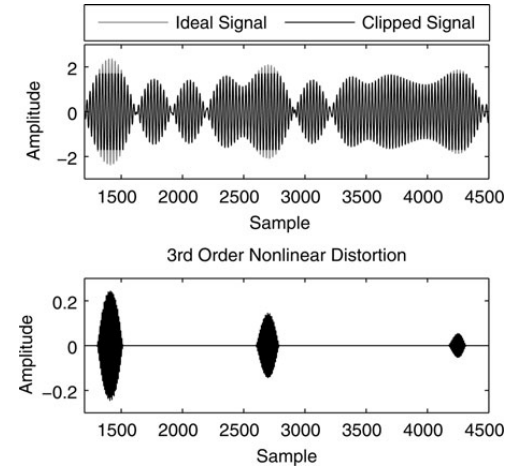

Fig. 7. Upper part: a block of time domain waveform of the communications signal (shown in Fig. 6) before and after zero-symmetric clipping. Lower part: third-order distortion due to the clipping.

The last step of AIC is to use an adaptive filter for the regenerated distortion signal before subtracting it from the weak signal band of the original band-split filtered signal. The adaptive filter coefficient(s) are defined in such a manner that the interference power at the weak signal band is minimized. The ideal situation is visualized in spectrum *F* of Fig. 8. The filter coefficient adaptation can be implemented using, e.g., the well-known least-mean-square (LMS) algorithm which is simple enough to be used in actual real-time systems [22]. From the practical point of view, each order of IMD has its own adaptive filter coefficient(s) and the overall processing can be carried out either in parallel or serial manner. This choice obviously has effect on processing speed and the amount of required computational resources. In addition, an outer-loop control mechanism can be used to manage the overall system on a received packet-by-packet basis. It controls the overall coefficient adaptation, degrees of IMD to be canceled, and the design of the band-split filtering stage. This can be achieved using, e.g., FFT in order to make coarse measurements of the spectrum density of the received packet after A/D conversion. Then according to these measurements, the band-split filter properties are tuned to isolate the most sensitive signal bands. Furthermore, the basis for choosing the IMD orders being canceled is obtained by sensing the locations of the strongest signal energy levels with respect to the weak bands.

The exact implementation of the proposed AIC method for clipping mitigation is illustrated in Fig. 9 starting from the digitized signal denoted with $r(n)$. The index n refers to samples inside one packet. In general, the mathematical notation is so that the real and the imaginary parts of the vector $\mathbf{x}$ are marked with $\mathbf{x}_I$ and $\mathbf{x}_Q$, respectively. The lengths of filters $\mathbf{h}_a$, $\mathbf{h}_b$, and $\mathbf{w}_l$ are M_a, M_b, and M_w, respectively. In the band-split filtering stage the weak signal band is separated using pre-designed filter $\mathbf{h}_a$, which is tuned according to parameters given by the coarse spectrum sensing block. Therefore, the signal containing the weak signal band is defined as

$$d(n) = \mathbf{h}_a^T \mathbf{r}_a(n), \tag{16}$$

where $\mathbf{r}_a(n) = [r(n), r(n-1), \ldots, r(n-M_a)]^T$. The filter $\mathbf{h}_b$ is used to form a signal containing all the spectral content outside the weak signal band and it is then used to generate L different reference signals for removing distortion of different orders. For example, the lth order distortion is

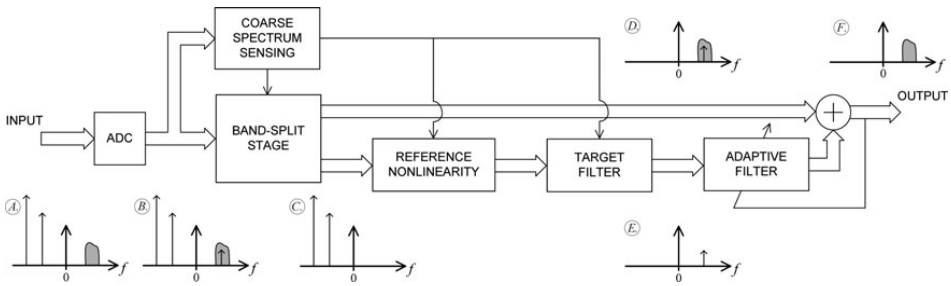

Fig. 8. AIC method for reducing A/D converter nonlinear distortion at a weak signal band originating from considerably stronger blocking signals. The lower branch regenerates the distortion caused by the strong signals and subtracts it from the weak signal band. In the simplified spectrum figures above, only a single intermodulation component is drawn on top of the weak signal for illustration purposes.

described with

$$v_l(n) = \mathrm{Re}[\mathbf{h}_b^T \mathbf{r}_b(n)]^l + j\mathrm{Im}[\mathbf{h}_b^T \mathbf{r}_b(n)]^l, \tag{17}$$

where $\mathbf{r}_b(n) = [r(n),\ r(n-1), \ldots,\ r(n-M_b)]^T$. Because only the distortion at the weak signal band is of interest, the signal is filtered with the target filter $\mathbf{h}_a$ and the outcome is

$$u_l(n) = \mathbf{h}_a^T \mathbf{v}_l(n), \tag{18}$$

where the lth-order distortion signal vector is $\mathbf{v}_l(n) = [v_l(n), v_l(n-1), \ldots, v_l(n-M_a)]^T$. After that, adaptive filters $\mathbf{w}_{l,I}$ and $\mathbf{w}_{l,Q}$ are applied separately for the real and the imaginary parts of the distortion signal $u_l(n)$. The overall output of the adaptive filter stage is defined as

$$y_l(n) = \mathbf{w}_{l,I}^T(n)\,\mathbf{u}_{l,I}(n) + j\mathbf{w}_{l,Q}^T(n)\,\mathbf{u}_{l,Q}(n), \tag{19}$$

where $\mathbf{u}_{l,I}(n) = [u_{l,I}(n), u_{l,I}(n-1), \ldots, u_{l,I}(n-M_w)]^T$ and $\mathbf{u}_{l,Q}(n) = [u_{l,Q}(n), u_{l,Q}(n-1), \ldots, u_{l,Q}(n-M_w)]^T$.

When using LMS for finding the filter coefficients for the adaptive filters, the algorithm goes as follows. Here, only the I branch of the lth-order distortion filter adaptation is described. Algorithm for the Q branch and all the other distortion orders are implemented in a similar manner. In the beginning, all the coefficients are set to zero, i.e.,

$$\mathbf{w}_{l,I}(0) = \mathbf{0}. \tag{20}$$

All reference branches are using the overall output $e(n)$ for the adaptation. For the I branch it is defined as

$$e_I(n) = d_I(n-\Delta) - \sum_{i=2}^{(L+1)/2} y_{2i-1,I}(n), \tag{21}$$

where Δ is a delay required for the reference signal processing. The actual coefficient update for the I branch of the lth-order distortion filter is then

$$\mathbf{w}_{l,I}(n+1) = \mathbf{w}_{l,I}(n) + \mu_l \mathbf{u}_{l,I}(n) e_I(n), \tag{22}$$

where μ_l is the LMS step-size parameter for the lth-order distortion branch.

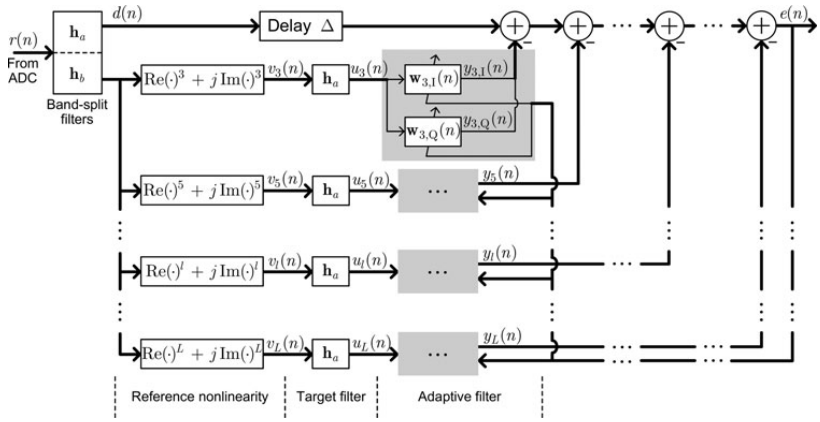

Fig. 9. Mathematical notation for the proposed AIC method in case of clipping compensation. The input $r(n)$ is a digitized signal from the A/D converter and the enhanced output signal is denoted with $e(n)$.

V. PERFORMANCE EXAMPLES OF THE DIGITAL POST-PROCESSING METHOD

This section is devoted to demonstrate the applicability of the AIC concept for removing A/D converter nonlinearities. Both INL and clipping effects are considered in separate examples. The performance studies are based on commercially available A/D converters.

A) INL reduction experiment

In this performance example, a commercial 10-bit A/D converter [18] is deployed whose INL behavior is shown in Fig. 2. The experiment is conducted as a computer simulation where the chosen A/D converter is simulated using a behavioral model [23] provided by the component vendor. The test signal used in this example consists of five separate frequency channels with different channel bandwidths and power levels as illustrated in Fig. 10. The overall dynamic range of the test signal is approximately 60 dB and PAPR is 5 dB. Sampling frequency of 32 MHz is used in the A/D conversion for both I and Q branch. The target signal in the detection, and therefore in the interference cancelation, is the weak signal at 3 MHz (downconverted) center frequency which is a QPSK modulated waveform with roughly 1 MHz bandwidth. The other signals shown in the spectrum simply act as sources of interference.

Due to the INL in the A/D converter, third-order IMD of the strongest signal located at center frequency of -1 MHz is falling on top of the weak signal with center frequency of 3 MHz. In the lower part of Fig. 10 signal constellations of the demodulated weak QPSK signal is shown without and with AIC processing. In the implementation of the AIC, only third order is used to model the nonlinearity independently for I and Q branches. Additionally, in the adaptive filter stage, single-tap filters are used to scale the regenerated IMD before being subtracted from the weak frequency channel. The filter coefficient adaptation is implemented using the LMS algorithm with an adaptation block length of 5000 samples.

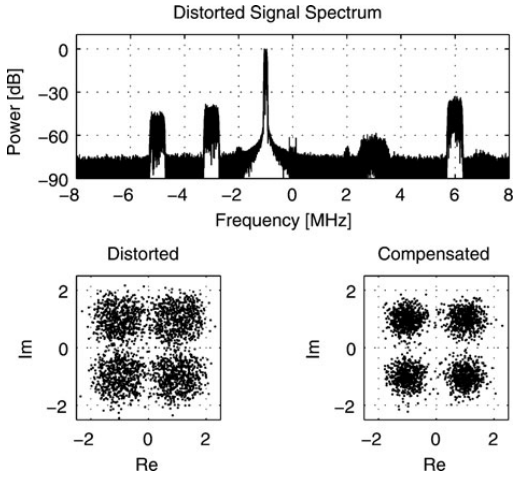

Fig. 10. INL reduction experiment. Upper part: spectrum of the test signal with five frequency channels after the 10-bit A/D converter. Lower part: demodulated signal constelations of the weak QPSK signal at 3 MHz without and with AIC.

It is evident from the provided constellations in Fig. 10 that the AIC method is able to reduce the IMD considerably. In this example, the signal-to-noise-and-distortion ratio (SNDR) in the weak signal band is enhanced from 6.4 to 10 dB by using the AIC. The SNDR is here calculated as a ratio of the useful signal power to the combined power of noise and distortion components at the band of interest. However, the performance is limited due to quantization noise and also since AIC is only able to remove the LCF part of INL. Different kind of approach would be required in order to remove the HCF part of INL [12].

B) Clipping mitigation experiment

This experiment demonstrates signal clipping caused by improper A/D converter input conditioning. Real laboratory measurements are used in order to verify the clipping behavior in practice. A commercial 14-bit A/D converter [24] with evaluation board (illustrated in Fig. 11) is used among necessary laboratory equipment. Spectrum of the test signal for this experiment is shown in upper part of Fig. 12 and it consists of, as in the previous case, five frequency channels with different bandwidths and power levels, the overall dynamic range being 50 dB. PAPR for the test signal is 7 dB and used sampling frequency is 64 MHz for I and Q branches. State-of-the-art laboratory signal generators are used for generating composite measurement waveform. Power of the waveform in the A/D converter input is adjusted so that the signal is clipped 5 dB above the average power level of the test signal. After A/D conversion, blocks of the digitized I and Q signals are transferred from the memory of evaluation board to PC for post-processing purposes. Again the target signal in the detection is the weak QPSK waveform at 3 MHz IF-frequency.

In this example, especially third-order IMD of the strong signal located at -1 MHz is falling on top of the weak signal located at 3 MHz due to clipping of the waveform. This is shown in the lower spectrum plot in Fig. 12. AIC is applied to remove the IMD, and the constellations of the detected weak signal are presented in Fig. 13 without compensation (left side) and with compensation (right side). To take into account the nature of clipping, third-, fifth-, and seventh-order operators are used in AIC method for regenerating the distortion. Then single-tap adaptive filters are used for proper weighting and, again, the LMS algorithm is

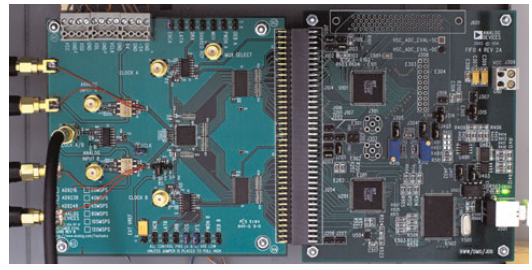

Fig. 11. A commercial 14-bit A/D converter [24] with its evaluation board employed in the clipping mitigation experiment.

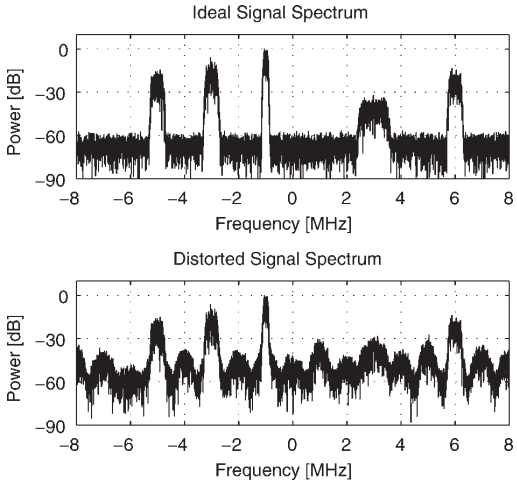

Fig. 12. Clipping experiment using laboratory measurements. Upper part: spectrum of the test signal prior to A/D conversion. Lower part: the signal spectrum after 14-bit A/D converter when clipping level is 5 dB above the average power level.

deployed for the filter coefficient adaptation. After adaptive filtering the regenerated IMD is subtracted from the weak signal band.

It is clearly visible also in this experiment that AIC can significantly reduce IMD on the weak signal band. SNDR of the weak signal band is improved from 0.3 to 8.8 dB when AIC is used in this example. One limitation for the post-processing performance is the quality of the distortion regeneration. That is because the strong signals are also distorted to some extent due to clipping and thus they are not the same as the originals where the IMD to the weak signal band is originating from.

C) Further performance considerations

The amount of nonlinear distortion in the clipping case depends on how much the signal is clipped, i.e., strong clipping reduces the inband SNDR significantly. However, the proposed AIC method is able to provide considerable gain by removing distortion. Fig. 14 illustrates that gain as a function of clipping level in the example case described in the previous subsection. Here the clipping level is defined as a number of dBs above the average power level of the test signal. The results in Fig. 14 are averaged over 20 random

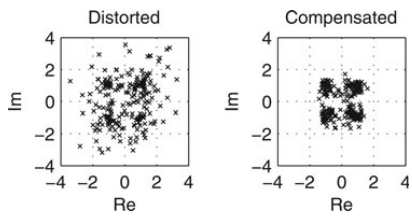

Fig. 13. Corresponding demodulated signal constllations of the weak QPSK signal at center frequency of 3 MHz without and with AIC in the clipping experiment.

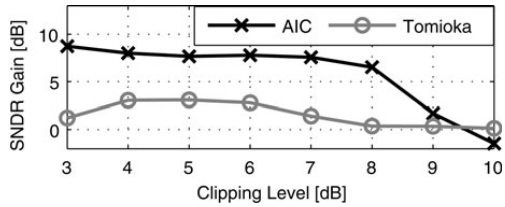

Fig. 14. SNDR gain provided by the proposed AIC method in the clipping mitigation experiment. Clipping level is defined as a number of dBs above the average power level of the test signal. Performance of a state-of-the-art technique based on interpolation by Tomioka *et al.* [15] has been used as a reference.

realizations of the test signal to obtain reliable performance statistics. The performance of the AIC is rather steady in case of strong or medium clipping, but the gain decreases when there is only very mild clipping. This is stemming from the fact that there is not so much distortion to remove in the first place. The 10-dB clipping level in Fig. 14 represents a situation where clipping happens very rarely. Then it is better to bypass the whole AIC stage to decrease the power consumption of the receiver. For concrete comparison to other techniques, Fig. 14 also shows the performance of a state-of-the-art clipping mitigation technique based on interpolation by Tomioka *et al.* [15]. When using real laboratory equipment instead of computer simulations, as is the case here, the proposed AIC method is clearly performing better.

In highly time-varying conditions, such as cognitive radio receivers, one of the key issues is the adaptation speed of the post-processing. Fig. 15 illustrates how the adaptive filter coefficients behave when LMS algorithm is used in the clipping mitigation experiment described in the previous subsection. Because the overall output $e(n)$ is used for the adaptation, an overall balance among the different order filter coefficients can be found. The sudden change in the adaptation direction of the third-order filter coefficient in Fig. 15 is stemming from the dependence between different distortion orders. In other words, the fifth- and seventh-order reference signals contain partially same frequencies as the third-order reference signal. It should be noted that Fig. 15 is not trying to illustrate

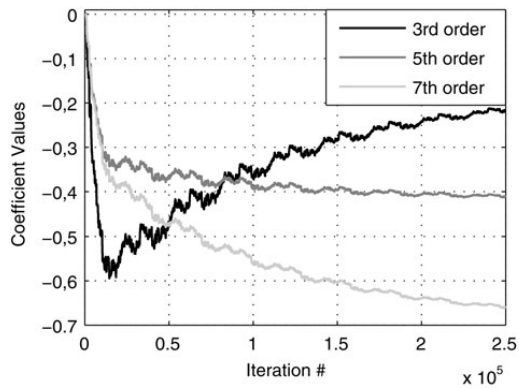

Fig. 15. LMS adaptation of the adaptive filter coefficients for I branch in the clipping mitigation experiment.

the optimal performance of the AIC method, but acts more as a proof of concept. It is a well known fact that, e.g., recursive-least-squares (RLS) algorithm can provide significantly better adaptation speed [22, 25]. All adaptive filtering algorithms provide a certain trade-off between adaptation speed and accuracy. For example, normalized LMS [22], Gauss–Newton RLS [25], and fast approximate RLS [26] are proposed in the literature.

VI. CONCLUSION

This article focused on the A/D converter nonlinearities from the wideband radio receiver point of view where the signal to be digitized may have very large dynamics. Mathematical model for zero-symmetric clipping due to improper input signal conditioning was proposed based on Fourier series with time-variant coefficients. Furthermore, DSP-based AIC method was presented for reducing nonlinear distortion, originating from strong blocker signals, at weak signal bands. It was demonstrated through both computer simulations and laboratory measurements using commercially available A/D converters that the presented method is able to significantly reduce IMD stemming from input signal clipping and A/D converter INL.

ACKNOWLEDGEMENTS

This work was supported by the Academy of Finland, the Finnish Funding Agency for Technology and Innovation (Tekes), and the Technology Industries of Finland Centennial Foundation.

REFERENCES

[1] Mak, P.-I.; U, S.-P.; Martins, R.P.: Transceiver architecture selection: review, state-of-the-art survey and case study. IEEE Circuits Syst. Mag., **7** (2007), 6–25. doi: 10.1109/MCAS.2007.369072.

[2] Araujo, T.; Dinis, R.: Analytical evaluation and optimization of the ADC (analog-to-digital converter) in software radio architectures, in Proc. IEEE Global Telecommunication Conf. (GLOBECOM-04), vol. **2**, (2004), 1066–1070, doi: 10.1109/GLOCOM.2004.1378121.

[3] Yang, J.; Brodersen, R.W.; Tse, D.: Addressing the dynamic range problem in cognitive radios, in *Proc. IEEE Int. Conf. on Communications* (ICC-07), 2007, 5183–5188. doi: 10.1109/ICC.2007.857.

[4] Rusu, A.; Rodriguez de Llera Gonzalez, D.; Ismail, M.: Reconfigurable ADCs enable smart radios for 4G wireless connectivity. IEEE Circuits Devices Mag., **22** (2006), 6–11. doi: 10.1109/MCD.2006.1657844.

[5] Vun, N.; Premkumar, A.B.: ADC systems for SDR digital front-end, in Proc. Ninth Int. Symp. on Consumer Electronics, 2005, 359–363. doi: 10.1109/ISCE.2005.1502403.

[6] Maloberti, F.: Data Converters, *Springer*, Dordrecht, The Netherlands, 2008 doi: 10.1007/978-0-387-32486-9.

[7] Wepman, J.A.: Analog-to-digital converters and their applications in radio receivers. IEEE Commun. Mag., **33** (1995), 39–45. doi: 10.1109/35.393000.

[8] Walden, R.H.: Analog-to-digital converter survey and analysis. IEEE J. Sel. Areas Commun., **17** (1999), 539–550. doi: 10.1109/49.761034.

[9] Le, B.; Rondeau, T.; Reed, J.; Bostian, C.: Analog-to-digital converters. IEEE Signal Process. Mag., **22** (2005), 69–77. doi:10.1109/MSP.2005.1550190.

[10] ITU-R. Requirements Related to Technical Performance for IMT-Advanced Radio Interface(s), Report ITU-R M.2134, 2008. Available online at http://www.itu.int/.

[11] Arpaia, P.; Daponte, P.; Rapuano, S.: A state of the art on ADC modeling. Comput. Stand. Interfaces, **26** (2004), 31–42. doi: 10.1016/S0920-5489(03)00060-6.

[12] Björsell, N.; Händel, P.: Dynamic behavior models of analog to digital converters aimed for post-correction in wideband applications, in XVIII Imeko World Congress 11th Workshop on ADC Modelling and Testing, 2006.

[13] Valkama, M.; Shahed, A.; Anttila, L.; Renfors, M.: Advanced digital signal processing techniques for compensation of nonlinear distortion in wideband multicarrier radio receivers. IEEE Trans. Microwave Theory Techn., **54** (2006), 2356–2366. doi: 10.1109/TMTT.2006.875274.

[14] Keehr, E.; Hajimiri, A.: Equalization of IM3 products in wideband direct-conversion receivers. IEEE J. Solid-State Circuits, **43** (2008), 2853–2867. doi: 10.1109/JSSC.2008.2005701.

[15] Tomioka, T.; Sakata, R.; Horiguchi, T.; Tomizawa, T.; Inoue, K.: A/D converter clipping noise suppression for high-sensitivity carrier-sensing of cognitive radio transceiver, in IEEE Global Telecommunications Conf. 2007, 2007 doi: 10.1109/GLOCOM.2007.793.

[16] IEEE-SA Standards Board. IEEE Standard for Terminology and Test Methods for Analog-to-Digital Converters, IEEE Std #1241-2000, 2001.

[17] Dardari, D.: Joint clip and quantization effects characterization in OFDM receivers. IEEE Trans. Circuits Syst. I, **53** (2006), 1741–1748. doi: 10.1109/TCSI.2006.875170.

[18] Analog Devices. AD9218 Data Sheet, rev. C, 2006. Available online at http://www.analog.com/.

[19] Michaeli, L.; Michalko, P.; Saliga, J.: Unified ADC nonlinearity error model for SAR ADC. Measurement, **41** (2008), 198–204. doi: 10.1016/j.measurement.2006.10.004.

[20] Cruz, P.; Carvalho, N.; Remley, K.: Evaluation of nonlinear distortion in ADCs using multisines, in IEEE MTT-S Int. Microwave Symp. Digest., 2008. doi: 10.1109/MWSYM.2008.4633048.

[21] Allén, M.; Marttila, J.; Valkama, M.: Digital post-processing for reducing A/D converter nonlinear distortion in wideband radio receivers, in Forty-Third Asilomar Conf. on Signals, Systems and Computers, 2009.

[22] Haykin, S.: Adaptive Filter Theory, 3rd ed., *Prentice-Hall*, Upper Saddle River, NJ, 1996.

[23] Analog Devices. How ADIsimADC Models an ADC, Application Note AN-737, rev. B, 2009. Available online at http://www.analog.com/

[24] Analog Devices. AD9248 Data Sheet, rev. A., 2005 Available online at http://www.analog.com/

[25] Sayed, A.H.: Adaptive Filters, *John Wiley & Sons*, Hoboken, NJ, 2008.

[26] Chansarkar, M.M.; Desai, U.B.: A fast approximate RLS algorithm, in IEEE Region 10 Conf. on Computer, Communication, Control and Power Engineering, TENCON'93., 1993. doi: 10.1109/TENCON.1993.328038.

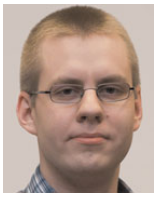

Markus Allén was born in Ypäjä, Finland, on October 28, 1985. He received the B.Sc. degree in communications electronics from Tampere University of Technology (TUT), Finland, in 2008 and is now heading towards the M.Sc. degree in signal processing and communications engineering at TUT. He is currently working at Department of Communications Engineering at TUT as a Research Assistant. His general research interests include analog-to-digital converters (ADC) in software defined radios, non-idealities of ADCs, and their mitigation algorithms.

Jaakko Marttila was born in Tampere, Finland, on March 30, 1982. He is heading toward M.Sc. degree in signal processing and communications engineering, in Tampere University of Technology (TUT), Tampere, Finland. He is currently working at TUT, Department of Communications Engineering as a Research Assistant. At present, his main research topic is quadrature sigma-delta analog-to-digital (AD) converters. Generally, his research interests include AD techniques, such as sigma-delta variants and related interference mitigation algorithms.

Mikko Valkama was born in Pirkkala, Finland, on November 27, 1975. He received the M.Sc. and Ph.D. degrees (both with honors) in electrical engineering (EE) from Tampere University of Technology (TUT), Finland, in 2000 and 2001, respectively. In 2002 he received the Best Ph.D. Thesis – award by the Finnish Academy of Science and Letters for his dissertation entitled "Advanced I/Q signal processing for wideband receivers: models and algorithms." In 2003, he was working as a visiting researcher with the Communications Systems and Signal Processing Institute at SDSU, San Diego, CA. Currently, he is a Full Professor at the Department of Communications Engineering at TUT, Finland. He has been involved in organizing conferences, like the IEEE SPAWC'07 (Publications Chair) held in Helsinki, Finland. His general research interests include communications signal processing, estimation and detection techniques, signal processing algorithms for software defined flexible radios, digital transmission techniques such as different variants of multicarrier modulation methods and OFDM, and radio resource management for *ad hoc* and mobile networks.

Publication 3

M. Allén, J. Marttila, and M. Valkama, "Digitally-enhanced wideband analog-digital interfaces for future cognitive radio devices," in *Proceedings of the 8th IEEE International NEWCAS Conference (NEWCAS2010)*, Montréal, QC, Canada, June 2010, pp. 361–364. DOI: 10.1109/NEWCAS.2010.5604009

© 2010 IEEE. Reprinted, with permission, from the Proceedings of the 8th IEEE International NEWCAS Conference (NEWCAS2010).

In reference to IEEE copyrighted material which is used with permission in this thesis, the IEEE does not endorse any of Tampere University of Technology's products or services. Internal or personal use of this material is permitted. If interested in reprinting/republishing IEEE copyrighted material for advertising or promotional purposes or for creating new collective works for resale or redistribution, please go to http://www.ieee.org/publications_standards/publications/rights/rights_link.html to learn how to obtain a License from RightsLink.

Digitally-Enhanced Wideband Analog-Digital Interfaces for Future Cognitive Radio Devices

Markus Allén, Jaakko Marttila and Mikko Valkama
Department of Communications Engineering
Tampere University of Technology
P.O. Box 553, FI-33101, Tampere, FINLAND
markus.allen@tut.fi, jaakko.marttila@tut.fi, mikko.e.valkama@tut.fi

***Abstract*—The cognitive radio concept has gained widespread interest to avoid spectral scarcity in next generation mobile communications systems. However, there are major challenges from the radio transceiver electronics point of view. This paper addresses the analog-to-digital converter saturation problem due to highly-varying signal conditions in wideband cognitive radio receivers. Two different post-processing approaches are proposed here to mitigate this nonlinear distortion. Their performance is compared to current state-of-the-art methods using laboratory radio signal measurements with commercially available hardware.**

I. Introduction

Several recent studies have indicated that there are considerable temporal and spatial variations (i.e., inactivity) in the truly realized radio spectrum utilization [1]. This offers room for intelligent or cognitive radio (CR) devices, being able to sense the characteristics of their spectral environment and flexibly adapt their own radio waveforms, to communicate over the spatially and/or temporally unused spectral chunks as secondary users without affecting the licensed or primary operation. However, one major bottleneck related to the deployment of CR devices is the implementation of the needed radio transmitters and receivers [2]-[4]. The used radios should operate over extremely wide bandwidths, covering possibly several decades of radio spectrum as a whole, and be able to sense and communicate under extreme dynamic range conditions (possibly up to 100 dB). Especially for analog radio frequency (RF) modules and analog-digital (A/D) interfaces, the requirements on the sensitivity and linearity are essentially pushed way beyond the reach of state-of-the-art radio electronics [5], [6].

In a wideband receiver, with this kind of dynamics in the received signal, any nonlinearity in the receiver can be crucial from the weak signal point of view. The weak desired signal can be lost if, e.g., intermodulation distortion (IMD) from a strong blocking signal falls on this frequency band [1]. This is the main scenario discussed in this paper from the A/D converter (ADC) nonlinearity point of view. The source of nonlinearity is here assumed to be waveform clipping in the input of the ADC of a radio receiver due to improper signal conditioning. This is a probable case in a wideband receiver, where multiple high-power blocking signals can be present causing large fluctuations in the instantaneous signal dynamics [7].

ADC nonidealities, and related mitigation methods, have been widely discussed in the current literature, but most of the proposed methods demand calibration or offline characterization [8]-[11], which is not usually feasible for mobile receivers. Clipping, as a phenomenon, also differs from the other nonlinearities because look-up table based compensation is not possible. This is because there is no information left about the original waveform behavior during clipping.

In Section II, this paper proposes an enhanced adaptive interference cancellation (E-AIC) method which is an online post-processing technique and thus appropriate for mobile devices. Compared to our earlier adaptive interference cancellation (AIC) method [12], [13], it requires an additional ADC but its performance is significantly better. The secondary ADC is allowed to have low resolution and thus it can be very low-cost. Notice that conceptually similar ideas of using alternate or additional analog signal branches have been proposed in [14] for receiver LNA and mixer linearization.

Section III, in turn, proposes a different kind of approach to mitigate clipping distortion by recovering the clipping waveform using interpolation. The proposed maximum selection interpolation (MSI) technique is partly based on the interpolation method proposed by T. Tomioka *et al.* [15]. However, the MSI performs better due to more optimized filter design, lower computational complexity and different kind of decision logic. In Section IV, all the discussed methods are compared using radio signal laboratory measurements with commercially available hardware. Finally, Section V concludes the paper.

II. Enhanced Adaptive Interference Cancellation Method

In the A/D conversion context, the original AIC method for reducing nonlinear distortion was discussed in [12] and [13]. From the clipping distortion mitigation point of view, it has a limited performance due to the distorted reference signal. This problem is bypassed in the E-AIC method, which is proposed in this section.

This work was supported by the Academy of Finland (under the project "Understanding and Mitigation of Analog RF Impairments in Multiantenna Transmission Systems"), the Finnish Funding Agency for Technology and Innovation (Tekes, under the project "Advanced Techniques for RF Impairment Mitigation in Future Wireless Radio Systems") and the Technology Industries of Finland Centennial Foundation.

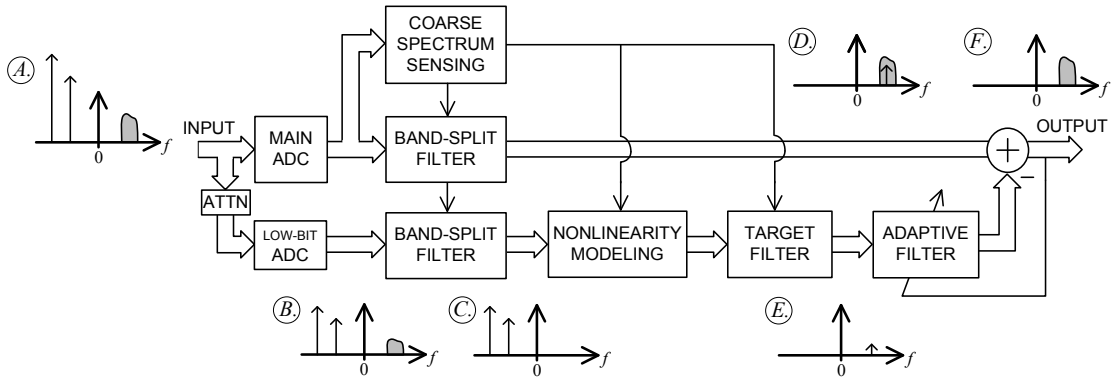

Fig. 1. Enhanced adaptive interference cancellation (E-AIC) method for reducing A/D converter clipping distortion at a weak signal band stemming from high-power blocking signals. Simplified spectra illustrate the processing flow using only a single intermodulation component as an example.

The working principle of E-AIC is illustrated in Fig. 1 with simplified spectrum examples. Due to improper input signal conditioning the received signal (see spectrum figure *A*) is unintentionally clipped in the main ADC and thus the IMD of the strong blocker signals is falling on top of the weak signal. The band-split filter removes the out-of-band spectral content and the distorted weak signal is shown in spectrum *D* (for simplification only a single IMD component is shown here). Concurrently, the input signal is digitized with a low-bit ADC using proper attenuation to prevent clipping (see spectrum *B*). Here only the strongest blocking signals are of interest to create an accurate reference signal for interference cancellation. The band-split filter preserves only the signal content outside the weak signal band as shown in spectrum *C*. The purpose of the nonlinearity modeling block is to regenerate the IMD present in the weak signal band based on the polynomial model of the form

$$\hat{s}_{\mathrm{ref}} = c_3 s_{\mathrm{ref}}^3 + c_5 s_{\mathrm{ref}}^5 + \ldots \quad (1)$$

where s_{ref} and $\hat{s}_{\mathrm{ref}}$ are the reference signal before and after the nonlinearity modeling, respectively. Equation (1) is assuming zero-symmetric clipping, but non-symmetric clipping (contains DC offset prior to clipping) can be taken into account by adding also even powers to the model. After the modeling stage, the target filter is used to select only the distortion located at the weak signal band (see spectrum *E*). The coefficients $c_3, c_5, \ldots$ are found using an adaptive filter, which can be implemented, e.g., using the LMS algorithm. After that, the regenerated distortion is subtracted from the weak signal in order to remove the clipping-induced intermodulation distortion. The compensated signal without the distortion is illustrated in spectrum *F*.

The coarse spectrum sensing block in Fig. 1 represents the outer-loop control mechanism which manages the nonlinearity modeling stage and all the filters according to the locations of the most sensitive frequency bands. The required location information can be acquired rather straightforwardly in frequency domain. This functionality brings additional flexibility to the proposed compensation technique and actually it is a fundamental requirement in cognitive radio solutions.

III. Clipping Compensation Using Interpolation

In a digitized waveform all the clipped samples can be thought as lost samples and interpolation is one way to replace those with better estimates. Fig. 2 (a) illustrates a waveform after oversampling A/D conversion. Due to the oversampling the waveform can be represented as a polyphase decomposition which is shown in Fig. 2 (a) using different colors and symbols for samples in different polyphase branches. The fundamental idea behind the proposed interpolation method is based on the fact that the subsequent samples in the oversampled waveform contain redundant information, i.e., a clipped sample in one polyphase branch can be recovered based on the corresponding samples in other branches using a proper fractional delay filter. In Fig. 2 (a) this would mean that we can recover the clipped samples in Branch 1 using samples in Branches 2, 3 and 4.

The block diagram of the proposed MSI method is shown in Fig. 2 (b). After the oversampling A/D conversion the polyphase decomposition is formed. Unclipped samples can be passed through intact meaning that they are filtered with a filter corresponding to a pure delay. When there is a clipped sample in one polyphase branch, the other branches provide estimates to replace the clipped sample. After that, the decision logic chooses the estimate that has the largest absolute value and the chosen estimate replaces the clipped sample in the oversampled waveform. This overall procedure inside the interpolation processing block (see the gray box in Fig. 2 (b)) can be iterated several times to achieve more accurate results. The iteration essentially means that more and more information about the clipped sample is extracted from the other samples. This is stemming from the fact that usually there are clipped samples involved in the estimation calculation meaning that the estimate is not perfect. However, in the next iteration round we have better estimates for all the clipped samples involved in calculating new estimates. After all the interpolation processing is carried out, the enhanced signal is downsampled as shown in Fig. 2 (b).

In the proposed MSI method, the polyphase branch filters are formed by first designing a low-pass FIR filter of which pass-band corresponds to the non-oversampled signal band-

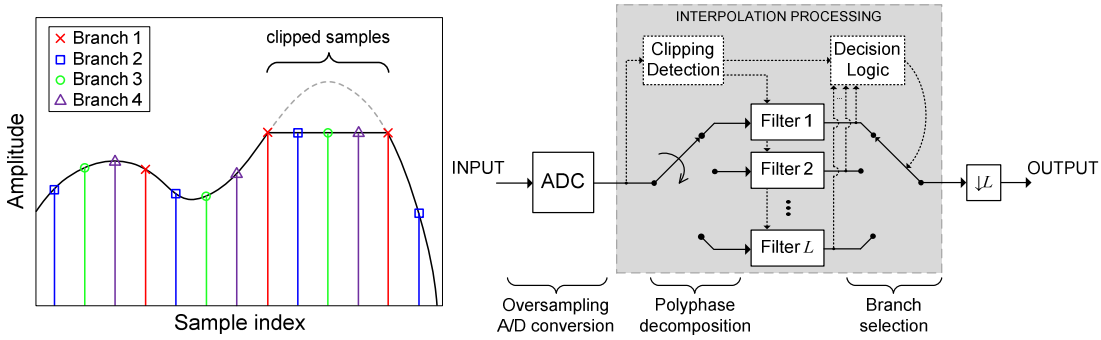

Fig. 2. (a) Illustration of a clipped waveform with oversampling factor of 4. Each polyphase branch has been depicted with different symbol and color. (b) Block diagram of the proposed maximum selection interpolation (MSI) method. A/D converter samples the input L times the rate of the final desired sampling rate. Polyphase filters provide estimates for a clipped sample and the decision logic chooses the estimate which has the highest absolute value to replace the clipped sample.

width, i.e., the normalized bandwidth of the pass-band is $1/L$, where L is the oversampling factor. If the overall impulse response is $h(n)$, the branch filters are

$$\begin{aligned} h_0(n) &= \{h(0), h(L), h(2L), \ldots\} \\ h_1(n) &= \{h(1), h(L+1), h(2L+1), \ldots\} \\ &\vdots \\ h_{L-1}(n) &= \{h(L-1), h(2L-1), h(3L-1), \ldots\}. \end{aligned} \tag{2}$$

The clipping detection box in Fig. 2 (b) is responsible for assigning right impulse response for every polyphase branch. The assignment depends on the location of the clipped sample, i.e., the filter $h_0(n)$ should be always in the branch where the current clipped sample is. For example, if the clipped sample is in the second branch, the Filters 1, 2, …, L in Fig. 2 (b) would be $h_{L-1}(n), h_0(n), h_1(n), \ldots, h_{L-2}(n)$, respectively.

IV. Measurement Results

This Section provides performance results from laboratory radio signal measurements using a commercial 14-bit ADC [16] and post-processing methods implemented in software. Both E-AIC and MSI methods are applied to the same test signal to obtain comparable results. In addition, performance of our original AIC method [12], [13] and Tomioka's interpolation technique [15] are given as a reference. Due to the limited amount of hardware reserved for the measurements, the low-bit ADC in E-AIC method is realized with the same 14-bit ADC and then the resolution is reduced by software.

The used test signal before and after clipping is illustrated in Fig. 3 both in time and frequency domain. It consists of five separate frequency bands with different bandwidths and power levels the overall dynamic range being in the order of 45 dB as a practical example case. The peak-to-average power ratio (PAPR) of the test signal is 7 dB before clipping and the sampling rate is 64 MHz for I and Q branches. Clipping level of 6 dB over the average power level of the test signal is chosen in Fig. 3 to demonstrate clipping phenomenon in time and frequency domain. Especially the strong blocker at -1 MHz is causing third order IMD to the weak signal band around +3 MHz which is considered to be the band of interest.

The performances of the post-processing methods are compared using signal-to-noise-and-distortion ratio (SNDR) gain as a figure-of-merit. The SNDR gain is defined as a relation of SNDRs of the weak signal band (around +3 MHz) before and after applying the post-processing method. The results with different clipping levels are shown in Fig. 4. Four iteration rounds were performed for interpolation techniques (MSI and Tomioka) using 32-tap polyphase branch filters to achieve the presented results. The proposed MSI method is clearly performing better although its complexity is smaller than Tomioka's. This is because MSI doesn't require the preliminary polynomial interpolation stage used in Tomioka's method (see [15] for details). In addition, MSI employs a properly designed FIR filter whereas Tomioka's method uses a truncated sinc function. From the performance point of view, also the decision logic for branch selection has a great effect. However, the performance of both interpolation methods is limited due to other ADC nonidealities which affect the estimation accuracy.

In AIC and E-AIC methods third, fifth and seventh order nonlinearities were modeled to obtain the results in Fig. 4. Both are performing better than the interpolation techniques, because AIC and E-AIC are able to remove any kind of nonlinear distortion regardless of its source (like mixer and LNA nonlinearities in practice) whereas the interpolation can only consider the clipping distortion. The proposed E-AIC method is almost able to reach the ideal AIC performance level when a 7-bit secondary ADC is used with 7-dB input attenuation. Here the ideal AIC means that third, fifth and seventh order nonlinear distortion is removed using a perfect reference signal. The low SNDR gain with clipping levels 8-10 dB can be explained with the fact that there is not much distortion to remove at first place due to very mild clipping. Other reasons for the limited performance gains are inaccuracies in the nonlinearity modeling as well as in adaptive filter coefficients.

V. Conclusions

This paper focused on the saturation problem of ADCs stemming from highly-varying signal dynamics in wideband cognitive radio receivers. Two post-processing techniques were proposed to compensate the nonlinear distortion in a clipped signal. Their performance were verified using laboratory radio signal measurements and both the techniques showed significant improvement in performance compared to the current state-of-the-art methods in the literature.

References

[1] J. Yang, R. W. Brodersen and D. Tse, "Addressing the dynamic range problem in cognitive radios," in *Proc. IEEE Int. Conf. Communications* (ICC-07), Glasgow, Scotland, June 2007, pp. 5183-5188.

[2] B. Razavi, "Challenges in the design of cognitive radios," in *Proc. IEEE Custom Integrated Circuits Conf.* (CICC-09), San Jose, CA, Sept. 2009, pp. 391-398.

[3] D. Cabric, "Addressing feasibility of cognitive radios," *IEEE Signal Processing Mag.*, vol. 25, no. 6, pp. 85-93, Nov. 2008.

[4] P.-I. Mak, S.-P. U, and R. P. Martins, "Transceiver architecture selection: review, state-of-the-art survey and case study", *IEEE Circuits and Systems Mag.*, vol. 7, 2nd quarter 2007, pp. 6-25.

[5] B. Le, T. W. Rondeau, J. H. Reed and C. W. Bostian, "Analog-to-digital converters," *IEEE Signal Processing Mag.*, vol. 22, no. 6, pp. 69-77, Nov. 2005.

[6] A. Rusu, D. Rodriguez de Llera Gonzalez and M. Ismail, "Reconfigurable ADCs enable smart radios for 4G wireless connectivity," *IEEE Circuits Devices Mag.*, vol. 22, no. 3, pp. 6-11, May-June 2006.

[7] C. Svensson, "The blocker challenge when implementing software defined radio receiver RF frontends," *Analog Integrated Circuits and Signal Processing*, Dec. 2009.

[8] P. Arpaia, P. Daponte and S. Rapuano, "A state of the art on ADC modeling," *Elsevier J. Computer Standards & Interfaces*, vol. 26, no. 1, pp. 31-42, Jan. 2004.

[9] N. Björsell and P. Händel, "Dynamic behavior models of analog to digital converters aimed for post-correction in wideband applications," in *XVIII Imeko World Congress 11th Workshop on ADC Modelling and Testing*, Rio de Janeiro, Brazil, 2006.

[10] L. De Vito, H. Lundin and S. Rapuano, "Bayesian calibration of a lookup table for ADC error correction," *IEEE Trans. Instrum. Meas.*, vol. 56, no. 3, pp. 873-878, June 2007.

[11] P. Arpaia, L. Michaeli and S. Rapuano, "Model-based compensation of SAR nonlinearity," *IEEE Trans. Instrum. Meas.*, vol. 58, no. 3, pp. 541-550, March 2009.

[12] M. Allén, J. Marttila and M. Valkama, "Digital post-processing for reducing A/D converter nonlinear distortion in wideband radio receivers," in *Proc. Forty-Third Asilomar Conf. Signals, Syst., and Computers*, Pacific Grove, CA, Nov. 2009.

[13] M. Allén, J. Marttila and M. Valkama, "Modeling and mitigation of nonlinear distortion in wideband A/D converters for cognitive radio receivers," *European Microwave Assoc. Int. J. Microwave and Wireless Technologies*, April 2010.

[14] E. A. Keehr and A. Hajimiri, "Equalization of third-order intermodulation products in wideband direct conversion receivers," *IEEE J. Solid-State Circuits*, vol. 43, no. 12, pp. 2853-2867, Dec. 2008.

[15] T. Tomioka, R. Sakata, T. Horiguchi, T. Tomizawa and K. Inoue, "A/D converter clipping noise suppression for high-sensitivity carrier-sensing of cognitive radio transceiver," in *IEEE Global Telecommunications Conference* (GLOBECOM'07), Washington, DC, Nov. 2007.

[16] Analog Devices, *AD9248 Data Sheet*, rev. A, March 2005. Available online at http://www.analog.com/

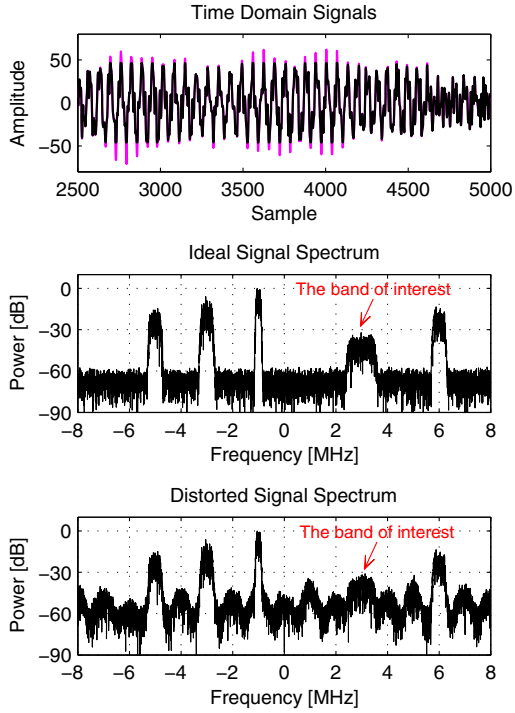

Fig. 3. Upper part: digitized waveform in time domain with and without clipping. Middle part: the unclipped waveform in frequency domain. Lower part: the clipped waveform in frequency domain illustrating the third-order intermodulation distortion at the weak signal around +3 MHz originating from the signal at -1 MHz. This laboratory measurement was carried out using 14-bit A/D converter clipping level being 6 dB over the average power level of the signal.

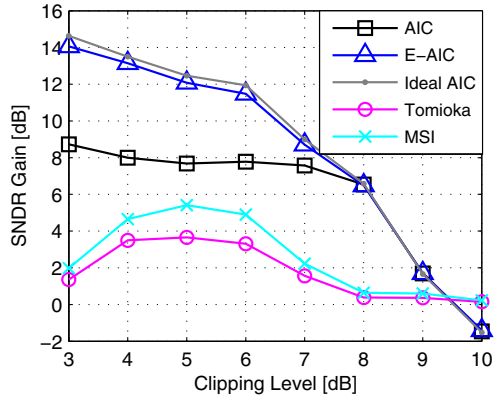

Fig. 4. SNDR gain comparison between different clipping compensation techniques. Clipping level is described as a number of dBs above the average power level of the signal.

Publication 4

M. Allén, J. Marttila, and M. Valkama, "Iterative signal processing for mitigation of wideband ADC nonidealities in cognitive radio receiver," in *Proceedings of the 19th European Signal Processing Conference (EUSIPCO2011)*, Barcelona, Spain, Aug. 2011, pp. 2279–2283.

© 2011 EURASIP. First published in the Proceedings of the 19th European Signal Processing Conference (EUSIPCO-2011) in 2011, published by EURASIP.

ITERATIVE SIGNAL PROCESSING FOR MITIGATION OF WIDEBAND ADC NONIDEALITIES IN COGNITIVE RADIO RECEIVER

Markus Allén, Jaakko Marttila, and Mikko Valkama

Department of Communications Engineering, Tampere University of Technology
P.O. Box 553, FI-33101, Tampere, FINLAND
markus.allen@tut.fi, jaakko.marttila@tut.fi, mikko.e.valkama@tut.fi

ABSTRACT

Large input signal dynamics is an essential problem in modern wideband communication receivers such as cognitive radios. If the receiver front-end and analog-to-digital interface cannot respond to varying conditions, a high amount of nonlinear distortion is caused due to the clipping. This paper proposes a robust digital signal processing method to iteratively remove unintentional clipping distortion in OFDM receivers. Using computer simulations it is shown that the symbol error ratio of a heavily clipped signal in a fading channel situation can be reduced practically to the level of an equivalent non-clipped signal. In other words, the proposed method can remove all the essential clipping distortion.

1. INTRODUCTION

In modern wideband cognitive radio receivers, unintentional signal clipping is a potential problem due to the highly variable signal dynamics. This is partially stemming from the high peak-to-average power ratio (PAPR) of modern communication waveforms. Other crucial cause for the variable signal dynamics in a cognitive radio front-end is high-power transmissions of adjacent-channel users. This paper proposes a novel decision-aided iterative approach for digitally compensating unintentional clipping of analog-to-digital (A/D) converters in a scenario where multiple users are transmitting orthogonal frequency division multiplexing (OFDM) signals. The focus is particularly on the case where the reception of a weak signal is compromised due to the high amount of clipping distortion stemming from a considerably stronger adjacent-channel signal.

In the current literature, there are just a few digital signal processing methods for reducing unintentional signal clipping occurring *on the receiver side* [1], [2], [3]. All of them are rather general methods and do not take into account the specific properties of OFDM signals. On the other hand, OFDM-related clipping mitigation methods in the current literature focus on deliberate clipping to reduce signal PAPR *on the transmitter side* [4], [5], [6]. These methods assume that the exact clipping level is known, which is a fair assumption when the clipping is intentional. However, this paper proposes a method against unintentional clipping, which means that also the occurred clipping level has to be estimated. Another challenge in this scenario is the channel estimation since the clipping occurs after the signal has propagated through the radio channel.

The proposed method is based on the idea that bit decisions can be exploited to create an estimate of the clipping distortion in the received signal. In the literature, decision-based approaches have been found to be successful for mitigating many RF impairments, e.g., phase noise [7], [8]. The method proposed in this paper is using the PAPR reduction scheme discussed in [5], [6] as a starting point, and extends that to the challenging case of receiver clipping in the presence of neighboring channels. This paper shows through computer simulations that the proposed method is robust against different kind of estimation errors and is able to extensively remove clipping distortion.

The rest of the paper is organized as follows. Section 2 gives the basics of modeling the clipping of OFDM signals relying on the results provided in the current literature. Based on this signal modeling, Section 3 proposes a novel clipping compensation approach. Its performance is analyzed with computer simulations in Section 4 and finally Section 5 draws conclusions.

2. CLIPPING OF OFDM SIGNALS

One OFDM symbol with $N = JN_A$ subcarriers (SC) has N_A active SCs and J denotes the oversampling factor. All SC indices are defined as a set $\Omega = \{-N/2, -N/2+1, ..., N/2-1\}$. The active SCs contain a sequence of complex data symbols X_k, $k \in \Omega_A = \{-N_A/2, ..., -1, 1, ..., N_A/2\}$. Zero padding is used so that $X_k = 0$, $k \in \Omega \setminus \Omega_A$. Now the baseband OFDM symbol is defined as

$$x(t) = \frac{1}{\sqrt{N}} \sum_{k=-N/2}^{N/2-1} X_k e^{j2\pi kt/T_s}, \quad 0 \le t \le T_s, \tag{1}$$

where T_s is the OFDM symbol duration. This model does not include the cyclic prefix (CP), which is required for a successfully working OFDM system in frequency-selective fading scenarios. The CP is omitted from the mathematical notation of the paper to make it simpler. This is justified since the CP does not have any significance in the presented analysis. However, due to the importance of CP in practical systems, it is implemented in the simulations shown in Section 4.

This paper assumes that the signal clipping in the A/D conversion stage can be approximated with a zero-symmetric hard clipping. Denoting a general received signal by $y(t) = y_I(t) + jy_Q(t) = h(t) * x(t) + w(t)$, where $h(t)$ is the channel impulse response and $w(t)$ denotes additive noise, the clipped received signal $\tilde{y}(t) = \tilde{y}_I(t) + j\tilde{y}_Q(t)$ is given by

$$\tilde{y}_I(t) = \begin{cases} y_I(t), & |y_I(t)| < V_0 \\ V_0, & y_I(t) \ge V_0 \\ -V_0, & y_I(t) \le -V_0 \end{cases} \tag{2}$$

for the I branch and similarly for the Q branch. Here V_0 is the maximum acceptable input level of the A/D converter and it is assumed to be equal for both branches. In practice, it is convenient

© EURASIP, 2011 - ISSN 2076-1465

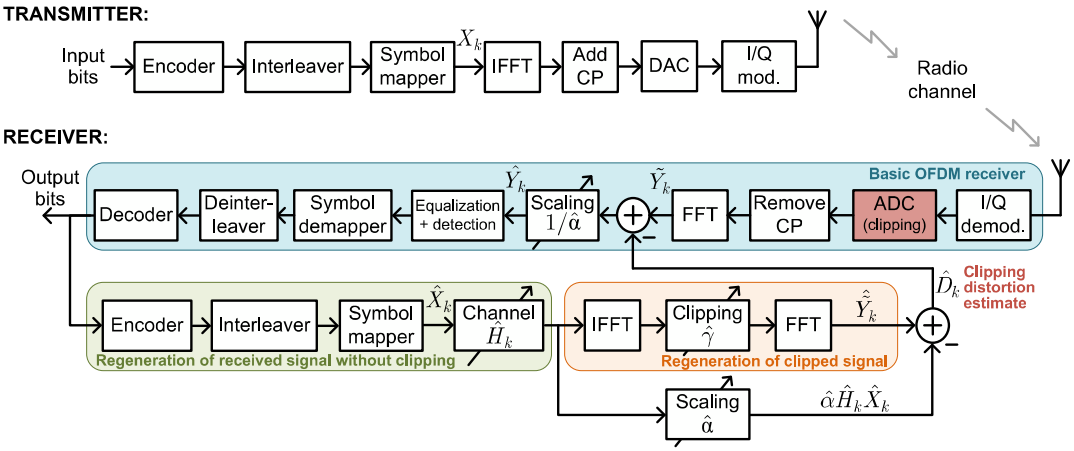

Figure 1 – Block diagram of the overall OFDM system for one transmitter and receiver. ADC on the receiver side causes undesired clipping distortion, which can be removed using the proposed method. Capital letters denote frequency domain signals at different stages.

to define the clipping level as a ratio of V_0 and the average power level of the complex signal before clipping P_{in}. Therefore, the clipping level γ is defined as

$$\gamma = \frac{V_0}{\sqrt{P_{\text{in}}/2}}. \tag{3}$$

However, it is not very simple to directly apply the clipping model in (2) for clipping compensation purposes. Therefore, this paper models clipping distortion using Bussgang's theorem [9]. This has already been shown to be an appropriate approach [10], [11]. Clipping is a memoryless nonlinearity and assuming $y(t)$ to be Gaussian, it is possible to write according to Bussgang's theorem that the clipped version is then

$$\tilde{y}(t) = \alpha y(t) + d(t). \tag{4}$$

This means that the clipping attenuates the original signal with a factor α and additionally causes additive clipping distortion $d(t)$, which is uncorrelated with $y(t)$. It is shown in [12] that the attenuation factor is

$$\alpha = \text{erf}\left(\frac{\gamma}{\sqrt{2}}\right) \tag{5}$$

in the case where $y_I(t)$ and $y_Q(t)$ are Gaussian.

3. DECISION-AIDED ITERATIVE CLIPPING COMPENSATION APPROACH

Subsection 3.1 introduces the clipping compensation algorithm in general. After that Subsection 3.2 discusses about details of implementation in multi-user scenarios.

3.1 Algorithm Description

The whole OFDM transmission chain is illustrated with a block diagram in Figure 1. For simplification, the figure shows only one transmitter although the proposed compensation algorithm on the receiver side is able to jointly process the data of several users as is discussed in Subsection 3.2. In order to simplify the notation of the algorithm description, only one OFDM symbol duration is considered in the equations. This is reasonable since the clipping compensation can be performed individually for every OFDM symbol.

If the received signal gets clipped in the A/D converter (ADC) due to the improper input signal conditioning, the resulting clipping distortion can be mitigated as shown in Figure 1. The basic idea is that the received signal is first detected in a traditional manner. Then, an estimate of the received signal with and without clipping is generated based on the obtained bit decisions. An estimate of the clipping distortion can be found by subtracting the estimate of the non-clipped signal from the clipped one. Now, this estimated clipping distortion can be removed from the original received signal and the signal is detected again. In the following paragraphs, the compensation approach is described in more detailed manner and Table 1 summarizes the key steps.

In ideal case, the received signal would be digitized without any clipping. After A/D conversion, CP removing and taking FFT, this frequency-domain signal can be expressed as

$$Y_k = H_k X_k + W_k, \quad k \in \Omega, \tag{6}$$

where H_k and W_k are the channel gain and the additive white Gaussian noise term for the kth SC, respectively. On the other hand, in case of clipping, the received signal in frequency domain (see Figure 1) is

$$\begin{aligned} \tilde{Y}_k &= \alpha Y_k + D_k \\ &= \alpha (H_k X_k + W_k) + D_k, \quad k \in \Omega \end{aligned} \tag{7}$$

as defined according to Bussgang's theorem in (4). Before starting the clipping compensation procedure, the data symbols are detected using $\tilde{Y}_k$, $k \in \Omega_A$. This is illustrated with the "equalization + detection" block in Figure 1. This stage also includes channel estimation and compensation using pilot SCs since it is an essential requirement for the symbol detection. The channel gain estimates for active SCs are denoted with $\hat{H}_k$, $k \in \Omega_A$. Finally, the output bits are obtained after deinterleaving and decoding.

In the first stage of the clipping compensation, the detected output bits are used to regenerate the transmitted OFDM signal. Since this is an estimate of the sent data, the frequency-domain signal is denoted as $\hat{X}_k$, $k \in \Omega$ in Figure 1. The signal is then exposed to the estimated channel and clipping process in order to regenerate the clipped received signal. The clipping regeneration is performed in time domain using the estimated clipping level $\hat{\gamma}$,

which can be obtained by estimating (3), i.e., by checking the absolute maximum level of the signal after ADC ($\hat{V}_0$) and calculating the average power level of $\hat{X}_k,\ k \in \Omega$ ($\hat{P}_{\text{in}}$). The time domain clipping process essentially creates a signal that can be expressed in frequency domain as $\hat{\tilde{Y}}_k = \hat{\alpha}\hat{H}_k\hat{X}_k + \hat{D}_k,\ k \in \Omega_A$, where $\hat{\alpha}$ is the estimate of the attenuation factor. From $\hat{\tilde{Y}}_k,\ k \in \Omega_A$ it is possible to extract the clipping distortion estimate $\hat{D}_k,\ k \in \Omega_A$ by removing the wanted signal part. The lowest branch in Figure 1 is illustrating this by generating a non-clipped but attenuated estimate of the received signal, namely $\hat{\alpha}\hat{H}_k\hat{X}_k,\ k \in \Omega_A$, where $\hat{\alpha}$ is calculated from (5) using $\hat{\gamma}$. Now the estimate of the clipping distortion $\hat{D}_k,\ k \in \Omega_A$ can be obtained as

$$\hat{D}_k = \hat{\tilde{Y}}_k - \hat{\alpha}\hat{H}_k\hat{X}_k, \quad k \in \Omega_A. \tag{8}$$

The out-of-band clipping distortion is ignored since the processing focuses only to active SCs Ω_A as implied in (8). Finally, the estimated clipping distortion is removed from the received signal $\tilde{Y}_k,\ k \in \Omega_A$ to provide cleaner signal

$$\hat{Y}_k = \frac{1}{\hat{\alpha}}\left(\tilde{Y}_k - \hat{D}_k\right), \quad k \in \Omega_A \tag{9}$$

for a new round of channel estimation and symbol detection. If (7) is substituted in (9), the estimate of the received signal without clipping can be written as

$$\hat{Y}_k = \frac{\alpha}{\hat{\alpha}}(H_kX_k + W_k) + \frac{1}{\hat{\alpha}}\left(D_k - \hat{D}_k\right), \quad k \in \Omega_A. \tag{10}$$

From this form it is easy to see that having exactly correct estimates $\hat{\alpha}$ and $\hat{D}_k,\ k \in \Omega_A$ will produce totally non-clipped signal, which is equivalent to (6).

Errors in the first symbol detection cause that all the clipping distortion is not removed on the first round. By iterating, the compensation process will produce better and better estimate of the clipping distortion and therefore symbol detection results improve. In every iteration, new channel estimates $\hat{H}_k,\ k \in \Omega_A$, clipping level $\hat{\gamma}$, and attenuation factor $\hat{\alpha}$ are calculated.

3.2 Multi-User Aspects

The proposed compensation approach is applicable both in uplink (UL) and downlink (DL) scenarios, but there are certain differences in case of multiple users. In DL direction, the sequence $X_k,\ k \in \Omega_A$ consists of symbols belonging to several users. In order to compensate clipping distortion in the best possible manner, the mobile receiver should be able to process the symbols of all users and estimate the channel over the whole band. This increases the amount of required processing compared to the case where the mobile concentrates only on its dedicated band.

Also in UL direction the sequence $X_k,\ k \in \Omega_A$ contains symbols of several users. Additionally, channel estimates $\hat{H}_k,\ k \in \Omega_A$ have to be obtained piecewise since different users have different channels. The UL scenario is more feasible than DL from the implementation point of view, because the base station processes the signals of every user in any case even if there is no clipping compensation. In addition, base stations have more computing power making more complex DSP algorithms viable.

4. SIMULATION RESULTS

Presented computer simulations consider an UL scenario of two individual users whose signals propagate through different realizations of extended ITU-R Vehicular A channel [13]. It is assumed

Table 1 – The proposed receiver clipping compensation algorithm.

Initialization: for $k \in \Omega_A$

1. Set $i = 0$, $\hat{\alpha}^{(0)} = 1$ and $\hat{D}_k^{(0)} = 0$
2. Obtain $\hat{H}_k^{(i)}$ from $\hat{Y}_k^{(i)} = \frac{1}{\hat{\alpha}^{(i)}}\left(\tilde{Y}_k - \hat{D}_k^{(i)}\right)$
3. Detect/decode $\hat{Y}_k^{(i)}$ after channel compensation

Iteration: Increase i by one and do the following steps for $k \in \Omega_A$

1. Create $\hat{X}_k^{(i)}$ based on the decoded bits
2. Estimate $\hat{\gamma}^{(i)}$ and $\hat{\alpha}^{(i)}$
3. Clip $\hat{H}_k^{(i-1)}\hat{X}_k^{(i)}$ in *time domain* to create $\hat{\tilde{Y}}_k^{(i)}$
4. Calculate $\hat{D}_k^{(i)} = \hat{\tilde{Y}}_k^{(i)} - \hat{\alpha}^{(i)}\hat{H}_k^{(i-1)}\hat{X}_k^{(i)}$
5. Remove distortion, i.e., $\hat{Y}_k^{(i)} = \frac{1}{\hat{\alpha}^{(i)}}\left(\tilde{Y}_k - \hat{D}_k^{(i)}\right)$
6. Obtain $\hat{H}_k^{(i)}$ from $\hat{Y}_k^{(i)}$
7. Detect/decode $\hat{Y}_k^{(i)}$ after channel compensation

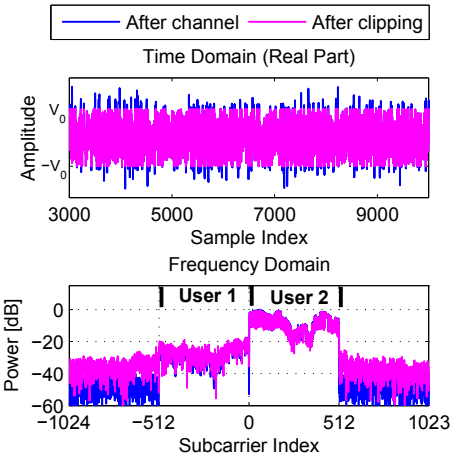

Figure 2 – Upper part: piece of the real branch signal illustrated in time domain before and after clipping, the clipping level being 6 dB above the average power level of the signal. Lower part: spectrum illustration of the signal before and after clipping. Frequency bands corresponding to Users 1 and 2 are denoted in the spectrum.

that the channels stay static over ten OFDM symbols. The average received signal power for User 1 is 15 dB less than for User 2. Both signals contain 512 active SCs of which every eighth SC is used as a pilot. Thus for the composite signal processed on the receiver side $N_A = 1024$. It is also assumed that the oversampling factor $J = 2$. The sampling rate in the simulations is 30.72 MHz, SC spacing is 15 kHz, and the SC modulation for both users is 16-QAM. Channel coding and interleaving are not used in the simulations since they are not on the main focus of this paper. Thus only raw symbol decisions are used in the iterative processing. Figure 2 illustrates the overall simulation scenario in time and frequency domains when $\gamma = 6$ dB and PAPR for the overall waveform is 10.5 dB.

Raw symbol error ratios (SER) for User 1 and 2 as a function of compensation iteration rounds are presented in Figure 3 for the scenario described earlier. All the results are averaged over 10,000 OFDM symbols, i.e., 1,000 independent channel realizations. Iteration round 0 refers to the received uncompensated signal. Using ideal channel estimates and non-clipped signal, the lower bound for SER in this scenario can be found. As shown in Figure 3, the proposed compensation algorithm is able to remove almost all the clipping distortion from the signal in case of perfect channel knowledge. There is a difference between SERs of User 1 and 2 because the signal of User 1 is more attenuated and therefore more affected by the noise. Here the average received signal-to-noise ratio (SNR) is defined as

$$SNR_{k,u} = \frac{E\left[|H_k X_k|^2\right]}{E\left[|W_k|^2\right]}, \quad k \in \Omega_{A,u}, \tag{11}$$

where u is user index. For User 1 $\Omega_{A,1} = \{-N_A/2,\ldots,-1\}$ and for User 2 $\Omega_{A,2} = \{1,\ldots,N_A/2\}$. In the case shown in Figure 3, $SNR_{k,1} = 26\,\text{dB}$, $k \in \Omega_{A,1}$ and $SNR_{k,2} = 41\,\text{dB}$, $k \in \Omega_{A,2}$.

In the simulations, the channel estimates for the data SCs are calculated using linear interpolation between pilot SCs. The acquired channel estimates are heavily affected by the clipping distortion and hence it takes several iterations to minimize SER. However, the proposed algorithm is robust enough to successfully remove most of the clipping distortion although there are channel estimation errors. In Figure 3, the performance gap between the non-clipped results with and without ideal channel knowledge is due to the limited accuracy of the used channel estimation method (pilot interpolation), which is not in any way related to the clipping phenomenon.

As more and more clipping distortion can be removed from the received signal by every iteration, also the channel estimates become more accurate. This is illustrated in Figure 4 where the mean square error (MSE) of the channel estimates is plotted subcarrier-wise. In this particular simulation scenario, the proposed algorithm is able to decrease the MSE approximately by 15 dB. The MSE after the compensation is very close to the ideal performance of the used channel estimation approach, which is illustrated with the MSE plot of non-clipped signal in Figure 4. Noticeable edge behavior in the figure is stemming from the applied channel estimation scheme. The distinct MSE peaks are due to the lack of pilot SCs on the right side of both user bands. The channel estimate provided by the last pilot SC is used as such for the remaining data SCs.

Another way to present the performance of the proposed clipping compensation algorithm is subcarrier-wise clipping distortion ratio (CDR). It describes the ratio of received signal power and clipping distortion power. Hence, the definition is

$$CDR_k = \frac{E\left[|Y_k|^2\right]}{E\left[\left|\hat{Y}_k - Y_k\right|^2\right]}, \quad k \in \Omega_A. \tag{12}$$

In Figure 5, the CDR results are shown for the previously described case before and after 10 iterations of the clipping compensation.

Especially on the first iteration round, the clipping distortion heavily affects the channel estimation accuracy which leads to symbol detection errors. If there are a lot of detection errors, the clipping distortion estimate is poor and it takes a considerable amount of iterations to make the received signal any cleaner. This can be seen from Figure 6, where SER results are plotted as a function of clipping level after ten iterations of the clipping compensation. It can be concluded from Figure 6 that heavy clipping causes

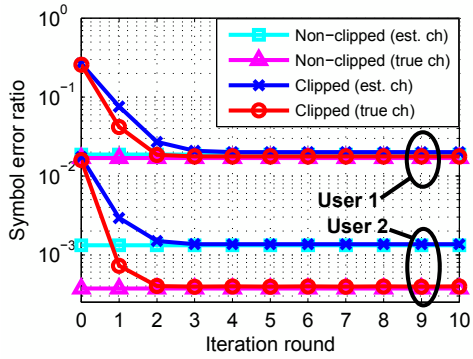

Figure 3 – SERs as a function of compensation iteration rounds for Users 1 and 2 when the clipping level is 6 dB over the average power level of the signal and average received SNR is 26 dB for User 1 and 41 dB for User 2. Iteration round 0 refers to uncompensated signal.

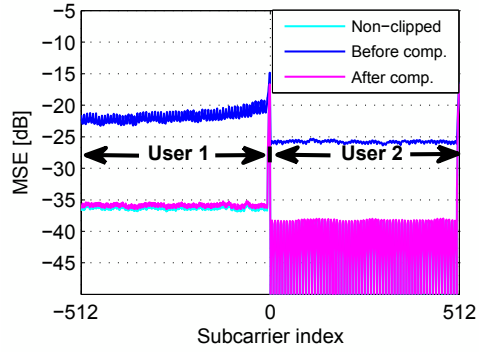

Figure 4 – Subcarrier-wise mean square error of channel estimates for both users before clipping compensation and after ten iterations of the proposed compensation. MSE for the non-clipped signal gives lower bound for the used channel estimation approach.

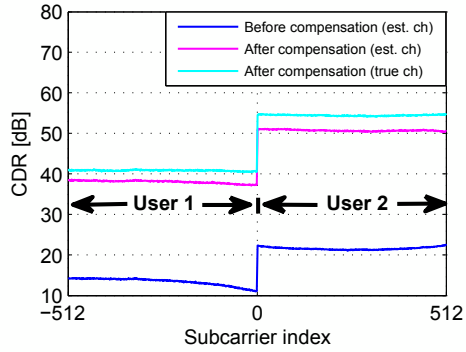

Figure 5 – Subcarrier-wise clipping distortion ratio for the case where clipping level is 6 dB over the average signal power level.

the channel estimation accuracy to decrease so much that the clipping compensation algorithm is unable to remove all the clipping distortion within 10 iterations. However, if the channel is known perfectly, the proposed clipping compensation algorithm performs

better in extreme clipping situations. This is also verified by Figure 7, which illustrates SERs after 10 iterations of the clipping compensation as a function of average received SNR of User 1. On average, the received SNR of User 2 is 15 dB more. In addition to channel estimation accuracy, also the accuracy of the clipping level estimate $\hat{\gamma}$ has effect on the compensation performance. However, the effect is rather small in the simulations, if the error in $\hat{\gamma}$ is within ± 0.5 dB. This conclusion was obtained from a simulation, where $\gamma = 6$ dB and the value of $\hat{\gamma}$ was intentionally varied.

5. CONCLUSION

This paper proposed a novel iterative method for removing unintentional clipping occurring in the A/D converter of a wideband OFDM receiver. The method was shown to be able to remove almost all the clipping distortion even in extreme conditions and therefore recover the performance to the level of non-clipped signals. It was found out that under heavy clipping the compensation performance is mostly limited by the accuracy of the channel estimation. In the future, it should be studied, if it is possible to take the clipping phenomenon better into account in the channel estimation process.

ACKNOWLEDGMENT

This work was supported by the Academy of Finland (under the project "Understanding and Mitigation of Analog RF Impairments in Multiantenna Transmission Systems"), the Finnish Funding Agency for Technology and Innovation (Tekes, under the project "Advanced Techniques for RF Impairment Mitigation in Future Wireless Radio Systems"), Austrian Center of Competence in Mechatronics (ACCM), Jenny and Antti Wihuri Foundation, and Tampere University of Technology Graduate School.

REFERENCES

[1] T. Tomioka, R. Sakata, T. Horiguchi, T. Tomizawa and K. Inoue, "A/D converter clipping noise suppression for high-sensitivity carrier-sensing of cognitive radio transceiver," in *Proc. IEEE Global Telecommunications Conf.*, Washington, DC, Nov. 2007, pp. 4170–4174

[2] M. Allén, J. Marttila and M. Valkama, "Modeling and mitigation of nonlinear distortion in wideband A/D converters for cognitive radio receivers," *European Microwave Assoc. Int. J. Microwave and Wireless Technologies*, vol. 2, no. 2, pp. 183–192, Apr. 2010.

[3] M. Allén, J. Marttila and M. Valkama, "Digitally-enhanced wideband analog-digital interfaces for future cognitive radio devices," in *Proc. 8th IEEE Int. NEWCAS Conf.*, Montréal, QC, Canada, June 2010, pp. 361–364.

[4] S. H. Han and J. H. Lee, "An overview of peak-to-average power ratio reduction techniques for multicarrier transmission," *IEEE Wireless Commun.*, vol. 12, no. 2, pp. 56–65, Apr. 2005.

[5] H. Chen and A. M. Haimovich, "Iterative estimation and cancellation of clipping noise for OFDM signals," *IEEE Commun. Lett.*, vol. 7, no. 7, pp. 305–307, July 2003.

[6] H. Zhang, X.-G. Xia, Q. Zhang and W. Zhu, "Iterative decision-aided clipping compensation its application to scalable video transmission with multiband OFDM," *IEEE Trans. Veh. Technol.*, vol. 56, no. 2, pp. 756–765, Mar. 2007.

[7] D. Petrovic, W. Rave and G. Fettweis, "Effects of phase noise on OFDM systems with and without PLL: Characterization and compensation," *IEEE Trans. Commun.*, vol. 55, no. 8, pp. 1607–1616, Aug. 2007.

[8] V. Syrjälä and M. Valkama, "Receiver DSP for OFDM systems impaired by transmitter and receiver phase noise," in *Proc. Int. Conf. Communications 2011*, Kyoto, Japan, June 2011.

[9] J. J. Bussgang, "Crosscorrelation functions of amplitude distorted Gaussian signals," MIT Res. Lab. Electron., Cambridge, MA, Tech. Rep. 216, Mar. 1952.

[10] H. Ochiai and H. Imai, "Performance analysis of deliberately clipped OFDM signals," *IEEE Trans. Commun.*, vol. 50, no. 1, pp. 89–101, Jan. 2002.

[11] H. E. Rowe, "Memoryless nonlinearities with Gaussian inputs: Elementary results," *Bell Syst. Tech. J.*, vol. 61, no. 7, pp. 1519–1525, Sept. 1982.

[12] L. Cheded, "Invariance property of Gaussian signals: a new interpretation, extension and applications," *Circuits, Syst., and Signal Process.*, vol. 16, no. 5, pp. 523–536, Sept. 1997.

[13] T. B. Sørensen, P. E. Mogensen and F. Frederiksen, "Extension of the ITU channel models for wideband (OFDM) systems," in *Proc. IEEE 62nd Vehicular Technology Conf.*, Dallas, TX, Sept. 2005, pp. 392–396.

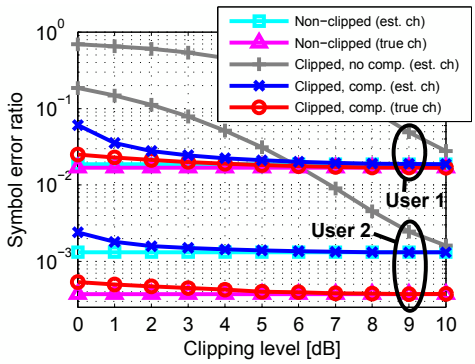

Figure 6 – SERs as a function of clipping level for Users 1 and 2 after 10 iterations of clipping compensation, average received SNR being 26 dB for User 1 and 41 dB for User 2.

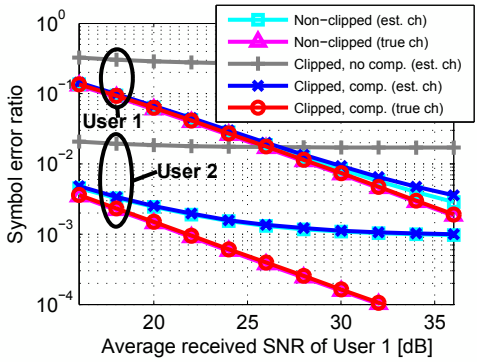

Figure 7 – SERs as a function of average received SNR of the weaker signal (User 1) after 10 iterations of clipping compensation, clipping level being 6 dB. The average received SNR for User 2 is 15 dB higher than for User 1.

Publication 5

M. Allén, T. Levanen, J. Marttila, and M. Valkama, "Iterative signal processing for mitigation of analog-to-digital converter clipping distortion in multiband OFDMA receivers," *Journal of Electrical and Computer Engineering*, vol. 2012, 16 pages. DOI: 10.1155/2012/532560

Copyright © 2012 Markus Allén et al. This is an open access article distributed under the Creative Commons Attribution License, which permits unrestricted use, distribution, and reproduction in any medium, provided the original work is properly cited.

Hindawi Publishing Corporation
Journal of Electrical and Computer Engineering
Volume 2012, Article ID 532560, 16 pages
doi:10.1155/2012/532560

Research Article

Iterative Signal Processing for Mitigation of Analog-to-Digital Converter Clipping Distortion in Multiband OFDMA Receivers

Markus Allén, Toni Levanen, Jaakko Marttila, and Mikko Valkama

Department of Communications Engineering, Tampere University of Technology, P.O. Box 553, 33101 Tampere, Finland

Correspondence should be addressed to Markus Allén, markus.allen@tut.fi

Received 31 May 2011; Revised 23 October 2011; Accepted 31 October 2011

Academic Editor: Tzi-Dar Chiueh

Copyright © 2012 Markus Allén et al. This is an open access article distributed under the Creative Commons Attribution License, which permits unrestricted use, distribution, and reproduction in any medium, provided the original work is properly cited.

In modern wideband communication receivers, the large input-signal dynamics is a fundamental problem. Unintentional signal clipping occurs, if the receiver front-end with the analog-to-digital interface cannot respond to rapidly varying conditions. This paper discusses digital postprocessing compensation of such unintentional clipping in multiband OFDMA receivers. The proposed method iteratively mitigates the clipping distortion by exploiting the symbol decisions. The performance of the proposed method is illustrated with various computer simulations and also verified by concrete laboratory measurements with commercially available analog-to-digital hardware. It is shown that the clipping compensation algorithm implemented in a turbo decoding OFDM receiver is able to remove almost all the clipping distortion even under significant clipping in fading channel circumstances. That is to say, it is possible to nearly recover the receiver performance to the level, which would be achieved in the equivalent nonclipped situation.

1. Introduction

Modern wideband radio receivers, such as cognitive radios, are setting significant challenges for the design of the receiver front-end. One of the key issues is to have enough dynamic range [1, 2]. Current communication waveforms tend to have a high peak-to-average-power ratio (PAPR), which makes it challenging to optimize the usage of power amplifier on the transmitter side, and it can also increase the required dynamic range in the receiver. Moreover, the reception becomes even more challenging, if a wide frequency band with several independent signals is received with a single receiver front-end and A/D interface. Those independent signals can have considerably different power levels and hence the required dynamic range is not determined only by the PAPR of a single-user signal but by the dynamic range of the overall received waveform [3, 4]. The power difference between two independent signals in mobile environment can be several tens of dBs, which is a particularly important issue to take into account in cognitive radios. Due to the continuously changing conditions, the automatic gain control (AGC) of the receiver might not be able to follow the signal dynamics. Especially the suddenly appearing strong adjacent-channel signals, with no power control from secondary (cognitive) radio point of view will cause problems. The AGC failure causes too high input level for the A/D converter and therefore the amplitude of the digitized waveform is saturated, that is, the highest signal peaks are clipped. This causes considerable signal distortion especially at the weak signal bands due to intermodulation of strong input components.

This paper discusses the compensation of unintentional receiver clipping occurring in A/D converters using digital postprocessing. More specifically, the focus is on orthogonal frequency division multiplexing- (OFDM-) based multiple access scheme, noted in the literature as OFDMA. The reception of a weak signal can be seriously compromised in the presence of a stronger adjacent-channel signal, because clipping causes relatively high amount of nonlinear distortion to the weak signal band of interest. The current literature has only a very limited number of publications proposing digital signal processing methods for reducing unintentional clipping taking place *on the receiver side* [5–7]. The aforementioned references contain rather general methods, which can be applied to different kinds of communication systems. Nevertheless, a compensation method, which is designed for a certain system, can perform better from the accuracy or computational complexity point of view. Therefore, this paper specifically focuses on OFDM,

which is widely used in emerging radio systems, and the receiver clipping compensation methods are likely to be needed. Currently, most of the OFDM-related clipping compensation algorithms in the literature concentrate on deliberate clipping to reduce signal PAPR *on the transmitter side* [8–10]. These methods are not directly applicable to mitigate clipping occurring on the receiver since the exact clipping level is not known in the case of unintentional clipping. In addition, the receiver-side clipping case is more challenging, because it happens after the radio channel and hence interferes with the channel estimation.

The proposed receiver clipping compensation method relies on the idea that most of the bit decisions made on the receiver are still correct and hence they can be exploited in clipping distortion estimation. This kind of decision-based digital compensation methods have been proposed in the literature for mitigation of various RF impairments, for example, phase noise [11, 12] and power amplifier nonlinearity [13]. This paper extends the work initiated in [14], which uses the PAPR reduction scheme of [9, 10] as a starting point and then modifies it to be suitable for the challenging task of removing unintentional receiver-side clipping. This paper provides more thorough signal modeling, performance analysis, and considers the use of turbo codec as well as more advanced channel estimation than what is presented in [14]. Additionally, the performance of the receiver clipping compensation method is verified with laboratory measurements employing commercially available A/D hardware. The results show that the proposed receiver clipping compensation method effectively mitigates the clipping distortion, is robust against various estimation errors, and is implementable with reasonable hardware costs in practice.

The remainder of the paper is organized as follows. Section 2 provides background information about the modeling of A/D converter clipping and also defines the notation used in the paper to express OFDM(A) signals. Section 3 then introduces the postprocessing algorithm for compensating clipping distortion and discusses its implementation details. The performance of the proposed algorithm is carefully studied in Section 4 using computer simulations. In addition, practical laboratory measurements with real A/D hardware are used to verify the functionality of the algorithm. After that, the computational complexity of the algorithm in general is discussed. Section 5 finishes the paper by drawing conclusions.

2. Received OFDM Signal Model and Clipping Phenomenon

This paper considers the traditional OFDM signal model, where the transmitted baseband OFDM symbol in time domain is first expressed as

$$x(t) = \frac{1}{\sqrt{N}} \sum_{k=-N/2}^{N/2-1} X_k e^{j2\pi kt/T_s}, \quad 0 \le t \le T_s, \tag{1}$$

where X_k is the kth complex data symbol (subcarrier k) and T_s is the OFDM symbol duration. This OFDM symbol contains N_A active subcarriers (SC) and has an oversampling factor J. Therefore, the total amount of SCs is $N = JN_A$ and the SC indices are expressed as a set $\Omega = \{-N/2, -N/2 + 1, \ldots, N/2 - 1\}$. The active SCs carry the data symbol sequence X_k, $k \in \Omega_A = \{-N_A/2, \ldots, -1, 1, \ldots, N_A/2\}$, whereas the nonactive SCs contain zeros, that is, $X_k = 0$, $k \in \Omega \setminus \Omega_A$. It is worth noticing that the presented OFDM signal model does not include cyclic prefix (CP), which is required in practice to avoid intersymbol interference in frequency-selective mobile environments. This paper omits the CP from the mathematical notation in order to make it simpler. This simplification does not affect the presented clipping analysis in any way, because clipping is a memoryless phenomenon. On the other hand, the CP is taken into account in the proposed receiver structures of Section 3 and in the simulations of Section 4 due to the CP's essential role in implementations of practical communication systems.

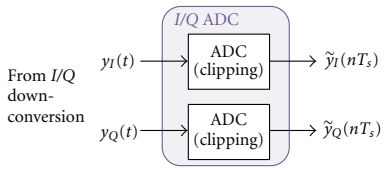

Figure 1: Illustration of an I/Q A/D converter, which contains separate converters for the I and Q branches of the received downconverted signal $y(t) = y_I(t) + jy_Q(t)$.

A zero-symmetric hard-clipping model is a simple but accurate way to characterize signal clipping in receiver A/D converters. Let us first define a general received waveform as $y(t) = y_I(t) + jy_Q(t) = h(t) * x(t) + w(t)$, where the noise $w(t)$ is added to the convolution of the channel impulse response $h(t)$ and the transmitted signal $x(t)$. After an I/Q A/D converter (see Figure 1), clipping occurring separately in both branches, the discrete-time received signal is $\tilde{y}(nT_s) = \tilde{y}_I(nT_s) + j\tilde{y}_Q(nT_s)$, where the zero-symmetric hard-clipping model determines that

$$\begin{aligned} \tilde{y}_I(t) &= \begin{cases} y_I(t), & |y_I(t)| < V_{0,I} \\ V_{0,I}, & y_I(t) \ge V_{0,I} \\ -V_{0,I}, & y_I(t) \le -V_{0,I}, \end{cases} \\ \tilde{y}_Q(t) &= \begin{cases} y_Q(t), & |y_Q(t)| < V_{0,Q} \\ V_{0,Q}, & y_Q(t) \ge V_{0,Q} \\ -V_{0,Q}, & y_Q(t) \le -V_{0,Q}, \end{cases} \end{aligned} \tag{2}$$

where $V_{0,I}$ and $V_{0,Q}$ denote the maximum output levels of the A/D converters of I and Q branches, respectively. Often in practice, a convenient way to express the clipping level of the signal is needed, but $V_{0,I}$ ($V_{0,Q}$) by itself is not very descriptive if nothing about the signal is known. Therefore, the common practice is to define the clipping level using a ratio of $V_{0,I}$ ($V_{0,Q}$) and the average branch power level of

the nonclipped signal $P_{\text{in},I}$ ($P_{\text{in},Q}$). In other words, the clipping level for I branch γ_I can be written in the form of

$$\gamma_I = \frac{V_{0,I}}{\sqrt{P_{\text{in},I}}}, \tag{3}$$

and similarly

$$\gamma_Q = \frac{V_{0,Q}}{\sqrt{P_{\text{in},Q}}}, \tag{4}$$

for the Q branch. These variables give a precise understanding of how intensely the signal branch is actually clipped. In addition, it can be concluded from (3) and (4) that the clipping level γ is different for I and Q branches, if the maximum input levels of the converters are different ($V_{0,I} \neq V_{0,Q}$) or the branch signal powers are not equal ($P_{\text{in},I} \neq P_{\text{in},Q}$). Notice that even though $V_{0,I}$ and $V_{0,Q}$ are most likely designed to be equal, unavoidable implementation tolerances of two physical separate converter circuits are indeed likely to cause small relative deviations between them.

The clipping phenomenon removes the highest signal amplitudes and hence causes nonlinear distortion. This process defined in (2) is not directly invertible. Therefore, another kind of approach is required for compensating the clipping distortion, especially at weak signal bands. This paper exploits Bussgang's theorem [15] for the compensation purpose. It has already been proven to be an adequate way to model the clipping distortion [14, 16–18]. Basically, Bussgang's theorem states that the clipping attenuates the received signal $y(nT_s)$ with a factor α and also causes additive clipping distortion $d(nT_s)$, which is uncorrelated with the nonclipped $y(nT_s)$. Therefore, the clipped signal branches can be expressed as

$$\begin{aligned} \tilde{y}_I(nT_s) &= \alpha_I y_I(nT_s) + d_I(nT_s), \\ \tilde{y}_Q(nT_s) &= \alpha_Q y_Q(nT_s) + d_Q(nT_s), \end{aligned} \tag{5}$$

when for modeling purposes $y_I(nT_s)$ and $y_Q(nT_s)$ are assumed to be Gaussian. Here, α_I and α_Q depend on γ_I and γ_Q, respectively. For the corresponding complex signal $\tilde{y}(nT_s)$, it can be written that

$$\begin{aligned} \tilde{y}(nT_s) &= \alpha_I y_I(nT_s) + d_I(nT_s) + j\left[\alpha_Q y_Q(nT_s) + d_Q(nT_s)\right] \\ &= \alpha_1 y(nT_s) + \alpha_2 y^*(nT_s) + d(nT_s) \\ &= \alpha_1 y(nT_s) + z(nT_s), \end{aligned} \tag{6}$$

where $\alpha_1 = (\alpha_I + \alpha_Q)/2$, $\alpha_2 = (\alpha_I - \alpha_Q)/2$, complex clipping distortion $d(nT_s) = d_I(nT_s) + jd_Q(nT_s)$, and total interference $z(nT_s) = \alpha_2 y^*(nT_s) + d(nT_s)$. In the general case with unequal clipping levels in the I and Q branches, the total interference $z(nT_s)$ contains both the nonlinear clipping distortion $d(nT_s)$ and the conjugate signal interference $\alpha_2 y^*(nT_s)$, which in the frequency domain corresponds to mirror-frequency interference. In the special case of identical clipping levels for both branches, $\gamma_I = \gamma_Q = \gamma$, the attenuation factor is $\alpha = \alpha_I = \alpha_Q$ and, therefore, $\alpha_1 = \alpha$ and $\alpha_2 = 0$. This means that the general complex signal model presented in (6) reduces to

$$\tilde{y}(nT_s) = \alpha y(nT_s) + d(nT_s), \tag{7}$$

which is in accordance with the traditional Bussgang's theorem for a complex signal.

Even a clipping model as simple as (6) or (7) is justified due to the memoryless nature of the clipping phenomenon. In addition, the model is linear and hence straightforward to utilize in clipping compensation purposes as described in Section 3. In short, if α_1 and $z(nT_s)$ can be estimated, recovery of the nonclipped signal $y(t)$ is simple using (6). The Gaussianity assumption for $y_I(nT_s)$ and $y_Q(nT_s)$ also makes it possible to derive concise equations for α_I and α_Q, namely,

$$\begin{aligned} \alpha_I &= \frac{E\left[y_I(nT_s)\tilde{y}_I(nT_s)\right]}{E\left[y_I(nT_s)y_I(nT_s)\right]} = \operatorname{erf}\left(\frac{\gamma_I}{\sqrt{2}}\right), \\ \alpha_Q &= \frac{E\left[y_Q(nT_s)\tilde{y}_Q(nT_s)\right]}{E\left[y_Q(nT_s)y_Q(nT_s)\right]} = \operatorname{erf}\left(\frac{\gamma_Q}{\sqrt{2}}\right). \end{aligned} \tag{8}$$

Here the error function $\operatorname{erf}(x)$ is defined as

$$\operatorname{erf}(x) = \frac{2}{\sqrt{\pi}} \int_0^x e^{-t^2} dt. \tag{9}$$

The details related to the derivation of (8) are presented in [19].

3. Iterative Decision-Aided Method for Compensating Unintentional Receiver Clipping

This section proposes a compensation algorithm for removing signal distortion caused by unintentional clipping in the A/D interface of an OFDM receiver. First, the basic compensation idea and its justification through mathematical analysis are described in Section 3.1 with the help of a block diagram presented in Figure 2. After that, the most essential details from the implementation point of view are discussed in Section 3.2. Unintentional clipping is most likely to happen in multiuser/multiband situations. Therefore, Section 3.3 deals with the multiuser aspects of the compensation algorithm implementation from the uplink (UL) and downlink (DL) point of view.

3.1. The Compensation Algorithm. On top part of Figure 2, a traditional OFDM transmitter exploiting turbo coding is illustrated. After channel coding and interleaving, the coded bits $c_{1,\ldots,M}^{(X_k)}, k \in \Omega_A$, are mapped to data symbols $X_k, k \in \Omega_A$, and then the time-domain signal with a CP is formed to be sent on the radio channel. Here, M denotes the number of bits in one data symbol. Figure 2 also illustrated two different receiver options for implementing the proposed clipping compensation algorithm. In other words, the purpose of Figure 2 is to illustrate the proposed receiver structures in a simplified manner. It does not present system-level hierarchy, where there are several users and, therefore, several transmitters and receivers. However, the proposed clipping

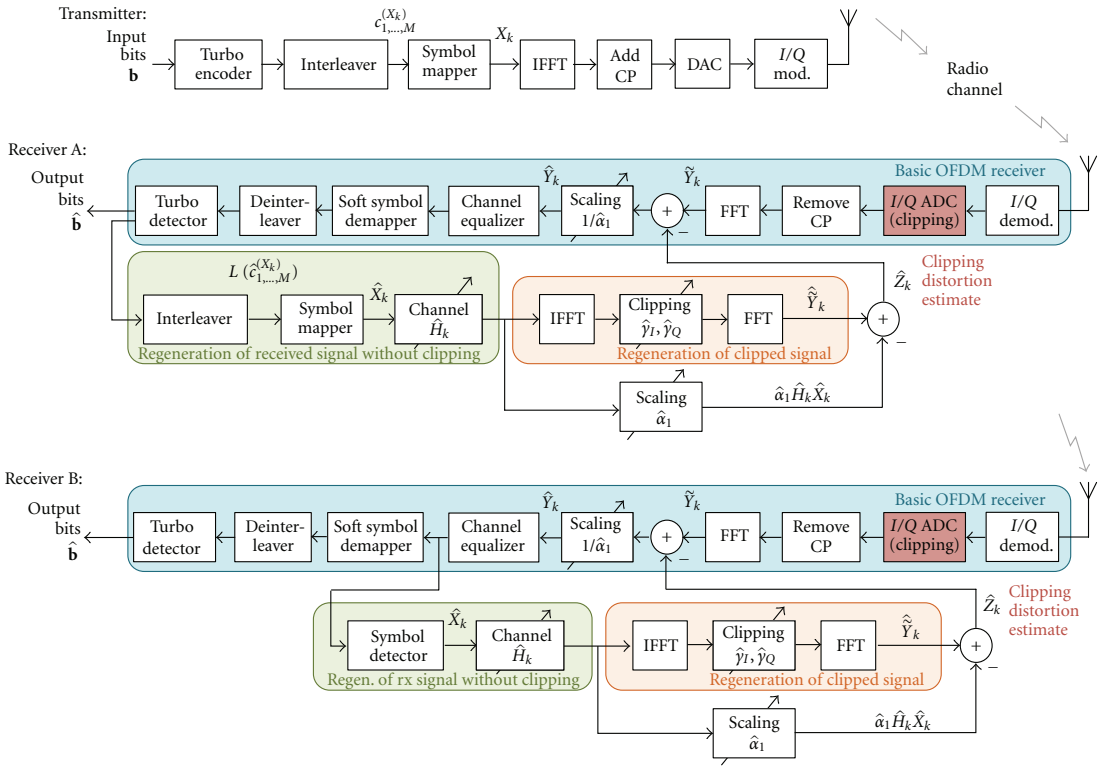

Figure 2: Undesired clipping distortion is caused by the A/D converter on the receiver side. Block diagrams of traditional OFDM transmitter and two alternative receivers implementing the proposed clipping compensation algorithm are illustrated. In Receiver A, bits are decoded on every compensation iteration round whereas Receiver B first iterates the clipping compensation on symbol level and only in the end decodes the information bits.

compensation algorithm is able to jointly process multiuser data inside one receiver as is discussed in Section 3.3.

Receiver A in Figure 2 presents the first proposition of this paper on how to remove the clipping distortion caused by the A/D interface of the receiver. In brief, the received and digitized signal is first detected in a conventional manner, that is, transformed to frequency domain, equalized, mapped to bits, deinterleaved, and decoded. Now, the decoded bits are exploited in the clipping compensation feedback loop by generating an estimate of the received signal with and without clipping. Based on (6), an estimate of the clipping distortion in the original received signal can be obtained by subtracting the scaled nonclipped estimate of the received signal from the clipped one. After that, the clipping distortion estimate can be subtracted from the original received signal in order to enhance it and obtain better detection results. Then, the whole process is iterated, because a better clipping distortion estimate can be obtained based on the enhanced detection results. Receiver B in Figure 2 implements this same clipping compensation idea, but the symbol demapper, deinterleaver, and turbo decoder are now located outside the clipping compensation loop. Hence, the computational complexity is greatly reduced since the data is kept on symbol level until the end of the clipping compensation iterations and after that the turbo decoder is used only once. The trade-off is that without turbo decoding, there are likely to be more symbol errors and, therefore, the clipping distortion estimate is not as accurate as it could be.

The following paragraphs describe the proposed clipping compensation algorithm in details by providing the exact mathematical notation. The key steps are also summarized in Algorithms 1 and 2 for Receiver A and B, respectively. It is worth noticing that only one OFDM symbol duration is considered in the equations in order to simplify the notation. The clipping compensation can be done separately for each OFDM symbol and hence the simplified notation does not omit any important details. However, in practice, the processing block length may be longer than one OFDM symbol due to the other receiver functions such as channel decoding, deinterleaving, and equalization, but this does not affect the execution of the clipping compensation, which is performed subcarrierwise.

Initialization: for all $k \in \Omega_A$

(1) Set $i = 0$, $\hat{\alpha}_1^{(0)} = 1$ and $\hat{Z}_k^{(0)} = 0$

(2) Obtain channel estimates $\hat{H}_k^{(i)}$ using signal $\hat{Y}_k^{(i)} = (1/\hat{\alpha}_1^{(i)})\,(\tilde{Y}_k - \hat{Z}_k^{(i)})$

(3) Channel equalization: $\hat{Y}_k^{(i)}/\hat{H}_k^{(i)}$

(4) Demap symbols $\hat{Y}_k^{(i)}/\hat{H}_k^{(i)}$ to bits, deinterleave and decode to obtain output data bits $\hat{\mathbf{b}}^{(i)}$

Iteration: Increase i by one and do the following steps for all $k \in \Omega_A$

(5) Create $\hat{X}_k^{(i)}$ based on the coded bits $\hat{c}_{1,\ldots,M}^{(X_k^{(i-1)})}$ (hard) or $L(\hat{c}_{1,\ldots,M}^{(X_k^{(i-1)})})$ (soft)

(6) Estimate clipping levels $\hat{\gamma}_I^{(i)}$ and $\hat{\gamma}_Q^{(i)}$ as well as attenuation factor $\hat{\alpha}_1^{(i)}$

(7) Clip $\hat{H}_k^{(i-1)}\hat{X}_k^{(i)}$ according to $\hat{\gamma}_I^{(i)}$ and $\hat{\gamma}_Q^{(i)}$ in *time domain* to produce $\hat{\tilde{Y}}_k^{(i)}$

(8) Calculate clipping distortion estimate $\hat{Z}_k^{(i)} = \hat{\tilde{Y}}_k^{(i)} - \hat{\alpha}_1^{(i)}\hat{H}_k^{(\mathrm{i}-1)}\hat{X}_k^{(\mathrm{i})}$

(9) Remove the distortion from the received signal, that is, $\hat{Y}_k^{(i)} = (1/\hat{\alpha}_1^{(i)})(\tilde{Y}_k - \hat{Z}_k^{(i)})$

(10) Obtain new channel estimates $\hat{H}_k^{(i)}$ using signal $\hat{Y}_k^{(i)}$

(11) Channel equalization: $\hat{Y}_k^{(i)}/\hat{H}_k^{(i)}$

(12) Demap symbols $\hat{Y}_k^{(i)}/\hat{H}_k^{(i)}$ to bits, deinterleave and decode to obtain output data bits $\hat{\mathbf{b}}^{(i)}$

Algorithm 1: Key steps of the proposed receiver clipping compensation algorithm for Receiver A.

Initialization: for all $k \in \Omega_A$

(1) Set $i = 0$, $\hat{\alpha}_1^{(0)} = 1$ and $\hat{Z}_k^{(0)} = 0$

(2) Obtain channel estimates $\hat{H}_k^{(i)}$ using signal $\hat{Y}_k^{(i)} = (1/\hat{\alpha}_1^{(i)})(\tilde{Y}_k - \hat{Z}_k^{(i)})$

(3) Channel equalization: $\hat{Y}_k^{(i)}/\hat{H}_k^{(i)}$

Iteration: Increase i by one and do the following steps for all $k \in \Omega_A$

(4) Detect $\hat{Y}_k^{(i-1)}/\hat{H}_k^{(i-1)}$ to obtain symbols $\hat{X}_k^{(i)}$

(5) Estimate clipping levels $\hat{\gamma}_I^{(i)}$ and $\hat{\gamma}_Q^{(i)}$ as well as attenuation factor $\hat{\alpha}_1^{(i)}$

(6) Clip $\hat{H}_k^{(i-1)}\hat{X}_k^{(i)}$ according to $\hat{\gamma}_I^{(i)}$ and $\hat{\gamma}_Q^{(i)}$ in *time domain* to produce $\hat{\tilde{Y}}_k^{(i)}$

(7) Calculate clipping distortion estimate $\hat{Z}_k^{(i)} = \hat{\tilde{Y}}_k^{(i)} - \hat{\alpha}_1^{(i)}\hat{H}_k^{(i-1)}\hat{X}_k^{(i)}$

(8) Remove the distortion from the received signal, that is, $\hat{Y}_k^{(i)} = (1/\hat{\alpha}_1^{(i)})(\tilde{Y}_k - \hat{Z}_k^{(i)})$

(9) Obtain new channel estimates $\hat{H}_k^{(i)}$ using signal $\hat{Y}_k^{(i)}$

(10) Channel equalization: $\hat{Y}_k^{(i)}/\hat{H}_k^{(i)}$

After iteration:

(11) Demap symbols $\hat{Y}_k^{(i)}/\hat{H}_k^{(i)}$ to bits, deinterleave and decode to obtain output data bits $\hat{\mathbf{b}}^{(i)}$

Algorithm 2: Key steps of the proposed receiver clipping compensation algorithm for Receiver B.

If the signal is received perfectly without clipping in the A/D interface, it can be written as

$$Y_k = H_k X_k + W_k, \quad k \in \Omega \tag{10}$$

in frequency domain after removing CP and taking FFT. In (10), H_k is the channel gain and W_k is the additive white Gaussian noise component for the kth SC. In other words, this equation represents the ideal case for reference. However, if the A/D converter clips the signal, the frequency-domain version of it is then

$$\begin{aligned}\widetilde{Y}_k &= \alpha_1 Y_k + \alpha_2 Y^*_{-k} + D_k \\ &= \alpha_1 (H_k X_k + W_k) + \alpha_2 \left(H^*_{-k} X^*_{-k} + W^*_{-k}\right) + D_k \\ &= \alpha_1 H_k X_k + Z_k + \alpha_1 W_k + \alpha_2 W^*_{-k}, \quad k \in \Omega,\end{aligned} \tag{11}$$

as can be derived from (6). This signal is also illustrated in Figure 2. In (11), $Z_k = \alpha_2 H^*_{-k} X^*_{-k} + D_k$, $k \in \Omega$, which essentially means that unequal clipping levels γ_I and γ_Q cause mirror-subcarrier interference ($\alpha_2 H^*_{-k} X^*_{-k}$, $k \in \Omega$) in addition to the clipping distortion (D_k, $k \in \Omega$). However, if $\gamma_I = \gamma_Q$, then $\alpha_2 = 0$ and thus $Z_k = D_k$, $k \in \Omega$. Because all the interference in Z_k, $k \in \Omega$, stems from the clipping phenomenon, it is called clipping distortion in the rest of the paper. As shown in Figure 2, prior to the clipping compensation, the data symbols $\widetilde{Y}_k$, $k \in \Omega_A$ are equalized, mapped to soft bits, deinterleaved, and then decoded. In the channel equalization stage, the channel gain estimates $\widehat{H}_k$, $k \in \Omega_A$, for active SCs are obtained based on pilot SCs. Section 3.2 contains more discussion about the channel estimation.

In the first step of the clipping compensation, Receiver A uses the bit estimates after the turbo decoder to regenerate the originally transmitted OFDM signal. All the decoded bits may not be correct and, therefore, it is possible that the regenerated signal does not exactly match the transmitted signal. Hence, the regenerated signal is called the estimate of the transmitted signal and it is denoted as $\widehat{X}_k$, $k \in \Omega$, in Figure 2. The data bit estimates $\widehat{\mathbf{b}}$ are not re-encoded in the clipping compensation feedback loop, but rather the soft-coded bit estimates $L(\hat{c}^{(X_k)}_{1,\ldots,M})$, $k \in \Omega_A$, from the turbo decoder output (after interleaving) are used. Here, $\hat{c}^{(X_k)}_{1,\ldots,M}$ are hard bit estimates related to the symbol X_k and $L(\hat{c}^{(X_k)}_{1,\ldots,M})$ are the log-likelihood ratio (LLR) values for the bit estimates $\hat{c}^{(X_k)}_{1,\ldots,M}$. It is possible to generate either hard or soft symbol estimates and hence both options are studied in Section 4. In Receiver B, it is enough to obtain hard symbol estimates using directly the channel equalizer output. This way, the symbol demapping, channel decoding, and symbol mapping process can be avoided during the clipping compensation process. Since channel decoding is usually the most complex process in the receiver chain, significant savings in computational complexity and latency can be achieved if the channel decoder is located outside the clipping compensation loop. From this point onward, both the Receiver A and B proceed in the same way.

The estimate of the transmitted signal is exposed to the estimated channel and then to the estimated clipping process (separately for I and Q branches) in order to obtain a regenerated version of the clipped received signal $\widehat{\widetilde{Y}}_k$, $k \in \Omega_A$. The clipping process is performed in time domain using the estimated clipping levels $\hat{\gamma}_I$ and $\hat{\gamma}_Q$, which should be as close as possible to the clipping levels originally occurred in the A/D converter during the reception of the signal. The knowledge of the exact clipping levels γ_I and γ_Q is not available, but the estimates $\hat{\gamma}_I$ and $\hat{\gamma}_Q$ can be calculated as shown in (3). Here, the maximum output levels of the A/D converter $V_{0,I}$ and $V_{0,Q}$ are approximated by following the absolute maximum level of the corresponding signal branch after the A/D converter. An estimate of $P_{\text{in},I}$ and $P_{\text{in},Q}$ can be calculated from the hard symbol estimates $\widehat{X}_k$, $k \in \Omega$. The clipping process performed in time domain essentially produces a signal, which according to Bussgang's theorem can be written in frequency domain as $\widehat{\widetilde{Y}}_k = \hat{\alpha}_1 \widehat{H}_k \widehat{X}_k + \widehat{Z}_k$, $k \in \Omega_A$, where $\hat{\alpha}_1$ is the estimate of the attenuation factor. Now, the clipping distortion estimate $\widehat{Z}_k$, $k \in \Omega_A$ can be extracted from $\widehat{\widetilde{Y}}_k$, $k \in \Omega_A$, by removing the attenuated desired signal part $\hat{\alpha}_1 \widehat{H}_k \widehat{X}_k$, $k \in \Omega_A$, from it. This estimated desired signal can easily be produced from the nonclipped version of the regenerated received signal as illustrated with the lower branch in the clipping compensation loop in Figure 2 (both in Receivers A and B). That is to say, the estimate of the clipping distortion $\widehat{Z}_k$, $k \in \Omega_A$, is calculated as

$$\widehat{Z}_k = \widehat{\widetilde{Y}}_k - \hat{\alpha}_1 \widehat{H}_k \widehat{X}_k, \quad k \in \Omega_A, \tag{12}$$

where $\hat{\alpha}_1 = (\hat{\alpha}_I + \hat{\alpha}_Q)/2$ is calculated from (8) using $\hat{\gamma}_I$ and $\hat{\gamma}_Q$. The out-of-band clipping distortion can be ignored and this is easy to do by processing only the active SCs Ω_A, as indicated in (12). Now, the last step in clipping compensation is to improve the received signal $\widetilde{Y}_k$, $k \in \Omega_A$, by removing the estimated clipping distortion $\widehat{Z}_k$, $k \in \Omega_A$, from it. The compensated signal is expressed as

$$\widehat{Y}_k = \frac{1}{\hat{\alpha}_1}\left(\widetilde{Y}_k - \widehat{Z}_k\right), \quad k \in \Omega_A, \tag{13}$$

and it is used as a starting point for a new processing round, which begins with the channel estimation and equalization.

One way to show the validity of the clipping compensation approach is to substitute (11) into (13). This leads to the equation that expresses the estimate of the received signal without clipping as

$$\begin{aligned}\widehat{Y}_k = {} & \frac{\alpha_1}{\hat{\alpha}_1}(H_k X_k + W_k) \\ & + \frac{1}{\hat{\alpha}_1}\left(Z_k - \widehat{Z}_k\right) + \frac{\alpha_2}{\hat{\alpha}_1} W^*_{-k}, \quad k \in \Omega_A.\end{aligned} \tag{14}$$

If exactly correct estimates $\hat{\alpha}_1$ and $\widehat{Z}_k$, $k \in \Omega_A$, can be achieved, all essential clipping distortion is thus removed. This is straightforward to see from (14), because with the correct estimates, it reduces to the form of (10) plus additional scaled mirror-subcarrier noise $(\alpha_2/\hat{\alpha}_1) W^*_{-k}$, $k \in \Omega_A$. However, it is impossible to actually produce exactly

correct clipping estimate, because the noise W_k, $k \in \Omega$, gets also clipped in the A/D converter, but the model cannot reproduce the clipping distortion term of the noise.

In practice, it is usually the case that there are errors in the symbol estimates $\hat{X}_k$, $k \in \Omega_A$, on the first processing round. This leads to the inaccurate clipping distortion estimate and, therefore, all the distortion is not removed from the received signal on the first round. However, on every processing iteration round the symbol estimates get better since more and more accurate estimate of the clipping distortion can be obtained. In other words, the compensation algorithm works in the desired manner, if high enough portion of the initial symbol estimates are correct. In order to make the proposed algorithm work in the best possible manner, all the estimated parameters should be recalculated on every iteration. This means the estimates of the channel $\hat{H}_k$, $k \in \Omega_A$, the clipping levels $\hat{\gamma}_I$ and $\hat{\gamma}_Q$ as well as the attenuation factor $\hat{\alpha}_1$.

The receiver clipping compensation discussed in this paper has similarities with the deliberate transmitter-clipping compensation presented, for example, in [9] and [10] as well as to the power amplifier nonlinearity compensation in [13]. However, there are several fundamental differences, which can be analyzed comparing the aforementioned references to the equations shown in Sections 2 and 3 of this paper. Using consistent notation, the received signal under deliberate *transmitter clipping* can be expressed as $\widetilde{Y}_k = H_k(\alpha X_k + D_k) + W_k$, $k \in \Omega$. When compared to (11), it is evident that the role of the channel is different. In the transmitter clipping case, the clipping is applied before transmission and hence the channel estimation in the receiver is less challenging compared to the receiver clipping case. It is shown in Section 4 that the channel estimation is severely interfered in the receiver clipping case, if clipping compensation is not used. Another essential difference is the clipping model itself. In the deliberate transmitter clipping, the amplitude of a complex signal is limited, that is,

$$|\widetilde{x}(t)| = \begin{cases} |x(t)|, & |x(t)| \le V_0, \\ V_0, & |x(t)| > V_0, \end{cases} \tag{15}$$

where as the receiver clipping means that the I and Q signal branches are clipped separately as expressed in (2). This means that it is possible in the receiver clipping case that different clipping levels take place in I and Q branches. Nevertheless, since our signal modeling takes it into account, the clipping compensation with unequal clipping levels is possible as verified in Section 4.

3.2. Implementation Details. In this paper, a zero-forcing channel equalizer is used for simplicity. The channel estimates $\hat{H}_k$, $k \in \Omega_A$, are obtained using part of the active SCs Ω_A, as pilots, which are denoted here as Ω_P. These are evenly distributed among the data SCs $\Omega_D = \Omega_A \setminus \Omega_P$ so that every Lth SC is a pilot. The channel estimates of pilot SCs are $\hat{H}_{P,k} = \hat{Y}_k / X_k$, $k \in \Omega_P$, which are exploited to obtain channel estimates for the data SCs using low-pass interpolation. This means that, first, $L-1$ zeros are inserted between every pilot SC channel estimate. Then, a properly designed FIR lowpass interpolation filter is used to obtain the channel estimates for data SCs. The width of the passband of the interpolation filter corresponds to the original data bandwidth and, therefore, the mean-squared error (MSE) of the interpolated SCs is minimized assuming that the pilot SC channel estimates are correct. As the channel estimation is performed in frequency domain, the use of interpolation filter means calculating convolution between the impulse response of the interpolation filter and the zero-padded channel estimates of the pilots in frequency domain.

From the second clipping compensation iteration round onward, also the symbol estimates from the previous iteration round can be exploited in the channel estimation task. Due to the symbol errors, purely data-symbol-based channel estimation may give poorer results than the estimation using pilots. Therefore, a heuristic approach, which combines these two methods, is proposed in this paper. In the combining, the channel estimates are weighted with the corresponding symbol reliabilities $p(X_k)$, $k \in \Omega_A$, so that the channel estimates after combining are

$$\hat{H}_k = \frac{p(X_k)}{2}\hat{H}_{D,k} + \left(1 - \frac{p(X_k)}{2}\right)\hat{H}_{P,k}, \quad k \in \Omega_A, \tag{16}$$

where $\hat{H}_{D,k} = \hat{Y}_k / \hat{X}_k$, $k \in \Omega_D$ are the channel estimates obtained from the latest data symbol estimates and $\hat{H}_{P,k}$, $k \in \Omega_A$, are the latest channel estimates obtained using pilots. The estimates $\hat{H}_{D,k}$, $k \in \Omega_P$ for pilot SCs are not needed since (16) implicates that $\hat{H}_k = \hat{H}_{P,k}$, $k \in \Omega_P$. This is guaranteed by setting $p(X_k) = 0$, $k \in \Omega_P$. For the data symbols, the reliabilities are calculated as

$$p(X_k) = \prod_{j=1}^{M} \frac{\exp\left[\hat{c}_j^{(X_k)} L\left(\hat{c}_j^{(X_k)}\right)\right]}{1 + \exp\left[L\left(\hat{c}_j^{(X_k)}\right)\right]}, \quad k \in \Omega_D. \tag{17}$$

This data-symbol-based estimation is used in Receiver A. Since the LLR values for the bits are not calculated in Receiver B in every iteration, it uses only the pilot-based channel estimation. One variation of the data-symbol-based channel estimation proposed above would be such that a certain threshold is used for the symbol reliabilities. In other words, only the symbols which are reliable enough, let us say $p(X_k) > 0.95$, are used in the channel estimation. However, this variation of the proposed channel estimation technique is omitted from the performance analysis of Section 4 and is left for future studies.

The output of the zero-forcing channel equalizer should be limited so that the maximum amplitude is

$$V_{\max,\mathrm{eq}} = \max_r \|A_r\| + \frac{3.29}{\sqrt{2}}\sigma_n, \tag{18}$$

where A_r, $r = 1, \ldots, 2^M$ denotes all the possible symbols from the used alphabet and σ_n is the standard deviation of the complex noise $w(t)$, which is assumed to be Gaussian. The factor of 3.29 corresponds to the 99.9% confidence level of one-dimensional Gaussian distribution and, therefore, the standard deviation of the complex noise has to be scaled with $\sqrt{2}$. The amplitude limit of the equalizer output

does not have to be exactly what is proposed in (18), but significantly too tight or loose limit affects decoding results. The reason to use such an amplitude limiter after the channel equalizer is the soft symbol demapper defined based on an assumption of Gaussian noise. The clipping distortion and the channel equalizer cause interference peaks, which degrade the performance of the soft symbol demapper. In this paper, it is chosen to set the LLR values of the bits related to the amplitude-limited symbols to zero. This is justified, because if there is a significant distortion term present in a symbol, all the usable information carried by the symbol has already been lost. The main target in the limiting of the equalizer output is to tell the decoder which symbols are very unreliable due to the channel fading or unintentional clipping, but in the same time avoid affecting the symbols which are spread only because of the Gaussian noise.

The channel codec used in this paper is a turbo codec [20] with a generator matrix:

$$G = \left[1 \quad \frac{1\,5}{1\,3}\right]. \tag{19}$$

The used interleavers are bit-wise S-interleavers [21] for which the distance parameter is defined as $S = \sqrt{U/2}$, where U is the length of the unit to be interleaved. In channel interleaving, the unit is the whole coded block (U_{out}). Inside the turbo encoder/decoder, the length of the interleaved unit is equal to one uncoded data block (U_{in}). This is defined as $U_{\text{in}} = \lfloor R(U_{\text{out}} - 2m) \rfloor$, where $m = 3$, is the memory length of the component encoder and the term $2m$ is due to the unpunctured termination bits [22]. Different coding rates are achieved by puncturing the parity bits, which is done based on [22]. The turbo decoder uses the Max-Log-MAP algorithm for decoding, and it does not have a correction function for the max-operator [23]. The iteration of turbo decoding is stopped based on the hard-data-aided (HDA) criterion presented in [24].

3.3. Multiuser Considerations. Since the proposed receiver clipping compensation method is very general, it can be used both in UL and DL directions. However, there are some essential differences when a multiuser scenario is concerned. In DL direction, the data symbol sequence X_k, $k \in \Omega_A$, contains symbols, which belong to several individual mobile users. A single mobile receiver should be able to process, in addition to its own data, also the symbols of neighboring users in order to exploit the clipping compensation method in an optimal manner. This is because of the nonlinear behavior of clipping, which causes that part of the clipping distortion is stemming from outside the frequency band of the user. If the signal power for the neighboring users is higher than for the interested user, the amount of clipping distortion can be very high. Therefore, joint clipping compensation processing of all neighboring users is preferable. The challenge in the implementation of the clipping compensation in mobile receiver is that the amount of signal processing is significantly increased when the symbols of neighboring users are processed and the channel estimation is performed over the whole frequency band instead of concentrating on one user only as the mobile receiver usually does. The proposed Receiver B model is especially suitable for DL direction due to its considerably lower computational complexity but still relatively good performance, as shown in Section 4.1. One way to decrease the computational burden even more is to exploit cooperative interference cancellation among the users so that they exchange information of their own data and interference using short-range communications. For example, spatial correlation of the channels can be exploited, if users are close to each other.

Similarly as in the DL direction, also in the UL scenario the data symbol sequence X_k, $k \in \Omega_A$, contains data of multiple users. Furthermore, in UL, a band-wise channel estimation for each user must be performed individually, since the different mobile signals have propagated through different channels. Therefore, the channel estimate sequence $\hat{H}_k$, $k \in \Omega_A$, is not continuous. In general, the implementation of the clipping compensation method is more viable in the UL scenario since the base station has to receive and process the signals of all users anyway. Hence, including the clipping compensation processing is not going to excessively increase the computational complexity. On the other hand, modern base stations can also have vast amount of computing power, which makes complex digital signal processing algorithms feasible. Due to its higher computational complexity, Receiver A model is proposed for the UL direction. More discussion of the receiver complexity and performance can be found in Section 4.1.

4. Performance Results for the Clipping Compensation Approach

In this section, the performance of the proposed receiver-side clipping compensation algorithm is analyzed and discussed in details. This is done using a UL scenario with two individual users in the block-fading extended ITU-R Vehicular A channel [25]. First, Section 4.1 analyzes the performance of the clipping compensation algorithm through computer simulations. After that, Section 4.2 considers the same scenario using laboratory measurements with real A/D hardware. Finally, Section 4.3 presents analysis of computational complexity for Receivers A and B in the considered scenario.

Since an UL scenario is considered, both users experience different realizations of the fading channel. Here, it is also assumed that the channels stays static for ten consecutive OFDM symbols, which makes possible to average obtained channel estimates over this period. The channel conditions are set so that the average received power level for User 1 is 15 dB less than for User 2. In this section, it is assumed that there is perfect delay and frequency alignment between the users. The most essential parameters of the simulated scenario are collected into Table 1. Both users have 512 active SCs of which every eighth is a pilot ($L = 8$). Therefore, $N_A = 1024$ in the receiver side, when the composite signal of two users is processed. The pilot power is adjusted so that it corresponds to the average power of the data symbols.

Table 1: Parameters for the simulated uplink multiuser scenario.

Parameter	Value
Number of users	2
FFT size N	2048
Active subcarriers per user	512
Scattered pilots per user	64
CP length	128 samples
Sampling rate	30.72 MHz
Subcarrier spacing	15 kHz
Subcarrier modulation	16-QAM ($M = 4$)
Channel profile	Extended ITU-R Veh. A [25]
Channel codec	Turbo codec (Max-Log-MAP)
Coding rate R	1/2
Coded block length U_{out}	3584 bits (2 OFDM symbols)
Decoding iterations	Max. 5
Clipping comp. iterations I	5 (or 10)
Clipping level γ	0–10 dB
SNR for User 1 SNR_I	16–36 dB

Both users have 16-QAM as an SC modulation and hence $M = 4$. The oversampling factor used is $J = 2$ and the overall sampling rate is 30.72 MHz, which results in the SC spacing of 15 kHz. The length of CP is $(1/16)N = 128$ samples. On average, the PAPR of the composite signal of two users is 10.1 dB. For the channel coding, the turbo codec is used and its coded block length is $\text{U}_{\text{out}} = 3584$ bits, meaning that two consecutive OFDM symbols form one coded block. Coding rate of $R = 1/2$ is used and hence $\text{U}_{\text{in}} = 1789$ bits. In every clipping compensation iteration, the turbo decoder is allowed to do five decoding iterations, if not stopped earlier based on the HDA criterion. In the following, five clipping compensation iterations ($I = 5$) have been performed in all cases, if not specifically stated otherwise. In practical receiver, unnecessary iterations can be avoided, to decrease the amount of computation, by stopping iterations for the user, if its bit-error ratio (BER) goes to zero before the maximum amount of iterations has been performed. This can be checked, for example, by exploiting the cyclic redundancy check (CRC).

4.1. Simulation Results. Figure 3 gives an overall illustration of the above-defined scenario, when the clipping level $\gamma = 6$ dB occurs. For simplicity, equal clipping levels $\gamma_{\text{I}} = \gamma_{\text{Q}} = \gamma$ are assumed in this section, if not otherwise stated. Figure 3(a) shows a piece of the real branch signal before and after clipping. Correspondingly, Figure 3(b) illustrates the received waveform in frequency domain before and after clipping. It is clearly visible that the weak User 1 suffers from the nonlinear clipping distortion stemming from the band of the considerably stronger User 2.

The progress of the clipping compensation process for User 1 is illustrated in Figure 4 when Receiver A is used for the case shown in Figure 3. The BER results are averaged over 20,000 OFDM symbols, that is, 2000 independent channel realizations, as is done also for all the other performance figures in this Section. In this paper, BER is calculated for the data bits **b**. Figure 4 shows that the proposed clipping compensation algorithm is able to almost reach the BER of the nonclipped signal, which represents here the error floor. For the nonclipped signal, perfect channel knowledge is used in order to present the ideal reference case whereas the channel estimation proposed in Section 3.2 is used in the clipping compensation. Figure 4 also illustrates the information flow inside the receiver. Decoding arrow (D) refers to the turbo decoding process and feedback arrow (F) denotes the process where bit decisions are exploited to remove clipping distortion from the received signal. It can be seen from Figure 4 that the turbo decoder cannot reduce the BER of the noncompensated signal very much due to the significant amount of clipping distortion. Nonetheless, the clipping compensation method is still able to reduce the amount of distortion, and in the next iteration, the turbo decoder reduces the BER more. This means that the clipping compensation performs well even without turbo decoding and thus the Receiver B model is justified.

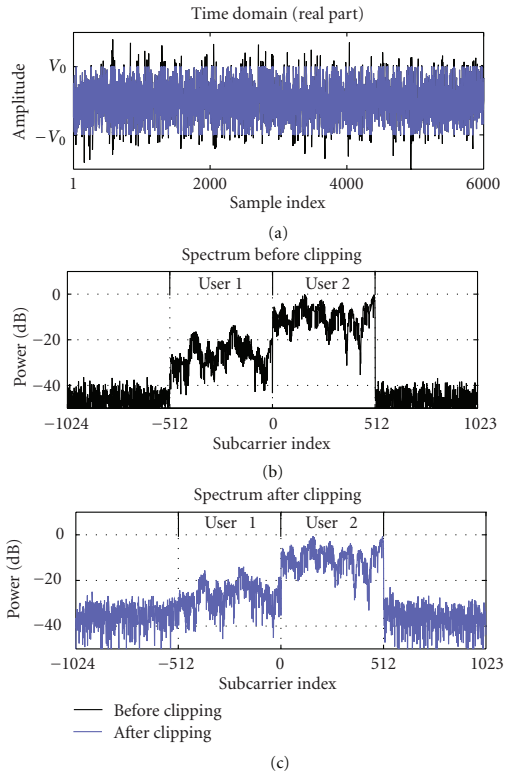

Figure 3: (a) Time domain illustration of the real part of the received signal before and after clipping, $\gamma = 6$ dB (b) spectrum of the received signal before clipping (c) spectrum of the signal after clipping.

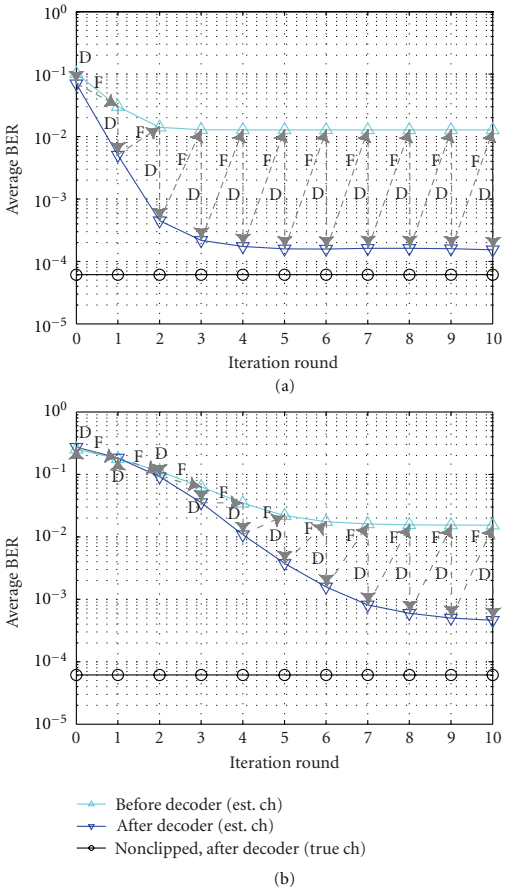

Figure 4: Average BER as a function of clipping compensation iterations for User 1 using Receiver A when $SNR_I = 21.9$ dB and (a) $\gamma = 6$ dB or (b) $\gamma = 2$ dB. Iteration round 0 corresponds to the noncompensated signal. Arrows refers to the decoding (D) and compensation feedback (F) stages.

A detailed performance comparison between Receiver A and B is given later in this Section. For the results shown in Figure 4, the average received signal-to-noise ratio (SNR) for User 1 is 21.9 dB whereas for User 2 it is 36.9 dB. Here, the average received SNR is defined using the average signal and noise powers on the user frequency band, that is,

$$SNR_u = \frac{E\left[\sum_{k\in\Omega_{A,u}} |H_k X_k|^2\right]}{E\left[\sum_{k\in\Omega_{A,u}} |W_k|^2\right]}, \tag{20}$$

where u is the user index, $\Omega_{A,1} = \{-N_A/2, \ldots, -1\}$ for User 1 and $\Omega_{A,2} = \{1, \ldots, N_A/2\}$ for User 2. By comparing Figures 4(a) and 4(b), it can be concluded that stronger clipping requires more compensation iterations rounds, but eventually most of the clipping distortion is removed.

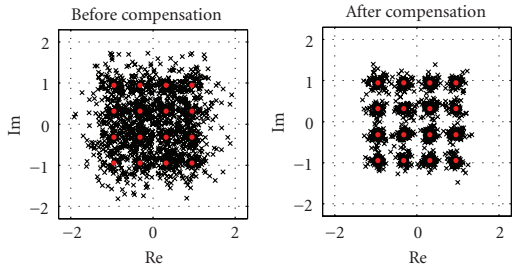

Figure 5: Example realization of the received constellation for User 1 before and after clipping compensation in Receiver A when $\gamma = 6$ dB and $SNR_I = 21.9$ dB.

An example of the received constellation before and after the clipping compensation for User 1 is provided in Figure 5 to visually illustrate the reduction of clipping distortion due to the applied compensation method. This matches with the cases shown in Figures 3 and 4. In addition to BER results, one way to illustrate the performance of the clipping compensation method is the subcarrier-wise signal-to-clipping-distortion ratio ($SCDR$), which is defined as

$$SCDR_k = \frac{E\left[|Y_k|^2\right]}{E\left[\left|\hat{Y}_k - Y_k\right|^2\right]}, \quad k \in \Omega_A. \tag{21}$$

It describes how much there is clipping distortion compared to the ideal nonclipped situation. Figure 6 shows SCDR results for both users when $\gamma = 6$ dB, which is the same case that is considered in Figures 3–5. It can be seen from Figure 6 that in this particular case the amount of clipping distortion is decreased over 20 dB for both users. It should be kept in mind that SCDR values are relative. User 1 has considerably more clipping distortion than User 2 in the beginning and hence the improvement in SCDR has much more significant effect for User 1. Naturally, the employed channel estimation approach has a finite accuracy, but this is a minor matter compared to the fact that the receiver-side clipping affects the pilots and, therefore, notably distorts the channel estimates. On the other hand, the clipping compensation also effectively enhances the channel estimates. The subcarrier-wise channel estimation MSE is given in Figure 7 for the currently discussed case of $\gamma = 6$ dB. This figure verifies that the clipping compensation without a doubt improves the channel estimates. The channel estimation MSE for the nonclipped signal in Figure 7 illustrates the error floor for this particular channel estimation method and noise level. The relatively high error on the sides of the user bands is stemming from the interpolation filter transients.

In order to provide a wider view of the clipping compensation performance, Figure 8 illustrates the simulated BER results for User 1 as a function of occurred clipping level when $SNR_I = 21.9$ dB. The same figure also provides a comparison between the proposed channel estimation and perfect channel knowledge. Although the channel estimation works well when $\gamma > 4$ dB, the channel estimates gets

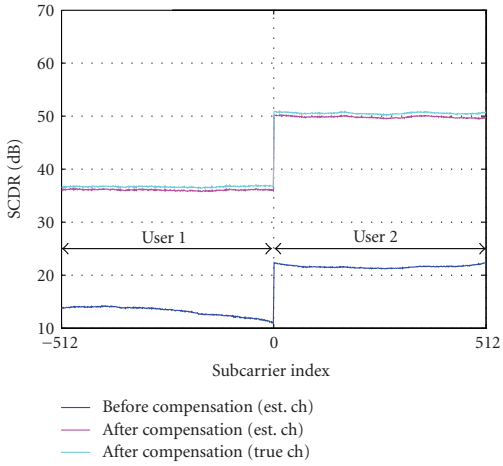

Figure 6: Subcarrier-wise signal-to-clipping-distortion ratio when $\gamma = 6$ dB, $SNR_1 = 21.9$ dB and $SNR_2 = 36.9$ dB. The results are obtained after 5 clipping compensation iterations using Receiver A.

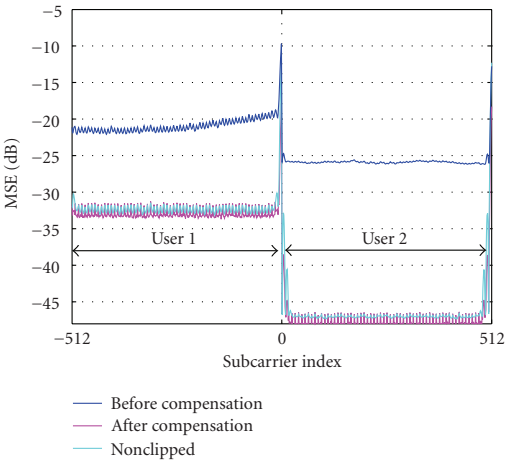

Figure 7: Mean squared error of channel estimates when $\gamma = 6$ dB, $SNR_1 = 21.9$ dB and $SNR_2 = 36.9$ dB. The results are obtained after 5 clipping compensation iterations using Receiver A.

significantly poorer if heavier clipping occurs. Because the input SNR is the same for all clipping levels, it can be concluded that the channel estimation accuracy is limited due to the clipping distortion and not because of the noise. These results were obtained after five clipping compensation iterations, which does not guarantee that BER is always minimized. Under heavy clipping, additional iterations would provide lower BER to some extent, but there is always a certain error floor despite the number of iterations. Another support for this issue is provided in Figure 9, where the

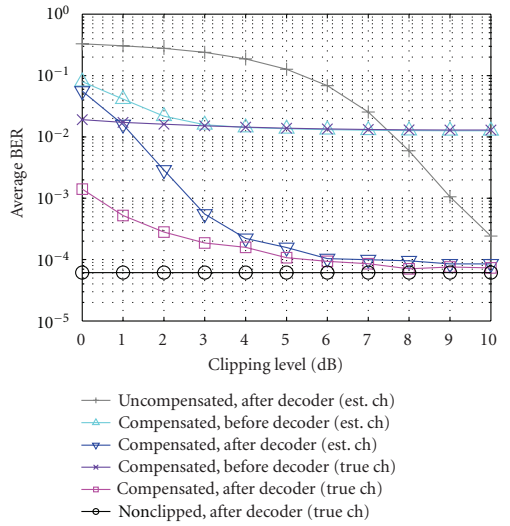

Figure 8: Performance of the clipping compensation for User 1 as a function of clipping level when $SNR_1 = 21.9$ dB. The results are obtained after 5 clipping compensation iterations using Receiver A.

BER of User 1 is illustrated as a function SNR_1 for clipping levels $\gamma = 6$ dB and $\gamma = 2$ dB. From here, it can be seen that the clipping compensation performs decently, if the noise level and the clipping level are reasonable. The limited channel estimation accuracy due to the heavy clipping can be seen in Figure 9(b) by comparing the BER curves in cases of estimated channel and perfect channel knowledge. This means that the clipping compensation method is able to recover the BER almost to the level of nonclipped signal even under heavy clipping, if the channel estimation could be performed accurately. The limitations of the channel estimation can be relieved to some extend by increasing the number of compensation iterations, but in order to minimize the number of iterations, the optimal channel estimation approach under clipping is an interesting topic for future research. Figure 10 shows the BER of User 1 separately for every clipping compensation iteration round when $\gamma = 6$ dB. From here, it can be concluded that almost the maximum performance is achieved within only three iterations. The rapid saturation of the performance is also observable from Figure 4(a) whereas stronger clipping would require a few iterations more. It is desirable to minimize the number of iterations since it directly affects the processing time of the clipping compensation per code block and thus also the overall latency of the receiver.

One interesting question: does the performance of the clipping compensation method change if soft symbol estimates are used instead of the hard ones. Figures 11 and 12 show that the performance for User 1 using Receiver A is practically the same for hard and soft symbol estimates. It is worth clarifying that the soft symbol estimates are used only for the regeneration of the transmitted signal

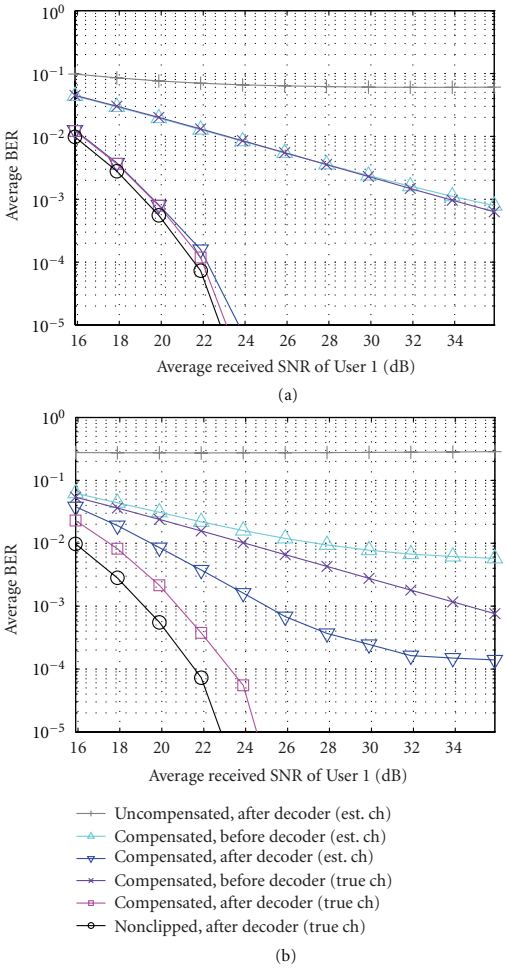

Figure 9: Performance of the clipping compensation for User 1 as a function of average received SNR for clipping levels (a) 6 dB and (b) 2 dB. The results are obtained after 5 clipping compensation iterations using Receiver A.

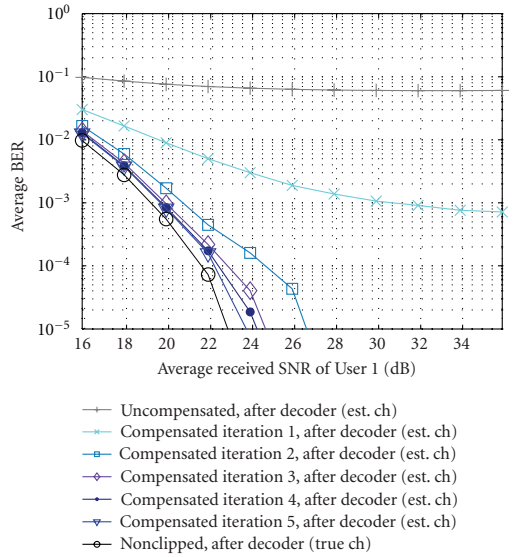

Figure 10: Average BER of User 1 separately for every clipping compensation iteration round as a function of average received SNR when Receiver A is used and $\gamma = 6$ dB.

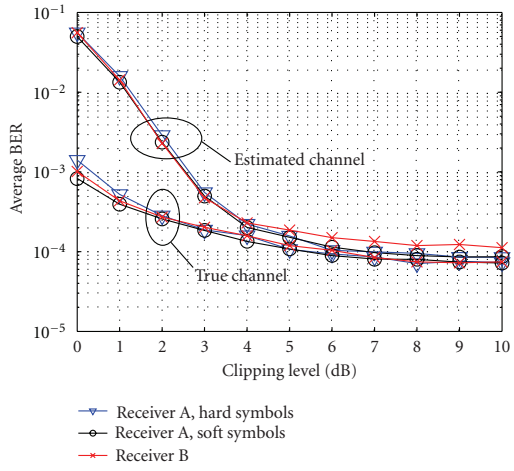

Figure 11: Performance comparison between Receivers A and B for User 1 as a function of clipping level when $SNR_1 = 21.9$ dB and 5 compensation iterations is performed.

in the compensation feedback loop. The channel estimates $\hat{H}_{D,k}$, $k \in \Omega_D$, and the estimate of P_{in} are always obtained using the hard symbol estimates, because the soft symbol estimates would give misleading results. For a deliberate transmitter clipping compensation, it is reported in [10] that the soft symbol estimates lead to equal or even worse performance compared to the hard symbol estimates. Based on Figures 11 and 12, it can be stated that the hard symbol estimates should be used in Receiver A, since the soft symbol estimates would only unnecessarily increase the computational load. Another comparison made in Figures 11 and 12 is between Receivers A and B. Even though the computational complexity of Receiver B is significantly lower, it performs only marginally worse than Receiver A with all the clipping levels and SNRs studied. Therefore, the Receiver B model is suggested especially for mobile receivers. In practice, one option would be to consider a hybrid of Receiver A and B. This means first iterating the clipping compensation on the symbol level until the performance saturates, then perform the turbo decoding, and finally do

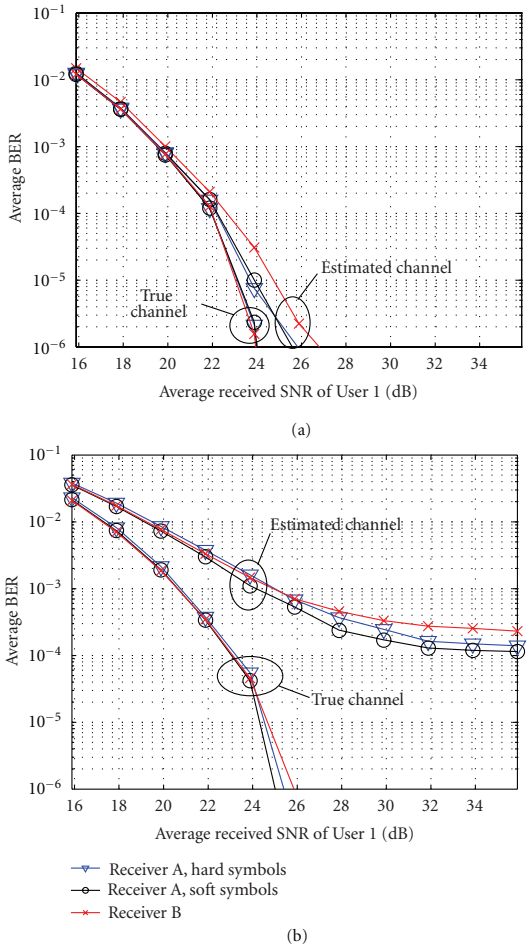

Figure 12: Performance comparison between Receivers A and B for User 1 as a function of average received SNR when 5 compensation iterations is performed and clipping level is (a) 6 dB or (b) 2 dB.

one more clipping compensation iteration as well as the final turbo decoding. This would provide a compromise between the performance and computational complexity.

Generally in this section, equal clipping levels in I and Q branches are assumed. However, the proposed clipping compensation algorithm completely supports unequal clipping levels as discussed in Sections 2 and 3. This feature is desired, since in practice there can be slight differences between the A/D converters of I and Q branch. In addition, other imbalances of analog circuitry can also affect the clipping levels. Figure 13 presents BER results for a clipping compensation example, where $\gamma_I = 6$ dB and $\gamma_Q = 3$ dB. The 3-dB difference in clipping levels can be considered to be a rather extreme situation but is used for demonstration purposes. However, the clipping compensation algorithm is

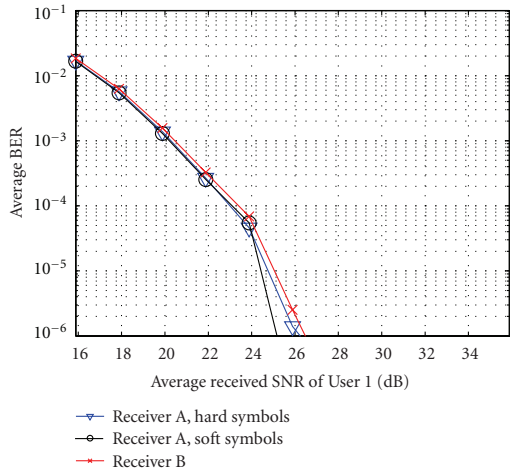

Figure 13: Performance comparison between Receivers A and B with channel estimation for User 1 as a function of average received SNR when 5 compensation iterations is performed and the clipping levels for I and Q branches are $\gamma_I = 6$ dB and $\gamma_Q = 3$ dB.

able to perform very well as can be seen from Figure 13. There is only a slight performance decrease compared to the Figure 12(a), where equal clipping levels ($\gamma = 6$ dB) are assumed. The small performance decrease is expected, because stronger clipping is more challenging to compensate as was shown in Figure 8.

4.2. Laboratory Measurement Experiment. The same two-user scenario used in the simulations of the previous Section is also used in laboratory measurements in order to provide comparable results. Only difference is that 10,000 OFDM symbols (instead of 20,000) are used in averaging the BER results due to the slowness of performing the measurements. The complete measurement setup is illustrated in Figure 14. First, a composite waveform of two users is created with a PC. Also the fading channel model is applied to the waveform already on the PC and noise is added so that the SNR of the overall waveform is 31 dB. This corresponds to the case used in the simulations, where $SNR_1 = 21.9$ dB and $SNR_2 = 36.9$ dB were calculated. This digital waveform is then sent to the baseband signal generator [26] in order to convert it to the analog domain. The communication interface between the PC and the signal generator is implemented with TCP/IP. The typical spurious free dynamic range of the used signal generator with a 14-bit D/A converter is 83 dBc [26]. Therefore, it can be assumed that the signal generator does not significantly change the generated waveform. The analog waveform is then fed to the 14-bit A/D converter [27] using balanced coaxial cable connection. The output voltage of the signal generator is adjusted so that it exceeds the maximum voltage level of the A/D converter input and the waveform gets clipped. The digitized clipped waveform is then read from the buffer memory of the A/D converter

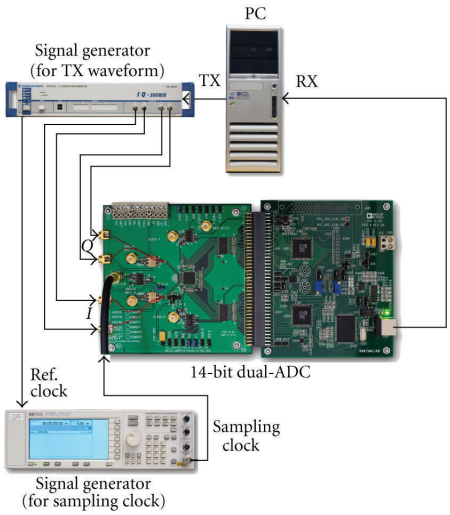

Figure 14: Laboratory measurement set-up. A signal waveform with fading channel is generated using the PC and fed to the baseband signal generator [26] to create an analog waveform. The output power of the signal generator is adjusted so that the signal is clipped in the A/D converter [27]. The digitized signal is then collected to the PC for clipping compensation.

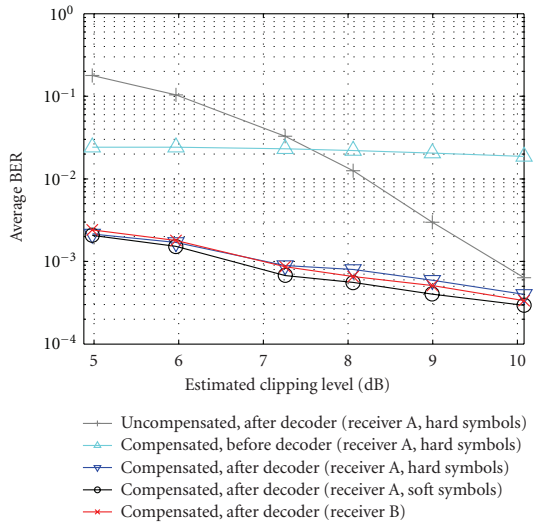

Figure 15: Laboratory measurement results for User 1 when $SNDR_1 = 21.7$ dB and 5 clipping compensation iterations is performed.

board to the PC using USB interface. Finally, the PC applies the proposed iterative clipping compensation method to the clipped waveform. The other signal generator shown on the lower left corner of Figure 14 is used to feed sampling clock signal for the A/D converter. The sampling rate is 30.72 MHz as specified in Table 1. There is also a reference clock signal between the signal generators to synchronize their internal oscillators.

The amount of noise and distortion the measurement setup creates can be obtained by running the measurements with a low voltage level so that the waveform does not clip in the A/D converter. The estimated SNR after measurements for the overall nonclipped waveform was 30.87 dB. In order to take also the distortion into account, the signal-to-noise-and-distortion ratio ($SNDR$) for the frequency band of user u is defined as

$$SNDR_u = \frac{E\left[\sum_{k\in\Omega_{A,u}} |H_k X_k|^2\right]}{E\left[\sum_{k\in\Omega_{A,u}} \left|\tilde{Y}_k - H_k X_k\right|^2\right]}. \quad (22)$$

Using the measured nonclipped waveform, it was observed that $SNDR_1 = 21.7$ dB and $SNDR_2 = 36.5$ dB. Figure 15 illustrates the clipping compensation results for User 1 in the laboratory measurement cases in which the occurred clipping is 5–10 dB. These are average estimated clipping levels for certain output voltage levels of the signal generator since the exact knowledge of clipping levels is not available. By comparing the BERs before and after the clipping compensation in Figure 15, it can be concluded that considerable gain is obtained. In addition, the performance difference between Receivers A and B is small as was indicated in the simulations of Section 4.1.

4.3. Computational Complexity of Clipping Compensation. Preceding Sections show that, in many cases, Receiver A and B provide rather similar performance. However, there is a significant difference in computational complexity. This is more formally shown in Table 2, which provides rough estimates of required real additions and multiplications per data symbol in the scenario discussed in Section 4. The numbers of operations are only suggestive since they are strongly depending on implementation platform in practice and the way how the particular functions are carried out. Only the usage of hard symbols estimates in clipping compensation is considered in this Section, because the usage of soft symbols does not change any main conclusions drawn here.

The channel estimation in Receiver A is more complex than the one of Receiver B, because it has to calculate the symbol reliabilities in (17) and combine estimates as defined in (16). For pilot-based channel estimates, the length of the used interpolation filter is 65 and $L = 8$ is considered in Table 2. The complexity of the turbo decoder is defined in [28] using the so-called equivalent additions meaning that computational costs of all mathematical and logical operations are expressed as multiples of one real addition operation. The same principle is adapted to all parts of Table 2 where needed. The complexity of FFT and IFFT operations are assumed to be as defined in [29].

As can be concluded from Table 2, the most complex part of the receivers is the turbo decoder. Receiver A uses the symbol demapper and turbo decoder in every clipping compensation iteration, that is, I times in total, whereas

Table 2: Rough estimate for computational complexity of the clipping compensation per data symbol expressed with real addition and real multiplication operations.

Operation	Additions	Multiplications
Scaling with $1/\hat{\alpha}_1$	0	2
Channel estimation (Receiver A)	$13M + 17$	$20 + M$
Channel estimation (Receiver B)	14	16
Channel equalization	0	4
Soft symbol demapping	$27M \cdot 2^M$	$3M \cdot 2^M$
Turbo decoding	$2130MR$	0
Apply channel estimate to symbol estimate ($\hat{H}_k\hat{X}_k$)	0	4
IFFT	$(2N\log_2 N)/((1 - 1/L)N_A)$	$(N\log_2 N)/((1 - 1/L)N_A)$
Clipping	$(2N)/((1 - 1/L)N_A)$	0
Scaling with $\hat{\alpha}_1$	0	2
FFT	$(2N\log_2 N)/((1 - 1/L)N_A)$	$(N\log_2 N)/((1 - 1/L)N_A)$
Calculating $\hat{Z}_k$ and subtracting it from $\tilde{Y}_k$	4	0
Estimating $\hat{\alpha}_1$	$(3N - 1)/((1 - 1/L)N_A)$	$(N + 7)/((1 - 1/L)N_A)$
Total (Receiver A)	$[((5 + 4\log_2 N)N - 1)/((1 - 1/L)N_A)$ $+(27 \cdot 2^M + 2130R + 13)M + 21]I$	$[((1 + 2\log_2 N)N + 7)/((1 - 1/L)N_A)$ $+(1 + 3 \cdot 2^M)M + 32]I$
Total (Receiver B)	$[((5 + 4\log_2 N)N - 1)/((1 - 1/L)N_A) + 18]I$ $+(27 \cdot 2^M + 2130R)M$	$[((1 + 2\log_2 N)N + 7)/((1 - 1/L)N_A) + 28]I$ $+3M \cdot 2^M$

Receiver B uses them only once. Therefore, Receiver B can be considered to be noticeably less complex. When using the parameter values from Table 1 and five clipping compensation iterations, it can be calculated from Table 2 that Receiver A requires 30865 additions and 1403 multiplications per data symbol whereas Receiver B needs only 6638 additions and 595 multiplications.

5. Conclusions

This paper discussed the compensation of unintentional clipping occurring in the A/D converter of a radio receiver. A digital postprocessing compensation method iteratively exploiting the symbol decisions and clipping distortion regeneration was proposed for multiband OFDMA receivers. The performance of the method was carefully studied in fading channel circumstances using computer simulations and also verified using concrete laboratory measurements with real A/D hardware. It was shown that it is possible to recover the system performance under significant clipping almost to the level of a nonclipped situation. The performance is mostly limited by the accuracy of the channel estimation, which is compromised under heavy clipping. Although it cannot be avoided that the clipping interferes with the channel estimation, it should be studied in the future what is the optimal channel estimation scheme under heavy unintentional clipping. This paper also discussed the complexity of the proposed clipping compensation. It was proven that it is possible, without considerably decreasing the performance, to iterate the compensation process on symbol level and perform the symbol demapping and channel decoding only once after finishing the clipping compensation. This way the computational complexity of the receiver signal processing can be kept at reasonable level.

Acknowledgments

This work was supported by the Academy of Finland (under the project "Digitally-Enhanced RF for Cognitive Radio Devices"), the Finnish Funding Agency for Technology and Innovation (Tekes, under the projects "Advanced Techniques for RF Impairment Mitigation in Future Wireless Radio Systems" and "Enabling Methods for Dynamic Spectrum Access and Cognitive Radio"), Austrian Center of Competence in Mechatronics (ACCM), Jenny and Antti Wihuri Foundation, Finnish Foundation for Technology Promotion, and Tampere University of Technology Graduate School.

References

[1] J. Yang, R. W. Brodersen, and D. Tse, "Addressing the dynamic range problem in cognitive radios," in *Proceedings of the IEEE International Conference on Communications (ICC '07)*, pp. 5183–5188, Glasgow, UK, June 2007.

[2] B. Razavi, "Cognitive radio design challenges and techniques," *IEEE Journal of Solid-State Circuits*, vol. 45, no. 8, Article ID 5518490, pp. 1542–1553, 2010.

[3] C. Svensson, "The blocker challenge when implementing software defined radio receiver RF frontends," *Analog Integrated Circuits and Signal Processing*, vol. 64, no. 2, pp. 81–89, 2010.

[4] A. Rusu, D. Rodríguez de Llera González, and M. Ismail, "Reconfigurable ADCs enable smart radios for 4G wireless

connectivity," *IEEE Circuits and Devices Magazine*, vol. 22, no. 3, pp. 6–11, 2006.

[5] T. Tomioka, R. Sakata, T. Horiguchi, T. Tomizawa, and K. Inoue, "A/D converter clipping noise suppression for high-sensitivity carrier-sensing of cognitive radio transceiver," in *Proceedings of the 50th Annual IEEE Global Telecommunications Conference (GLOBECOM '07)*, pp. 4170–4174, Washington, DC, USA, November 2007.

[6] M. Allén, J. Marttila, and M. Valkama, "Modeling and mitigation of nonlinear distortion in wideband A/D converters for cognitive radio receivers," *International Journal of Microwave and Wireless Technologies*, vol. 2, no. 2, pp. 183–192, 2010.

[7] M. Allén, J. Marttila, and M. Valkama, "Digitally-enhanced wideband analog-digital interfaces for future cognitive radio devices," in *Proceedings of the 8th IEEE International NEWCAS Conference (NEWCAS '10)*, pp. 361–364, Montréal, Canada, June 2010.

[8] S. H. Han and J. H. Lee, "An overview of peak-to-average power ratio reduction techniques for multicarrier transmission," *IEEE Wireless Communications*, vol. 12, no. 2, pp. 56–65, 2005.

[9] H. Chen and A. M. Haimovich, "Iterative estimation and cancellation of clipping noise for OFDM signals," *IEEE Communications Letters*, vol. 7, no. 7, pp. 305–307, 2003.

[10] H. Zhang, X.-G. Xia, Q. Zhang, and W. Zhu, "Iterative decision-aided clipping compensation and its application to scalable video transmission with multiband OFDM," *IEEE Transactions on Vehicular Technology*, vol. 56, no. 2, pp. 756–765, 2007.

[11] D. Petrovic, W. Rave, and G. Fettweis, "Effects of phase noise on OFDM systems with and without PLL: characterization and compensation," *IEEE Transactions on Communications*, vol. 55, no. 8, pp. 1607–1616, 2007.

[12] V. Syrjälä and M. Valkama, "Receiver DSP for OFDM systems impaired by transmitter and receiver phase noise," in *Proceedings of the IEEE International Conference on Communications (ICC '11)*, Kyoto, Japan, June 2011.

[13] J. Šterba, J. Gazda, M. Deumal, and D. Kocur, "Iterative algorithm for nonlinear noise cancellation and channel re-estimation in nonlinearly distorted OFDM system," in *Proceedings of the 8th International Symposium on Applied Machine Intelligence and Informatics (SAMI '10)*, pp. 65–70, Herl'any, Slovakia, January 2010.

[14] M. Allén, J. Marttila, and M. Valkama, "Iterative signal processing for mitigation of wideband ADC nonidealities in cognitive radio receiver," in *Proceedings of the 19th European Signal Processing Conference (EUSIPCO '11)*, pp. 2279–2283, Barcelona, Spain, August 2011.

[15] J. J. Bussgang, "Crosscorrelation functions of amplitude distorted Gaussian signals," Tech. Rep. 216, MIT Research Laboratory of Electronics, Cambridge, Mass, USA, 1952.

[16] H. Ochiai and H. Imai, "Performance analysis of deliberately clipped OFDM signals," *IEEE Transactions on Communications*, vol. 50, no. 1, pp. 89–101, 2002.

[17] H. E. Rowe, "Memoryless nonlinearities with gaussian inputs: elementary results," *The Bell System Technical Journal*, vol. 61, no. 7, pp. 1519–1525, 1982.

[18] H. Ochiai and H. Imai, "Performance of the deliberate clipping with adaptive symbol selection for strictly band-limited OFDM systems," *IEEE Journal on Selected Areas in Communications*, vol. 18, no. 11, pp. 2270–2277, 2000.

[19] L. Cheded, "Invariance property of gaussian signals: a new interpretation, extension and applications," *Circuits, Systems, and Signal Processing*, vol. 16, no. 5, pp. 523–536, 1997.

[20] C. Berrou, A. Glavieux, and P. Thitimajshima, "Near Shannon limit error-correcting coding and encoding: turbo-codes," in *IEEE International Conference on Communications (ICC '93)*, pp. 1064–1070, Geneva, Switzerland, May 1993.

[21] D. Divsalar and F. Pollara, "Turbo codes for PCS applications," in *Proceedings of the IEEE International Conference on Communications (ICC '95)*, pp. 54–59, Seattle, Wash, USA, June 1995.

[22] 3rd Generation Partnership Project, "3GPP TS 25.212 V7.2.0, technical specification group radio access network, multiplexing and channel coding (FDD), Release 7," 2006, http://www.3gpp.org/ftp/Specs/2006-09/Rel-7/25_series/25212-720.zip.

[23] P. Robertson, E. Villebrun, and P. Hoeher, "Comparison of optimal and sub-optimal MAP decoding algorithms operating in the log domain," in *Proceedings of the IEEE International Conference on Communications (ICC '95)*, pp. 1009–1013, Seattle, Wash, USA, June 1995.

[24] C. L. Kei and W. H. Mow, "Improved stopping criteria for iterative decoding of short-frame multi-component turbo codes," in *Proceedings of the IEEE International Conference on Communications, Circuits and Systems and West Sino Expositions (ICCCAS & WeSino Expo '02)*, pp. 42–45, Chengdu, China, June 2002.

[25] T. B. Sørensen, P. E. Mogensen, and F. Frederiksen, "Extension of the ITU channel models for wideband (OFDM) systems," in *Proceedings of the IEEE 62nd Vehicular Technology Conference (VTC-2005-Fall)*, pp. 392–396, Dallas, Tex, USA, September 2005.

[26] Rohde and Schwarz, "R&S AFQ100A/B I/Q modulation generator—data sheet," 2008, http://www2.rohde-schwarz.com/file_10716/AFQ100A_AFQ100B_dat_sw_en.pdf.

[27] Analog Devices Inc., "AD9248 data sheet, ver. B," 2010, http://www.analog.com/static/imported-files/data_sheets/AD9248.pdf.

[28] P. H.-Y. Wu, "On the complexity of turbo decoding algorithms," in *Proceedings of the IEEE VTS 53rd Vehicular Technology Conference (VTC-2001-Spring)*, pp. 1439–1443, Rhodes, Greece, May 2001.

[29] S. Winograd, *Arithmetic Complexity of Computations*, Society for Industrial and Applied Mathematics, Philadelphia, Pa, USA, 1980.

Publication 6

M. Allén, J. Marttila, and M. Valkama, "General clipping modeling and DSP-based mitigation for wideband A/D interface and RF front-end of emerging radio receivers," in *Proceedings of the IEEE 55th International Midwest Symposium on Circuits and Systems (MWSCAS2012)*, Boise, ID, USA, Aug. 2012, pp. 1148–1151. DOI: 10.1109/MWSCAS.2012.6292228

© 2012 IEEE. Reprinted, with permission, from the Proceedings of the IEEE 55th International Midwest Symposium on Circuits and Systems (MWSCAS2012).

In reference to IEEE copyrighted material which is used with permission in this thesis, the IEEE does not endorse any of Tampere University of Technology's products or services. Internal or personal use of this material is permitted. If interested in reprinting/republishing IEEE copyrighted material for advertising or promotional purposes or for creating new collective works for resale or redistribution, please go to http://www.ieee.org/publications_standards/publications/rights/rights_link.html to learn how to obtain a License from RightsLink.

General Clipping Modeling and DSP-Based Mitigation for Wideband A/D Interface and RF Front-End of Emerging Radio Receivers

Markus Allén, Jaakko Marttila and Mikko Valkama
Department of Communications Engineering
Tampere University of Technology
P.O. Box 553, FI-33101, Tampere, FINLAND
markus.allen@tut.fi, jaakko.marttila@tut.fi, mikko.e.valkama@tut.fi

***Abstract*—Emerging wireless communications concepts, such as cognitive radio, bring various challenges in the implementation of radio receivers. One of the concerns is the dynamic range of the receiver front-end, which might be insufficient in certain situations, e.g., if strong blocker signals are present concurrently with weaker interesting signals. Overdrive of the receiver front-end causes signal clipping and therefore considerable amount of nonlinear distortion is created. This paper derives a general parametric clipping model using time-dependent Fourier series and analyses the model in different clipping scenarios. The paper also proposes a method to exploit the derived model in a radio receiver for digital post-processing in order to mitigate unwanted clipping distortion.**

I. Introduction

Dynamic range is one of the main concerns in emerging wideband radio receivers for wireless communications, the ultimate example being a cognitive radio [1], [2]. Partially the requirement for high dynamic range is due to the modern communication waveforms, which tend to have high peak-to-average power ratio [3]. However, even more important reason is that wideband radio receivers suffers from a blocker problem [4]. It is possible that the receiver front-end is not selective enough to attenuate out-of-band blockers, which may cause inband interference because of receiver nonlinearities. Other scenario is a wideband receiver digitizing several signals at once, which may cause high-power signals to block weaker signals due to the receiver nonlinearities. Strong blocker signals can overdrive the A/D interface and therefore induce signal clipping, which heavily distorts the received waveform causing a vast amount of nonlinear distortion.

This paper proposes that time-dependent Fourier series can be used to model clipping occurring in the A/D interface of a radio receiver. Similar approach is also proposed in [5], but it considers only zero-symmetric clipping occurring equally in I and Q branches of a complex signal. In this paper, the clipping model is expanded to cover also more realistic scenarios, where clipping is non-symmetric w.r.t. zero and unequal in I and Q branches. This is important since real radio receivers suffer from non-idealities such as DC offset and I/Q imbalance [6]. The derived clipping model is useful for understanding better the clipping phenomenon and nonlinear distortion it causes. In addition, this paper proposes a clipping mitigation technique based on the derived parametric model.

This work was supported by the Academy of Finland (under the project "Digitally-Enhanced RF for Cognitive Radio Devices"), the Finnish Funding Agency for Technology and Innovation (Tekes, under projects "Advanced Techniques for RF Impairment Mitigation in Future Wireless Radio Systems" and "Enabling Methods for Dynamic Spectrum Access and Cognitive Radio"), Austrian Center of Competence in Mechatronics (ACCM) and Tampere University of Technology Graduate School.

II. A General Clipping Model

A homodyne receiver architecture is a typical structure for modern communications receivers. A complex signal comprising I and Q branches are separately digitized using two A/D converters, which together are called an I/Q ADC. This is depicted in Fig. 1. Due to the differences in A/D converters and other electrical components, the clipping may occur differently in I and Q branches. Hence the following clipping model is physically well-grounded.

The input signal for the I/Q ADC in Fig. 1 is defined here as an analytic bandpass signal

$$v_{IN}(t) = v_{IN,I}(t) + jv_{IN,Q}(t) = A(t)e^{j\theta_c(t)}, \tag{1}$$

where $A(t) \in [0,1]$ is the normalized signal envelope and $\theta_c(t) = \omega_c t + \varphi(t)$ includes angular frequency ω_c and phase $\varphi(t)$. Signal $v_{IN}(t)$ gets clipped, if it exceeds the full-scale range of the I/Q ADC. Therefore, the clipped output signal of the I/Q ADC is $v_{OUT}(t) = v_{OUT,I}(t) + jv_{OUT,Q}(t)$, where

$$v_{OUT,I}(t) = \begin{cases} v_{IN,I}(t), & V_{L,I} \le v_{IN,I}(t) \le V_{H,I} \\ V_{H,I}, & v_{IN,I}(t) > V_{H,I} \\ V_{L,I}, & v_{IN,I}(t) < V_{L,I}, \end{cases} \tag{2}$$

$$v_{OUT,Q}(t) = \begin{cases} v_{IN,Q}(t), & V_{L,Q} \le v_{IN,Q}(t) \le V_{H,Q} \\ V_{H,Q}, & v_{IN,Q}(t) > V_{H,Q} \\ V_{L,Q}, & v_{IN,Q}(t) < V_{L,Q}. \end{cases} \tag{3}$$

As can be seen from (2) and (3), clipping levels are defined separately for I and Q branches. In order to create even more

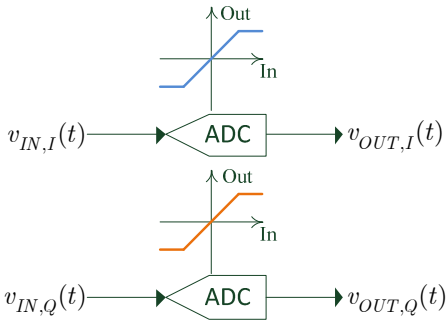

Fig. 1. Communication receivers typically use an I/Q ADC, which consists of two separate analog-to-digital converters. Input-output characteristics are depicted in the block diagram in order to illustrate the clipping phenomenon.

general model, for both branches the higher clipping levels $V_{H,I}$, $V_{H,Q} \in [0,1]$ and the lower clipping levels $V_{L,I}$, $V_{L,Q} \in [-1,0]$ are described independently.

Signal clipping causes nonlinear distortion to the signal and different distortion orders can be modeled separately using time-dependent Fourier series. Hence, the output signal can be written as

$$v_{OUT}(t) = \sum_{m=-\infty}^{\infty} a_m(t) e^{jm\theta_c(t)}, \tag{4}$$

where $a_m(t) = a_{m,I}(t) + j a_{m,Q}(t)$ are the time-dependent Fourier coefficients. The same approach is also used in [5], but this paper expands the model to more general case, where clipping is non-symmetric w.r.t. zero and the clipping levels are unequal in I and Q branches. Fig. 2 illustrates the signal clipping as a function of θ_c over a period of 2π and therefore covers all the possible values θ_c can have at a certain time moment t. Generally, the Fourier coefficients for I branch are calculated as

$$a_{m,I}(t) = \frac{1}{2\pi} \int_{2\pi} v_{OUT,I}(t) e^{-jm\theta_c(t)} \mathrm{d}\theta_c(t). \tag{5}$$

As shown in Fig. 2, the integration period is divided into five parts, i.e., the I branch Fourier coefficients are

$$\begin{aligned} a_{m,I}(t) = \frac{1}{2\pi} \Bigg[& \int_{-\pi/2}^{-r_{H,I}(t)} v_{IN,I}(t) e^{-jm\theta_c(t)} d\theta_c(t) \\ & + \int_{-r_{H,I}(t)}^{r_{H,I}(t)} V_{H,I} e^{-jm\theta_c(t)} d\theta_c(t) + \int_{r_{H,I}(t)}^{\pi - r_{L,I}(t)} v_{IN,I}(t) e^{-jm\theta_c(t)} d\theta_c(t) \\ & + \int_{\pi - r_{L,I}(t)}^{r_{L,I}(t)+\pi} V_{L,I} e^{-jm\theta_c(t)} d\theta_c(t) + \int_{r_{L,I}(t)+\pi}^{3\pi/2} v_{IN,I}(t) e^{-jm\theta_c(t)} d\theta_c(t) \Bigg] \end{aligned} \tag{6}$$

and similarly the Q branch Fourier coefficients are

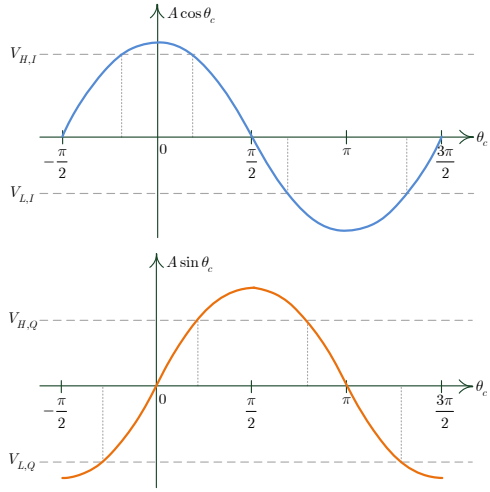

Fig. 2. Illustration of signal clipping for I and Q branches. Signals are presented as a function of the instantaneous angle θ_c over one period of 2π, i.e., the model covers all the possible values of θ_c.

$$\begin{aligned} a_{m,Q}(t) = \frac{1}{2\pi} \Bigg[& \int_{-\pi/2}^{-r_{L,Q}(t)} V_{L,Q} e^{-jm\theta_c(t)} d\theta_c(t) \\ & + \int_{-r_{L,Q}(t)}^{r_{H,Q}(t)} v_{IN,Q}(t) e^{-jm\theta_c(t)} d\theta_c(t) + \int_{r_{H,Q}(t)}^{\pi - r_{H,Q}(t)} V_{H,Q} e^{-jm\theta_c(t)} d\theta_c(t) \\ & + \int_{\pi - r_{H,Q}(t)}^{r_{L,Q}(t)+\pi} v_{IN,Q}(t) e^{-jm\theta_c(t)} d\theta_c(t) + \int_{r_{L,Q}(t)+\pi}^{3\pi/2} V_{L,Q} e^{-jm\theta_c(t)} d\theta_c(t) \Bigg], \end{aligned} \tag{7}$$

where the following auxiliary variables are utilized:

$$r_{H,I}(t) = \arccos \frac{V_{H,I}}{A(t)}, \tag{8}$$

$$r_{L,I}(t) = \arccos \frac{-V_{L,I}}{A(t)}, \tag{9}$$

$$r_{H,Q}(t) = \arcsin \frac{V_{H,Q}}{A(t)}, \tag{10}$$

$$r_{L,Q}(t) = \arcsin \frac{-V_{L,Q}}{A(t)}. \tag{11}$$

In addition, the following auxiliary variables are introduced to make subsequent equations more concise:

$$s_{H,I}(t) = \sin\big(r_{H,I}(t)\big) = \sqrt{1 - \left(\frac{V_{H,I}}{A(t)}\right)^2}, \tag{12}$$

$$s_{L,I}(t) = \sin\big(r_{L,I}(t)\big) = \sqrt{1 - \left(\frac{V_{L,I}}{A(t)}\right)^2}, \tag{13}$$

$$s_{H,Q}(t) = \cos\big(r_{H,Q}(t)\big) = \sqrt{1 - \left(\frac{V_{H,Q}}{A(t)}\right)^2}, \tag{14}$$

$$s_{L,Q}(t) = \cos\big(r_{L,Q}(t)\big) = \sqrt{1 - \left(\frac{V_{L,Q}}{A(t)}\right)^2}. \qquad (15)$$

The final form of Fourier coefficients after calculating the integrals are shown on the bottom of the page, where time index t is omitted in order to make the presentation more concise. Additionally, the equations for the Fourier coefficients are represented (on the bottom of the page) in a case, where clipping is non-symmetric w.r.t. zero but equal in I and Q branches. Notation of $\pm$ and $\mp$ is used in such a manner that the upper signs in an equation are valid at the same time and correspondingly the lower signs. An important note about the model is that it is assuming, for all t, that $A(t) \geq V_{H,I}$, $A(t) \geq V_{H,Q}, A(t) \geq -V_{L,I}$ and $A(t) \geq -V_{L,Q}$, i.e., the signal envelope is always clipped or at the clipping level. When this is not the case (the signal envelope is not clipping at the moment), the corresponding clipping levels should be set equal to $\pm A(t)$, depending if it is the higher $(+)$ or the lower $(-)$ clipping level, for computational purposes. When the envelope is equal to clipping level, it means that the signal is not clipped, but the clipping model is still valid and hence the model can be used also for the unclipped signal parts by tuning the clipping levels as described. In practice, e.g. in clipping mitigation, it is often unnecessary to apply the model for unclipped signal parts since obviously $v_{OUT}(t) = v_{IN}(t)$.

Simplifications of the clipping model can be carried out even further by considering a case, where clipping is zero-symmetric but unequal in I and Q branches, i.e., $V_I = V_{H,I} = -V_{L,I}$, $V_Q = V_{H,Q} = -V_{L,Q}$, $r_I(t) = r_{L,I}(t) = r_{H,I}(t)$, $r_Q(t) = r_{L,Q}(t) = r_{H,Q}(t)$, $s_I(t) = s_{L,I}(t) = s_{H,I}(t)$, $s_Q(t) = s_{L,Q}(t) = s_{H,Q}(t)$. Then the Fourier coefficients can be presented in a form of

$$a_m(t) = \begin{cases} \frac{A(t)}{2} \pm \frac{1}{\pi}\big[A(t)\big(r_Q(t) \mp r_I(t)\big) \\ +V_Q s_Q(t) \pm V_I s_I(t)\big], & m = \pm 1 \\ 0, & m = 0, \pm 2, \pm 4, \ldots \\ \frac{2}{\pi m(m^2-1)}\big[mA\big(s_I(t)\cos(mr_I(t)) \\ +s_Q(t)\sin(mr_Q(t))\big) \\ -V_I \sin(mr_I(t)) \\ -V_Q \cos(mr_Q(t))\big], & m = \pm 3, \pm 5, \ldots \end{cases} \qquad (16)$$

The most simple case (also presented in [5]) is the one, where zero-symmetric clipping occurs equally in I and Q branches, i.e., $V = V_I = V_Q$, $s(t) = s_I(t) = s_Q(t)$. It follows that the Fourier coefficients are then

$$a_m(t) = \begin{cases} A(t) + \frac{2}{\pi}\big[Vs(t) - A(t)r_I(t)\big], & m = +1 \\ 0, & m = 0, \pm 2, \pm 4, \ldots \\ 0, & m = -1, +3, -5, \ldots \\ \frac{4}{\pi m(m^2-1)} \\ \cdot\big[mA(t)s(t)\cos(mr_I(t)) & m = -3, +5, -7, \ldots \\ -V\sin(mr_I(t))\big], \end{cases} \qquad (17)$$

Due to the symmetry and equality of the clipping levels, the last case presented in (17) provides the most simple model. This is stemming from the fact that only odd-order nonlinear distortion is caused. To be more specific, there is distortion only on every other odd order, i.e., on +1, –3, +5, –7,... as defined in (17).

For general case (non-symmetric w.r.t. zero and unequal clipping in I and Q branches):

$$a_m = \begin{cases} \frac{1}{\pi}\Big\{A(s_{L,I} - s_{H,I}) + V_{H,I}r_{H,I} + V_{L,I}r_{L,I} + j\big[A(s_{L,Q} - S_{H,Q}) + V_{H,Q}(\frac{\pi}{2} - r_{H,Q}) + V_{L,Q}(\frac{\pi}{2} - r_{L,Q})\big]\Big\}, & m = 0 \\ \frac{A}{2} \pm \frac{1}{2\pi}\big[A(r_{L,Q} \pm r_{L,I} + r_{H,Q} \mp r_{H,I}) + V_{H,Q}s_{H,Q} \pm V_{H,I}s_{H,I} - V_{L,Q}s_{L,Q} \mp V_{L,I}s_{L,I}\big] & m = \pm 1 \\ \frac{1}{\pi m(m^2-1)}\Big\{mA\big(s_{H,I}\cos(mr_{H,I}) - s_{L,I}\cos(mr_{L,I})\big) - V_{H,I}\sin(mr_{H,I}) - V_{L,I}\sin(mr_{L,I}) \\ -j[mA\big(s_{H,Q}\cos(mr_{H,Q}) - s_{L,Q}\cos(mr_{L,Q})\big) + V_{H,Q}\sin(mr_{H,Q}) - V_{L,Q}\sin(mr_{L,Q})]\Big\}, & m = \pm 2, \pm 4, \ldots \\ \frac{1}{\pi m(m^2-1)}\Big\{mA\big(s_{H,I}\cos(mr_{H,I}) + s_{L,I}\cos(mr_{L,I}) + s_{H,Q}\sin(mr_{H,Q}) + s_{L,Q}\sin(mr_{L,Q})\big) \\ -V_{H,I}\sin(mr_{H,I}) + V_{L,I}\sin(mr_{L,I}) - V_{H,Q}\cos(mr_{H,Q}) + V_{L,Q}\cos(mr_{L,Q})\Big\}, & m = \pm 3, \pm 5, \ldots \end{cases}$$

For non-symmetric case with equal clipping in I and Q branches ($V_L = V_{L,I} = V_{L,Q}$, $V_H = V_{H,I} = V_{H,Q}$, $s_L = s_{L,I} = s_{L,Q}$, $s_H = s_{H,I} = s_{H,Q}$):

$$a_m = \begin{cases} \frac{1+j}{\pi}\big[A(s_L - s_H) + V_H r_{H,I} + V_L r_{L,I}\big], & m = 0 \\ A + \frac{1}{\pi}\big[A(-r_{L,I} - r_{H,I}) + V_H s_H - V_L s_L\big], & m = +1 \\ \frac{1-j}{\pi m(m^2-1)}\big[mA\big(s_H\cos(mr_{H,I}) - s_L\cos(mr_{L,I})\big) - V_H\sin(mr_{H,I}) - V_L\sin(mr_{L,I})\big], & m = \pm 2, \pm 6, \ldots \\ \frac{1+j}{\pi m(m^2-1)}\big[mA\big(s_H\cos(mr_{H,I}) - s_L\cos(mr_{L,I})\big) - V_H\sin(mr_{H,I}) - V_L\sin(mr_{L,I})\big], & m = \pm 4, \pm 8, \ldots \\ \frac{2}{\pi m(m^2-1)}\big[mA\big(s_H\cos(mr_{H,I}) + s_L\cos(mr_{L,I})\big) - V_H\sin(mr_{H,I}) + V_L\sin(mr_{L,I})\big], & m = -3, +5, -7, \ldots \\ 0, & m = -1, +3, -5, \ldots \end{cases}$$

III. Clipping Mitigation

The derived clipping model can also be used for clipping mitigation purposes, e.g., in a radio receiver. From the received signal $v_{OUT}(t)$, it is possible to extract the estimate of $a_{0,I}(t)$, which is here denoted as $\hat{a}_{0,I}(t)$ and corresponds to the signal content around 0 Hz. The extraction can be done, e.g., using a narrow lowpass filter. If reliable estimates of the angular frequency ω_c and the phase $\varphi(t)$ can be obtained, then the only unknown variable in the equation of the sent signal $v_{IN}(t)$, see (1), is the signal envelope $A(t)$.

In the derivation of the envelope estimate $\hat{A}(t)$, the well-known infinite series representations

$$\sqrt{1-x} = 1 - \frac{x}{2} - \frac{x^2}{8} - \frac{x^3}{16} - \ldots \quad (18)$$

$$\arccos x = \frac{\pi}{2} - x - \frac{1}{2}\frac{x^3}{3} - \frac{1\cdot 3}{2\cdot 4}\frac{x^5}{5} - \frac{1\cdot 3\cdot 5}{2\cdot 4\cdot 6}\frac{x^7}{7} - \ldots \quad (19)$$

are employed. A rough estimate of $A(t)$ is obtained using only the first two terms of (18) and (19). In case of non-symmetric but equal clipping in I and Q, the envelope estimate is

$$\hat{A}(t) = \frac{V_L^2 - V_H^2}{\pi(2\hat{a}_{0,I}(t) - V_H - V_L)}. \quad (20)$$

After calculating $\hat{A}(t)$, the values can be used in (1) to obtain an estimate of unclipped signal. It is worth noticing that (20) is exploiting the fact that $a_{0,I}(t) \neq 0$, when clipping is not symmetric w.r.t. zero. In a real hardware, this can considered to be a rather realistic assumption. The estimator in (20) requires knowledge about the clipping levels and these can be estimated in practice as shown, e.g., in [7].

IV. Simulation Example and Compensation Performance

Fig. 3 shows a simulation example of a QPSK signal, which is clipped non-symmetrically but equally in I and Q branches. The original signal has a center frequency of 10 MHz and oversampling ratio of 256 is used here only for illustrational purposes, i.e., to show the clipping distortion without aliasing. The clipped signal has new frequency content around zero (among others), but not at -10 MHz, 30 MHz, -50 MHz, ... and therefore matches with the clipping model derived in Section II for non-symmetric but equal I and Q clipping.

The bottom part of Fig. 3 illustrates the spectrum after the signal has been reconstructed using the mitigation technique proposed in Section III, when perfect estimates of ω_c, $\varphi(t)$ and clipping levels are assumed. It can be seen that the strongest distortion components are considerably suppressed. For example, the third order distortion is here suppressed by 17 dB. However, due the rough approximations made in the derivation of (20), the clipping mitigation is not perfect. More accurate estimates of $\hat{A}(t)$ could be obtained, but then also an increase in computational complexity is expected.

V. Conclusion

The paper derived a general signal clipping model using time-dependent Fourier series and also proposed a simple clipping mitigation method based on the derived model. The mitigation technique showed promising performance for clipping distortion suppression and has potential for even better performance, if combined with other clipping mitigation techniques or if the derived Fourier model is exploited even more extensively.

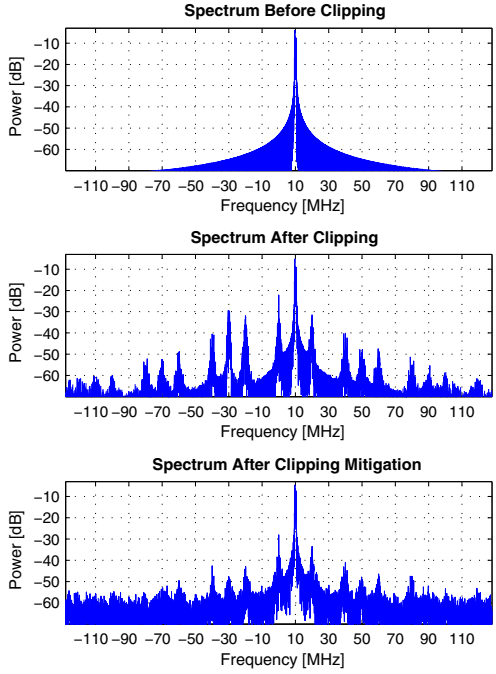

Fig. 3. Simulation example of a QPSK signal, which gets clipping non-symmetrically w.r.t. zero but equally in I and Q branches. The clipping distortion is then mitigated using the proposed method.

References

[1] B. Razavi, "Cognitive radio design challenges and techniques," *IEEE J. Solid-State Circuits*, vol. 45, no. 8, pp. 1542–1553, Aug. 2010.

[2] J. Yang, R. W. Brodersen and D. Tse, "Addressing the dynamic range problem in cognitive radios," in *Proc. IEEE Int. Conf. Communications (ICC-07)*, Glasgow, Scotland, June 2007, pp. 5183–5188.

[3] S. H. Han and J. H. Lee, "An overview of peak-to-average power ratio reduction techniques for multicarrier transmission," *IEEE Wireless Commun.*, vol. 12, no. 2, pp. 56–65, Apr. 2005.

[4] C. Svensson, "The blocker challenge when implementing software defined radio receiver RF frontends," *Analog Integrated Circuits and Signal Processing*, vol. 64, no. 2, pp. 81–89, 2010.

[5] M. Allén, J. Marttila and M. Valkama, "Modeling and mitigation of nonlinear distortion in wideband A/D converters for cognitive radio receivers," *European Microwave Assoc. Int. J. Microwave and Wireless Technologies*, vol. 2, no. 2, pp. 183–192, Apr. 2010.

[6] L. Anttila, M. Valkama and M. Renfors, "Circularity-based I/Q imbalance compensation in wideband direct-conversion receivers," *IEEE Trans. Veh. Technol.*, vol. 57, no. 4, pp. 2099–2113, July 2008.

[7] M. Allén, T. Levanen, J. Marttila and M. Valkama, "Iterative signal processing for mitigation of analog-to-digital converter clipping distortion in multiband OFDMA receivers," *Journal of Electrical and Computer Engineering*, vol. 2012.

Publication 7

M. Allén, J. Marttila, M. Valkama, S. Mäkinen, M. Kosunen, and J. Ryynänen, "Digital linearization of direct-conversion spectrum sensing receiver," in *Proceedings of the 1st IEEE Global Conference on Signal and Information Processing (GlobalSIP2013)*, Austin, TX, USA, Dec. 2013, pp. 1158–1161. DOI: 10.1109/GlobalSIP.2013.6737112

© 2013 IEEE. Reprinted, with permission, from the Proceedings of the 1st IEEE Global Conference on Signal and Information Processing (GlobalSIP2013).

In reference to IEEE copyrighted material which is used with permission in this thesis, the IEEE does not endorse any of Tampere University of Technology's products or services. Internal or personal use of this material is permitted. If interested in reprinting/republishing IEEE copyrighted material for advertising or promotional purposes or for creating new collective works for resale or redistribution, please go to http://www.ieee.org/publications_standards/publications/rights/rights_link.html to learn how to obtain a License from RightsLink.

Digital Linearization of Direct-Conversion Spectrum Sensing Receiver

Markus Allén, Jaakko Marttila, and Mikko Valkama
Dept. of Electronics and Communications Engineering
Tampere University of Technology
P.O. Box 692, FI-33101 Tampere, Finland
{markus.allen, jaakko.marttila, mikko.e.valkama}@tut.fi

Semu Mäkinen, Marko Kosunen, and Jussi Ryynänen
Department of Micro- and Nanosciences
Aalto University
FI-00076 Espoo, Finland
{semu.makinen, marko.kosunen, jussi.ryynanen}@aalto.fi

***Abstract*—Reliable spectrum sensing ability is a key factor in cognitive radios. However, there are many aspects that impact the sensing reliability. One important aspect is impairments in the cognitive radio receiver hardware. Received signals tend to have high dynamic range which drives the receiver to the nonlinear zone. This may cause nonlinear distortion falling to the sensing band and therefore either triggers a false alarm or missed detection. This paper specifically focuses on the digital compensation of sensing receiver LNA nonlinearities which are typically the most significant sources of nonlinearity. The proposed method is able to notably remove nonlinear distortion from the received signal and thus spectrum sensing algorithms become more reliable. With the help of simulations, this is shown not only for a classical energy detector but also for a cyclostationary feature detector.**

***Index Terms*—Cognitive radio, interference cancellation, low-noise amplifier, nonlinear distortion, spectrum sensing**

I. Introduction

Spectrum sensing is one central ingredient in cognitive radio systems to identify temporally or spatially vacant frequencies for opportunistic radio communications [1]. In order to scan large frequency bands in varying conditions, stringent requirements are set for sensing receiver hardware [2]. Presence of strong signals can make it difficult to sense neighboring bands due to the limited dynamic range of receiver front-end. Because of limited filtering, especially low-noise amplifier (LNA) nonlinearities can cause distortion to an empty frequency band and falsely trigger the sensing algorithm [3]. If energy detector is used, the additional power of the nonlinear distortion causes a false alarm. On the other hand, also more advanced spectrum sensing algorithms, such as feature detectors [4], suffer from receiver nonlinearities. This is due to the fact that the nonlinear distortion contains similar features as the signal where it originates from. This typically causes a false alarm. In addition, a strong noncyclic signal causes noncyclic nonlinear distortion, which may mask the weak cyclic signal to be sensed with feature detectors and therefore a missed detection is also possible.

This work was supported by the Finnish Funding Agency for Technology and Innovation (Tekes) under the project "Enabling Methods for Dynamic Spectrum Access and Cognitive Radio," The Academy of Finland under the project 251138 "Digitally-Enhanced RF for Cognitive Radio Devices", Austrian Competence Center in Mechatronics (ACCM), and Tampere University of Technology Graduate School.

This paper exploits the fully digital compensation approach introduced in [5], [6], specifically tailored for direct-conversion sensing receiver. A similar approach, but with additional hardware, is proposed in [7]. This paper shows that the fully digital approach is feasible also for cognitive radios. The emphasis is on proving that the selected approach enhances the performance and reliability of spectrum sensing algorithms. This is rather self-evident for energy detectors, but the performance of cyclic feature detectors is more complicated to predict. This is because a reduction in the distortion power does not always guarantee that the cyclic features of the distortion are removed. This topic is analyzed in detail with computer simulations in this paper.

The rest of the paper is structured as follows. First, Section II discusses about receiver nonlinearity effects from the spectrum sensing point of view and provides some concrete examples. Section III gives the description of the nonlinearity compensation algorithm and then Section IV provides computer simulation results of spectrum sensing performance. Finally, Section V concludes the paper.

II. RF Nonlinearity Challenges in Spectrum Sensing

A cognitive radio receiver employing direct-conversion architecture is illustrated in Fig. 1. The LNA after the antenna is typically the main source of odd-order nonlinear distortion although other components also have their contribution. The distortion deteriorates spectrum sensing performance by causing significant amount of false alarms. This problem has been confronted in real-world spectrum sensing devices [8].

The main contribution of different nonlinear components can be categorized in terms of order of nonlinearity, and probability of caused false detection. Second-order nonlinearity in the down-conversion and following stages will fold energy from all the channels containing a signal. Cyclostationary features of, e.g., an OFDM modulated signal will be preserved while signal undergoes second-order distortion. Furthermore, if the signals present are from the same system having the same OFDM symbol length and cyclic prefix length, all the folded signals will contribute on energy on the same cyclic frequency, therefore resulting in cumulative error mechanisms for both the energy and cyclostationary feature detectors. However, because the even-order nonlinearity of the receiver

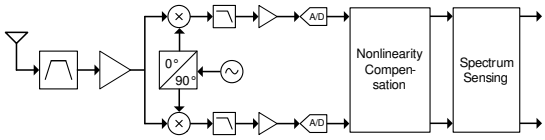

Fig. 1. Block diagram for cognitive radio receiver employing direct-conversion principle.

can be made sufficiently good with careful circuit design, and because presence of multiple strong carriers simultaneously is not so likely, accumulation of second-order nonlinearity products is not usually the primary source of false detections in cognitive radio spectrum sensors [2], [9]. In addition, even-order distortion terms of RF components fall far away from the original center frequency and are filtered out by the lowpass filters after down-conversion.

Third-order nonlinearity products also cause false detection through self-modulation and intermodulation. The contribution of self- and intermodulation to energy detection is evident, but for cyclostationary feature detectors the false detection mechanism is not so straightforward. In the third-order inter-modulation, the prerequisites for the false detection to occur in cyclostationary feature detector is that the two strong signals of the same system coexist and the signals are synchronized so that the cyclic prefixes overlap. The contribution of the intermodulation to the cyclostationary feature is proportional to probabilities of coexistence and synchronization.

The mechanisms for false detections due to third-order self-modulation is similar to the error mechanism of second-order distortion, but instead of zero frequency, third-order self-modulation causes leakage of strong signals to the adjacent channels. As for second-order nonlinearity, cyclostationary features are preserved and contribution to cyclic frequency component is cumulative for the signals with same features. Taking into account the targeted sensitivity level of the spectrum sensor, the third-order linearity should be better than for the receivers of current systems. In other words, a typical feature detector is able to work reliably even if the SNR is negative, but the linearity of current systems has not been designed for such scenarios. On the other hand, improving the linearity performance beyond the state of the art with the circuit design techniques is very challenging. Based on the aforementioned observations, this paper concentrates on the digital compensation of third-order self-modulation in spectrum sensors for cognitive radios.

A measurement-based example is provided in Fig. 2, where spectrum sensing results using cyclostationary feature detection algorithm [10] for DVB-T channels in different measurement locations are shown. Channels 44, 45, 46, and 53 are truly occupied due to the DVB-T broadcast and the spectrum sensing algorithm detects them as expected. However, some other channels are also falsely claimed to be occupied. This is because the broadcast signals are strong, especially in the northern coast area, and therefore it causes nonlinear distortion in the receiver, which then obfuscates the spectrum sensing.

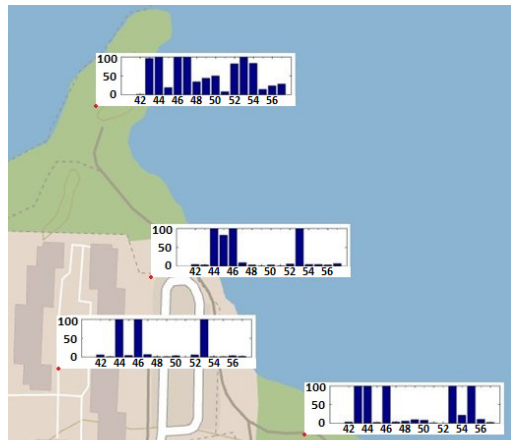

Fig. 2. Illustration of spectrum sensing results of DVB-T measurements in Otaniemi area, Espoo, Finland. Broadcast transmitters use channels 44, 45 46, and 53. Some of the channels are falsely detected as occupied due to the nonlinear distortion caused by the spectrum-sensing receiver itself, especially in the northern coast area where the broadcast signals are strong.

TABLE I
SYSTEM CALCULATION EXAMPLE FOR THE IMPACT OF ADJACENT CHANNEL SIGNAL THIRD-ORDER INTERMODULATION DISTORTION

Input noise power	-105	dBm
Input blocker signal power	-35	dBm
LNA gain	15	dB
LNA noise figure	5	dB
LNA IIP3	-10	dBm
Output IMD3 power	-70	dBm
Output noise power	-85	dBm
IMD3 above noise	**15**	**dB**

It is easy to show with a receiver system-level calculation that strong neighboring channels can cause considerable amount of nonlinear distortion. An example calculation is provided in Table I. It assumes a DVB-T signal with 8 MHz bandwidth and -35 dBm power level at receiver input, which is considered to be realistic, e.g., in [11]. Given the LNA specifications, it can be calculated that LNA third-order intermodulation distortion (IMD3) power in the LNA output is -70 dBm. The noise level in the LNA output being -85 dBm, the IMD3 is thus 15 dB above the noise floor. In practice, only portion of the IMD3 power falls to the potentially empty adjacent channel. However, it is typically still enough to trigger the sensing algorithms.

The LNA input can be written as

$$x_{\mathrm{RF}}(t) = 2\,\mathrm{Re}[x(t)e^{j\omega_c t}] = x(t)e^{j\omega_c t} + x^*(t)e^{-j\omega_c t}, \quad (1)$$

where ω_c is the angular center frequency and $x(t)$ is the complex baseband equivalent signal for $x_{\mathrm{RF}}(t)$. If the LNA is modeled with a third-order memoryless polynomial model, the LNA output is

$$y_{\mathrm{RF}}(t) = a_1 x_{\mathrm{RF}}(t) + a_2 x^3_{\mathrm{RF}}(t), \quad (2)$$

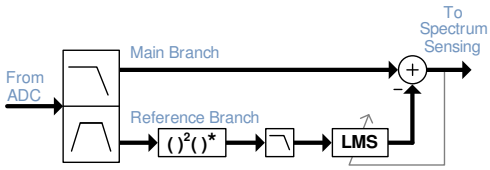

Fig. 3. Block diagram for digital compensation of third-order RF nonlinearity.

where a_1 and a_2 are complex coefficients. By substituting (1) into (2), it is straightforward to derive that the nonlinear distortion around the original center frequency is $3a_2x^2(t)x^*(t)e^{j\omega_c t}$. Therefore, the baseband equivalent model for the third-order RF nonlinearity is

$$y(t) = a_1x(t) + 3a_2x^2(t)x^*(t), \tag{3}$$

which can be exploited in the digital compensation of RF nonlinearities.

III. Compensation of RF Front-End Nonlinearities

By removing third-order nonlinear RF distortion from the band of interest, the sensing reliability can be increased significantly. The compensation approach employed in this paper originates from [5], [6], developed originally for classical communications receivers for enhancing demodulation. Here it is specifically used for compensating third-order RF distortion as shown in Fig. 3.

After digitization, the signal is split into two branches. The main branch contains the sensing band. The reference branch contains the strong blocker signal or even more than one blocker signal. The nonlinear distortion in the band of interest is stemming from the blockers, which are now exploited to regenerate the distortion by applying the reference model $(\,)^2(\,)^*$ in accordance with (3). Then filtering is applied to pick up only the regenerated distortion falling on the band of interest. Finally an adaptive algorithm, such as LMS, is employed to control the amplitudes and phases of the regenerated distortion products such that distortion cancellation is as accurate as possible. After compensating the nonlinear distortion from the band of interest, the cleaned signal is then fed to the spectrum sensing algorithm.

IV. Simulation Results for Compensation Performance

In this section, a simulation example is given for a DVB-T sensing scenario. Two channels are considered to be occupied by strong DVB-T signals, which act as blockers and drives the receiver front-end to the nonlinear region. This is causing nonlinear distortion to the channel between the blockers. In simulations, only third-order RF nonlinearity caused by an LNA is considered and it is modeled as described in (3).

Simulation parameters are given in Table II. In all power calculations 1 Ω nominal load is assumed. The gain of the remaining receiver chain, down to the ADC input, is assumed to be properly controlled such that ADC full-scale voltage range is properly utilized without clipping. Fig. 4 illustrates

TABLE II
Simulation Parameters

Sampling rate	40	MHz
Quantization	12	bits
ADC analog input range	±1	V
Channel bandwidth	8	MHz
Number of blocker signals	2	
Number of subcarriers	8192	
Number of active subcarriers	6817	
Guard interval	1/8	
Subcarrier modulation	64-QAM	
LNA gain	15	dB
LNA IIP3	-10	dBm
Receiver noise figure	9	dB

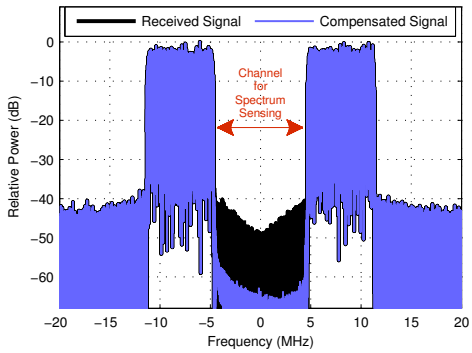

Fig. 4. Spectrum illustrations before and after digital compensation of nonlinear distortion when the average LNA input power is -15 dBm. The channel in the middle is empty in this example, i.e., all the energy is due to the noise and nonlinear distortion leaking from the neighboring channels.

the spectrum of the signal scenario. In the input of the LNA, the average power is -15 dBm, which consists of two blocker signals. The channel in the center from -4 to +4 MHz is vacant, but after the LNA it contains nonlinear distortion from the neighboring channels. The compensation algorithm described in Section III is employed to remove the distortion. The compensation outcome is also shown in Fig. 4. In this particular example, the compensation algorithm is able to reduce the power of nonlinear distortion by 22 dB within the channel used for spectrum sensing.

The compensation algorithm performance is more generally depicted in Fig. 5 where false alarm probability is given as a function of LNA input power for an energy detector as well as for a cyclic feature detector. The set false alarm probability for the detectors is 0.05. However, there is uncertainty in the calculated threshold level of the energy detector due to the implementation inaccuracies (filters etc.) and hence the false alarm probability can fall to zero in Fig. 5. From the false alarm point of view, the gain achieved with the nonlinearity compensation is approx. 10 dB in input power for the energy detector. The gain can be interpreted as dynamic range extension for the receiver. The results show similar dynamic range extension for the cyclic feature detector. It means that

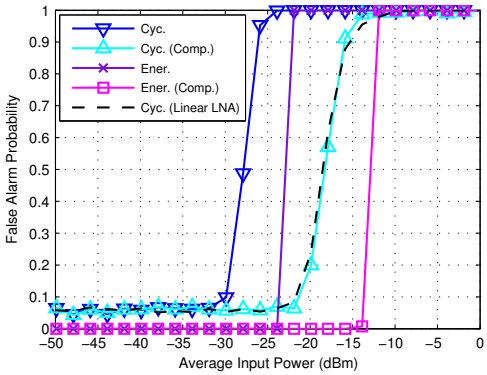

Fig. 5. False alarm simulation results as a function of LNA input power for cyclic feature detector (cyc.) and for energy detector (ener.) before and after nonlinearity compensation.

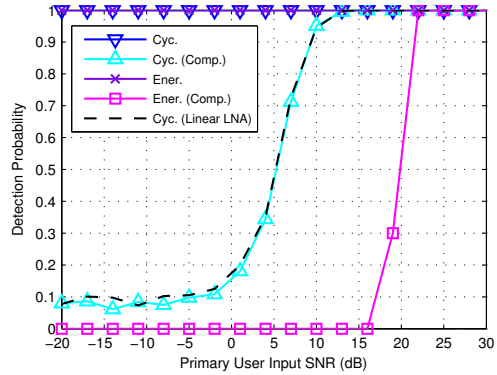

Fig. 7. Signal detection probability as a function of primary user SNR in the LNA input when the average input blocker power is -22 dBm.

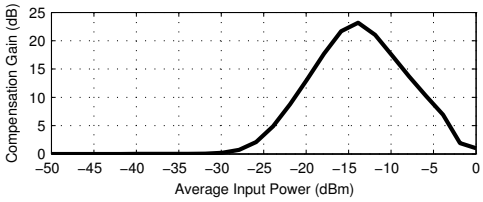

Fig. 6. Nonlinearity compensation gain as a function of LNA input power. The compensation gain is defined as a relationship between the distortion power levels before and after compensation.

the nonlinear distortion is reduced enough so the detector is not finding the false cyclic features of the distortion anymore. The dashed line curve illustrates cyclic detector behavior for a perfectly linear reference receiver. It is noteworthy that the cyclic detector false alarm probability is high for high input power levels even in the linear receiver. This is due to the fact that in high SNR scenarios the quantization noise becomes significant and triggers the detector because the quantization noise contains the cyclic features of the blockers.

Fig. 6 shows how much the compensation algorithm is able to reduce the distortion power in the sensing band. With low input signal levels there is no nonlinear distortion to be removed so the compensation gain is zero. With very strong input signals, the compensation performance decreases due to the self-distortion of the blockers. Signal detection probability is illustrated in Fig. 7 for both detectors before and after the nonlinearity compensation when the LNA input power for the blocker signals is -22 dBm. The dashed line shows cyclic feature detector performance in the case of perfectly linear LNA. The nonlinearity compensation is able to recover the cyclic feature detector performance close to linear LNA case, which maximizes the detector reliability.

V. Conclusion

The paper discussed how spectrum sensing receiver nonlinearities, especially stemming from an LNA, can deteriorate the sensing performance. A digital nonlinearity compensation was used to enhance the sensing performance for energy and cyclic feature detectors. With the help of computer simulations it was shown that clear dynamic range extension can be achieved for both type of detectors using the digital compensation.

References

[1] E. Axell, G. Leus, E. G. Larsson, and H. V. Poor, "Spectrum sensing for cognitive radio : State-of-the-art and recent advances," *IEEE Signal Process. Mag.*, vol. 29, no. 3, pp. 101–116, May 2012.

[2] B. Razavi, "Cognitive radio design challenges and techniques," *IEEE J. Solid-State Circuits*, vol. 45, no. 8, pp. 1542–1553, Aug. 2010.

[3] D. H. Mahrof, E. A. M. Klumperink, J. C. Haartsen, and B. Nauta, "On the effect of spectral location of interferers on linearity requirements for wideband cognitive radio receivers," in *Proc. IEEE Symp. on New Frontiers in Dynamic Spectrum (DySPAN2010)*, Singapore, Apr. 2010, pp. 1–9.

[4] V. Turunen, M. Kosunen, M. Vääräkangas, and J. Ryynänen, "Correlation-based detection of OFDM signals in the angular domain," *IEEE Trans. Veh. Technol.*, vol. 61, no. 3, pp. 951–958, Mar. 2012.

[5] M. Valkama, A. Shahed hagh ghadam, L. Anttila, and M. Renfors, "Advanced digital signal processing techniques for compensation of nonlinear distortion in wideband multicarrier radio receivers," *IEEE Trans. Microw. Theory Tech.*, vol. 54, no. 6, pp. 2356–2366, June 2006.

[6] A. Shahed hagh ghadam, "Contributions to analysis and DSP-based mitigation of nonlinear distortion in radio transceivers," Ph.D. dissertation, Dept. Commun. Eng., Tampere University of Technology, Tampere, Finland, 2011.

[7] E. Keehr and A. Hajimiri, "Equalization of third-order intermodulation products in wideband direct conversion receivers," *IEEE J. Solid-State Circuits*, vol. 43, no. 12, pp. 2853–2867, Dec. 2008.

[8] M. Vääräkangas, S. Kallioinen, A. Pärssinen, V. Turunen, and J. Ryynänen, "Trade-offs in primary detection using a mobile phone as a sensing device," in *Proc. 6th Int. ICST Conf. on Cognitive Radio Oriented Wireless Networks and Communications (CROWNCOM2011)*, Osaka, Japan, June 2011, pp. 241–245.

[9] S. C. Blaakmeer, E. A. M. Klumperink, D. M. W. Leenaerts, and B. Nauta, "Wideband balun-LNA with simultaneous output balancing, noise-canceling and distortion-canceling," *IEEE J. Solid-State Circuits*, vol. 43, no. 6, pp. 1341–1350, June 2008.

[10] V. Turunen, M. Kosunen, A. Huttunen, S. Kallioinen, P. Ikonen, A. Pärssinen, and J. Ryynänen, "Implementation of cyclostationary feature detector for cognitive radios," in *Proc. 4th Int. Conf. on Cognitive Radio Oriented Wireless Networks and Communications (CROWNCOM2009)*, Hannover, Germany, June 2009, pp. 1–4.

[11] C. L. Heng and W. Y. Ali-Ahmad, "Non-linearity requirements for UMTS and DVB RF receivers with higher blocking margins," in *Proc. IEEE Int. Workshop on Radio-Frequency Integration Technology (RFIT2007)*, Singapore, Dec. 2007, pp. 131–134.

Publication 8

M. Grimm, M. Allén, J. Marttila, M. Valkama, and R. Thomä, "Joint mitigation of nonlinear RF and baseband distortions in wideband direct-conversion receivers," *IEEE Transactions on Microwave Theory and Techniques*, vol. 62, no. 1, pp. 166–182, Jan. 2014. DOI: 10.1109/TMTT.2013.2292603

© 2014 IEEE. Reprinted, with permission, from the IEEE Transactions on Microwave Theory and Techniques.

In reference to IEEE copyrighted material which is used with permission in this thesis, the IEEE does not endorse any of Tampere University of Technology's products or services. Internal or personal use of this material is permitted. If interested in reprinting/republishing IEEE copyrighted material for advertising or promotional purposes or for creating new collective works for resale or redistribution, please go to http://www.ieee.org/publications_standards/publications/rights/rights_link.html to learn how to obtain a License from RightsLink.

Joint Mitigation of Nonlinear RF and Baseband Distortions in Wideband Direct-Conversion Receivers

Michael Grimm, Markus Allén, *Student Member, IEEE,* Jaakko Marttila, *Student Member, IEEE,* Mikko Valkama, *Member, IEEE,* and Reiner Thomä, *Fellow, IEEE*

***Abstract*—Software-defined radio technology is experiencing more and more attention in modern communication and radar systems. The main practical challenge in deploying such technology is related to achieving sufficient linearity and spurious-free dynamic range in the RF front-end, especially in low-cost mass-product devices. This paper focuses on the analysis and digital mitigation of nonlinear distortion in software-defined radio devices, building on wideband multicarrier/multiradio direct-conversion receiver principle where a wide collection of radio frequencies is I/Q down-converted as a whole. A complete behavioral model for the total nonlinear distortion of the whole receiver chain is first derived, taking into account the third-order nonlinear distortion effects in all individual components, namely RF low-noise amplifier, I/Q mixer and baseband I/Q amplifiers. Stemming from this modeling, adaptive digital feed-forward linearization structure is then developed, to efficiently mitigate the joint nonlinear distortion of the whole receiver. The effectiveness of this approach is verified through extensive simulations and actual RF system measurements with a commercially available software defined radio platform, which clearly outperforms the existing state-of-the-art methods that do not jointly consider RF and baseband nonlinearities.**

***Index Terms*—Cognitive radio, software-defined radio, adaptive signal processing, linearization techniques, nonlinear distortion, interference cancellation, intermodulation distortion**

I. Introduction

THE commercial availability of various software-defined radio (SDR) platforms has provided an easy way for experimental radio system research with a highly flexible RF interface. This plays an important role in communications and passive radar applications. Multiradio basestation transceivers in mobile cellular radio systems, with capability of simultaneous transmission and reception at multiple cellular bands and access technologies, form a good example of potential SDR deployment scenarios. In this kind of flexible RF spectrum use, obtaining sufficient linearity and spurious-free dynamic range (SFDR) is one of the biggest challenges [1], especially if one wideband RF chain is deployed, instead of multiple parallel RF chains. Similar challenges are faced in wideband cognitive radio (CR) sensing receivers, as discussed, e.g., in [2] when trying to extract wideband instantaneous radio environment knowledge.

This paper focuses on nonlinear distortion and SFDR challenges in wideband multicarrier/multiradio direct-conversion receivers (DCRs) where a wide collection of radio frequencies is in-phase/quadrature (I/Q) down-converted as a whole. In contrast to the *transmitter* side, the perspective on nonlinear distortion at *receiver* side is fundamentally different. In transmitters, especially when simultaneously transmitting multiple carriers of a single or possibly even multiple radio access technologies through a single power amplifier (PA), there are big challenges with obtaining sufficient linearity [3]. In wideband multiradio receivers, however, nonlinear distortion problems are even more challenging due to the presence of multiple unknown signals, with different power levels and dynamics due to the specific propagation conditions. As the dynamic range within the overall down-converted frequency range can be in the order of 60–100 dB [1], [2], such wideband receivers are extremely prone to any imperfections in the RF analog components. In general, essential receiver RF impairments include DC offsets due to self-mixing, oscillator phase noise, I/Q imbalance, and nonlinear distortions [1]. In particular, I/Q imbalance and nonlinear distortion effects of the receiver components can severely degrade the demodulation performance at weak signal bands, and also heavily affect the reliability of spectrum monitoring or sensing in CR [2], [4]–[8]. In multiradio receivers, the most challenging scenarios arise when the same wideband RF chain is simultaneously receiving multiple GSM, UMTS/WCDMA and LTE carriers, and some of them are close to the maximum allowed blocking signal level whereas some others are close to the receiver sensitivity level. In these kind of scenarios, the intermodulation distortion (IMD) of strong blocking carriers can easily mask the weaker signals, thus requiring extreme linearity from the receiver. Similar challenges exist in wideband CR sensing receivers, where some of the primary user signals can be close to the thermal noise floor, but should still be identified in the presence of other strong co-existing signals. Additionally,

Manuscript received July 8, 2013; revised November 8, 2013; accepted November 15, 2013. This work was supported by the Finnish Funding Agency for Technology and Innovation (Tekes) under the project "Enabling Methods for Dynamic Spectrum Access and Cognitive Radio," the Academy of Finland under the project 251138 "Digitally-Enhanced RF for Cognitive Radio Devices," Austrian Competence Center in Mechatronics (ACCM), TUT Graduate School, Nokia Foundation, and the International Graduate School on Mobile Communications supported by the German Research Foundation (DFG GRK1487).

M. Grimm and R. Thomä are with the Electronic Measurement Research Lab, Institute for Information Technology, Ilmenau University of Technology, 98684 Ilmenau, Germany (e-mail: michael.grimm@tu-ilmenau.de, reiner.thomae@tu-ilmenau.de).

M. Allén, J. Marttila, and Mikko Valkama are with the Department of Electronics and Communications Engineering, Tampere University of Technology, P.O. Box 692, FI-33101 Tampere, Finland (e-mail: markus.allen@tut.fi, jaakko.marttila@tut.fi, mikko.e.valkama@tut.fi).

strong nonlinear distortion can cause false alarms in spectrum sensing when a vacant channel contains the distortion and is falsely interpreted as being occupied by a primary user [7]. Compared to conventional receiver architectures with multiple intermediate frequency (IF) stages, most of the selectivity in DCR front-ends is implemented at the baseband (BB) or only in digital domain in favor of flexibility and operation over a wide bandwidth. Therefore, linearity and dynamic range requirements are extremely stringent.

In this paper, we address the modeling and digital mitigation of nonlinear distortion of all the essential RF analog components of a wideband DCR. In the existing literature, mitigating receiver nonlinear distortion by means of BB digital signal processing has been proposed in [9], [10], and subsequently followed in [7], [11]–[15], among others. Furthermore, specific even-order distortion mitigation in classical narrowband DCR context is addressed in [16]. In all these works, specific reference models of considered nonlinear components are applied, either in analog or digital domain, to regenerate considered distortion products and to subtract them from the received signal. Previous works [7], [9], [10], [12], [13], [17] all focus on specific receiver component only, namely RF low-noise amplifier (LNA), BB amplifiers or analog-to-digital converter (ADC), whereas [14] provides specific application of distortion mitigation to interference scenarios in GSM downlink. Furthermore, customized analog receiver designs were proposed in [11] and [12] to overcome specific limitations of entirely digital processing based approaches.

According to the best knowledge of the authors, however, modeling and mitigation of the nonlinearities induced by a complete DCR chain, including RF LNA, I/Q mixer and BB I/Q amplifiers, as well as their interaction with mixer I/Q imbalance is missing from the existing state-of-the-art literature. As all these components behave in a nonlinear manner in practice, understanding and being able to mitigate the joint nonlinear distortion effects are seen critical and therefore addressed in this paper. Contrary to conventional spectral regrowth around the distortion-producing signal, distortion products in DCRs are created by RF and BB receiver components and may fall within the BB bandwidth. Thus, we first derive the complete behavioral model for the total nonlinear distortion, which takes into account the third-order nonlinear distortion of the RF LNA, I/Q imbalance of the I/Q mixer, and third-order nonlinear distortion of the mixer and BB amplifiers. Individual component modeling is kept at third-order level since third-order distortion is the most dominant one in practice, and the presentation and notations are also simplified. Notice, however, that from the total receiver distortion modeling perspective, up to ninth-order distortion modeling is supported by joint modeling of RF and BB distortion. Stemming from this modeling, efficient DSP-based linearization structure, together with practical adaptive filtering based learning algorithms, are then developed. All the signal processing developments are non-data-aided (blind), as in general received signals are unknown due to unknown modulating data and unknown propagation conditions. Thus, the developed linearization can be carried out in the very first stages of the receiver digital front-end, prior to any modulation- or system-specific processing and carrier-/timing synchronization. This is a substantial practical benefit, compared to data-aided approaches, since heavy nonlinear distortion can also easily hinder the operation of, e.g., synchronization algorithms. Finally, extensive computer simulation results, as well as actual RF system measurements with commercial SDR platform, namely Universal Software Radio Peripheral (USRP) [18], are provided. Based on the obtained results, the developed linearization scheme clearly outperforms the existing reference methods, which can only suppress the effects of individual receiver components. Thus, the developed linearization solution can be seen as one key enabling technique towards practical deployment of SDR technology with digitally-enhanced wideband RF front-ends.

The outline of the remainder of the paper is as follows. In the following Section II, nonlinear distortion effects and mirror-frequency interference created in the DCR chain are discussed and modeled in detail, first component-wise and then accumulated into a total composite model. Based on that joint model, Section III then develops the proposed digital mitigation architecture and associated parameter learning algorithms. Simulation and RF measurement results are presented and analyzed in Section IV, whereas Section V gives further discussions, result analysis, and outlook on future work. Finally, conclusions are drawn in Section VI.

II. Nonlinear Distortion Analysis in Wideband Direct-Conversion Receivers

This section gives a detailed description of nonlinearities occurring in DCRs and a derivation of a complete mathematical model, combining RF and BB stage nonlinearities.

A. Receiver Architecture and Signal Scenario of Interest

DCRs have become more popular due to their inherent advantages over superheterodyne receivers [1], [19]. The DCR architecture is compact since the frequency translation from RF to BB is performed by a single mixing stage. The direct down-conversion allows signal amplification and filtering at BB, therefore, decreasing power consumption and simplifying image rejection. Altogether, these benefits ease the implementation of the whole receiver as a monolithic integrated circuit and decrease its manufacturing cost. However, DCRs suffer from the RF and BB impairments, such as I/Q imbalance and nonlinear distortion, as discussed in Section I.

Fig. 1 depicts a basic block diagram of a DCR with quadrature down-conversion, which generally consists of analog RF, mixer, analog BB, and digital post-processing stages. In practice, analog RF and BB stages suffer from unavoidable nonlinear behavior. Distortions that are created at the RF amplifier are typically dominating distortions created at the BB stages. However, they depend on the deployed components. In addition, the RF filtering provides very low selectivity. Thus, strong out-of-band signals can easily enter the front-end amplification and mixing stages. Beside receiver nonlinearity, I/Q imbalance of the mixer and the BB I/Q branches cause distorting mirror signal components that may interfere with other useful signals.

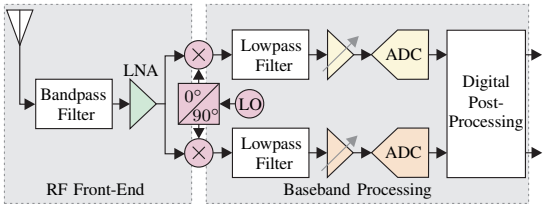

Fig. 1. Conceptual direct-conversion receiver block diagram. In wideband receiver scenario, multiple carriers and possibly also radio access technologies are received simultaneously, and selectivity filtering is implemented in the digital parts.

The most challenging case in deploying the direct-conversion radio architecture is the wideband multicarrier/multiradio scenario where the down-converted signal contains multiple carriers of multiple co-existing radio access technologies, throughout the whole receiver chain through the A/D interface. This kind of scenario leads to high dynamic range signal configurations with weak and strong signals simultaneously present. It is then likely that nonlinear distortions caused by strong signals fall on top of weak desired signals or leak into free frequency bands in case of CR sensing receiver. In CR context, free frequency bands are typically called white spaces [4]. Receiver distortion may mask a white space so that spectrum sensing algorithms falsely consider it to be occupied, which causes the CR to be less efficient from the spectrum exploitation point of view. Since multiple signals from different sources may, in general, arrive at the antenna input, mitigation of distortions created in the receiver becomes more challenging than in a transmitter, where the signal sources are well-known inside the device. Therefore, proper modeling of DCRs is essential to clean the whole BB from all distortions stemming from the strong input signals.

B. RF Nonlinearities

In this paper, BB equivalent signal modeling is used as it is notationally convenient and widely adopted convention [20]. The received bandpass signal $x_{\mathrm{RF}}(t)$ can be presented as

$$x_{\mathrm{RF}}(t) = 2\,\mathrm{Re}[x(t)e^{j\omega_{\mathrm{c}}t}] = x(t)e^{j\omega_{\mathrm{c}}t} + x^*(t)e^{-j\omega_{\mathrm{c}}t}, \quad (1)$$

where ω_{c} is the angular center frequency of the total RF signal to be down-converted and $x(t)$ is the corresponding BB equivalent signal of $x_{\mathrm{RF}}(t)$ ($(\cdot)^*$ denotes complex conjugate). Notice that in this notation, in case of wideband multicarrier down-conversion, the BB equivalent signal $x(t)$ contains all individual carrier waveforms at different complex IFs. Furthermore, $x(t)$ is defined as

$$x(t) = A(t)e^{j\phi(t)} = x_{\mathrm{I}}(t) + jx_{\mathrm{Q}}(t), \quad (2)$$

where $A(t)$ and $\phi(t)$ are the total envelope and phase of the overall down-converted RF signal $x(t)$, whereas $x_{\mathrm{I}}(t)$ and $x_{\mathrm{Q}}(t)$ denote the corresponding composite I and Q signals, respectively. The signal model (2) provides a starting point for modeling RF and BB nonlinearities of DCRs. This leads to the structure shown in Fig. 2, where also simplified BB equivalent spectra are illustrated, with only one active carrier for visualization purposes. Next, more detailed modeling of the RF LNA nonlinearities is addressed.

From the actual RF signal perspective, the RF nonlinearities can be modeled using a generalized Hammerstein model

$$y_{\mathrm{RF}}(t) = b_1(t) * x_{\mathrm{RF}}(t) + b_2(t) * x_{\mathrm{RF}}^2(t) + \ldots, \quad (3)$$

where $b_1(t), b_2(t), b_3(t), \ldots$ are impulse responses for each nonlinearity order taking memory effects into account [21]. In practice, (3) models the nonlinear behavior of the LNA in the RF stage. Using this notation, the input of the LNA in Fig. 1 is $x_{\mathrm{RF}}(t)$ and the output is $y_{\mathrm{RF}}(t)$. While (3) provides the general model, it is possible to simplify it and still capture the most essential behavior of the DCR. Even-order RF nonlinearities produce new frequency components, which are in most cases far away from ω_{c} and thus most likely to be filtered out. For example, an equation obtained from (1) and (3) for the second-order nonlinearity

$$x_{\mathrm{RF}}^2(t) = 2x(t)x^*(t) + x^2(t)e^{j2\omega_{\mathrm{c}}t} + [x^*(t)]^2e^{-j2\omega_{\mathrm{c}}t} \quad (4)$$

illustrates the new frequencies appearing around $\pm 2\omega_{\mathrm{c}}$ and DC (zero frequency), but no IMD components are created within the interesting RF bandwidth around ω_{c}. However, IMD contained in $x_{\mathrm{RF}}(t)$ cannot be seen directly from (4). These even-order RF IMD components are usually not harmful, except if the RF front-end is extremely wideband and $x_{\mathrm{RF}}(t)$ consists of several strong signals, which are far away from each other [2]. Even in this case, the even-order effects are not significant when proper circuit design methodologies providing high second-order intercept points are employed [2], [22]. In addition, the even-order nonlinearities induce spectral content around DC, such as $2x(t)x^*(t) = 2A^2(t)$ in (4), but it can be removed effectively with AC-coupling or filtering [2], [23]. Odd-order nonlinearities are, however, more critical since they cause new frequency components near ω_{c}, i.e., within the total frequency band of interest. In practice, the third-order nonlinearity is usually the strongest and the only one among the RF nonlinearity orders that appears clearly above the noise level. Therefore, a simplified RF nonlinearity model

$$y'_{\mathrm{RF}}(t) = a_1x_{\mathrm{RF}}(t) + a_2x_{\mathrm{RF}}^3(t) \quad (5)$$

is considered here, in which memory effects are omitted for notational simplicity and hence scalar coefficients a_1 and a_2, instead of filters $b_1(t)$ and $b_3(t)$, are used. This leads to the widely-used memoryless polynomial model [10], [24]. The lack of memory simplifies the notation in this analysis so that the most essential interpretations of the nonlinearity phenomenon can be made more easily. The memory effects are then taken into account later in the next section when impairment mitigation is discussed. The coefficients a_1 and a_2 are chosen to be complex in order to model AM/PM distortion of the LNA [24].

To further analyze the new spectral content by the third-order RF nonlinearity, the latter term of (5) can be written as

$$\begin{aligned} a_2x_{\mathrm{RF}}^3(t) &= a_2\{x(t)e^{j\omega_{\mathrm{c}}t} + x^*(t)e^{-j\omega_{\mathrm{c}}t}\}^3 \\ &= a_2\{x^3(t)e^{j3\omega_{\mathrm{c}}t} + [x^*(t)]^3e^{-j3\omega_{\mathrm{c}}t} \\ &\quad + 3x^2(t)x^*(t)e^{j\omega_{\mathrm{c}}t} + 3x(t)[x^*(t)]^2e^{-j\omega_{\mathrm{c}}t}\}. \end{aligned} \quad (6)$$

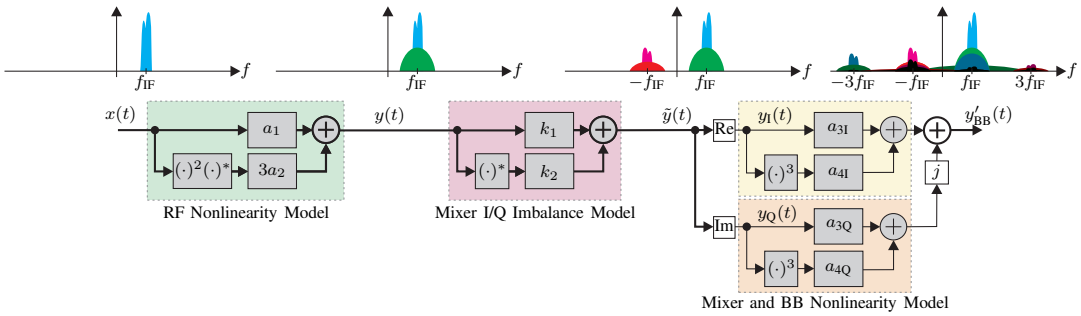

Fig. 2. Cascaded model considering third-order RF and BB nonlinearities in the presence of mixer and BB I/Q imbalance. Due to the generality of the nonlinearity models, they also take mixer nonlinearities into account. The spectrum illustrations are sketched for BB equivalent signals matching to the mathematical modeling in the paper, and only a single carrier is shown for visualization purposes.

From (6) it is apparent that there is only one term that causes new frequency content around ω_{c}, i.e., $3a_2x^2(t)x^*(t)e^{j\omega_{\mathrm{c}}t}$. The effective RF nonlinearity contribution comes from this particular term since it is shifted to the BB in the I/Q down-conversion stage whereas the other three terms in (6) do not hit the BB and are hence filtered out. Therefore, the essential BB equivalent form of (5) after the BB filtering becomes

$$\begin{aligned} y(t) &= y_{\mathrm{I}}(t) + jy_{\mathrm{Q}}(t) \\ &= a_1x(t) + 3a_2x^2(t)x^*(t) \\ &= a_1x(t) + 3a_2A^2(t)x(t) \\ &= a_1x(t) + 3a_2z(t). \end{aligned} \tag{7}$$

The second-last form of (7) is stemming from the fact that $x(t)x^*(t) = |x(t)|^2 = A^2(t)$. An auxiliary variable $z(t)$ is introduced here to denote the RF distortion contribution and make some of the further equations easier to interpret. The real and imaginary parts of $y(t)$ can be written as

$$\begin{aligned} y_{\mathrm{I}}(t) &= a_1x_{\mathrm{I}}(t) + 3a_2[x_{\mathrm{I}}^3(t) + x_{\mathrm{I}}(t)x_{\mathrm{Q}}^2(t)] \\ &= a_1x_{\mathrm{I}}(t) + 3a_2A^2(t)x_{\mathrm{I}}(t) \\ &= a_1x_{\mathrm{I}}(t) + 3a_2z_{\mathrm{I}}(t), \end{aligned} \tag{8a}$$

$$\begin{aligned} y_{\mathrm{Q}}(t) &= a_1x_{\mathrm{Q}}(t) + 3a_2[x_{\mathrm{I}}^2(t)x_{\mathrm{Q}}(t) + x_{\mathrm{Q}}^3(t)] \\ &= a_1x_{\mathrm{Q}}(t) + 3a_2A^2(t)x_{\mathrm{Q}}(t) \\ &= a_1x_{\mathrm{Q}}(t) + 3a_2z_{\mathrm{Q}}(t). \end{aligned} \tag{8b}$$

It is worth noticing that the term $3a_2A^2(t)x(t)$ only causes distortion around the center frequency of $x(t)$. However, the bandwidth of the distortion is wider than of $x(t)$, because of the multiplication with the squared envelope $A^2(t)$.

After the LNA, the signal goes through a wideband I/Q down-conversion stage as depicted in Fig. 1. In practice, an I/Q mixer cannot provide exactly 90° phase shift as desired but sustains a phase mismatch of ϕ_{m} (rad). Additionally, the I/Q mixer suffers from a relative amplitude mismatch g_{m} between the I and Q branches. These mismatches cause I/Q imbalance, which is seen as mirroring of frequency content of $y(t)$. More detailed information about I/Q imbalance can be found in [25], [26], and references therein. The I/Q imbalance of the down-conversion stage is here modeled as

$$\tilde{y}(t) = k_1y(t) + k_2y^*(t), \tag{9}$$

where the complex mismatch coefficients are

$$k_1 = \left(1 + g_{\mathrm{m}}e^{-j\phi_{\mathrm{m}}}\right)/2, \tag{10a}$$

$$k_2 = \left(1 - g_{\mathrm{m}}e^{j\phi_{\mathrm{m}}}\right)/2. \tag{10b}$$

With perfect I/Q balance, $g_{\mathrm{m}} = 1$, $\phi_{\mathrm{m}} = 0$ and hence $k_1 = 1$, $k_2 = 0$. The RF-distorted signal with I/Q imbalance $\tilde{y}(t) = \tilde{y}_{\mathrm{I}}(t) + j\tilde{y}_{\mathrm{Q}}(t)$ can now be expressed as

$$\tilde{y}_{\mathrm{I}}(t) = y_{\mathrm{I}}(t), \tag{11a}$$

$$\tilde{y}_{\mathrm{Q}}(t) = g_{\mathrm{m}}\cos(\phi_{\mathrm{m}})y_{\mathrm{Q}}(t) - g_{\mathrm{m}}\sin(\phi_{\mathrm{m}})y_{\mathrm{I}}(t). \tag{11b}$$

The results presented in (8) and (11) are important in a sense that $\tilde{y}(t)$ is the signal distorted by both RF nonlinearities and mixer I/Q imbalance, and hence describes their joint impact. More specifically, the signal at this point contains the intermodulation distortion created by the RF LNA and its mirror image symmetrically around zero-frequency, as well as the actual mirror image of the ideal signal. These are illustrated in Fig. 2. Next, the I and Q signals become further distorted through mixer and baseband nonlinearities. This is elaborated further in the following subsection.

C. Mixer and Baseband Nonlinearities

BB nonlinearity modeling differs from RF nonlinearities in such a way that in the BB there are physically separate I and Q branches in which the nonlinearities occur independently. In general, for the distorted BB signal $y_{\mathrm{BB}}(t) = y_{\mathrm{I,BB}}(t) + jy_{\mathrm{Q,BB}}(t)$, the generalized Hammerstein model is

$$y_{\mathrm{I,BB}}(t) = c_{1\mathrm{I}}(t) * \tilde{y}_{\mathrm{I}}(t) + c_{2\mathrm{I}}(t) * \tilde{y}_{\mathrm{I}}^2(t) + \ldots, \tag{12a}$$

$$y_{\mathrm{Q,BB}}(t) = c_{1\mathrm{Q}}(t) * \tilde{y}_{\mathrm{Q}}(t) + c_{2\mathrm{Q}}(t) * \tilde{y}_{\mathrm{Q}}^2(t) + \ldots, \tag{12b}$$

where $c_{1\mathrm{I}}(t), c_{2\mathrm{I}}(t), c_{3\mathrm{I}}(t), \ldots$ and $c_{1\mathrm{Q}}(t), c_{2\mathrm{Q}}(t), c_{3\mathrm{Q}}(t), \ldots$ are impulse responses for each nonlinearity order in the I and Q branches. This model basically takes into account all the nonlinearities of BB components shown in Fig. 1, specifically amplifiers and ADCs, and also mixers since the I/Q mixer outputs are already at down-converted frequencies. In the following, the term "BB nonlinearities" is used to cover these as a whole. There are different impulse responses for I and Q polynomials, because nonlinearities themselves can be different in the I and Q branches since those contain

physically separate components in practice. Furthermore, BB circuit components in the I and Q branches typically have slightly different gain characteristics, which introduce I/Q imbalance. In general, this I/Q imbalance is frequency-dependent as discussed in [25], [26].

Similar to the RF nonlinearities, simplifications to the BB model are justifiable. Only the third-order BB nonlinearity is considered here as it describes the most significant distortions. Even-order distortions are very weak due to efficient circuit design solutions such as differential signaling [27]. In typical DCRs, signaling behind the LNA is performed symmetrically, i.e., by using two signals that are ideally 180° out of phase. The differential voltage can be written as $V_{\text{diff}} = V_+ - V_-$. By writing down (12a) or (12b) for V_+ and V_- and computing the differential voltage V_{diff}, it can be shown that even-order terms cancel out, whereas odd-order terms increase by factor two [27]. However, even-order cancellation by differential signaling requires a symmetrical layout and matched amplifiers to ensure perfect balance among the signals. The minor importance of even-order distortions is also presented by the measurements in Section IV. Furthermore, higher odd-order distortions are typically masked by noise in practice. Therefore, the simplified model becomes

$$y'_{\text{I,BB}}(t) = a_{3\text{I}}\tilde{y}_{\text{I}}(t) + a_{4\text{I}}\tilde{y}_{\text{I}}^3(t), \tag{13a}$$

$$y'_{\text{Q,BB}}(t) = a_{3\text{Q}}\tilde{y}_{\text{Q}}(t) + a_{4\text{Q}}\tilde{y}_{\text{Q}}^3(t), \tag{13b}$$

where the real-valued scalar coefficients $a_{3\text{I}}$, $a_{3\text{Q}}$, $a_{4\text{I}}$, and $a_{4\text{Q}}$ are used, instead of the filters $c_{1\text{I}}(t)$, $c_{1\text{Q}}(t)$, $c_{3\text{I}}(t)$, and $c_{3\text{Q}}(t)$. This means that the memory effects are omitted in this analysis phase similar to the RF nonlinearities in (5). However, the forthcoming digital mitigation signal processing in Section III is devised such that also frequency-dependent effects can be tackled. The obtained complete nonlinearity model, combining RF and BB nonlinearities with I/Q imbalances, is visualized with a block diagram in Fig. 2.

D. Model Interactions and Interpretations

First, assuming perfectly balanced I/Q mixer, i.e. $\tilde{y}(t) = y(t)$, Equations (13a) and (13b) can be further modified by substituting $y_{\text{I}}(t)$ and $y_{\text{Q}}(t)$ from (8a) and (8b) so that

$$\begin{aligned} y'_{\text{I,BB}}(t) &= a_{3\text{I}}a_1x_{\text{I}}(t) + 3a_{3\text{I}}a_2z_{\text{I}}(t) \\ &\quad + a_{4\text{I}}a_1^3x_{\text{I}}^3(t) + 9a_{4\text{I}}a_1^2a_2x_{\text{I}}^2(t)z_{\text{I}}(t) \\ &\quad + 27a_{4\text{I}}a_1a_2^2x_{\text{I}}(t)z_{\text{I}}^2(t) + 27a_{4\text{I}}a_2^3z_{\text{I}}^3(t) \\ &= a_{3\text{I}}[a_1 + 3a_2A^2(t)]x_{\text{I}}(t) \\ &\quad + a_{4\text{I}}[a_1^3 + 9a_1^2a_2A^2(t) \\ &\quad + 27a_1a_2^2A^4(t) + 27a_2^3A^6(t)]x_{\text{I}}^3(t), \end{aligned} \tag{14a}$$

$$\begin{aligned} y'_{\text{Q,BB}}(t) &= a_{3\text{Q}}a_1x_{\text{Q}}(t) + 3a_{3\text{Q}}a_2z_{\text{Q}}(t) \\ &\quad + a_{4\text{Q}}a_1^3x_{\text{Q}}^3(t) + 9a_{4\text{Q}}a_1^2a_2x_{\text{Q}}^2(t)z_{\text{Q}}(t) \\ &\quad + 27a_{4\text{Q}}a_1a_2^2x_{\text{Q}}(t)z_{\text{Q}}^2(t) + 27a_{4\text{Q}}a_2^3z_{\text{Q}}^3(t) \\ &= a_{3\text{Q}}[a_1 + 3a_2A^2(t)]x_{\text{Q}}(t) \\ &\quad + a_{4\text{Q}}[a_1^3 + 9a_1^2a_2A^2(t) \\ &\quad + 27a_1a_2^2A^4(t) + 27a_2^3A^6(t)]x_{\text{Q}}^3(t). \end{aligned} \tag{14b}$$

The expressions in (14) clearly show the interaction between the RF and BB stages. In other words, the BB nonlinearities are affecting the original signal as well as the RF distortion components and, therefore, more elaborate and complicated total intermodulation profile is created. It is noteworthy that some of the new frequency components would not appear, if RF and BB nonlinearities were modeled independently, i.e., in (12a) and (12b) there would be $x_{\text{I}}(t)$ and $x_{\text{Q}}(t)$ instead of $\tilde{y}_{\text{I}}(t)$ and $\tilde{y}_{\text{Q}}(t)$. It is noteworthy that (14a) and (14b) can be also written as

$$\begin{aligned} y'_{\text{I,BB}}(t) &= 27a_{4\text{I}}a_2^3x_{\text{I}}^9(t) + 81a_{4\text{I}}a_2^3x_{\text{I}}^7(t)x_{\text{Q}}^2(t) \\ &\quad + 27a_{4\text{I}}a_1a_2^2x_{\text{I}}^7(t) + 81a_{4\text{I}}a_2^3x_{\text{I}}^5x_{\text{Q}}^4 \\ &\quad + 54a_{4\text{I}}a_1a_2^2x_{\text{I}}^5(t)x_{\text{Q}}^2(t) + 9a_{4\text{I}}a_1^2a_2x_{\text{I}}^5(t) \\ &\quad + 27a_{4\text{I}}a_2^3x_{\text{I}}^3(t)x_{\text{Q}}^6(t) + 27a_{4\text{I}}a_1a_2^2x_{\text{I}}^3(t)x_{\text{Q}}^4(t) \\ &\quad + 9a_{4\text{I}}a_1^2a_2x_{\text{I}}^3(t)x_{\text{Q}}^2(t) + (a_{4\text{I}}a_1^3 + 3a_{3\text{I}}a_2)x_{\text{I}}^3(t) \\ &\quad + a_{3\text{I}}a_2 3x_{\text{I}}(t)x_{\text{Q}}^2(t) + a_{3\text{I}}a_1x_{\text{I}}(t), \end{aligned} \tag{15a}$$

$$\begin{aligned} y'_{\text{Q,BB}}(t) &= 27a_{4\text{Q}}a_2^3x_{\text{Q}}^9(t) + 81a_{4\text{Q}}a_2^3x_{\text{I}}^2(t)x_{\text{Q}}^7(t) \\ &\quad + 27a_{4\text{Q}}a_1a_2^2x_{\text{Q}}^7(t) + 81a_{4\text{Q}}a_2^3x_{\text{I}}^4x_{\text{Q}}^5 \\ &\quad + 54a_{4\text{Q}}a_1a_2^2x_{\text{I}}^2(t)x_{\text{Q}}^5(t) + 9a_{4\text{Q}}a_1^2a_2x_{\text{Q}}^5(t) \\ &\quad + 27a_{4\text{Q}}a_2^3x_{\text{I}}^6(t)x_{\text{Q}}^3(t) + 27a_{4\text{Q}}a_1a_2^2x_{\text{I}}^4(t)x_{\text{Q}}^3(t) \\ &\quad + 9a_{4\text{Q}}a_1^2a_2x_{\text{I}}^2(t)x_{\text{Q}}^3(t) \\ &\quad + (a_{4\text{Q}}a_1^3 + 3a_{3\text{Q}}a_2)x_{\text{Q}}^3(t) + a_{3\text{Q}}a_1x_{\text{Q}}(t) \\ &\quad + 3a_{3\text{Q}}a_2x_{\text{I}}^2(t)x_{\text{Q}}(t). \end{aligned} \tag{15b}$$

These equations are obtained using only $x_{\text{I}}(t)$ and $x_{\text{Q}}(t)$ instead of the envelope $A(t)$. From (15a) and (15b) it can be seen directly that the third-order nonlinearities in the RF and BB cause distortion components of up to ninth order. Due to the space limitations and extensive amount of terms (46 instead of 13), the I/Q imbalanced version of (15) is omitted here. However, the I/Q imbalance effects are considered in the next paragraph with the aid of complex equations, which contain the same information in more concise form.

The complex representation of (13a) and (13b), i.e., $y'_{\text{BB}}(t) = y'_{\text{I,BB}}(t) + jy'_{\text{Q,BB}}(t)$ is useful from the analysis point of view, because it reveals how the distortion components are spectrally distributed in relation to the original signal. In the general form with the I/Q imbalance included, the complete distorted signal is as written in (16) (next page). As $y(t)$ comprises the original signal and its RF distortion components, both have also mirror components, i.e. $y^*(t)$, if mixer and/or BB I/Q imbalance occurs. In addition, the BB nonlinearities cause third-order terms, $y^3(t)$ and $[y^*(t)]^3$, which contribute to the harmonics and IMD of the original down-converted signal and associated RF distortion components. There is also another pair of third-order terms stemming from the BB nonlinearities, namely $y^2(t)y^*(t)$ and $y(t)[y^*(t)]^2$. These represent further spreading around the already existing frequency components similarly as is discussed in the previous subsection for the RF distortions. It is noteworthy that the mixer I/Q imbalance has essential impact as it propagates to all aforementioned terms. If perfect I/Q mixer balance ($k_1 = 1, k_2 = 0$) is assumed, the expression in (16) shortens significantly from the coefficients' perspective, but the number of y-terms stays the same. This

is seen by writing the signal explicitly as

$$\begin{aligned} y'_{\mathrm{BB}}(t) = & \frac{a_{3\mathrm{I}}+a_{3\mathrm{Q}}}{2}y(t) + \frac{a_{3\mathrm{I}}-a_{3\mathrm{Q}}}{2}y^*(t) \\ & + \frac{a_{4\mathrm{I}}-a_{4\mathrm{Q}}}{8}y^3(t) + \frac{a_{4\mathrm{I}}+a_{4\mathrm{Q}}}{8}[y^*(t)]^3 \\ & + \frac{3a_{4\mathrm{I}}+3a_{4\mathrm{Q}}}{8}y^2(t)y^*(t) \\ & + \frac{3a_{4\mathrm{I}}-3a_{4\mathrm{Q}}}{8}y(t)[y^*(t)]^2. \end{aligned} \tag{17}$$

This form illustrates well how the BB I/Q imbalance affects the signal in the presence of nonlinearities. Notice that in case of perfect I/Q balance (both the mixer and BB), the number of terms in (17) reduces to three, namely $y(t)$, $[y^*(t)]^3$, and $y^2(t)y^*(t)$.

Table I provides a summary of the terms produced by the cascaded nonlinearity model without any kind of I/Q imbalance. In other words, the tabulated terms stem from $y(t)$, $[y^*(t)]^3$, and $y^2(t)y^*(t)$. The time variable (t) and all coefficients for the terms are omitted from Table I to enhance readability. The first column lists all nine terms using $x(t)$ and $z(t)$. In the second column, the same terms are written using $x(t)$ and its envelope $A(t)$. This form shows very intuitively the spectral contribution of each term separately as $x(t)$ means contributions around the original center frequency whereas $(x^*)^3$ refers to the opposite side of the spectrum with three times the original center frequency and triple the bandwidth. Different powers of $A(t)$ refer to the spreading with respect to the original bandwidth. The last column of Table I indicates the relationships between the complex terms and separate I and Q branch processing. It is noteworthy that each term having separate I and Q processing corresponds to two complex terms. In addition, any I/Q imbalance in the mixer or BB results in another nine terms, which are the complex conjugates of the ones shown in Table I.

TABLE I
ALTERNATIVE FORMS FOR THE TERMS PRODUCED BY THE CASCADED NONLINEARITY MODEL WITHOUT I/Q IMBALANCE

#	$z = x^2x^*$	$A^2 = xx^*$	I/Q Representation
1	x	x	$x_{\mathrm{I}} + jx_{\mathrm{Q}} = x$
2	z	A^2x	$x_{\mathrm{I}}^3 + jx_{\mathrm{Q}}^3 = \frac{1}{4}(x^*)^3 + \frac{3}{4}A^2x$
3	$(x^*)^3$	$(x^*)^3$	
4	x^2z^*	A^4x	$x_{\mathrm{I}}^2z_{\mathrm{I}} + jx_{\mathrm{Q}}^2z_{\mathrm{Q}} = \frac{1}{4}A^2(x^*)^3 + \frac{3}{4}A^4x$
5	$(x^*)^2z^*$	$A^2(x^*)^3$	
6	x^*z^2	A^6x	$x_{\mathrm{I}}z_{\mathrm{I}}^2 + jx_{\mathrm{Q}}z_{\mathrm{Q}}^2 = \frac{1}{4}A^4(x^*)^3 + \frac{3}{4}A^6x$
7	$x^*(z^*)^2$	$A^4(x^*)^3$	
8	z^2z^*	A^8x	$z_{\mathrm{I}}^3 + jz_{\mathrm{Q}}^3 = \frac{1}{4}A^6(x^*)^3 + \frac{3}{4}A^8x$
9	$(z^*)^3$	$A^6(x^*)^3$	

III. PROPOSED MITIGATION ARCHITECTURE FOR CASCADED NONLINEARITY

The digital nonlinearity mitigation approach proposed in this paper bases its foundation on the adaptive interference cancellation concept originally presented in [9], [10]. However, [9] and [10] consider only either RF or BB nonlinearities but not their joint effect, and are thus clearly limited in performance as shown by the nonlinearity analysis in the previous section. This section discusses in detail how the nonlinearity model from the previous section can be exploited for joint distortion mitigation purposes. Additionally, the differences between spectrum sensing and individual IF carrier demodulation scenarios are highlighted from the mitigation structure point of view. First, Subsection A explains the mitigation concept in detail and Subsection B then provides a practically implementable mitigation structure based on that concept.

A. Mitigation Concept

The basic mitigation principle is illustrated in Fig. 3 in case of *spectrum sensing scenario*, where the goal is to eliminate the distortions from the whole reception bandwidth in order to enhance the spectrum sensing [2], [4], [7]. This model is also valid in multicarrier/multiradio basestation receiver that is designed to demodulate all the down-converted carriers simultaneously. After digitalization, the received signal $y'_{\mathrm{BB}}(n)$ goes through a band-splitting stage, which divides the signal into a main path $d(n)$ and a reference path $\hat{x}(n)$. The main path contains the signal after the bandstop filter of the band-splitting stage, i.e., all the signal content except the strongest blocker(s). Correspondingly, the reference path contains only the strongest blocker(s) and regenerates the total nonlinear distortion stemming from them. Finally, the regenerated distortion is subtracted from the main path signal $d(n)$ in order to remove the distortions. In the reference path, the receiver RF and BB

$$\begin{aligned} y'_{\mathrm{BB}}(t) = & \left\{\frac{a_{3\mathrm{I}}+a_{3\mathrm{Q}}}{2}k_1 + \frac{a_{3\mathrm{I}}-a_{3\mathrm{Q}}}{2}k_2^*\right\}y(t) + \left\{\frac{a_{3\mathrm{I}}+a_{3\mathrm{Q}}}{2}k_2 + \frac{a_{3\mathrm{I}}-a_{3\mathrm{Q}}}{2}k_1^*\right\}y^*(t) \\ & + \left\{\frac{a_{4\mathrm{I}}-a_{4\mathrm{Q}}}{8}\left[k_1^3 + 3k_1(k_2^*)^2\right] + \frac{a_{4\mathrm{I}}+a_{4\mathrm{Q}}}{8}\left[(k_2^*)^3 + 3k_1^2k_2^*\right]\right\}y^3(t) \\ & + \left\{\frac{a_{4\mathrm{I}}-a_{4\mathrm{Q}}}{8}\left[k_2^3 + 3(k_1^*)^2k_2\right] + \frac{a_{4\mathrm{I}}+a_{4\mathrm{Q}}}{8}\left[(k_1^*)^3 + 3k_1^*k_2^2\right]\right\}[y^*(t)]^3 \\ & + \left\{\frac{a_{4\mathrm{I}}-a_{4\mathrm{Q}}}{8}3\left[{k_1}^2k_2 + |k_2|^2k_2^* + 2|k_1|^2k_2^*\right] + \frac{a_{4\mathrm{I}}+a_{4\mathrm{Q}}}{8}3\left[k_1^*(k_2^*)^2 + |k_1|^2k_1 + 2|k_2|^2k_1\right]\right\}y^2(t)y^*(t) \\ & + \left\{\frac{a_{4\mathrm{I}}-a_{4\mathrm{Q}}}{8}3\left[k_1k_2^2 + |k_1|^2k_1^* + 2|k_2|^2k_1^*\right] + \frac{a_{4\mathrm{I}}+a_{4\mathrm{Q}}}{8}3\left[(k_1^*)^2k_2^* + |k_2|^2k_2 + 2|k_1|^2k_2\right]\right\}y(t)[y^*(t)]^2 \end{aligned} \tag{16}$$

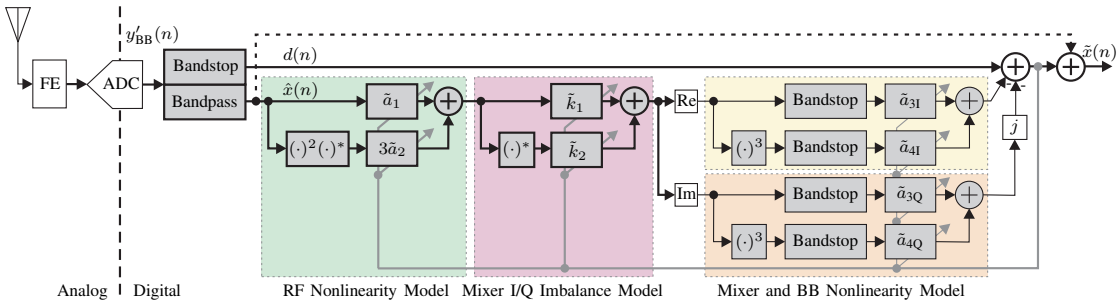

Fig. 3. Principal cascaded adaptive digital mitigation structure for cascaded RF and BB nonlinearities with mixer and BB I/Q imbalance.

nonlinearities and also I/Q imbalance are modeled as discussed in Section II in order to create the needed distortion estimates. The coefficients $\tilde{a}_1, \tilde{a}_2, \tilde{a}_{3\mathrm{I}}, \tilde{a}_{3\mathrm{Q}}, \tilde{a}_{4\mathrm{I}}, \tilde{a}_{4\mathrm{Q}}, \tilde{k}_1$, and $\tilde{k}_2$ refer to the estimates of the ideal coefficients without tilde ($\tilde{\ }$) used in Section II. The mitigation structure is only able to remove the distortion stemming from the strong blocker(s) in $\hat{x}(n)$. Therefore, it does not take into account the intermodulation between the blocker(s) in $\hat{x}(n)$ and some weaker signals in $d(n)$. However, this is not a relevant limitation in practice, because these IMD components are always relatively weak.

It is worth noticing that the bandstop filter of the main path filters out the strongest blocker(s), which is desirable in order to provide the best possible circumstances for the adaptive filters to converge. However, in some systems it might be desirable to have the strongest blocker(s) present after mitigating the distortions, e.g., if they are communication signals of interest. This is accomplished by adding back the blocker(s) after mitigation. In practice, this means adding the bandpass filter output $\hat{x}(n)$ to the output of the entire mitigation structure as is indicated by the dashed arrow line at the top of Fig. 3. This optional feature is employed in the examples of Section IV as is obvious from its spectrum figures.

With slight modifications, the mitigation structure in Fig. 3 can be used for enhancing weak *individual IF carrier demodulation*. In this scenario, the motivation is to remove distortions from a certain narrow band, which contains a weak signal of interest suffering from interference stemming from strong neighboring signals. Here, the narrowband signal refers to an information-bearing signal that does not occupy the entire reception bandwidth, but there are also neighboring signals digitized at the same time, e.g., for flexible digital channel selection filtering purposes. In practice, the cleaning of the certain band means that the bandstop filters in Fig. 3 should be changed to bandpass filters and correspondingly also the bandpass filter should be replaced with an appropriate bandstop filter. Thus, the signal band of interest is selected with the bandpass filter and the bandstop filter is then selecting the rest of the bandwidth for modeling the distortion. However, it is also possible to use a bandpass filter instead of the bandstop filter to pick up the strongest blockers and only use them for modeling the distortion to the band of interest. This would be preferable in a sense that those blockers are causing most of the interference. Also, the distortion regeneration would be more accurate since less distortion is passed to the modeling stage, which would cause additional distortion components not actually present in the received signal.

Designing the bandsplit filters needed in the mitigation structure is omitted from this paper as this is essentially a classical digital filter optimization task for given requirements. This depends on the specific use case, the receiver structure, and the desired complexity of the implementation. A general guideline is that the strongest blocker(s) should be extracted and used in the reference path for the distortion regeneration. This is because the strongest blockers cause also the strongest, and therefore, potentially the most harmful distortion. The selection of the strongest blocker(s) can be based, e.g., on a simple energy detector decisions. It is possible to select only a single blocker and design the filters with only one passband/stopband. However, it is equally feasible to select more than one blocker with a multiband filter. This is basically a matter of filter design and does not affect the processing in the reference path in any way, i.e., the nonlinearity modeling structure remains the same.

Although the structure in Fig. 3 explains conveniently the mitigation concept, it has one severe practical limitation. It works perfectly if the exact coefficients are known a priori. However, this is usually not the case in practice. Online adaptation of the coefficients is thus desired and even required in SDR applications. However, the coefficient adaptation cannot be done directly with this structure, because there are cascaded coefficients that should be adapted simultaneously. For example, if RF nonlinearity coefficients $\tilde{a}_1$ and $\tilde{a}_2$ are adapted alone, they converge to optimal values for completely removing the frequency components having RF nonlinearity contribution. However, as the analysis in Section II shows, the same frequency components have also BB nonlinearity contribution, which should not be removed. This is because it becomes difficult to adapt the BB nonlinearity coefficients $\tilde{a}_{3\mathrm{I}}, \tilde{a}_{3\mathrm{Q}}, \tilde{a}_{4\mathrm{I}}$, and $\tilde{a}_{4\mathrm{Q}}$, when some of the BB distortion components are not anymore in the signal to be cleaned. The same problem occurs if the BB distortion is removed before the RF distortion. The common frequency content in the RF and BB distortions implies time-domain correlation between the distortion components when they originate from the same original blocker(s). It is known that this type of correlation affects the adaptation process [28]. In addition, inefficiency

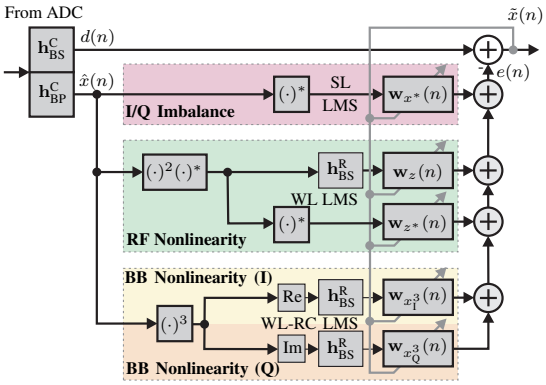

Fig. 4. Parallel adaptive digital mitigation structure for cascaded RF and BB nonlinearities with mixer and BB I/Q imbalance.

of removing only either RF or BB distortions is illustrated in Subsection IV-B with a two-tone simulation example. This motivates us to further develop the mitigation structure, as outlined in Subsection III-B below.

B. Practical Mitigation Structure

Since the online adaptation of cascaded nonlinearity coefficients is not feasible, the mitigation structure of Fig. 3 has to be modified so that all the coefficients can be adapted simultaneously. This becomes possible when the RF nonlinearity and mixer I/Q imbalance blocks are moved *in parallel* with the BB nonlinearity block in the reference generation processing. In principle, this means separate parallel branches for all the distortion terms derived in Subsection II-C. However, further optimization to reduce complexity can be performed since not all the terms are relevant in practice. The final proposed mitigation structure is illustrated in Fig. 4 and is explained in the following paragraphs in more detail. The complex bandpass, real bandstop, and complex bandstop filters are denoted by $\mathbf{h}^{\mathrm{C}}_{\mathrm{BP}}$, $\mathbf{h}^{\mathrm{R}}_{\mathrm{BS}}$, and $\mathbf{h}^{\mathrm{C}}_{\mathrm{BS}}$, respectively. In addition, please note that true multitap adaptive filters (AFs) are also now deployed, to support frequency-selective nature (memory) of associated nonlinearities.

Only the most important distortion terms and their complex conjugates should be selected from Table I for the mitigation structure. There are two reasons for that: 1) less terms means smaller computational burden, and 2) very weak terms are buried below the receiver noise level, which makes them negligible and impedes the convergence of AFs. Therefore, this paper proposes to use the terms in Table II for the mitigation, which should be enough for any practical DCR. The terms follow from the derivations in Section II, but hats ($\hat{}$) are used to indicate that these are calculated from $\hat{x}(n)$, which is the output of the filter $\mathbf{h}^{\mathrm{C}}_{\mathrm{BP}}$ containing the blocker(s). In fact, $\hat{x}(n)$ is only an estimate of the distortion-producing blocker(s), which also suffer(s) from in-band distortion.

We first discuss the role of the different essential terms on intuitive level, and describe the exact learning methods then later in Subsection III-C. Term 1 is usually the strongest

TABLE II
SELECTED TERMS FOR PARALLEL MITIGATION STRUCTURE

Term #	Equation	Filtering	Vector Notation
Term 1	$\hat{x}^*(n)$	SL	$\mathbf{s}_{x^*}(n)$
Term 2	$\hat{z}(n)$	WL	$\mathbf{s}_{z}(n), \mathbf{s}_{z^*}(n)$
Term 3	$\hat{x}^3(n)$	WL-RC	$\mathbf{s}_{x_{\mathrm{I}}^3}(n), \mathbf{s}_{x_{\mathrm{Q}}^3}(n)$

and its power level is easy to estimate from the power level of $\hat{x}(n)$ and image rejection ratio (IRR) of the receiver. Third column of Table II indicates whether the terms should have strictly-linear (SL), widely-linear (WL), or reduced-complexity widely-linear (WL-RC) filtering. In general, the term "widely-linear" refers to processing where both direct and conjugated signals are processed and finally summed together [26], [29]. Regarding Term 1, SL filtering means that the mitigation structure finds complex AF coefficients for $\hat{x}^*(n)$. Term 2 is important since it has contributions from both RF and BB nonlinearities. If any I/Q imbalance occurs, the complex conjugate of Term 2 is also significant. Therefore, WL filtering is applied for Term 2 meaning that separate complex AFs for $\hat{z}(n)$ and $\hat{z}^*(n)$ are deployed. After generating $\hat{z}(n)$, it has to be filtered with $\mathbf{h}^{\mathrm{R}}_{\mathrm{BS}}$ in order to remove spectral content from the original blocker frequency band. This is necessary since otherwise the adaptive algorithm would be misadjusted as $d(n)$ does not have any content in the original blocker frequency band. Regarding $\hat{z}^*(n)$, it is not necessary to use $\mathbf{h}^{\mathrm{R}}_{\mathrm{BS}}$, because it does not contain energy in the original blocker frequency band anyway. The WL filtering is also used for Term 3, which stems from the BB nonlinearity. Both $\hat{x}^3(n)$ and $[\hat{x}^*(n)]^3$ should be filtered with $\mathbf{h}^{\mathrm{R}}_{\mathrm{BS}}$. Therefore, it is actually possible to reduce the complexity of finding AFs for these terms by exploiting the WL-RC approach, which is discussed later in this subsection.

The selected terms in Table II are justified, because they cover the strongest distortion terms. In addition, the terms do not have much spectral overlapping. This is important since all the nonlinear distortion originates from the same blocker(s) and thus has also time-domain correlation, as mentioned earlier. By minimizing the spectral overlapping of the distortion terms, the time-domain correlation between the distortion terms is minimized. This feature is important for the convergence of adaptive algorithms used for finding the AFs.

Terms 4–9 from Table I are not used in the mitigation structure of Fig. 4 because they are negligible when receiver nonlinearities have physically realistic values. The minimal contribution of those terms is easy to understand, because they are 5th, 7th, and 9th order terms, whereas others have a maximum order of three. However, the order of importance for the meaningful terms can slightly vary. This claim is based on our own experiments as discussed in Section IV. In the end, the receiver noise level usually dictates which terms are negligible and which are not. Overall, the mitigation structure in Fig. 4 is a carefully found compromise between the implementation complexity and the achievable mitigation performance, and is directly stemming from the nonlinear distortion analysis provided in Section II. More discussion and examples about

the mitigation is provided in Section IV.

It is also important to understand that the sample rate used during the mitigation processing limits the nonlinearity modeling possibilities. If the ADC has the sampling rate f_s and the same rate is used also in the mitigation structure, the original blocker frequencies must be less than $f_\mathrm{s}/6$ in order to model the third-order nonlinearities correctly, i.e., without aliasing. This limitation comes from the fact that third-order nonlinear distortion occupies three times the original signal bandwidth. Naturally, aliasing does not occur in the analog BB of the receiver and, therefore, it has to be avoided also in the distortion modeling in digital domain. The limitation can be avoided by temporarily increasing the sample rate in digital processing while applying the nonlinearities in the mitigation branches of Fig. 4.

C. Practical Least-Mean-Square Based Learning Rules

The impulse response length, say M, of the AFs for all the distortion terms in Fig. 4 depends on the memory effects of the receiver front-end. The analysis in Section II considers memoryless situation ($M = 1$) to keep it concise. However, using $M > 1$ in the proposed mitigation structure is straightforward in practice and typically required as discussed in Subsection IV-E. According to our experiments, small M should be enough in many applications. However, if large M is required for proper modeling, sparse delay tap filters may provide better accuracy with lower complexity than the traditional non-sparse AFs described in this subsection [30].

As the goal of the mitigation is in general to minimize the spurious energy, the adaptation of the AFs can be performed, e.g., by using the least-mean square (LMS) algorithm or any similar adaptive algorithm [28]. The WL version of the LMS algorithm is extensively exploited in the current literature as discussed in [29] and references therein. Finding two complex AFs for a signal using the WL LMS would imply an increased computational complexity compared to the SL version of the LMS. However, it is possible to reduce the complexity of the WL LMS to that of the SL LMS. It is proven in [31] that the WL-RC LMS is able to provide the same mean-square error and convergence rate while reducing the computational complexity to the level of the SL LMS. Due to these pleasant features, the reduced-complexity WL LMS is also exploited in this paper as is indicated in Fig. 4. The intuition behind the reduced complexity is the fact that instead of finding two complex AFs for a complex signal it is equivalent to finding complex AFs for the real and imaginary parts of the signal [26], [31]. That is to say, finding filters $\mathbf{w}_{x^3}(n)$ and $\mathbf{w}_{x^3_\mathrm{c}}(n)$ for

$$\mathbf{w}_{x^3}(n) * \hat{x}^3(n) + \mathbf{w}_{x^3_\mathrm{c}}(n) * [\hat{x}^*(n)]^3 \tag{18}$$

is equivalent to finding filters $\mathbf{w}_{x^3_\mathrm{I}}(n)$ and $\mathbf{w}_{x^3_\mathrm{Q}}(n)$ for real and imaginary parts of $\hat{x}^3(n)$, i.e.,

$$\mathbf{w}_{x^3_\mathrm{I}}(n) * \mathrm{Re}[\hat{x}^3(n)] + \mathbf{w}_{x^3_\mathrm{Q}}(n) * \mathrm{Im}[\hat{x}^3(n)]. \tag{19}$$

This is valid because the relationships between the filters are

$$\begin{aligned}\mathbf{w}_{x^3_\mathrm{I}}(n) = &\,\mathrm{Re}[\mathbf{w}_{x^3}(n)] + \mathrm{Re}[\mathbf{w}_{x^3_\mathrm{c}}(n)] \\ &+ j\{\mathrm{Im}[\mathbf{w}_{x^3}(n)] + \mathrm{Im}[\mathbf{w}_{x^3_\mathrm{c}}(n)]\}\end{aligned} \tag{20a}$$

$$\begin{aligned}\mathbf{w}_{x^3_\mathrm{Q}}(n) = &\,\mathrm{Im}[\mathbf{w}_{x^3_\mathrm{c}}(n)] - \mathrm{Im}[\mathbf{w}_{x^3}(n)] \\ &+ j\{\mathrm{Re}[\mathbf{w}_{x^3}(n)] - \mathrm{Re}[\mathbf{w}_{x^3_\mathrm{c}}(n)]\}\end{aligned} \tag{20b}$$

The computational complexity is smaller in (19), because two complex filters are applied for real-valued signals instead of complex-valued signals as is the case in (18).

Due to the WL filtering of Terms 2 and 3, there are in total five distortion branches in the mitigation architecture of Fig. 4. For joint coefficient learning purposes, the distortion branch signals are combined into one vector $\mathbf{s}(n)$, namely

$$\mathbf{s}(n) = \left[\mathbf{s}_{x^*}(n), \mathbf{s}_z(n), \mathbf{s}_{z^*}(n), \mathbf{s}_{x^3_\mathrm{I}}(n), \mathbf{s}_{x^3_\mathrm{Q}}(n)\right]^\mathrm{T}, \tag{21}$$

where the subscripts indicate the distortion branches. Term 1 vector is $\mathbf{s}_{x^*}(n) = [\hat{x}^*(n), \hat{x}^*(n-1), \ldots, \hat{x}^*(n-M+1)]^\mathrm{T}$, where M is the AF length. The vectors $\mathbf{s}_z(n)$, $\mathbf{s}_{x^3_\mathrm{I}}(n)$, and $\mathbf{s}_{x^3_\mathrm{Q}}(n)$ also include filtering with $\mathbf{h}^\mathrm{R}_\mathrm{BS}$ and hence $\mathbf{s}_z(n) = [\hat{z}_\mathrm{filt}(n), \hat{z}_\mathrm{filt}(n-1), \ldots, \hat{z}_\mathrm{filt}(n-M+1)]^\mathrm{T}$, where $\hat{z}_\mathrm{filt}(n)$ refers to the filtered version of $\hat{z}(n)$. Similar notation applies to $\mathbf{s}_{x^3_\mathrm{I}}(n)$ and $\mathbf{s}_{x^3_\mathrm{Q}}(n)$. Also the AFs are combined into one vector, namely

$$\mathbf{w}(n) = \left[\mathbf{w}_{x^*}(n), \mathbf{w}_z(n), \mathbf{w}_{z^*}(n), \mathbf{w}_{x^3_\mathrm{I}}(n), \mathbf{w}_{x^3_\mathrm{Q}}(n)\right]^\mathrm{T}, \tag{22}$$

where the subscript indicates the corresponding distortion branch and each individual AF has length of M. Notice that it is also very straightforward to deploy different AF lengths for different distortion terms, if e.g. RF and BB amplifier(s) contain different levels of frequency-selectivity.

The complete joint LMS algorithm for all the coefficients of the mitigation structure in Fig. 4 can be then formulated as follows. First, the AF vector $\mathbf{w}$ is initialized as

$$\mathbf{w}(0) = \mathbf{0}_{5M\times 1}, \tag{23}$$

if no a priori information is available, e.g., through device measurements. For all $n = 0, 1, 2, \ldots$ the combined AF output is

$$e(n) = \mathbf{w}^\mathrm{H}(n)\mathbf{s}(n). \tag{24}$$

Then the error calculation step is

$$\tilde{x}(n) = d(n) - e(n) \tag{25}$$

and finally the AF update is given by

$$\mathbf{w}(n+1) = \mathbf{w}(n) + \mathrm{diag}(\boldsymbol{\mu})\tilde{x}^*(n)\mathbf{s}(n), \tag{26}$$

where $\mathrm{diag}(\cdot)$ denotes a function for converting a vector to a diagonal matrix. The step-size vector $\boldsymbol{\mu}$ contains a different step size for every distortion branch, i.e., $\boldsymbol{\mu} = [\mu_{x^*}, \mu_z, \mu_{z^*}, \mu_{x^3_\mathrm{I}}, \mu_{x^3_\mathrm{Q}}]$, where the subscripts indicate the corresponding distortion branches.

Normalized least-mean square (NLMS) can in practice provide more robust convergence behavior and eases the tuning of the step sizes [28]. Therefore, this approach is used in the mitigation examples of Section IV. The only difference between LMS and NLMS is that the step sizes are scaled with the squared Euclidean norm of the corresponding signal vector and with a selectable coefficient. Consequently, the step-size

vector for NLMS is

$$\boldsymbol{\mu}_{\mathrm{N}} = \left[\frac{\mu_{x^*}}{\alpha_{x^*} + \|\mathbf{s}_{x^*}(n)\|^2}, \ldots, \frac{\mu_{x_{\mathrm{Q}}^3}}{\alpha_{x_{\mathrm{Q}}^3} + \left\|\mathbf{s}_{x_{\mathrm{Q}}^3}(n)\right\|^2} \right], \quad (27)$$

where the additional selectable constants are $\boldsymbol{\alpha} = [\alpha_{x^*}, \alpha_z, \alpha_{z^*}, \alpha_{x_{\mathrm{I}}^3}, \alpha_{x_{\mathrm{Q}}^3}]$. These constants are included due to numerical difficulties in case the power of the distortion estimates is very low and the denominator in (27) is close to zero.

D. Computational Complexity

The computational complexity for creating the distortion estimates consists of 16 real multiplications and 8 real summations used in the complex-valued power operations shown in Fig. 4. In parallel, the cost of the adaptation is defined by the AF length M. For a single iteration of complex LMS the required operations are $8M + 2$ real multiplications and $8M$ real summations in the SL and WL-RC cases [31]. With complexity of a conventional LMS AF being $2M+1$ complex multiplications and $2M$ complex summations per iteration [28], the WL LMS takes $16M + 2$ real multiplications and $16M$ real summations [31]. When combined according to Table II, the overall complexity with the LMS adaptation is $32M + 6$ real multiplications and $32M$ real summations. Employing complex NLMS algorithm introduces an additional burden of $2M$ real multiplications and M real summations for calculating the squared euclidean norm and 1 real division and 1 real summation for finally scaling the step-size, per distortion estimate. Thus, the final number of operations for the adaptations is $42M$ real multiplications, 5 real divisions and 21 real summations.

On top of this, there is the computational cost of the five filters applied in the mitigation structure. There are two complex-valued filters operating on complex-valued signals (namely, $\mathbf{h}_{\mathrm{BP}}^{\mathrm{C}}$ and $\mathbf{h}_{\mathrm{BS}}^{\mathrm{C}}$) and one real-valued filter ($\mathbf{h}_{\mathrm{BS}}^{\mathrm{R}}$) operating once on a complex-valued signal and twice on a real valued signal, as shown in Fig. 4. Assuming all the filters are of order P and direct-form finite impulse response (FIR) structure (P multiplications and $P - 1$ summations for real filter and real signal), this introduces $12P$ real multiplications and $4P + 8(P - 1) = 12P - 8$ real summations assuming direct convolution. This cost can, however, be reduced, e.g., by precomputing the fast Fourier transforms (FFTs) of the filters and doing the filtering in frequency domain, if efficient FFT implementation is available. The details of filtering optimization are not considered herein and can be further checked, e.g., from [32].

Finally, the number of real multiplications, summations and divisions is summarized in Table III. In addition, the delay of the proposed algorithm, being $P+M$, is in practice dictated by the filter order P because it is usually significantly higher than the AF order M. A practical field-programmable gate array (FPGA) implementation of purely digital mitigation algorithm but considering only the RF LNA nonlinearity and hence being a greatly simplified setup, can be found in [15].

TABLE III
THE NUMBER OF REAL MULTIPLIERS, REAL ADDERS AND REAL DIVIDERS USED IN THE MITIGATION STRUCTURE

Operation	# Ops.	Muls	Adds	Divs
Ref. Modeling		16	8	-
SL LMS	1	$8M + 2$	$8M$	-
WL LMS	1	$16M + 2$	$16M$	-
WL-RC LMS	1	$8M + 2$	$8M$	-
NLMS Scaling	5	$10M + 5$	$5M + 5$	5
Static Filtering	5	$12P$	$12P - 8$	-
Overall		$12P + 42M + 27$	$12P + 37M + 5$	5

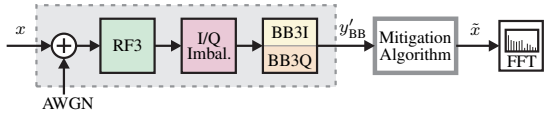

Fig. 5. Simulation architecture for performance evaluation of the mitigation algorithm in MATLAB.

IV. PERFORMANCE SIMULATIONS AND MEASUREMENTS

This section provides simulation and measurement results which evaluate the performance of the proposed mitigation architecture for the cascaded third-order nonlinearities with I/Q imbalance. We also provide explicit comparisons to RF-only and BB-only mitigation approaches, reported earlier in literature, to illustrate and quantify the achievable gain from the proposed joint processing.

A. Simulation Setup

First, simulations of a complete receive chain are performed in MATLAB. The basic architecture is illustrated in Fig. 5. Signal generation and processing take place at BB equivalent level. First, the input signal passes the additive white Gaussian noise (AWGN) source, the RF nonlinearity, the I/Q imbalance block, and the BB nonlinearity. All these components are applied to mimic the DCR front-end. In the blocker signal simulations, the signal-to-noise ratio (SNR) is 61 dB for the entire BB bandwidth of 25 MHz. The IRR is set to 30 dB, a value being realistic for an integrated DCR front-end [1]. The total composite signal, including noise and distortions, is then further processed by the mitigation algorithm presented in Subsection III-B.

Two-tone signals and binary phase shift keying (BPSK) modulated signals have been generated as input signals, in order to verify the algorithm with continuous wave and modulated signals. Throughout the paper, simplified signal configurations have been applied that do not consider detection of a specific information signal. Instead, results are interpreted from wideband nonlinear distortion mitigation use case perspective. Hence, the complete BB spectrum needs to be cleaned from distortions and only the strong input signal(s) should be left after mitigation. This is achieved by adding the original blocker(s) back to the output of the mitigation structure, as discussed in Section III.

Single-tap complex AFs are used in the simulations, as also the deployed circuit components models are memoryless. After mitigation, block-wise FFT with 1024 points is applied to analyze and illustrate the remaining nonlinear distortion. In the following subsections, the last one of 29 FFT blocks is shown in which the convergence of the coefficients is guaranteed.

As a figure of merit, the *mitigation gain* for the BPSK case is computed as the reduction in average signal power outside the original input (blocker) frequency band. Also the mirror-image band is excluded from the mitigation gain calculations as the focus is on the reduction in nonlinear distortion power. For the two-tone case, *average suppression of nonlinear distortion components* is used as a figure of merit, meaning that average power decrease only on the specific frequencies containing the nonlinear distortion is considered. For measurements, this means the average power decrease on the third-order distortion components whereas in the simulations also the mirrors of these components are taken into account as they also appear above the noise floor (see Fig. 7).

B. Two-tone Blocker Input

In order to demonstrate the most relevant distortion estimates, the power levels of Terms 1–6 (as listed in Table I) are next studied by means of a two-tone simulation. To keep the illustration simple, mirror images are not included in this particular example. In order to visualize all terms with respect to their power level, noise has been excluded in this particular simulation. Fig. 6a depicts the distortion estimates for dominating RF nonlinearity, i.e., having $|a_2| > |a_4|$. Vector $\mathbf{a}$ in the caption of Fig. 6 is defined as $\mathbf{a} = [a_1, a_2, a_3, a_4]$, where $a_3 = a_{3\mathrm{I}} = a_{3\mathrm{Q}}$ and similarly for a_4. The applied parameters correspond to the ones defined in Table IV. In Fig. 6, Term 2 is stemming from both the RF and BB distortion whereas the other terms are due to the BB nonlinearity only, as discussed in Sections II and III. Variable $\hat{x}$ (Term 1) depicts the BB spectrum of the filtered blocker signal that serves as an input for the reference nonlinearity. It is apparent that the Terms 2 and 3 are the most significant ones in this case. It is sufficient to consider common spectral content of multiple terms by only one term, as the AF adapts the term to the total distortion at these frequencies. Thus, only those distortions of higher-order terms need to be considered that have not been covered by lower-order terms. However, in this case, frequency components added by Terms 4–6 are 80 dB or more below the input power level and, therefore, likely to be masked by noise in practice. In addition, SNR of a typical ADC is approx. 60–80 dB depending on its resolution, hence making all terms below -80 dBFS to disappear below quantization noise. Fig. 6b illustrates then the power levels for dominating BB nonlinearity case, i.e., $|a_2| < |a_4|$. The same parameters values from Table I are used, but the gain and input-referred third-order intercept point (IIP3) of the RF stage are applied now for the BB and vice versa in order to make the BB dominating. In Fig. 6b, Term 2 and Term 3 are almost equally strong, but still these two terms are the most significant. The observations support the analysis in Sections II and III, and are assumed to be valid for practical values of RF and BB nonlinearities.

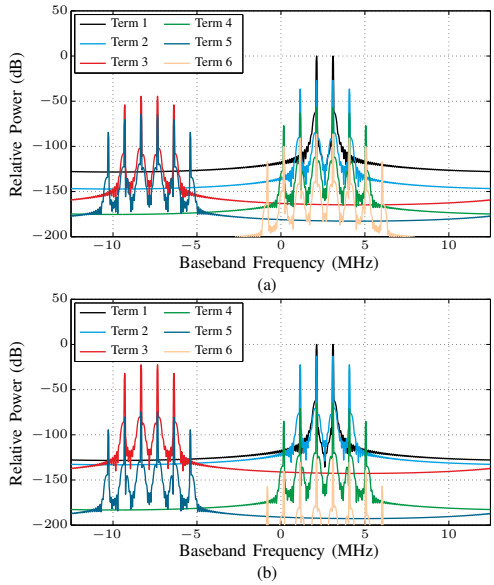

Fig. 6. Power levels of distortion estimates with (a) dominating RF nonlinearity $\mathbf{a} = [5.62, -(84351 + j74391), 3.16, -1588.7]$ and (b) dominating BB nonlinearity $\mathbf{a} = [3.16, -1588.7, 5.62, -(84351 + j74391)]$. For simplification, mirror terms are not visualized.

TABLE IV
PARAMETERS OF THE TWO-TONE SIMULATION

$IIP3_{\mathrm{RF}}$	-10 dBm
G_{RF}	15 dB
$IIP3_{\mathrm{BB}}$	$+6$ dBm
G_{BB}	10 dB
P_{input}	-30 dBm
$\mathbf{a}$	$[5.62, -(84351 + j74391), 3.16, -1588.7]$
g_{m}	0.99
ϕ_{m}	$0.0628 \mathrel{\widehat{=}} 3.6°$ } IRR ≈ 30 dB
$\boldsymbol{\mu}$	$[1, 1, 0.01, 1, 1]$
$\boldsymbol{\alpha}$	$[10^{-9}, 10^{-8}, 10^{-4}, 10^{-9}, 10^{-8}]$

The parameters for the actual performance simulations, including also mirror effects, are summarized in Table IV, where the coefficients of the nonlinearity models and the I/Q imbalance coefficients are taken into account according to (7), (13a), (13b), and (9). It is noteworthy that phase distortions created by LNA and mixer are considered by complex coefficients a_2, k_1, and k_2. The coefficients $a_1 \ldots a_4$ have been computed based on practical values for gain and IIP3 of the RF and BB amplifiers [12].

Fig. 7a illustrates the BB spectrum with a two-tone input before and after proposed mitigation. With the two-tone input, 16 signal components are created in total due to the receiver nonlinearities and I/Q imbalance. The mirror images appear 30 dB below the original tones, whereas the strongest distortion components due to the nonlineaties are 36 dB below the original tones. First, the two-tone signal

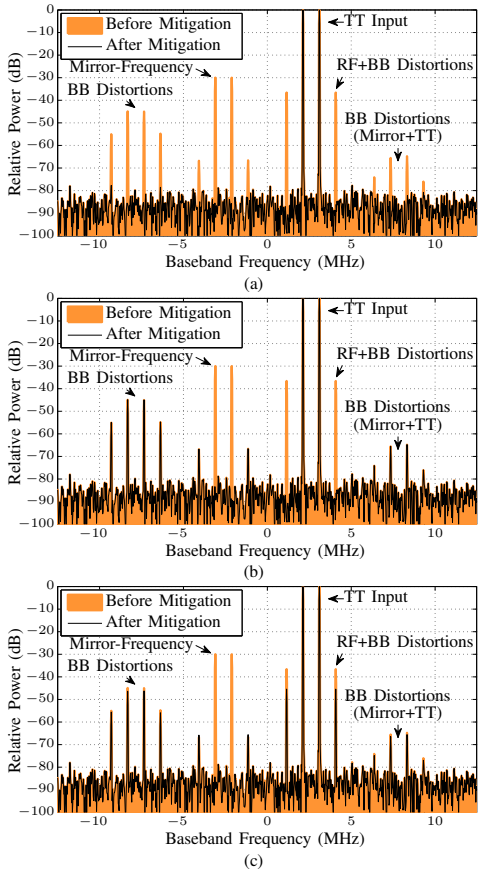

Fig. 7. Simulation results with two-tone input and mitigation with (a) the proposed cascaded model, (b) RF-only model, and (c) BB-only model.

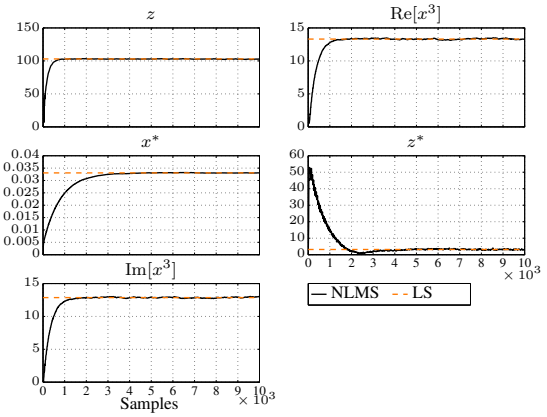

Fig. 8. Adaptation of the filter coefficients with two-tone input (magnitude of complex coefficients).

is distorted by the RF amplifier, causing IMDs nearby the original baseband-equivalent frequency at 2.6 MHz (center of the two tones). Second, mirror components of the original tones and the RF distortion components appear due to down-converting mixer I/Q mismatches. Third, the original tones plus the RF distortions and their respective mirror components are all further distorted by the BB I and Q nonlinearities. This creates distortions at the third harmonic zone of the original signal on the left side of the spectrum around -7.8 MHz and adds distortion around the original tones. In addition, the BB nonlinearity causes harmonics and IMD originating from the mirror components which then appear as low-power tones around $+7.8$ MHz. Furthermore, the BB distortions can have respective mirror components, if there is I/Q imbalance in the BB branches, although these components are very likely to remain below the noise floor in practice. In fact, the mirror components of the main RF and BB distortions are mitigated with the WL filters in the proposed structure if they do appear. Furthermore, AM/PM distortion caused at the RF amplifier [24] and phase mismatch introduced by the mixer are taken into account by the complex implementation of the AFs.

In this example setting, the average suppression of nonlinear distortion components with the proposed joint processing is 32.6 dB for Fig. 7a, fully canceling all distortion and mirror components. Fig. 8 illustrates the adaptation of the AFs using NLMS algorithm, as discussed in Subsection III-B. NLMS has been selected instead of conventional LMS as it usually provides more robust convergence behavior [28]. In addition, the selection of the step size is more simple due to the normalization to the power of the distortion estimates, which may vary by several orders of magnitude. The deployed NLMS parameters are given in Table IV. In Fig. 8, the magnitudes of the adapted complex coefficients are shown together with the corresponding least squares (LS) solutions for the coefficients which are indicated with dashed lines. Basically, there is a good match between the steady-state solution of the adapted coefficients and the LS solutions. The coefficients are converged after approx. 3000 samples.

In order to further demonstrate the significance of the cascaded nonlinearity model for mitigation performance, simulations with only the RF or only the BB model for mitigation are shown for the two-tone input. In the observation generation, however, the same full cascaded model is used as earlier, mimicking a realistic analog DCR front-end. In Fig. 7b, only the mirror image of the original signal and RF distortions have been treated (Terms $\hat{x}^*$ and $\hat{z}$). Further distortions at the BB have not been taken into account here, i.e., there are no distortions estimates for mitigating the components, e.g., in the third harmonic zone. In Fig. 7c, on the other hand, only the mirror image of the original signal and the third-order nonlinearity at the BB are considered (Terms $\hat{x}^*$, $\mathrm{Re}[\hat{x}]^3$, and $\mathrm{Im}[\hat{x}]^3$). The poor performance of the BB-only model is due to the fact that it is unable to take into account the RF distortion, which partially appears at the same frequencies as BB distortion. In addition, the BB-only model is unable to take into account harmonics and IMD of the mirror image. Only if the RF and mixer distortion is mild, the BB-only model is

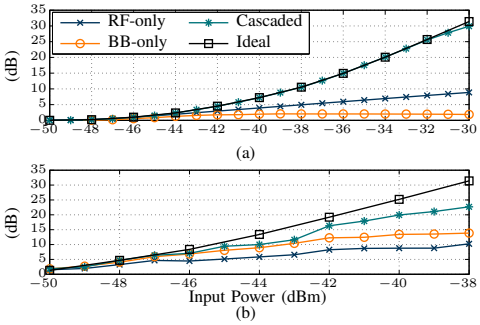

Fig. 9. Average suppression of nonlinear distortion components for different mitigation models, obtained with (a) simulated and (b) measured data.

able to perfectly remove all the occurring BB distortion [9]. Therefore, the cascaded nonlinearity model proposed in this paper clearly outperforms the RF-only and BB-only models considered in the current literature.

The average suppression of nonlinear distortion components vs. the power of the two-tone input achieved with the different models, and the ideal suppression, indicating how much spurious power has been added due to receiver nonlinearity, are illustrated in Fig. 9a. With the deployed analog components, there is almost no IMD generated up to input power -46 dBm and the mirror-frequency interference x^* is dominating. All the models include mitigation of the mirror with Term 1, hence, equal mirror suppression is achieved at these low power levels. Therefore, the mirror band is excluded from the mitigation gain calculations in order to better show the suppression of nonlinear distortion. With rising input power, the generated RF and BB distortions raise in Fig. 9a, and some suppression is achieved with the RF-only and BB-only models. However, the BB-only model is performing poorly due to the strong RF nonlinearity, which only partially accommodates the same frequencies. The cascaded model follows the ideal suppression, indicating that all nonlinear distortion products plus mirror terms are essentially canceled. To sum up, the total cascaded model provides much better performance than the RF-only or BB-only nonlinearity model because of their fundamental shortcomings. Using the BB-only model, i.e., the third-order term of the I and Q reference signal, is exactly the procedure followed in the state-of-the-art literature [7], [9], while RF LNA oriented results are reported in [12]. These results show that proper modeling of the underlying receiver architecture is essential to achieve improved mitigation performance in a broad variety of applications.

C. BPSK Blocker Input

The results with the BPSK input are shown in Fig. 10. The BPSK signal is generated with a raised-cosine pulse-shaping filter, with a roll-off factor of 0.5 and a symbol rate of approx. 788 ksym/s. These numbers have been chosen arbitrarily to generate a simple modulated blocker signal with approx. 1 MHz bandwidth. The parameters for the BPSK simulation are otherwise exactly the same as for the two-tone

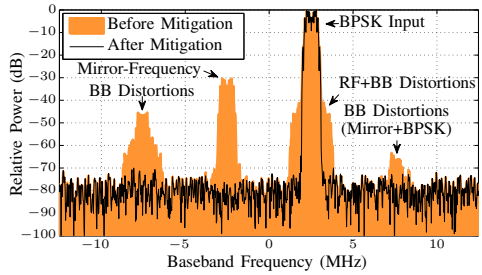

Fig. 10. Simulation results with BPSK input and mitigation with the proposed cascaded model.

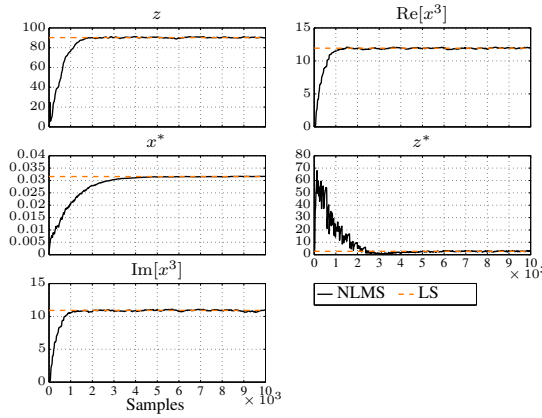

Fig. 11. Adaptation of the filter coefficients with BPSK input (magnitude of complex coefficients).

case summarized in Table IV. The root-mean-square power has been chosen to be equal to that in the two-tone case, whereas the peak-to-average power ratio (PAPR) of the BPSK signal is higher than that of the two-tone ($PAPR_{\mathrm{BPSK}} = 4.1$ dB vs. $PAPR_{\mathrm{TT}} = 3.01$ dB). It should be noted that the peak values are important in determining the level of distortion. Fig. 11 illustrates the adaptation of the coefficients using NLMS. The steady-state value is again reached at approx. 4000 samples, resulting in a mitigation gain of 20.4 dB. The results with BPSK input verify that the proposed algorithm is able to mitigate distortions induced by modulated blocker waveforms.

D. High-PAPR Input Signals

Especially in CR applications, typically high PAPR is encountered. Besides the fact that modern communications waveforms tend to have high PAPR, also receiving multiple low-PAPR signals with one receiver chain will cause the overall waveform to have high PAPR. As discussed in Subsection III-A, the proposed nonlinearity mitigation algorithm is able to handle situations with multiple blocker signal carriers while the computational complexity stays almost the same. This is due to the fact that only the band-splitting stage filters have to be designed to have multiple passbands while the

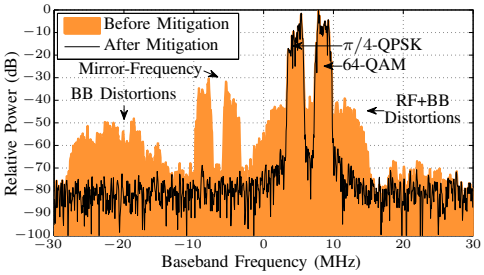

Fig. 12. Simulation with two single-carrier signals ($\pi/4$-QPSK and 64-QAM) at $-30.67\,\text{dBm}$, PAPR = $7.54\,\text{dB}$, and mitigation with proposed cascaded model.

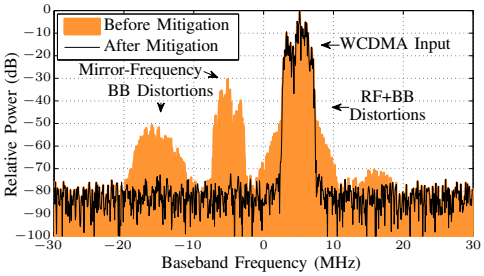

Fig. 13. Simulation with a WCDMA input at $-31.89\,\text{dBm}$, PAPR = $10.95\,\text{dB}$, and mitigation with proposed cascaded model.

nonlinearity modeling and adaptation stay the same.

In order to verify the feasibility of the approach under high-PAPR conditions, two more simulation examples (two single-carrier signals, one WCDMA signal) are illustrated in Fig. 12 and Fig. 13 providing a mitigation gain of $20.9\,\text{dB}$ and $16.6\,\text{dB}$, respectively. In order to make the simulation scenarios even more realistic, a frequency-selective Extended ITU Vehicular A channel is used [33]. Essentially the channel does not affect the mitigation performance, but may slightly increase fluctuations in AF coefficient adaptation behavior. The channel effects are discussed more in Section V.

The nonlinearity mitigation algorithm is able to handle high-PAPR waveforms since the nonlinearity modeling itself is not depending on PAPR. Therefore, it is justified to say that the proposed algorithm is suitable and effective in CR applications. However, it is worth noticing that challenges due to the amplifier saturation or ADC clipping may occur in practice. If the signal is pushed to the highly nonlinear region of the receiver, the nonlinearity modeling should be changed drastically and hence the proposed algorithm as it is may not provide the optimal mitigation performance. The changes to the nonlinearity modeling could include, e.g., higher than third-order polynomials. Nevertheless, this problem is fundamentally challenging as part of the signal information is lost in saturation/clipping process.

E. Experimental Evaluation with RF Measurements

Real-world measurements are also conducted to demonstrate and verify the mitigation capabilities of the proposed solution

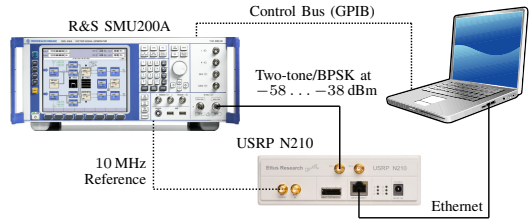

Fig. 14. Sketch of the two-tone and BPSK measurement setup.

with true RF signals and components. The automated setup for the experiments with the aforementioned signal scenarios is illustrated in Fig. 14. A vector signal generator of type Rohde & Schwarz SMU200A is used to generate the two-tone and BPSK signals. Before running measurements with an SDR under test, the spectral purity of the generator was checked with a conventional spectrum analyzer, as signal generators also exhibit a limited linearity. The generator itself has an SFDR better than $70\,\text{dB}$, i.e. a very clean signal can be provided to the device under test. The SDR USRP N210 with the wideband WBX front-end [18] is used as a receiver. Signal generator and receiver are synchronized using a $10\,\text{MHz}$ reference signal, enabling coherent sampling for precise power measurements.

The WBX is a typical DCR front-end with a low-IF architecture, providing a tuning range from $70\,\text{MHz}$ to $2.2\,\text{GHz}$. That is, from the perspective of a single signal of interest, the waveform is I/Q down-converted to a low-IF first, and subsequently down-converted to zero-IF in the digital domain. This is performed by a numerically controlled oscillator on an FPGA if the desired center frequency is not directly within the frequency grid of the analog local oscillator. The analog BB bandwidth of the daughterboard is $40\,\text{MHz}$, however, the transferable bandwidth to the host computer is limited to $25\,\text{MHz}$ due to the gigabit Ethernet interface. The nonlinear behavior of the WBX front-end is already known from prior studies [7]. The IIP3 of the total receiver including RF, BB and ADC nonlinearity is $13.8\,\text{dBm}$ on average, indicating a very good linearity in general. Moreover, the power of nonlinear distortions is independent from the chosen center frequency. The WBX has been chosen among a variety of USRP daughterboards as it provides a low noise figure (NF) of $5\,\text{dB}$, allowing observation of different distortion components.

Fig. 15a illustrates the mitigation performance achieved with a two-tone input. The tone frequencies are the same as in simulations and have been chosen within the grid of the 1024-point FFT. The generator power and the PAPR of the signal are $-39\,\text{dBm}$ and $3.06\,\text{dB}$, respectively. The center frequency of the receiver is $200\,\text{MHz}$, the BB bandwidth being $25\,\text{MHz}$. By using two taps for the AFs, the average suppression of nonlinear distortion components is $25.4\,\text{dB}$ in Fig. 15a. The additional taps have been introduced, because the real receiver suffers from memory effects that are excluded in the simulations. The obtained suppression of nonlinear distortion components at different input power levels for the two-tone case are illustrated in Fig. 9b. Compared to simulations, RF

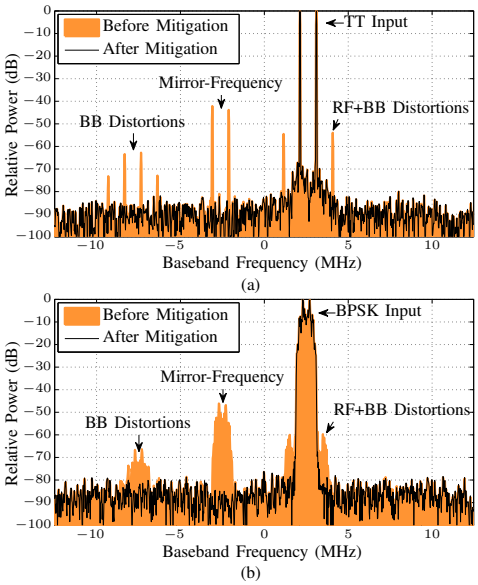

Fig. 15. Mitigation performance achieved with measured data in case of (a) two-tone input (at -39 dBm) and (b) BPSK input (at -44 dBm).

distortion is milder in measurements, explaining the relatively high suppression obtained by the BB-only model. However, the cascaded model still provides the best performance.

Similar mitigation performance is achieved with the BPSK signal shown in Fig. 15b. Here, the center frequency and the BB bandwidth are 570 MHz and 25 MHz, respectively. The BPSK signal has been generated with the same parameters as used in simulations, and the generator power and PAPR are -44 dBm and 3.35 dB, respectively. A mitigation gain of 7.1 dB is achieved using two taps for each AF.

To sum up, the co-existence of RF and BB distortions has been verified through real-world measurements, demonstrating the effectiveness of the proposed cascaded model. The suppression of the different distortion components is significantly better with the joint mitigation of the RF and BB stage nonlinearities, compared to the previous solutions presented in the literature which employ a model for only either of the stages. Moreover, joint mitigation of nonlinear distortions and corresponding mirror components due to I/Q imbalance has been demonstrated by measurements. Thus, the proposed mitigation method provides a high-performance linearization solution for complete wideband DCR chains, enabling flexible sensing and processing of the RF spectrum in radio communication and radar devices.

V. Results and Discussion

The results presented in Section IV show a very good match between the cascaded model in simulations and the real behavior in measurements. This confirms that the cascaded model addresses the most relevant distortions created by the DCR architecture. Thus, a complete model has been found capturing all essential distortions in the receiver chain. In general, only distortions that are created by the reference model can be mitigated with the AFs. In prior works, either distortions at RF or BB have been considered, but not together in a joint model. Adding more taps to the AF would not compensate for this inaccuracy, since only the provided reference signal content is filtered. In addition, mitigation of the mirror-frequency interference due to the I/Q imbalance is also properly handled in the proposed structure.

However, the proposed algorithm still has some limitations. First, purely digital mitigation can only be performed, if the distortion-producing signals are also received at the BB, i.e., only distortions by the interferers inside the A/D conversion band can be handled. Distortions created by the interferers out of the digitized bandwidth cannot be reproduced. The low RF selectivity typical for SDRs makes that even more difficult. This limitation has been solved in [11] by integrating an RF nonlinearity model into the RF front-end. In this case, all possible distortions that appear at the full receiver RF bandwidth are included, and only those falling into the desired BB are further processed in the digital domain. However, this solution requires considerable amount of additional hardware to be implemented on chip. An alternative would be to use an ADC with a higher sampling rate or parallel A/D interfaces, each digitizing a subset of the total receiver bandwidth. It is likely that ADCs with higher sampling rates will be feasible in the future due to fast-growing technology for digital circuits. On the other hand, purely digital mitigation has significant benefits. As desired and reference signals are obtained from a single A/D chain, both signals are perfectly aligned and the additional mismatch reported in [11] does not occur. Moreover, very flexible implementation of the algorithm on an FPGA or digital signal processor can be achieved without employing additional hardware. Thereby, runtime reconfigurability of filter characteristics, step sizes, and other parameters of the algorithm is realizable and perfectly meets the SDR concept.

Second, in-band distortions on top of the main distortion-producing signals at the BB, which are considered in the mitigation structure, cause an error for the distortion estimates, and thus reduce the mitigation performance. However, it has been found that the limitations set by these distortions can be alleviated by increasing the AF lengths. The same applies in the case of memory effects in receivers. In general, longer AFs can compensate mismatches between the real hardware and the simplified mitigation model to a certain extent. However, using a model that mimics the real situation as closely as possible is essential as has been shown in this paper.

Third, the achievable mitigation performance depends on the filter characteristics of the band-splitting stage, as discussed in Subsection III-A. In order to provide a clean reference signal for the nonlinearity modeling and AF stages, the filters need to have sufficient stopband attenuation. Moreover, filter characteristics are application-specific and depend on actual center frequency and bandwidth of the desired and blocker signals at hand. If the channel allocation is known to be static, re-tuning of the filters can be done based on simple energy detector decisions about strong signals currently being present. In case of dynamic carrier allocation with varying center

frequencies and bandwidths, e.g., for multicarrier signals, the correct filter cut-off frequencies can be defined via FFT. This is the typical scenario considered for CRs [2], [4], [7].

In Section IV, the efficiency of the nonlinearity mitigation algorithm is successfully verified in AWGN channels through simulations and RF measurements with cable connections. In addition, the performance is verified with more realistic high-PAPR signals in frequency-selective channel conditions in Subsection IV-D. The mitigation architecture stays essentially the same if the input signal level is varying due to a realistic radio channel with fading phenomena. The optimal coefficients for the AFs depend solely on the receiver hardware and its nonlinear behavior. Therefore, the optimal AF coefficients do not depend on input signal or channel variations. However, in practice, the adaptation of the AF coefficients is affected by the input signal power level variations, e.g., due to the channel fading. If the signal is in the linear region of the receiver, it is challenging to obtain the AF coefficients for the receiver nonlinearity. Other extreme case is when the signal is strongly saturating or clipping and the AF coefficient adaption is interfered because the nonlinearity model does not take into account the very strong nonlinear behavior. In [34], it has been shown through extensive system-level simulations for RF nonlinearities that this kind of nonlinearity mitigation algorithm can be applied even under demanding frequency-selective and fast-fading channels while providing a considerable mitigation performance. Other important conclusion is that it is beneficial to bypass the nonlinearity mitigation algorithm when the signal-to-interference ratio is already high without the mitigation [13], [34]. This way power consumption is reduced and it is also guaranteed that the nonlinearity mitigation algorithm does not limit the overall performance.

VI. Conclusions

In this paper, a novel approach for modeling the RF and BB distortions created in wideband DCR chain has been presented. Compared to prior work, a more complete model has been developed, taking into account the most significant distortions created by a DCR. This allows for cleaning the entire BB signal from nonlinear distortions and mirror-frequency interference. The design of a digital feed-forward mitigation algorithm, that incorporates the cascaded BB model, has been addressed in detail. Simulation results with the two-tone and BPSK-modulated signals were presented to show the effectiveness of this approach that provides a significant performance improvement over previous solutions. Moreover, the RF and BB distortions in real-world RF measurements have been successfully mitigated, hence proving that both types of nonlinear distortions really co-exist and confirming applicability of the proposed mitigation architecture in practice. Finally, significant enhancement in the linearity of the front-end has been achieved, allowing for simple and low-cost receiver architectures for SDR and CR. Furthermore, the presented algorithm is generally applicable for wideband DCRs and is not restricted to the SDR. Our future work will address, e.g., methods to relax the burden on the A/D interface, through alternative analog or hybrid analog-digital reference generation methods combined with reference ADC.

Acknowledgment

M. Grimm would like to thank Prof. Mikko Valkama and the administration of the International Graduate School on Mobile Communications that made his three-month research stay at Tampere University of Technology, Finland, possible.

References

[1] B. Razavi, "Design considerations for direct-conversion receivers," *IEEE Trans. Circuits Syst. II*, vol. 44, no. 6, pp. 428–435, June 1997.

[2] ——, "Cognitive radio design challenges and techniques," *IEEE J. Solid-State Circuits*, vol. 45, no. 8, pp. 1542–1553, Aug. 2010.

[3] E. Biglieri, S. Barberis, and M. Catena, "Analysis and compensation of nonlinearities in digital transmission systems," *IEEE J. Sel. Areas Commun.*, vol. 6, no. 1, pp. 42–51, Jan. 1988.

[4] E. Axell, G. Leus, E. G. Larsson, and H. V. Poor, "Spectrum sensing for cognitive radio : State-of-the-art and recent advances," *IEEE Signal Process. Mag.*, vol. 29, no. 3, pp. 101–116, May 2012.

[5] J. Verlant-Chenet, J. Renard, J.-M. Dricot, P. De Doncker, and F. Horlin, "Sensitivity of spectrum sensing techniques to RF impairments," in *Proc. IEEE 71st Vehicular Technology Conf. (VTC 2010-Spring)*, Taipei, Taiwan, May 2010, pp. 1–5.

[6] A. Zahedi-Ghasabeh, A. Tarighat, and B. Daneshrad, "Cyclo-stationary sensing of OFDM waveforms in the presence of receiver RF impairments," in *Proc. IEEE Wireless Communications and Networking Conf. (WCNC2010)*, Sydney, Australia, Apr. 2010, pp. 1–6.

[7] M. Grimm, R. K. Sharma, M. Hein, and R. Thomä, "DSP-based mitigation of RF front-end non-linearity in cognitive wideband receivers," *FREQUENZ Journal of RF-Engineering and Telecommunications, Special Issue WSR2012*, vol. 66, no. 9-10, pp. 303–310, Sept. 2012.

[8] D. H. Mahrof, E. A. M. Klumperink, J. C. Haartsen, and B. Nauta, "On the effect of spectral location of interferers on linearity requirements for wideband cognitive radio receivers," in *Proc. IEEE Symp. on New Frontiers in Dynamic Spectrum (DySPAN2010)*, Singapore, Apr. 2010, pp. 1–9.

[9] M. Valkama, A. Shahed hagh ghadam, L. Anttila, and M. Renfors, "Advanced digital signal processing techniques for compensation of nonlinear distortion in wideband multicarrier radio receivers," *IEEE Trans. Microw. Theory Tech.*, vol. 54, no. 6, pp. 2356 –2366, June 2006.

[10] A. Shahed hagh ghadam, "Contributions to analysis and DSP-based mitigation of nonlinear distortion in radio transceivers," Ph.D. dissertation, Dept. Commun. Eng., Tampere University of Technology, Tampere, Finland, 2011.

[11] E. Keehr and A. Hajimiri, "Equalization of third-order intermodulation products in wideband direct conversion receivers," *IEEE J. Solid-State Circuits*, vol. 43, no. 12, pp. 2853–2867, Dec. 2008.

[12] Q. Zou, M. Mikhemar, and A. H. Sayed, "Digital compensation of cross-modulation distortion in software-defined radios," *IEEE J. Sel. Topics Signal Process.*, vol. 3, pp. 348–361, June 2009.

[13] M. Allén, J. Marttila, and M. Valkama, "Modeling and mitigation of nonlinear distortion in wideband A/D converters for cognitive radio receivers," *European Microwave Assoc. Int. J. Microwave and Wireless Technologies*, vol. 2, no. 02, pp. 183–192, Apr. 2010.

[14] M. Grimm, R. K. Sharma, M. Hein, R. S. Thomä, and R. Zemmari, "Improved BER performance in GSM by mitigating non-linear distortions in the receiver," in *Proc. European Microwave Conf. (EuMC)*, Nuremberg, Germany, Oct. 2013.

[15] F. Schlembach, M. Grimm, and R. Thomä, "Real-time implementation of a DSP-based algorithm on USRP for mitigating non-linear distortions in the receiver RF front-end," in *Proc. 10th Int. Symp. on Wireless Communication Systems (ISWCS2013)*, Ilmenau, Germany, Aug. 2013.

[16] H.-H. Chen, P.-C. Huang, C.-K. Wen, and J.-T. Chen, "Adaptive compensation of even-order distortion in direct conversion receivers," in *Proc. IEEE 58th Vehicular Technology Conf. (VTC 2003-Fall)*, vol. 1, Orlando, FL, Oct. 2003, pp. 271–274.

[17] E. Rebeiz, A. Shahed hagh ghadam, M. Valkama, and D. Cabric, "Suppressing RF front-end nonlinearities in wideband spectrum sensing," in *Proc. 8th Int. Conf. Cognitive Radio Oriented Wireless Networks (CROWNCOM2013)*, Washington D.C., July 2013, pp. 87–92.

[18] *Universal Software Radio Peripheral*, Ettus Research LLC. [Online]. Available: http://www.ettus.com/

[19] A. A. Abidi, "Direct-conversion radio transceivers for digital communications," *IEEE J. Solid-State Circuits*, vol. 30, no. 12, pp. 1399–1410, Dec. 1995.

[20] A. B. Carlson, P. B. Crilly, and J. C. Rutledge, *Communication Systems: An Introduction to Signals and Noise in Electrical Communication*, 4th ed. New York: McGraw-Hill, 2001, pp. 143–147.
[21] D. R. Morgan, Z. Ma, J. Kim, M. G. Zierdt, and J. Pastalan, "A generalized memory polynomial model for digital predistortion of RF power amplifiers," *IEEE Trans. Signal Process.*, vol. 54, no. 10, pp. 3852–3860, Oct. 2006.
[22] S. C. Blaakmeer, E. A. M. Klumperink, D. M. W. Leenaerts, and B. Nauta, "Wideband balun-LNA with simultaneous output balancing, noise-canceling and distortion-canceling," *IEEE J. Solid-State Circuits*, vol. 43, no. 6, pp. 1341–1350, June 2008.
[23] K. Kivekäs, A. Pärssinen, and K. A. I. Halonen, "Characterization of IIP2 and DC-offsets in transconductance mixers," *IEEE Trans. Circuits Syst. II*, vol. 48, no. 11, pp. 1028–1038, Nov. 2001.
[24] P. B. Kenington, *High-Linearity RF Amplifier Design*. Norwood, MA: Artech House, 2000, pp. 74–77.
[25] L. Anttila, M. Valkama, and M. Renfors, "Circularity-based I/Q imbalance compensation in wideband direct-conversion receivers," *IEEE Trans. Veh. Technol.*, vol. 57, no. 4, pp. 2099–2113, July 2008.
[26] L. Anttila, "Digital front-end signal processing with widely-linear signal models in radio devices," Ph.D. dissertation, Dept. Commun. Eng., Tampere University of Technology, Tampere, Finland, 2011.
[27] J. L. Karki, "Designing for low distortion with high-speed op amps," *Texas Instruments Analog Applicat. J.*, pp. 25–33, July 2001. [Online]. Available: http://www.ti.com/lit/an/slyt133/slyt133.pdf
[28] S. Haykin, *Adaptive Filter Theory*, 4th ed. Upper Saddle river, NJ: Prentice Hall, 2002, pp. 231–341.
[29] T. Adali, H. Li, and R. Aloysius, "On properties of the widely linear MSE filter and its LMS implementation," in *Proc. 43rd Annu. Conf. Information Sciences and Systems (CISS2009)*, Baltimore, MD, Mar. 2009, pp. 876–881.
[30] H. Ku and J. S. Kenney, "Behavioral modeling of nonlinear RF power amplifiers considering memory effects," *IEEE Trans. Microw. Theory Tech.*, vol. 51, no. 12, pp. 2495–2504, Dec. 2003.
[31] F. G. A. Neto, V. H. Nascimento, and M. T. M. Silva, "Reduced-complexity widely linear adaptive estimation," in *Proc. 7th Int. Symp. Wireless Communication Systems (ISWCS2010)*, York, United Kingdom, Sept. 2010, pp. 399–403.
[32] R. Meyer, R. Reng, and K. Schwarz, "Convolution algorithms on DSP processors," in *Int. Conf. Acoustics, Speech, and Signal Process.*, vol. 3, Toronto, Canada, Apr. 1991, pp. 2193–2196.
[33] T. B. Sørensen, P. E. Mogensen, and F. Frederiksen, "Extension of the ITU channel models for wideband (OFDM) systems," in *Proc. IEEE 62nd Vehicular Technology Conf. (VTC 2005-Fall)*, vol. 1, Dallas, TX, Sept. 2005, pp. 392–396.
[34] D. Dupleich, M. Grimm, F. Schlembach, and R. S. Thomä, "Practical aspects of a digital feedforward approach for mitigating non-linear distortions in receivers," in *Proc. 11th Int. Conf. Telecommunications in Modern Satellite, Cable and Broadcasting Services (TELSIKS2013)*, Niš, Serbia, Oct. 2013, pp. 170–177.

Michael Grimm was born in Weimar, Germany, on January 7th, 1986. He received the Dipl.-Ing. degree in electrical engineering and information technology from Ilmenau University of Technology, Germany, in 2009.

He is currently with the Electronic Measurement Research Lab within the International Graduate School on Mobile Communications at Ilmenau University of Technology as a Researcher working towards the Dr.-Ing. degree (Ph.D.). His research interests include software defined and cognitive radio, RF impairment mitigation, mixed-signal circuit design, and FPGA-based embedded signal processing.

Markus Allén (S'10) was born in Ypäjä, Finland, on October 28, 1985. He received the B.Sc. and M.Sc. degrees in signal processing and communications engineering from Tampere University of Technology, Finland, in 2008 and 2010, respectively.

He is currently with the Department of Electronics and Communications Engineering at Tampere University of Technology as a Researcher heading towards the Ph.D. degree. His current research interests include cognitive radios, analog-to-digital converters, receiver front-end nonlinearities and their digital mitigation algorithms.

Jaakko Marttila (S'10) was born in Tampere, Finland, on March 30, 1982. He received the M.Sc. degree in signal processing and communications engineering from Tampere University of Technology (TUT), Tampere, Finland, in 2010.

He is currently working towards the Ph.D. degree at TUT, Department of Electronics and Communications Engineering as a Researcher. At present, his main research topic is quadrature sigma-delta analog-to-digital (AD) conversion. Generally, his research interests include AD techniques for software defined and cognitive radios, and related interference mitigation algorithms.

Mikko Valkama (S'00, M'02) was born in Pirkkala, Finland, on November 27, 1975. He received the M.Sc. and Ph.D. degrees (both with honours) in electrical engineering (EE) from Tampere University of Technology (TUT), Finland, in 2000 and 2001, respectively. In 2002 he received the Best Ph.D. Thesis award by the Finnish Academy of Science and Letters for his dissertation entitled "Advanced I/Q signal processing for wideband receivers: Models and algorithms".

In 2003, he was working as a visiting researcher with the Communications Systems and Signal Processing Institute at SDSU, San Diego, CA. Currently, he is a Full Professor and Department Vice Head at the Department of Electronics and Communications Engineering at TUT, Finland. He has been involved in organizing conferences, like the IEEE SPAWC'07 (Publications Chair) held in Helsinki, Finland. His general research interests include communications signal processing, estimation and detection techniques, signal processing algorithms for software defined flexible radios, cognitive radio, digital transmission techniques such as different variants of multicarrier modulation methods and OFDM, radio localization methods, and radio resource management for ad-hoc and mobile networks.

Reiner Thomä (M'92–SM'99–F'07) received the Dipl.-Ing. (M.S.E.E.), Dr.-Ing. (Ph.D.E.E.), and the Dr.-Ing. habil. degrees in electrical engineering and information technology from Technische Hochschule Ilmenau, Germany, in 1975, 1983, and 1989, respectively.

From 1975 to 1988, he was a Research Associate in the fields of electronic circuits, measurement engineering, and digital signal processing at the same university. From 1988 to 1990, he was a Research Engineer at the Akademie der Wissenschaften der DDR (Zentrum für Wissenschaftlichen Gerätebau). During this period he was working in the field of radio surveillance. In 1991, he spent a three-month sabbatical leave at the University of Erlangen-Nürnberg (Lehrstuhl für Nachrichtentechnik). Since 1992, he has been a Professor of electrical engineering (electronic measurement) at TU Ilmenau where he was the Director of the Institute of Communications and Measurement Engineering from 1999 until 2005. With his group, he has contributed to several European and German research projects and clusters such as WINNER, PULSERS, EUWB, NEWCOM, COST 273, 2100, IC 1004, EASY-A, EASY-C. Currently he is the speaker of the German nation-wide DFG-focus project UKoLOS, Ultra-Wideband Radio Technologies for Communications, Localization and Sensor Applications (SPP 1202). His research interests include measurement and digital signal processing methods (correlation and spectral analysis, system identification, sensor arrays, compressive sensing, time-frequency and cyclostationary signal analysis), their application in mobile radio and radar systems (multidimensional channel sounding, propagation measurement and parameter estimation, MIMO-, mm-wave-, and ultra-wideband radar), measurement-based performance evaluation of MIMO transmission systems including over-the-air testing in virtual electromagnetic environments, and UWB sensor systems for object detection, tracking and imaging.

Prof. Thomä is a member of URSI (Comm. A), VDE/ITG. Since 1999 he has been serving as chair of the IEEE-IM TC-13 on Measurement in Wireless and Telecommunications. In 2007 he was awarded IEEE Fellow Member and received the Thuringian State Research Award for Applied Research both for contributions to high-resolution multidimensional channel sounding.

Publication 9

M. Allén, J. Marttila, M. Valkama, M. Grimm, and R. Thomä, "Digital post-processing based wideband receiver linearization for enhanced spectrum sensing and access," in *Proceedings of the 9th International Conference on Cognitive Radio Oriented Wireless Networks and Communications (CROWNCOM2014)*, Oulu, Finland, June 2014, 6 pages. DOI: 10.4108/icst.crowncom.2014.255428

© 2014 The Institute for Computer Sciences, Social Informatics and Telecommunications Engineering (ICST). Reprinted with permission.

Digital Post-Processing Based Wideband Receiver Linearization for Enhanced Spectrum Sensing and Access

Markus Allén, Jaakko Marttila, and Mikko Valkama
Department of Electronics and Communications Engineering
Tampere University of Technology
P.O. Box 692, FI-33101 Tampere, Finland
{markus.allen, jaakko.marttila, mikko.e.valkama}@tut.fi

Michael Grimm and Reiner Thomä
Electronic Measurement Research Lab
Ilmenau University of Technology
98684 Ilmenau, Germany
{michael.grimm, reiner.thomae}@tu-ilmenau.de

***Abstract*—Wideband radio receivers provide the flexibility desired in many communications applications and are the key element in cognitive radios and software-defined radios in general. However, multi-channel reception scenarios tend to have high dynamic range which set hard-to-reach requirements for receiver linearity. This paper proposes a calibration-based digital post-inverse model for wideband receiver linearization and compares it with adaptive interference cancellation. Their advantages and disadvantages are highlighted together with numerical performance results in challenging non-contiguous spectrum access scenario. Both methods are waveform-independent, which make them applicable to many systems, but they have different trade-offs when linearization accuracy, computational complexity and real-time capability are compared. Therefore selecting the best method is highly system-specific matter.**

***Index Terms*—Interference cancellation, inverse modeling, nonlinear distortion, spectrum access, spectrum sensing**

I. Introduction

Wideband radio receivers and especially the ones employing direct-conversion architecture have gained more and more attention during the last decade. This is due to their flexibility, cost efficiency, and integrability [1], [2]. Wideband receivers are attractive in many emerging software-defined radio and cognitive radio applications as well as in traditional cellular communications networks. However, wideband multi-channel reception scenarios set stringent receiver linearity requirements and these cannot be always met even with state-of-the-art receiver hardware [3], [4].

In practice, the linearity problems have been encountered, e.g., in field measurements with mobile spectrum sensing devices [5], [6]. Due to the limited dynamic range of the receiver, significant amount of nonlinear distortion is caused to vacant channels or on top of weak signals, if there are strong neighboring signals present at the same time. This deteriorates spectrum sensing reliability in case of energy detection as well as when more advanced techniques, such as feature detectors, are utilized.

In some systems, the spectrum sensing problems can be avoided using a centralized database for providing information about vacant channels [7], [8]. However, spectrum access itself may be challenging due to the receiver nonlinearities. Especially non-contiguous spectrum access is challenging because there might be strong blocking signals between the desired channels causing nonlinear distortion [3], [4].

In mobile cellular radio systems, limited linearity of mobile devices is evident from their restrictions in size and cost. However, receiver nonlinearity challenges exist also in uplink communications. It is desired that wideband multi-standard base-stations are able to concurrently receive weak and strong signals with a single receiver chain. In addition, there might be strong blocking signals from co-located or nearby transmitters. For example, GSM, UMTS, and LTE specifications define blocker test scenarios which require at least 70 dB spurious-free dynamic range [9]–[11]. In reality, worst case scenarios can be even more challenging.

As shown by the aforementioned use cases, the nonlinearities of wideband receivers are crucial to be considered in order to create practical, more flexible and commercially attractive communications systems, especially when cognitive radio paradigm is exploited. The most prominent approach to tackle the nonlinearity problem is the use of digital post-processing. With behavioral modeling, versatile algorithms can be developed, which are applicable to many different kinds of systems. As one promising approach for receiver linearization, this paper proposes calibration-based post-inverse method. The principle itself is well known in the current literature [12]–[14], but a practical structure for receiver nonlinearity inverse model is an important aspect of this paper. Essential contribution is also comparison with another potential method called adaptive interference cancellation (AIC) [6], [15]–[17]. This is important since the methods have much in common, but have also some fundamental differences which may prevent or make possible their usage on certain applications.

The remainder of the paper is organized as follows. Sec-

This work was supported by the Finnish Funding Agency for Technology and Innovation (Tekes) under the project "Enabling Methods for Dynamic Spectrum Access and Cognitive Radio" within TRIAL technology programme, The Academy of Finland under the project 251138 "Digitally-Enhanced RF for Cognitive Radio Devices", Austrian Competence Center in Mechatronics (ACCM), and Tampere University of Technology Graduate School.

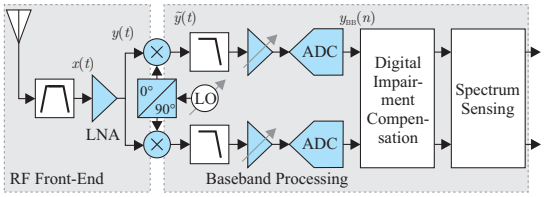

Fig. 1. Conceptual direct-conversion receiver block diagram highlighting the components which are considered as sources of nonlinearity and I/Q imbalance in this paper.

tion II presents mathematical modeling of receiver nonlinearities and discusses their effect on spectrum sensing and access. Section III introduces two nonlinearity compensation methods, namely AIC and calibration-based post-inverse. Performance simulation results and compensation method comparison are given in Section IV. Finally, the paper is concluded in Section V.

II. Receiver Nonlinearity Challenges in Spectrum Sensing and Access

This paper considers wideband direct-conversion receiver due to its integrability, cost-effectiveness, and general popularity. Fig. 1 illustrates a conceptual block diagram of a direct-conversion receiver. Components which are essential sources of nonlinearity and/or I/Q imbalance are highlighted. RF, mixing, and baseband (BB) stages are cascaded in reality and therefore proper nonlinearity modeling requires taking into account their joint effect.

The nonlinearity modeling discussed in this section follows the concept described in [15]. Starting point is the received bandpass signal at the input of the low-noise amplifier (LNA), which has not been distorted by the receiver yet. Its BB equivalent version is

$$x(t) = A(t)e^{j\phi(t)}, \tag{1}$$

which consist of the envelope $A(t)$ and phase $\phi(t)$. Please notice that in this paper $x(t)$ represents the overall received signal which may consist of several individual waveforms at different complex intermediate frequencies (IFs).

The RF distortion caused by the LNA is modeled here with a third-order polynomial. The essential part of the RF distortion can be modeled as

$$y(t) = a_1 x(t) + 3a_2 A^2(t)x(t), \tag{2}$$

where a_1 and a_2 are complex coefficients describing the non-ideal LNA behavior and $y(t)$ is the BB equivalent LNA output. This models the intermodulation distortion (IMD) around the original carrier. Third-order RF nonlinearity also causes harmonics, but those are typically far away from the original carrier and since straightforward to filter out.

In I/Q down-conversion stage, the mixer causes some I/Q imbalance. It is classically modeled as follows:

$$\tilde{y}(t) = k_1 y(t) + k_2 y^*(t), \tag{3}$$

TABLE I
All the Terms Generated by the Cascaded Nonlinearity Model

Terms	Conjugate Terms	Interpretation
$x(t)$	$x^*(t)$	Original undistorted signal
$A^2(t)x(t)$	$A^2(t)x^*(t)$	3rd-order IMD
$[x^*(t)]^3$	$x^3(t)$	3rd-order harmonics
$A^4(t)x(t)$	$A^4(t)x^*(t)$	5th-order IMD
$A^2(t)[x^*(t)]^3$	$A^2(t)x^3(t)$	IMD of 3rd-order harmonics (5th order)
$A^6(t)x(t)$	$A^6(t)x^*(t)$	7th-order IMD
$A^4(t)[x^*(t)]^3$	$A^4(t)x^3(t)$	IMD of 3rd-order harmonics (7th order)
$A^8(t)x(t)$	$A^8(t)x^*(t)$	9th-order IMD
$A^6(t)[x^*(t)]^3$	$A^6(t)x^3(t)$	IMD of 3rd-order harmonics (9th order)

where $k_1 = \left(1 + g_\mathrm{m}e^{-j\phi_\mathrm{m}}\right)/2$ and $k_2 = \left(1 - g_\mathrm{m}e^{j\phi_\mathrm{m}}\right)/2$, which are based on gain mismatch g_m and phase mismatch ϕ_m (in rad). Perfect I/Q balance would be achieved with $g_\mathrm{m} = 1$ and $\phi_\mathrm{m} = 0$. The mixer I/Q imbalance brings on mirror images of both the original signal $x(t)$ and its RF distortion.

After the mixer, the following analog stages are separate for the I and Q branches of the signal. This may cause some additional I/Q imbalance. In addition, the mixer and BB stages cause nonlinear distortion. Their effects are considered here together with a single model. Signal $\tilde{y}(t)$ after the third-order BB nonlinearity is denoted with $y_\mathrm{BB}(t) = B(t)e^{j\theta(t)} = y_\mathrm{I,BB}(t) + jy_\mathrm{Q,BB}(t)$ and can be defined as

$$y_\mathrm{I,BB}(t) = a_\mathrm{3I}\tilde{y}_\mathrm{I}(t) + a_\mathrm{4I}\tilde{y}_\mathrm{I}^3(t), \tag{4a}$$
$$y_\mathrm{Q,BB}(t) = a_\mathrm{3Q}\tilde{y}_\mathrm{Q}(t) + a_\mathrm{4Q}\tilde{y}_\mathrm{Q}^3(t), \tag{4b}$$

where real coefficients a_3I, a_3Q, a_4I, and a_4Q describe the nonlinear behavior independently for I and Q branches. This leads to the overall cascaded nonlinearity model comprising third-order RF and BB nonlinearities as well as the essential I/Q imbalance behavior.

The signal after all aforementioned cascaded impairments, $y_\mathrm{BB}(t)$, can also be written using the undistorted signal $x(t)$. The equation consist of 18 different terms and for the sake of presentation clarity, the terms are tabulated in Table I. The first column lists the terms generated by the cascaded third-order RF and BB nonlinearities without any I/Q imbalance. The second column contains the terms generated if either mixer or BB I/Q imbalance or both occur. All the terms have a different weighting factor, which is a combination of a_1, a_2, a_3I, a_3Q, a_4I, a_4Q, k_1, and k_2. However, these weighting factors are omitted from Table I in order to keep it concise. Further details can be found from [15]. Typically, many of these 18 terms are buried under the noise floor and do not have to be considered in practice. However, it is easy to conceptually interpret the meanings of all the terms. They can be divided in two categories: IMD around the original IF and harmonics/IMD around triple the original IF (third-order harmonics zone). The exponent of the envelope $A(t)$ is proportional to the bandwidth of the distortion.

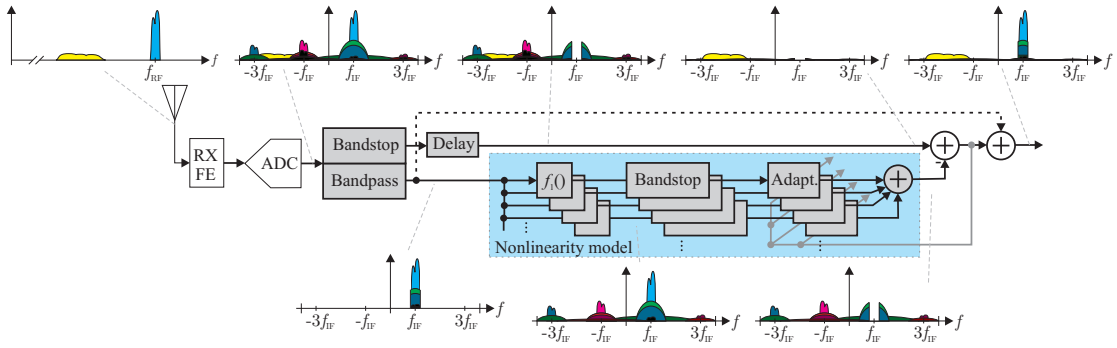

Fig. 2. Block diagram illustrating the principle of AIC method for receiver linearization. Conceptual spectra illustrate the processing flow for one weak signal and one strong blocking signal.

TABLE II
TERMS USED IN AIC FOR NONLINEARITY MODELING

Terms	Interpretation
$\hat{x}^*(n)$	Mirror image of the undistorted signal
$A^2(n)\hat{x}(n)$	3rd-order IMD
$A^2(n)\hat{x}^*(n)$	Mirror image of 3rd-order IMD
$[\hat{x}^*(n)]^3$	3rd-order harmonics
$\hat{x}^3(n)$	Mirror image of 3rd-order harmonics

The power of the distortion caused by receiver nonlinearities is proportional to the power of the signal. Therefore strong signals may cause significant amount of distortion to neighboring channels which can interfere with spectrum sensing. The interference impact is two-fold. On the one hand, the distortion may cause false alarms in energy detectors and also in cyclostationary feature detectors, if the distortion possess similar features as the original signal [6]. On the other hand, the distortion may mask weak signals so that feature detectors are not able to discover them, i.e., missed detections are caused.

Receiver nonlinearities may cause problems even if the spectrum sensing is not necessary. Vacant channels might be known, e.g., due to *a priori* information from a centralized database. However, spectrum access is challenging due to the receiver nonlinearities, if strong adjacent-channel signals are concurrently present. This is especially true in case of non-contiguous spectrum access, if the strong blocking signals are located between the exploited non-contiguous spectrum chunks.

III. COMPENSATION OF RECEIVER NONLINEARITIES

This section gives descriptions of two feasible methods for receiver linearization. First method adaptively finds a receiver nonlinearity model for cancelling nonlinear distortion, where as second method uses calibration signal to find post-inverse model for receiver nonlinearities.

A. Adaptive Interference Cancellation

AIC principle is described in [15] as it is also employed in this paper. The basic idea is illustrated with a block diagram in Fig. 2. A digitized signal is split into main branch and reference branch. The latter one contains only the blockers whereas the main branch all the other received signal content except the blockers. The nonlinear distortion generated by the received front-end is re-generated in the reference branch by applying in parallel different polynomial terms to the blockers. In order to avoid over-complicated system, only the essential terms are used from the overall model described in Section II. The selected nonlinearity terms for the AIC are listed in Table II. Notation $\hat{x}(t)$ refers to the estimate of $x(t)$ which is obtained with the bandpass filter shown in Fig. 2. The re-generated nonlinear distortion is then subtracted from the main branch thus compensating the nonlinear distortion in the received signal. Proper adaptive weights (or filters in case of nonlinearities with memory) can be found by using, e.g., the classical least-mean square (LMS) algorithm. If blocker signals are also desired to be received, they can be added back to the main branch signal after the processing as suggested by the dashed line in Fig. 2.

B. Calibration-Based Post-Inverse

In general, the effect of polynomial nonlinearity can be compensated with a post-inverse model. However, finding an exact inverse can be challenging and typically even simple polynomials have inverses of infinite order [13], [14]. For compensating receiver nonlinearities, this paper proposes using a post-inverse having terms listed in Table III. These terms are based on receiver modeling described in Section II. Only the most essential terms are selected to limit the complexity. Compared to the AIC terms in Table II, inverse modeling requires also the linear signal term and higher order IMD term. The principle of the proposed post-inverse processing is shown in Fig. 3. During the normal receiver operation, the received distorted signal after ADC is fed to the post-inverse nonlinearity model which then outputs the less distorted signal. The weights (or filters in case of nonlinearities with memory)

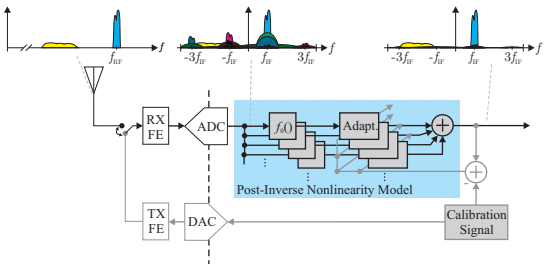

Fig. 3. Block diagram illustrating the principle of calibration-based post-inverse for receiver linearization. Conceptual spectra illustrate the processing flow for one weak signal and one strong blocking signal.

TABLE III
TERMS USED IN INVERSE NONLINEARITY MODELING

Terms	Interpretation
$y_{\mathrm{BB}}(n)$	Distorted signal
$y^*_{\mathrm{BB}}(n)$	Mirror image of distorted signal
$B^2(n)y_{\mathrm{BB}}(n)$	3rd-order IMD
$B^2(n)y^*_{\mathrm{BB}}(n)$	Mirror image of 3rd-order IMD
$[y^*_{\mathrm{BB}}(n)]^3$	3rd-order harmonics
$y^3_{\mathrm{BB}}(n)$	Mirror image of 3rd-order harmonics
$B^4(n)y_{\mathrm{BB}}(n)$	5th-order IMD

of the post-inverse nonlinearity model are adapted using a calibration signal. This can be done during the idle periods in the reception. Using the transmitter, the calibration signal is fed to the receiver front-end. Due to the known calibration signal, the weights/filters of the post-inverse nonlinearity model can be found using, e.g., the LMS algorithm. In principle, the calibration signal can be any wideband signal that the transmitter can properly generate and the digital version of it is known by the receiver.

IV. Simulation Results for Compensation Method Comparison

Simulations examples in this section focus on a wideband OFDM mobile receiver capable of non-contiguous spectrum access. All essential simulation parameters are given in Table IV. A two-tone calibration signal with -27 dBm average power at the receiver input is used by the inverse method in all the simulations presented here.

First example considers two 10-MHz wide blocker signals at down-converted center frequencies of 10 MHz and 30 MHz, average received signal power being -33 dBm. Spectrum illustration is given in Fig. 4. The mirror images of the blockers can be seen at -10 MHz and -30 MHz. The IMD of the blockers is widely spread around the spectrum. It consists of spreading around the center frequencies of the blockers and also IMD caused by interaction between the blockers. The latter IMD can be partially seen as a spreading around -10 MHz. In the simulations, the weights for the nonlinearity models in both

TABLE IV
SIMULATION PARAMETERS

Parameter	Value	
LNA gain	15	dB
LNA IIP3	-10	dBm
Mixer IRR	30	dB
Baseband gain	35	dB
Baseband IIP3	5	dBm
Sampling rate	80	MHz
Quantization	12	bits
Channel bandwidth	10	MHz
OFDM subcarrier spacing	15	kHz
Number of active subcarriers	600	
Subcarrier modulation	16-QAM	
Guard interval	1/4	

compensation methods are found with block least-squares in order to make the results as well comparable as possible. Fig. 4 illustrates also how well the compensation methods are able to remove the distortion. The post-inverse method performs slightly better due to the usage of calibration signal. AIC reference signal suffers from inband distortion of the blockers, because the reference is extracted from the received distorted signal. In addition, reference signal extraction causes degraded compensation performance at blocker band edges due to the bandpass filter transition bands.

Second example has two weak signals at center frequencies -20 MHz and 0 MHz in addition to the blockers of the previous example. This scenario is shown in Fig. 5. It is evident from the spectrum that reception of the weak signals is impossible due to the vast amount of nonlinear distortion. However, both compensation methods are performing well enough so that the weak signals are clearly observable from the spectrum.

In order to provide wider view on the performance of the compensation methods, distortion rejection ratio (DRR) is used as a figure of merit. It is defined as

$$DRR = \frac{S+N}{D}, \tag{5}$$

where S, N, and D are signal, noise, and distortion powers, respectively. Fig. 6 presents *wideband DRR* as a function of receiver signal power. Wideband DRR means that the values are calculated for the whole 80-MHz reception band excluding blocker signal bands. Received signal power is stated as average power of the whole received waveform in the LNA input. Weak signals are always having the same -80 dBm average power per channel, but the power of the blockers is varied. It is also interesting look at DRR of a specific signal band. These *narrowband DRR* values are given in Fig. 7 for the weak signal bands. When blocker power increases, the uncompensated narrowband DRR decreases and eventually there is more distortion power than useful signal power. The calibration-based post-inverse method is able to

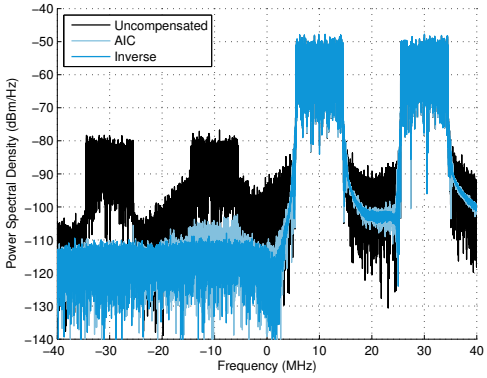

Fig. 4. Spectral illustration of nonlinearity compensation performance with two blocker signals having down-converted center frequencies 10 MHz and 30 MHz, average received signal power being -33 dBm.

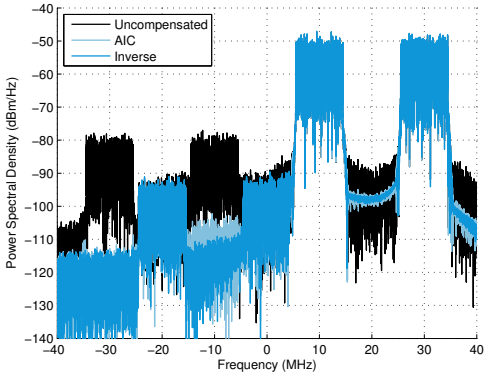

Fig. 5. Spectral illustration of nonlinearity compensation performance with two weak signals having down-converted center frequencies -20 MHz and 0 MHz concurrently with two blocker signals (at 10 MHz and 30 MHz), average received signal power being -33 dBm.

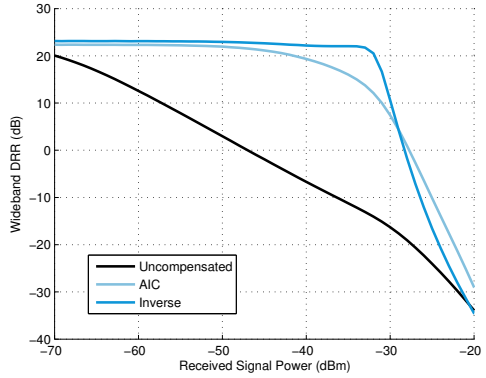

Fig. 6. Wideband distortion rejection ratio as a function of received signal power. The whole reception band excluding blockers are considered in wideband DRR.

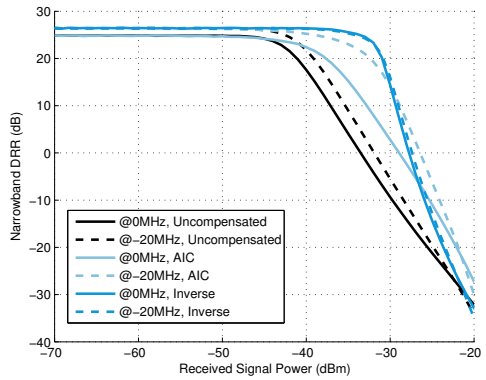

Fig. 7. Narrowband distortion rejection ratio as a function of received signal power. Narrowband DRR considers only a specific weak signal band.

provide similar DRR values for both weak signals where as AIC gives slightly lower DRR for the weak signal around 0 MHz. This is because AIC uses bandpass filter to pick the blockers and the compensation is not perfect in the filter transition band where the weak signal is partially located.

In the provided examples, both compensation methods are performing well. However, these methods have some fundamental differences which indicates that it is application specific issue which one is more suitable. AIC is able to adapt its model coefficients continuously during the normal receiver operation and is therefore able to quickly follow the changes in nonlinearities, which may happen due to the variations in environmental conditions such as in temperature. On the other hand, AIC extracts a reference signal from the received distorted signal, which decreases the accuracy of the interference cancellation. The post-inverse method uses calibration signal which guarantees more accurate nonlinearity modeling. However, the calibration cannot be done during the normal receiver operation. Other difference is that the post-inverse method removes distortion from the whole reception band whereas AIC is able to only cancel distortion outside the blocker bands. This may be a problem only if also the blocker signals are desired to be demodulated by the receiver. From the complexity point of view, the post-inverse method is more simple since it does not use the bandpass and bandstop filters required in AIC. Furthermore, the post-inverse method does not require the knowledge about blocker band locations and bandwidths.

It is worth noticing that the coefficients in the calibration-based post-inverse model are independent of the received signal power, at least up to the calibration signal power. However,

they depend on the receiver front-end nonlinearities and gains. Therefore the calibrated post-inverse model coefficients are directly valid only for certain receiver front-end configuration. If, e.g., amplifier gains are adjusted, also the optimal post-inverse model coefficients may change. One option is to calibrate different set of inverse-model coefficients for different receiver front-end configurations. Other option is to calibrate only once, but weight the inverse-model coefficients properly according to the gain adjustments. In both options, some knowledge about the receiver front-end configuration is required. This is a reasonable requirement because, e.g., the receiver gains are typically digitally controlled and therefore information about gain changes is available for the compensation method.

V. Conclusion

This paper discussed and developed digital post-processing methods for linearizing wideband radio receivers in order to enhance wideband non-contiguous spectrum sensing and access. Two methods, adaptive interference cancellation and calibration-based post-inverse, were compared with computer simulations in challenging non-contiguous spectrum access scenario with strong blocking signals. The post-inverse method is able to provide better linearization performance, but is only suitable for applications where calibration periods are allowed. Adaptive interference cancellation method is able to work without calibration, but is computationally more complex. However, both methods are waveform-independent and therefore applicable to wide variety of systems.

References

[1] A. A. Abidi, "Direct-conversion radio transceivers for digital communications," *IEEE J. Solid-State Circuits*, vol. 30, no. 12, pp. 1399–1410, Dec. 1995.

[2] B. Razavi, "Design considerations for direct-conversion receivers," *IEEE Trans. Circuits Syst. II*, vol. 44, no. 6, pp. 428–435, June 1997.

[3] D. H. Mahrof, E. A. M. Klumperink, J. C. Haartsen, and B. Nauta, "On the effect of spectral location of interferers on linearity requirements for wideband cognitive radio receivers," in *Proc. IEEE Symp. on New Frontiers in Dynamic Spectrum (DySPAN2010)*, Singapore, Apr. 2010, pp. 1–9.

[4] B. Razavi, "Cognitive radio design challenges and techniques," *IEEE J. Solid-State Circuits*, vol. 45, no. 8, pp. 1542–1553, Aug. 2010.

[5] M. Vääräkangas, S. Kallioinen, A. Pärssinen, V. Turunen, and J. Ryynänen, "Trade-offs in primary detection using a mobile phone as a sensing device," in *Proc. 6th Int. ICST Conf. on Cognitive Radio Oriented Wireless Networks and Communications (CROWNCOM2011)*, Osaka, Japan, June 2011, pp. 241–245.

[6] M. Allén, J. Marttila, M. Valkama, S. Mäkinen, M. Kosunen, and J. Ryynänen, "Digital linearization of direct-conversion spectrum sensing receiver," in *Proc. 1st IEEE Global Conf. Signal and Information Process. (GlobalSIP2013)*, Austin, TX, USA, Dec. 2013, pp. 1158–1161.

[7] D. Gurney, G. Buchwald, L. Ecklund, S. Kuffner, and J. Grosspietsch, "Geo-location database techniques for incumbent protection in the TV white space," in *Proc. 3rd IEEE Symp. on New Frontiers in Dynamic Spectrum Access Networks (DySPAN2008)*, Oct. 2008, pp. 1–9.

[8] R. Murty, R. Chandra, T. Moscibroda, and P. Bahl, "SenseLess: A database-driven white spaces network," *IEEE Trans. Mobile Comput.*, vol. 11, no. 2, pp. 189–203, Feb. 2012.

[9] *Digital cellular telecommunications system (Phase 2+); Radio transmission and reception*, 3GPP TS 45.005 version 11.4.0 Release 11, Jan. 2014.

[10] *Universal Mobile Telecommunications System (UMTS); Base Station (BS) radio transmission and reception (FDD)*, 3GPP TS 25.104 version 11.8.0 Release 11, Jan. 2014.

[11] *LTE; Evolved Universal Terrestrial Radio Access (E-UTRA); Base Station (BS) radio transmission and reception*, 3GPP TS 36.104 version 11.7.0 Release 11, Jan. 2014.

[12] H. F. Lundin, "Characterization and correction of analog-to-digital converters," Ph.D. dissertation, School Electrical Eng., Royal Inst.Technology, Stockholm, Sweden, 2005.

[13] J. Tsimbinos, "Identification and compensation of nonlinear distortion," Ph.D. dissertation, School Electronic Eng., Univ. of South Australia, Adelaide, Australia, 1995.

[14] J. Tsimbinos and K. V. Lever, "Nonlinear system compensation based on orthogonal polynomial inverses," *IEEE Transactions on Circuits and Systems: Fundamental Theory and Applications*, vol. 48, no. 4, pp. 406–417, Apr 2001.

[15] M. Grimm, M. Allén, J. Marttila, M. Valkama, and R. Thomä, "Joint mitigation of nonlinear RF and baseband distortions in wideband direct-conversion receivers," *IEEE Trans. Microw. Theory Tech.*, vol. 62, no. 1, pp. 166–182, Jan. 2014.

[16] M. Valkama, A. Shahed hagh ghadam, L. Anttila, and M. Renfors, "Advanced digital signal processing techniques for compensation of nonlinear distortion in wideband multicarrier radio receivers," *IEEE Trans. Microw. Theory Tech.*, vol. 54, no. 6, pp. 2356–2366, June 2006.

[17] E. Rebeiz, A. Shahed hagh ghadam, M. Valkama, and D. Cabric, "Suppressing RF front-end nonlinearities in wideband spectrum sensing," in *Proc. 8th Int. Conf. Cognitive Radio Oriented Wireless Networks (CROWNCOM2013)*, Washington D.C., July 2013, pp. 87–92.

Tampereen teknillinen yliopisto
PL 527
33101 Tampere

Tampere University of Technology
P.O.B. 527
FI-33101 Tampere, Finland

ISBN 978-952-15-3595-6
ISSN 1459-2045